The development of a β-decay tape station and the search for vibrations in Ruthenium isotopes

Lucky Maxwell Makhathini

Dissertation presented for the degree of Doctor of Philosophy
in the Faculty of Science at Stellenbosch University

Supervisor: Dr. R. A. Bark (iThemba LABS)
Co-supervisors: Prof. P. Papka (Stellenbosch University)
Prof. E.G. Rohwer (Stellenbosch University)
Dr. J.J. Van Zyl (Stellenbosch University)

March 2021

Declaration

By submitting this thesis electronically, I declare that the entirety of the work contained therein is my own, original work, that I am the sole author thereof (save to the extent explicitly otherwise stated), that reproduction and publication thereof by Stellenbosch University will not infringe any third party rights and that I have not previously in its entirety or in part submitted it for obtaining any qualification.

March 2021

Abstract

This work gives details of the new facility that is introduced to iThemba LABS for nuclear structure studies, called the tape station. The technical description of this device is presented along with an experimental demonstration. A user-friendly control system for this device is developed and it can easily be integrated into the existing beam control system for the iThemba LABS beamline line control systems. Two versions of this device were successfully used to conduct experiments.

The versatility of this device is demonstrated by performing multiple experiments, one with a shorter half-life and two with long half-lives. A method to produce "short-lived nuclei (radioactive nuclei)" at iThemba LABS is given. The low-lying states of ^{98,100}Ru were investigated using the γ-ray spectroscopy following the β-decay of ^{98,100}Rh. The source of activity for ^{162}Yb was produced using the ^{147}Sm(^{19}F, 4n) reaction while in ^{98}Ru and ^{100}Ru were produced using the ^{89}Y(^{12}C, 3n)^{98}Rh and ^{89}Y(^{14}N, p2n)^{100}Rh, ^{89}Y(^{14}N, 3n)^{100}Pd reactions at beam energies of 45 MeV and 47 MeV, respectively.

The results obtained from experimental data are given and analysed. The ^{162}Yb study demonstrated that this device is capable to be used to probe nuclei with shorter half-lives. While for ^{100}Ru the data confirmed the γ-rays observed in the previous measurement, while in ^{98}Ru new γ-rays were observed.

The newly assigned γ and 0_2^+ bands in ^{98}Ru fit well in the systematics of these excitations assigned in the heavier Ru isotopes while ^{100}Ru differs. Beyond-mean-field calculations employing the self-consistent configuration mixing method suggest that the Ru isotopes are triaxiality deformed and shape coexistence occurs around ^{98}Ru.

Uittreksel

'n Nuwe fasiliteit wat gebruik kan word in kern struktuur navorsing is beskikbaar by die iThemba Laboratory of Accelerator Based Sciences (LABS). Hierdie fasiliteit, die sogenaamde bandstasie (tapestation), sal in detail beskryf word, asook 'n tipiese eksperiment. 'n Gebruikersvriendelike beheerstelsel wat maklik geintegreer kan word met die bundel beheerstelsel wat by iThemba LABS gebruik word is ontwikkel. Daar bestaan twee weergawes van hierdie nuwe eksperimentele fasiliteit, en beide is reeds suksesvol gebruik.

Hierdie metings, twee waarvan die bestudeerde halfleeftyd lank was en een waarvan die halfleeftyd van belang kort was, toon duidelik die veelsydige aard van die bandstasie. In hierdie tesis word die eksperimentele proses bespreek wat gebruik is om radioaktiewe kerne met 'n kort halfleeftyd te vervaardig. Laagliggende energie toestande van ^{98,100}Ru is bestudeer met behulp van gamma-straal spektroskopie asook beta verval metings. Die radioaktiewe kern ^{162}Yb is ook bestudeer, en is verkry deur die ^{147}Sm(^{19}F, 4n) reaksie. Die kerne ^{98}Ru and ^{100}Ru is respektiewelik verkry deur die volgende reaksies: ^{89}Y(^{12}C, 3n)^{98}Rh en ^{89}Y(^{14}N, p2n)^{100}Rh, ^{89}Y(^{14}N, 3n)^{100}Pd.

Analise van die eksperimentele data vir die ^{162}Yb studie toon dat die bandstasie effektief gebruik kan word om kerne met 'n kort leeftyd te bestudeer. Bekende waardes vir gamma strale vanaf ^{100}Ru is bevestig in hierdie metings, terwyl nuwe gamma oorgange waargeneem is vir die ^{98}Ru kern.

Nuut toegekende waardes vir die and 0_2^+ bande in ^{98}Ru bevestig bestaande sistematiek soos bekend vir soortgelyke opwekkings in swaarder Ru isotope. Vir die ^{100}Ru kern is die situasie egter anders. Gesofistikeerde teoretiese berekening wat 'n stap verder gaan as die standaard gemiddelde veld aanname, en wat gebruik maak van die eie konsistente konfigurasie menging metode, toon aan dat Ru isotope beskou kan word as drie-as vervormed kerne, en dat ^{98}Ru aspekte van vorm naasbestaan toon.

Acknowledgements

"Remember to look up at the stars and not down at your feet. Try to make sense of what you see and wonder about what makes the universe exist. Be curious. And however difficult life may seem, there is always something you can do and succeed at. It matters that you dont just give up. While there is life, there is hope" Prof Stephen Hawking

My gratitude to the following people and organization:

I have to acknowledge the National Research Foundation-iThemba LABS for financial support and creating a research platform for young African students.

To Dr. RA Bark, I am grateful for the support, assistance, countless discussion which have contributed to the success of this project.

To Professor P Papka for providing the platform, countless advice, designing the cold trap, installing the filling system in the A-line vault and reading my manuscript.

To tape station crew: Dr. RA Bark, Mr. S Baard, Mr. L Makhathini, brilliant effort guys, job well done!

To my Canadian collaborators, professor PE Garrett for proposing the Ru experiment, which contributed immensely to this work.

To Tomaz Rodriguez for performing theoretical calculation.

To electronic division at iThemba LABS: Dr. W Duckitt, J Abrahams, and Peter Davids for assisting with setting up the electronics and stepper motor.

To Dr. F Nemulodi for countless assistance with Python and CSS programming.

To Dr. TS Dinoko, Dr. PP Meleka, and Dr. D Bucher for their comments on the manuscript and suggestions for further reading.

To my family for understanding and support, I know its been a tough journey.

To my wife: Nqobile, for countless support, at times I thought of giving up but you kept on

believing that one day everything will be alright.

To my siblings, Musawenkosi, Silindile, Lindokuhle and Amanda this one is for you guys, niyazi lasiphuma khona, and asikafiki ekugcineni.

To Dr. Rakes and Doris for fabricating the plastic scintillator, you guys did an amazing job.

To the workshop team, especially Peter Pulse, your assistance has been well received.

To everyone who contributed to making this work a success.

I have to thanks myself as well, it been a tough and rough journey, the words of my first lecture at university kept me going "there is no road that is not rough".

Dedication

To my family for their support and guidance, but most importantly, to my wife who suffered alone in-silence through these years while pursuing this dream.

Contents

List of Figures

List of Tables

Chapter 1

Introduction

1.1 Introduction

The iThemba for Laboratory Accelerator Based Science (LABS) provides particle beams for number of disciplines, including nuclear physics research, material research, biological research and production of radioisotopes for medical imaging. The current floor plan of iThemba LABS showing all of the vaults and beam-lines is given in figure 1.1. Particle beams of stable nuclides for both research and isotope production are delivered by the K=200 Separated Sector Cyclotron (SSC), to the respective vaults depending on the planned or scheduled experiment. This machine can only produce particle beams of stable nuclei. For the past decades, international research has been making use of different kinds of beams, especially particle beams of radioactive nuclei. These particle beams are not available at iThemba LABS. Radioactive nuclide must be produced artificially before they can be accelerated into a beam.

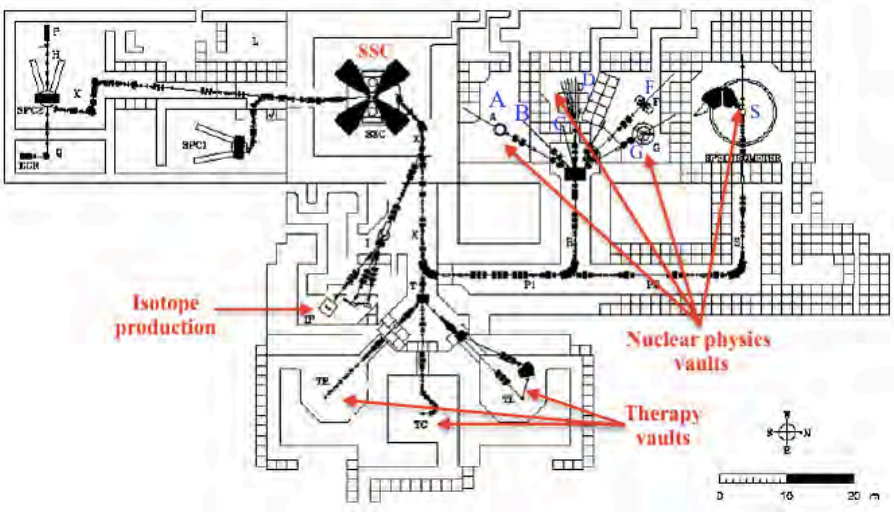

Figure 1.1. The current floor plan of iThemba LABS showing the vaults exposed to beam line.

1.1.1 Radioactive Beams

To maintain the scientific competitiveness of iThemba LABS, a Radioactive-Ion Beam (RIB) facility has been proposed. The first step to realize RIBs at iThemba LABS will be the development of a Low-Energy Radioactive-Ion Beam (LERIB) facility. This will be possible by producing fission fragments when a Uranium Carbide (UC_x) target is bombarded by a proton beam. Radioactive-ion beams can be produced by using the Isotope Separation On-Line (ISOL) method [1]. For example, neutron-rich nuclides can be produced by using proton-induced fission on a production target of uranium carbide or using a converter target e.g. using the proton beam to create neutrons, thereafter utilizing those those neutrons to induce fission in uranium carbide [1, 2].

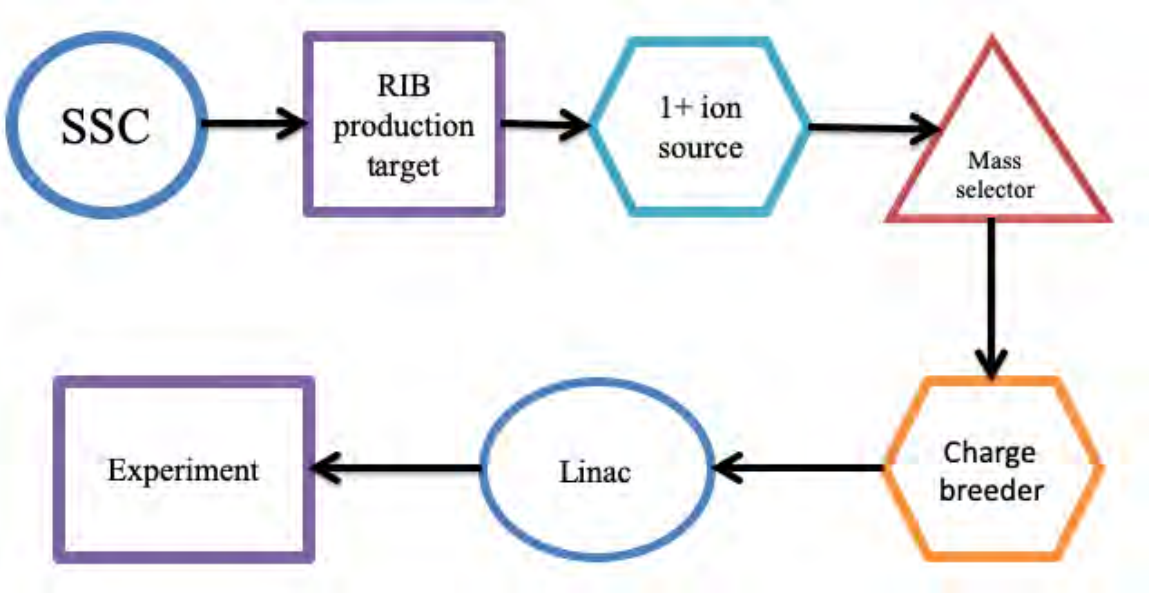

Figure 1.2. Planned stages/involved in the production of radioactive-ion beams at iThemba LABS [2].

Figure 1.2 illustrates the steps that would be implemented in the ISOL method at iThemba LABS to produce radioactive-ion beams. The collection of radioactive-atoms from the production target will occur in an ion-source (usually using a Resonant-Ionization Laser-Ion Source (RILIS)) directly connected to the target where the atoms are ionized to the 1^+ charge-state. Thereafter, a final mass selection is achieved by using a high-resolution magnetic spectrometer as a mass analyzer. The facility will not have a post-accelerator but over 10^{12} fissions/seconds will yield intense neutron-rich RIBs of about 60 keV energy. Hence, the major emphasis will be on β-decay studies with those beams. This typically involves a tape station to remove the unwanted activity from the daughters of the species of interest.

The commissioning of this project will be expected by 2024. Therefore, we are building and developing a β-decay station utilizing a tape station to gain knowledge for studying short-lived

radioactive nuclei. The simplest method to study short-lived nuclei is by β-decay, since the parent nucleus need only to be trapped in the sight of γ-ray and β-particle detectors, allowing its decay to the excited states of the daughter nucleus and their subsequent decay to the ground state to be observed. After the development of a tape station, it will be used for in-beam β-decay measurement to probe atomic nuclei.

The first-step in developing RIBs at iThemba LABS will be to develop the LERIB, Phase 0 facility, shown in figure 1.3. The proton beam from the SSC will be used to bombard the UC_x target which will be installed in the "front-end" target-ion source system. The front-end will be housed in a new building as illustrated in figure 1.3. The square blocks in figure 1.3 represent the concrete wall used for shielding and the LERIB facility is circled in red [2].

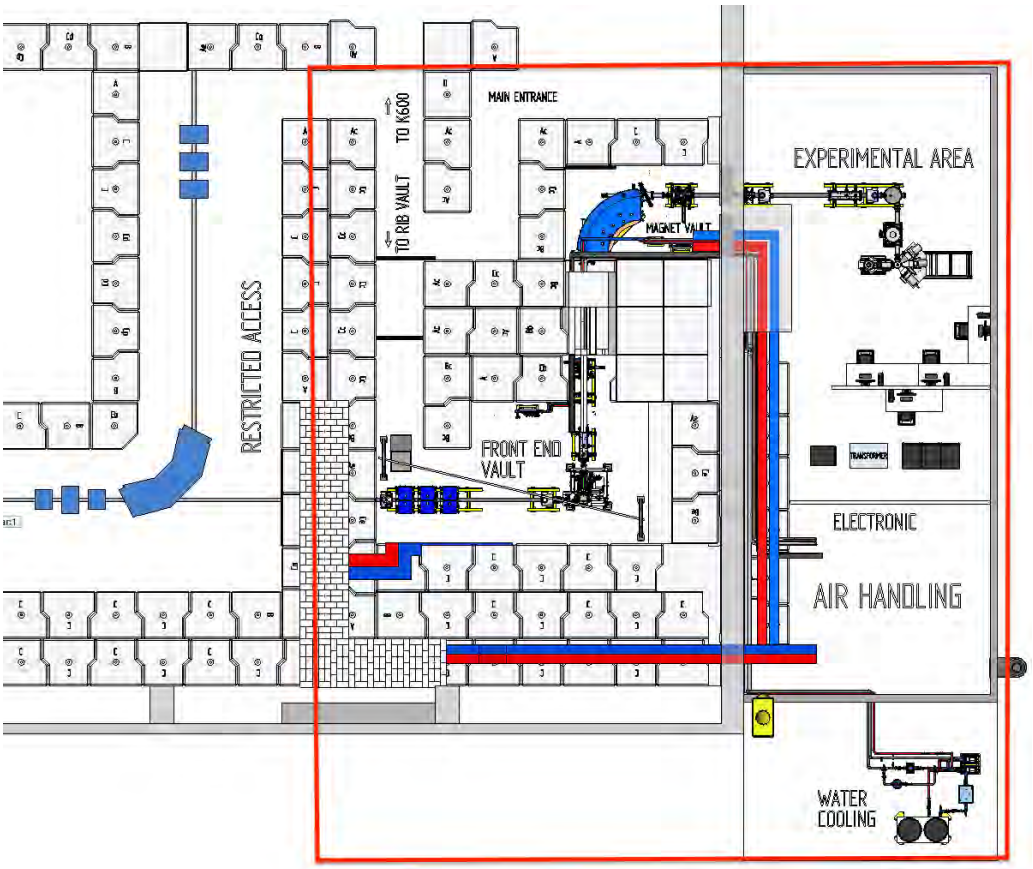

Figure 1.3. Schematic diagram of the recently proposed Low-Energy Radioactive-Ion Beam, phase 0 facility at iThemba LABS.

LERIB Phase 0, figure 1.3, will have limited beam current (< 1 μA) but will be used to develop and refine the techniques for RIB production and analysis. Knowledge, experience and equipment gained through LERIB Phase 0 will be carried forward into a full-fledged RIBs facility (Phase 1). A number of end-station for low-energy experiments will be provided [3].

1.2 Aim

This work is motivated by the near-term desire to study the properties of Ruthenium isotopes - to ask whether the low-spin levels of ^{98,100}Ru can be understood as an example of spherical vibrations - and to develop a tape station for the future RIB facility. Two measurements will be presented, firstly a test measurement on ^{162}Yb, with a half-life of 14 seconds followed by a study of ^{98,100}Ru isotopes from the β-decay of ^{98,100}Rh, with ^{98}Rh having a half life of 8.72 minutes while ^{100}Rh has two halflives, 4.6 minutes and 20.8 hours from the ground state decay and from an isomer, respectively. In both experiments, γ-rays and conversion electron will be measured. Two versions of the tape station will be used to study these nuclides, depending on the half-life of the nucleus of interest.

1.2.1 ^{98,100}Ru

A general survey has been performed by Kern *el al.* [4], seeking candidates for spherical vibrators on the nuclear chart. Figure 1.4 displays those nuclides found to be candidates: those in bold boxes were considered as having passed the criteria for spherical vibrators.

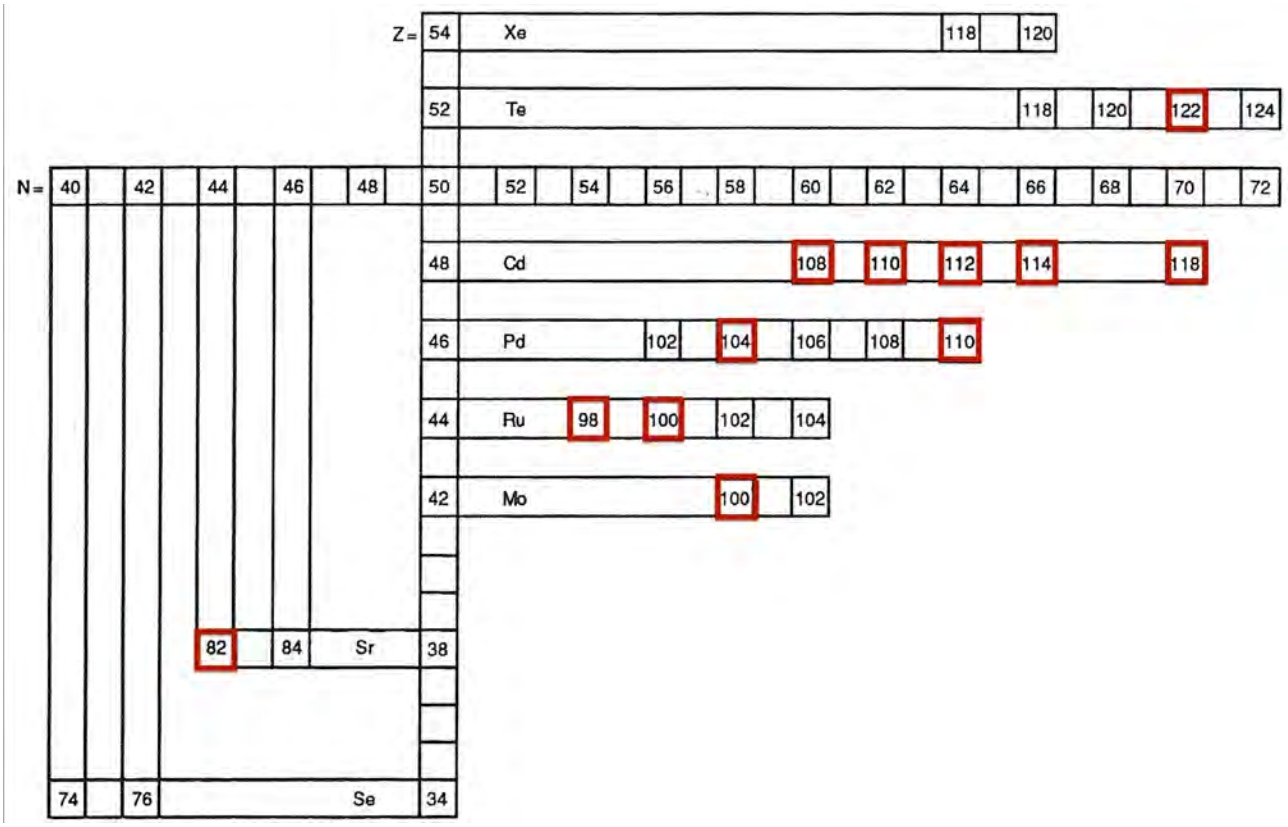

Figure 1.4. Nuclei considered to have passed the criteria for spherical vibrators by Kern. Boxes with bold lines were considered as the best candidates for vibrational behavior. Atomic number Z, neutron number N, are indicated along with atomic number A, inside the boxes. Figure taken from [4].

Another critical re-evaluation of nuclides that were regarded [4] as paradigms of spherical vibrational motion was conducted by P.E. Garrett *et. al.* [5], especially Cd isotopes. It was found that many previously suggested candidates spherical vibrators fail to meet the required guidelines. For example, Cd isotopes [6] have been known as the text-book examples of spherical vibrators but in fact are examples of shape coexistence. With the rejection of the Cd isotopes as spherical vibrators, a natural question arose: are there any examples of spherical vibrators?

The most promising candidates surviving the updated survey appear to be the Ruthenium isotopes, especially ^{98}Ru and ^{100}Ru. The decay of low spin levels in these candidate nuclei are rather poorly characterized, especially regarding the low energy γ-ray decay branches. These branches are likely to have gone undetected in previous experimental studies since they have low intensity due to competing high-energy γ-ray branches, rather than being due to the smallness of the transition matrix element.

This work will try to understand the nature of the low-lying states in Ru isotopes - whether they are of vibrational character, rotational, or have symptoms of shape coexistence. These concepts will be expanded-on in chapter 2. The aim is too remedy the poor state of knowledge of decays of the non-yrast states in ^{98,100}Ru by performing a highly sensitive β-decay study of ^{98,100}Rh using the tape station.

1.3 Dissertation Outline

This work presents the development of the tape station used in the spectroscopic investigation of ^{162}Yb and ^{98,100}Ru isotopes using β-decay technique. The goal is to perform an in-beam measurement to gain experience in the operation of this new facility while a scientific goal is to gain the understanding of origin of deformation in the rare-earth region and seeking candidates for spherical vibrational, especially in Ruthenium isotopes. Nuclear theory is presented in chapter 2 and 4, while the systematics of Ruthenium isotopes in presented in chapter 3. The design of the tape station in presented in chapter 5 while the commission test followed in chapter 6. Experimental results in presented in chapter 7, while chapter 8 interprets the experimental results. The last chapter concludes this work and gives future prospects.

Chapter 2

Nuclear theory

2.1 Liquid Drop model

The first model which described the behaviour of nuclear binding energies, hence nuclear masses, was the Semi-Empirical Mass Formula (SEMF), which was published in 1935 by Carl Friedrich Von Weizsacker. This formula was based on the liquid drop model proposed by George Gamow [7]. According to this model, the atomic nucleus behaves like a drop of liquid made out of nucleons which are held together by the strong nuclear force. Their mean free path is less than the nuclear radius, which is given by the following equation:

$$R_{av} = R_0 A^{1/3} \tag{2.1}$$

where R_0= 1.2 fm. The binding energy (BE) is expressed by the SEMF as follows:

$$BE(MeV) = a_v A - a_s A^{2/3} - a_C Z^2 A^{-1/3} - a_A \frac{(A-2Z)^2}{A} \pm \delta a_p(A,Z) \tag{2.2}$$

where

$$\delta = \begin{cases} \delta = +\delta_0 \text{ for even } Z \text{ and } N \\ 0 \\ \delta = -\delta_0 \text{ for odd } Z \text{ and } N \end{cases} \tag{2.3}$$

where N is the neutron number, Z is the proton number and A is mass number (A= N+Z).

The physical meaning of this formula can be understood by discussing the individual terms of equation 2.2. The first term a_v is referred to as the volume term. This term results from the strong nuclear force, which has a very limited range so that nucleons only interact with their nearest neighbours. The second term, a_s is referred to as the surface term. This term arises from the nuclear force but accounts for nucleons on the surface which do not have as many interactions as those inside the nucleus. The third term, a_C is called the Coulomb term. It arises from the electrostatic repulsion of protons in the nucleus. The fourth term, a_A accounts for the exclusion principle which describes the energy loss to the nucleus due to an unequal number of protons and neutrons. The last term, δ accounts for pairing. The strength of these terms have the following values: a_v = 15.85 MeV, a_s= 18.34 MeV, a_C = 0.71 MeV, a_A= 23.21 MeV and a_p =12 MeV [7]. The SEMF equation connects the experimental information on masses with prediction from theory.

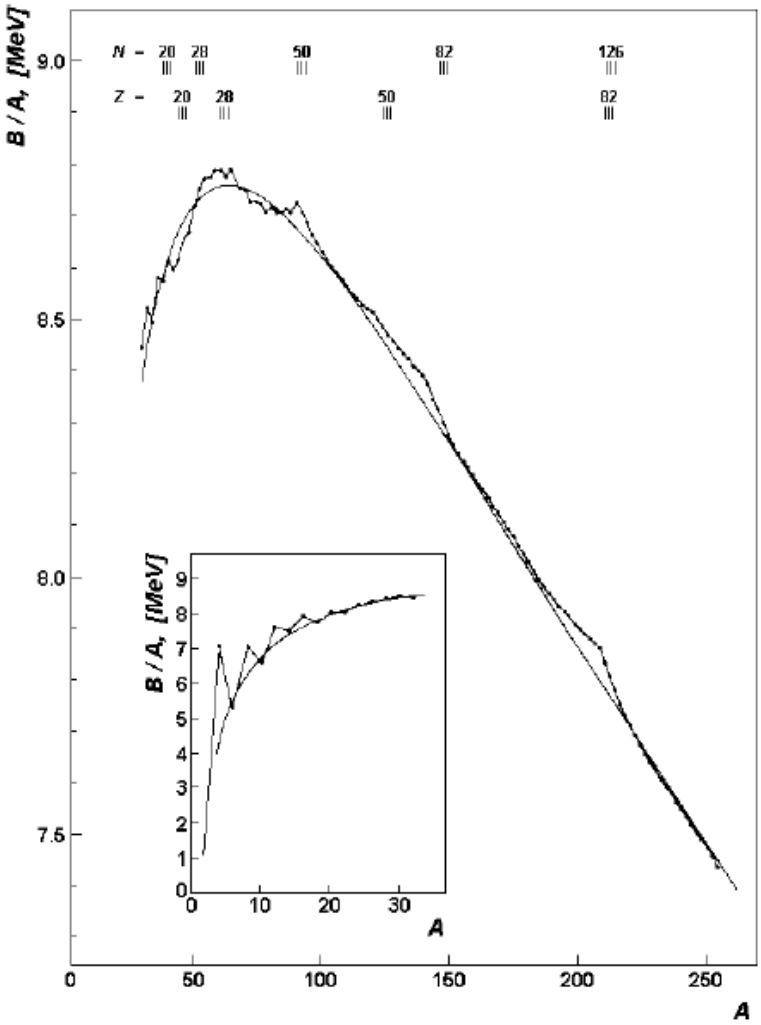

Figure 2.1. The illustration of binding energy per nucleon as function of atomic mass number. The curve symbolizes the liquid drop model without the correction of nucleon pairing while the small figure shows the region of nuclide with light masses [8].

Figure 2.1 shows the dependence of the observed binding energy per nucleon (B/A) on the

mass number A. In figure 2.1, there is a good agreement for the majority of nuclides at or near the β stability line. The power of the SEMF lies in providing some ideas of the general trend in nuclear binding energies. The importance of the SEMF is that it is regarded as the first attempt to apply a nuclear model to understand the systematic behaviour of nuclear properties and lays the foundation for the development of the collective model.

The importance of the magic numbers (2, 8, 20, 40, 50, 82 and 126), shown on figure 2.1, at these numbers, implying the existence of shells. The magic numbers can also be demonstrated by the evolution of the energy of the first 2^+ state of even-even nuclei a as function of neutron number N, as shown in figure 2.2. A similar trend can be seen for magic numbers corresponding to protons.

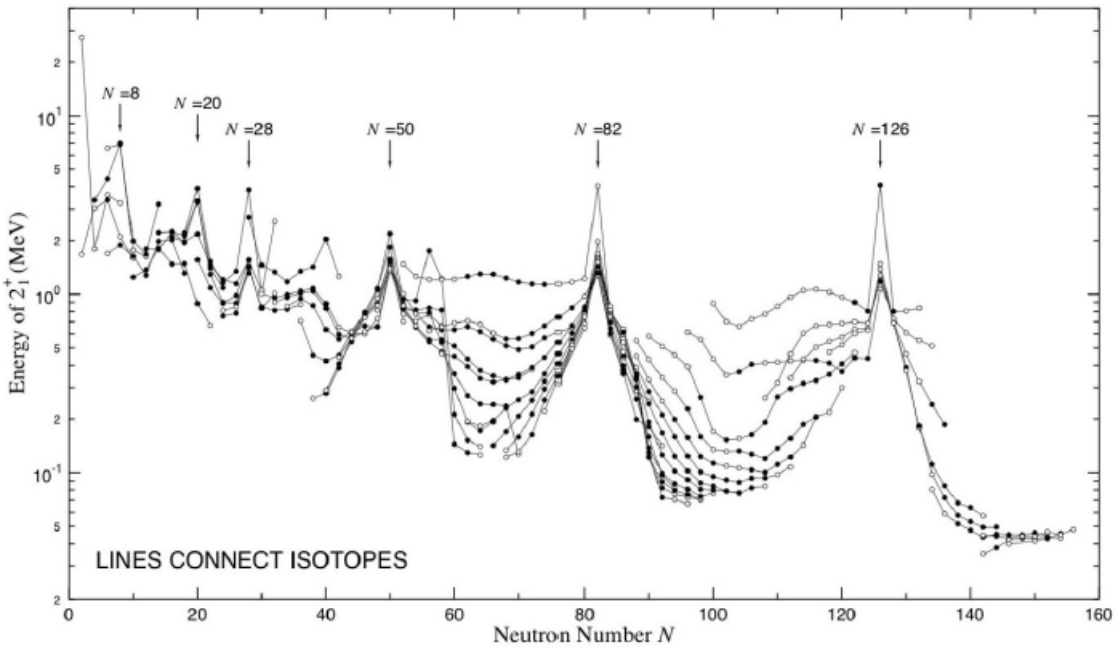

Figure 2.2. The energy of the first 2^+ excited state

2.2 Spherical Shell Model

The spherical shell model was developed to explain the magic numbers. This model describes the nucleons as quasi-independent particles moving in a particular orbital within the overall potential generated by the nucleons interacting together. Since nucleons are fermions, they obey the Pauli's exclusion principle which limits the number of nucleons that can be placed in a given orbital and causes shell filling.

Numerous potentials have been considered with the simplest being the square well and harmonic oscillator potentials. A potential that closely resembles the nuclear matter density is the Woods-Saxon potential. These potentials are illustrated in figure 2.3.

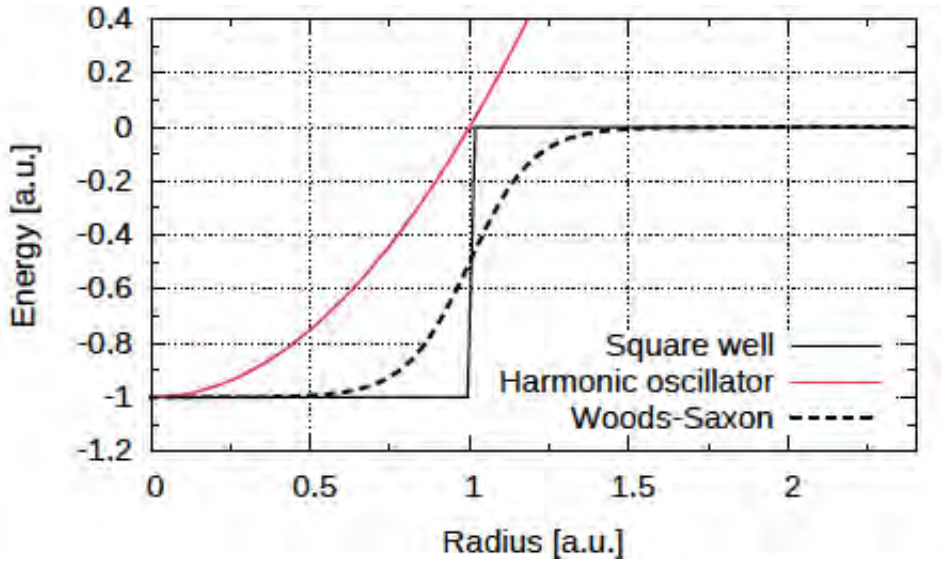

Figure 2.3. The behavior of various potential [9].

The Woods-Saxon potential has the following form:

$$V(r) = \frac{-V_0}{1 - exp^{[(r-R_{av})/a]}} \tag{2.4}$$

where R_{av} is given by equation 2.1 and a is called the diffuseness parameter, equal to 0.6 fm. Solving the Schrödinger equation with the Woods-Saxon potential yields the energy levels shown in figure 2.4. The states are labelled according to the orbital angular momentum l. The values of $l = 1, 2, 3...$ were historically assigned the letter name s (sharp), p (principal), d (diffuse), f (fundamental) and from g on-wards were assigned alphabetically as $h, i, j...$, respectively.

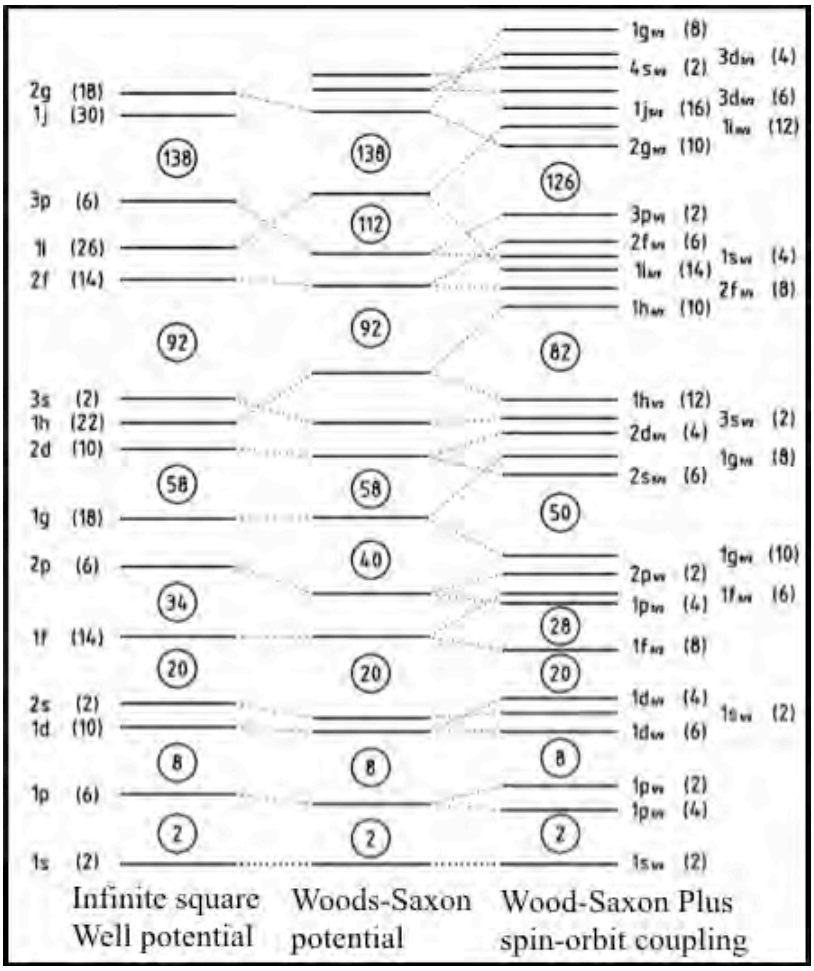

Figure 2.4. Single particle levels calculated with different potentials. The one on the left is infinite square well potential, followed by the Woods-Saxon potential in the middle, and the one on the right is the Woods-Saxon potential coupled to a spin-orbit potential. The magic numbers predicted by each potential are shown in circles.

Spin-orbit Coupling

However, the potentials shown in figure 2.3 do not reproduce the shell gaps that correspond to magic numbers. In 1949, it was shown by Mayer *et al.* [7, 10] that adding a spin-orbit potential could give the proper separation of sub-shells and a clear account of the magic numbers. The spin-orbit potential is given in the form $V_{so}(r)\vec{l}\cdot\vec{s}$ where $\vec{l}$ is the orbital angular momentum and $\vec{s}$ is the intrinsic spin angular momentum. The orbital and spin angular momentum can be coupled to produce a total angular momentum, given as:

$$\vec{j} = l \pm s \tag{2.5}$$

where the intrinsic spin angular moment has value of $s = \pm\frac{1}{2}$. The $(l \cdot s)$ factor causes the re-ordering of the levels to account for the magic numbers. When the spin-orbit term is added

to the Woods-Saxon potential, the single particle orbitals are shifted, as shown in figure 2.4. The accepted magic numbers 2, 8, 20, 28, 50, 82, and 126 correspond to large shell gaps.

2.3 Collective Structure

In the early 1950's, Bohr and Mottelson [11] proposed a description of excited states of a nucleus in terms of vibrations and rotations of a (deformed) liquid drop. There are properties which are reasonable to identify not with the motion of few valence nucleons, but instead with collective motion in which nucleons contribute together to the nuclear property. Collective proprieties change gradually with mass number and mostly are independent of the number and type of valence nucleons associated with filled sub-shells (while the valence nucleons may contribute to the shell structure that couples with collective structure). The properties of collective structure on even-even nuclei are demonstrated in figure 2.5, where two different properties that reveal collective behaviour can be extracted:

♢ Firstly, the energy of the first 2^+ excited states decrease in the regions between the closed shells (magic numbers).

♢ Secondly, in the region from A=150 to 190 the value of $E(2^+)$ is both exceptionally small and constant.

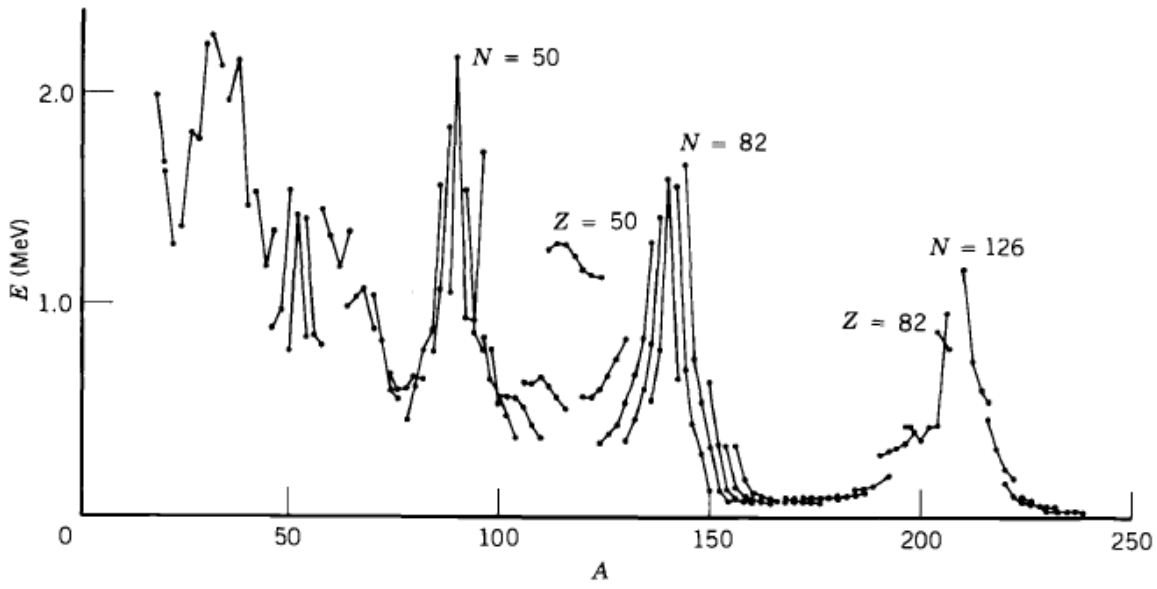

Figure 2.5. The energies of the 2^+ on the eve-even nucleus.

These regions are associated with collective structure. As we shall see, nuclei in the region between A = 150 to 190 exhibits rotational structure, while below A= 150 transitional and vibrational structures are common. This model is mostly referred to the liquid drop model for

vibrations and rotations of a nucleus because it resembles the properties of a suspended drop of liquid and thus it can be treated with similar mathematical analysis [7, 10, 12].

2.3.1 Nuclear Rotations

Quantum mechanically, rotation can only be observed in non-spherical nuclei. These nuclei are distorted from the spherical shape and are often called deformed nuclei. The shape of a nucleus with a quadrople distortion is represented by an ellipsoid whose surface is described by:

$$R(\theta, \phi) = R_{av} \left[1 + \beta Y_{20}(\theta, \phi)\right] \tag{2.6}$$

where β is the deformation parameter and it is related to the eccentricity of the ellipsoid as:

$$\beta = \frac{4}{3}\sqrt{\frac{\pi}{5}}\frac{\Delta R}{R_{av}} \tag{2.7}$$

where ΔR is the difference between the semi-major and semi-minor axes of the ellipsoid and R_{av} is given by equation 2.1. When $\beta > 0$, the nucleus forms a prolate shape (similar to rugby ball) while when $\beta < 0$, the nucleus forms an oblate shape (similar to a pumpkin).

The classical angular momentum of a rotating body is $L = \Im\omega$, where $\Im$ is the moment of inertia and ω is the angular velocity. Therefore, the kinetic energy of the classical rotating nucleus can be expressed as follows:

$$E_{rot} = \frac{1}{2}\Im\omega^2 = \frac{(\Im\omega)^2}{2\Im} = \frac{L^2}{2\Im} \tag{2.8}$$

The equivalent quantum mechanical expression is:

$$E_{rot} = \frac{\hbar^2}{2\Im} I(I+1) \tag{2.9}$$

where I is the angular momentum quantum number. The energy of a rotational nucleus can be increased by increasing the angular momentum quantum number I. The rotational motion

of the nucleus leads to a sequences of states with the following energies:

$$\begin{aligned} E_{rot}(0^+) &= 0 \\ E_{rot}(2^+) &= 6\frac{\hbar^2}{2\Im} \\ E_{rot}(4^+) &= 20\frac{\hbar^2}{2\Im} \\ E_{rot}(6^+) &= 42\frac{\hbar^2}{2\Im} \end{aligned} \tag{2.10}$$

The excited states of a rotating nucleus form a sequence known as a rotational band. A nucleus possessing rotational character has a ratio of $E(4^+)/E(2^+)$ equal to ≈ 3.33. Figure 2.6 shows experimental evidence of good rotors on the nuclear chart. They are located in the mass regions 150<A<190 and A> 230.

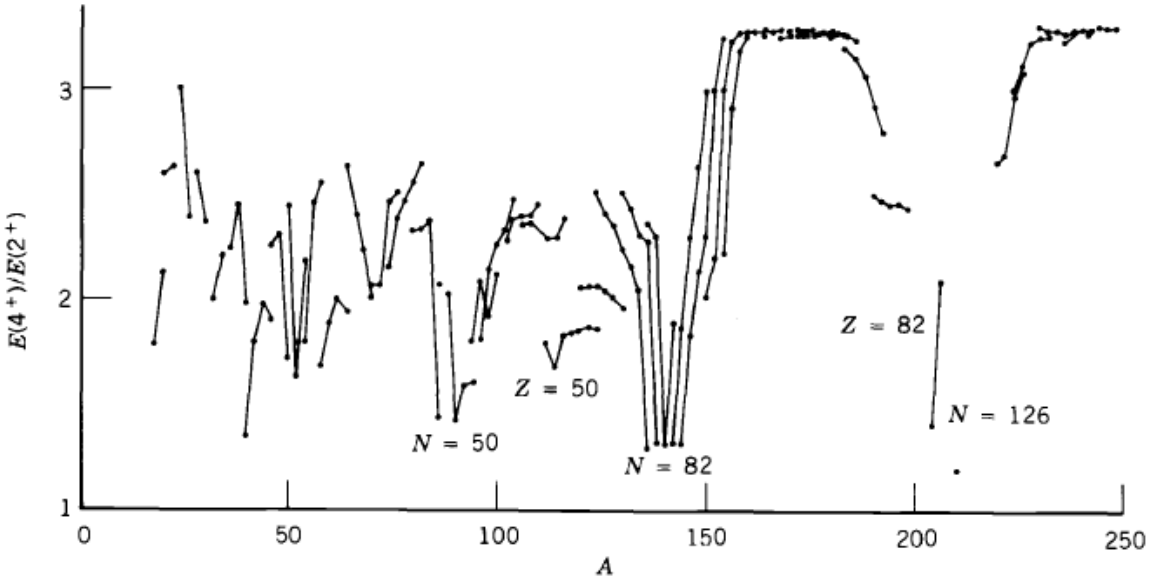

Figure 2.6. An example of the collective properties in the even-even nuclei across the entire nuclear chart. The ratio of $E(4^+)/E(2^+)$ of the lowest 2^+ and 4^+ on the even-even nuclei [7].

An example of a good rotational nucleus is ^{170}Yb, shown in figure 2.7, where the ratio of $E(4^+)/E(2^+) = 3.29$.

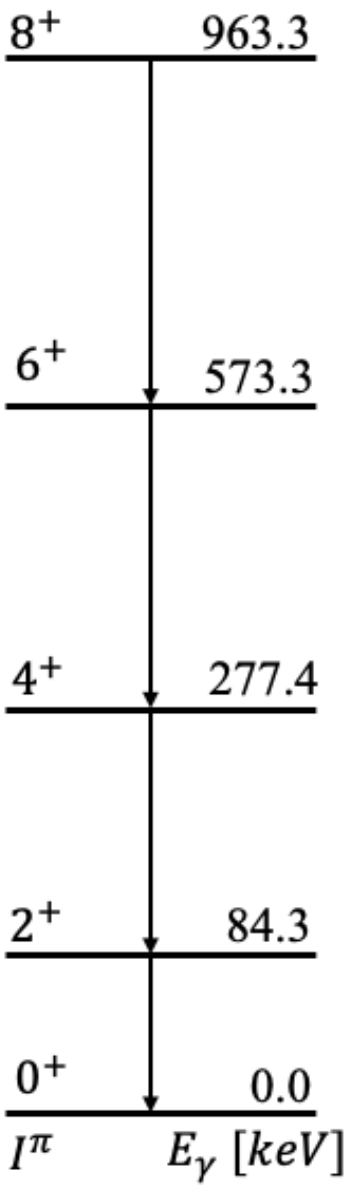

Figure 2.7. Rotational level scheme of ^{170}Yb, spin and parity are shown on the left, energy is shown on the right. Data taken from [13].

To obtain the correct spacing between the energy levels of a rotational band, the moment of inertia ($\Im$) needs to be calculated. Two extreme case are considered. In the first case, a rigid body, brought together by tightly-bounded nucleons with mass M, has moment of inertia given by:

$$\Im_{rigid} = \frac{2}{5} M R_{av} (1 + 0.31\beta) \tag{2.11}$$

In the second case, if we consider the nucleus as a fluid of weakly-bounded nucleons in a rotating

ellipsoid, the moment of inertia is given by:

$$\Im_{fluid} = \frac{9}{8\pi} M R_{av}^2 \beta \tag{2.12}$$

The observed rotational behaviour falls between a rigid rotor and a fluid in which particles are weakly bound. Therefore, the moment of inertia lies between the two cases.

$$\Im_{rigid} < \Im < \Im_{fluid} \tag{2.13}$$

2.3.2 Nuclear Vibrations around the Spherical Shape

If a spherical nucleus vibrates at high frequency (see figure 2.8) the average shape of the vibrating drop will be spherical, however its immediate shape is not and it can be described by spherical harmonics $Y_{\lambda\mu}(\theta, \phi)$. The surface $(R(t))$ of the vibrating liquid can be described by equation 2.14:

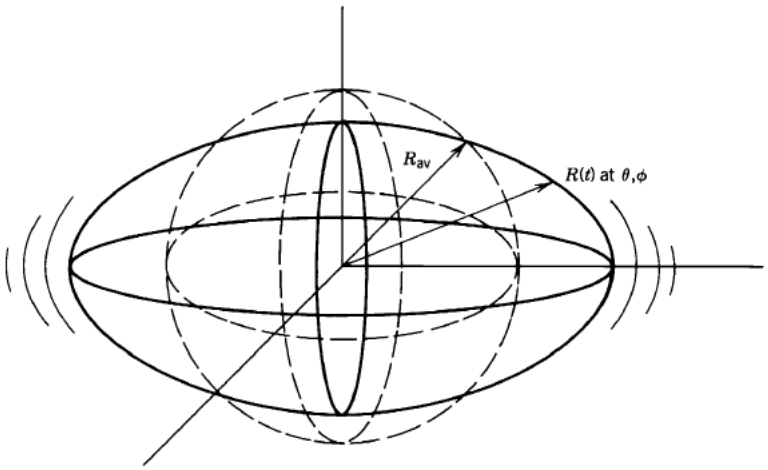

Figure 2.8. An illustration of a vibrating nuclei within a spherical equilibrium shape [7].

$$R(t) = R_{av} + \sum_{\lambda \geq 1} \sum_{\mu=-\mu}^{+\lambda} \alpha_{\lambda\mu}(t) Y_{\lambda\mu}(\theta, \phi) \tag{2.14}$$

where R_{av} is given in equation 2.1, and the $\alpha_{\lambda\mu}(t)$ represent the amplitudes of each spherical harmonic. If the coefficients, $\alpha_{\lambda\mu} = 0$, then the nuclear surface is spherical. The collective excitation of a spherical nucleus is the vibration around a spherical shape.

The components to λ = 0,1,2,3 correspond to monopole, dipole, quadrupole and octupole distortion, respectively. The lowest four multipole modes are illustrated in figure 2.9.

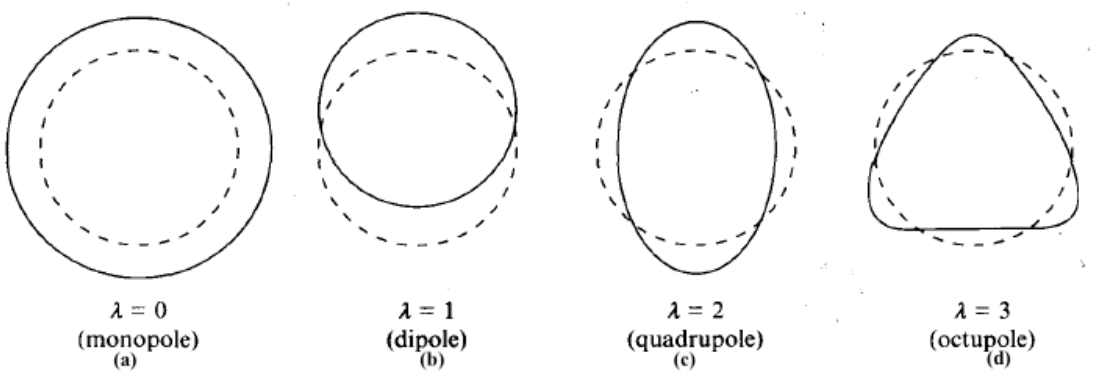

Figure 2.9. This figure shows different types of nuclear vibrational mode[7].

The lowest mode of vibration is a monopole vibration. This mode of vibration requires a large amount of energy and it is not observed at low excitation energy. The second lowest mode of vibration is the dipole vibration. This type of vibration gives a displacement of the centre of mass and therefore cannot result from the action of an internal nuclear force. A dipole vibration is shown in figure 2.9(b) and it has no effect on the nuclear shape because the displacement in structure is due to the fact that protons and neutrons oscillate in phase.

The third lowest mode of vibration is called the quadruple mode and it is shown in figure 2.9(c). This is the most important mode of vibration and we shall discuss it in detail below. The Hamiltonian of a vibrating liquid drop can be written as:

$$H = T + E_p = \frac{1}{2}\sum_{\lambda,\mu} B_\mu |\dot{\alpha}_{\lambda\mu}|^2 + \frac{1}{2}\sum_{\lambda,\mu} C_\lambda |\alpha_{\lambda\mu}|^2 \tag{2.15}$$

where T is the kinetic energy and E_p is the surface energy of undistorted sphere. The parameters C_λ and B_λ are referred to as the stiffness and collective mass parameters, respectively [5, 14, 15]. For quadrupole vibrations it has a eigenvalues given by:

$$E = \hbar\omega\left(N_{ph} + \frac{5}{2}\right) \tag{2.16}$$

where N_{ph} is the number of "phonons". Similar to the quantum theory of electromagnetism in which a single quantum unit of an electromagnetic field is called a photon, a single quantum of vibrational energy is called a phonon. One quadruple phonon carries two units of angular momentum, which means that if vibrational energy is added to the ground state of an even-

even nucleus, the first excited vibrational state will have spin and parity of 2^+. The harmonic vibrational model predicts that the two phonon states should occur at twice the energy of the first excited state. Likewise, the energy of the three phonon states should occur at three times the energy of the first excited state. The parity of the vibrational states is given by $\pi = (-1)^\lambda$, with λ being the multipole order. Adding a second quadrupole phonon creates a triplet of states $(0^+, 2^+, 4^+)$. Again, adding a third quadrupole phonon energy yield a quintuplet of states $(0^+, 2^+, 3^+, 4^+, 6^+)$. A simple level scheme of a harmonic vibrator based on equation 2.16 is shown in figure 2.10.

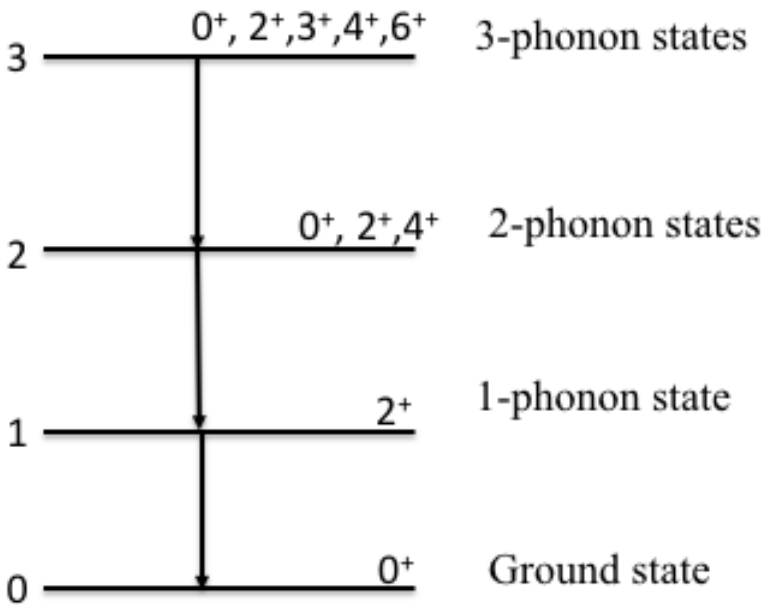

Figure 2.10. A theoretical example of low-lying level of the harmonic vibrator phonon model showing the ground state, the single quadrupole phonon state, the 2-phonon triplet, and the 3-phonon quintuplet.

The text book example showing low-lying vibrational states is shown in figure 3.1. The 2-phonon triplet state within the ^{62}Ni, ^{78}Se ,^{106}Pd, ^{114}Cd, and ^{198}Hg isotopes is clearly demonstrated.

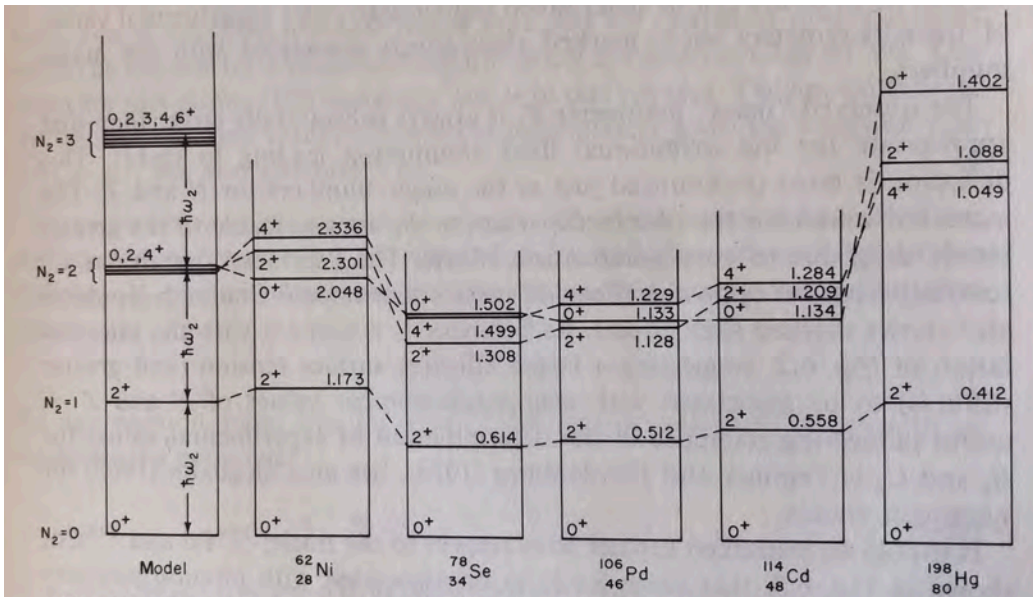

Figure 2.11. Partial level scheme of even-even ^{62}Ni, ^{78}Se, ^{106}Pd, ^{114}Cd, ^{198}Hg isotopes showing the vibrational state [14].

2.3.3 Rotation and vibrations of axially deformed nuclei

Quadrupole vibrations about an axially symmetric deformed nucleus are usually designated using the (β,γ) co-ordinates, defined in the body-fixed frame by

$$\alpha_{20} = \beta\cos\gamma, \quad \alpha_{22} = \frac{1}{\sqrt{2}}\sin\gamma$$

The β parameter is a measure of elongation along the symmetry axis (z), while the γ parameter is a measure of the deviation from axial symmetry around the z-axis. In these co-ordinates, the rotational-vibrational Hamiltonian may be expressed as

$$H = T_{vib} + T_{rot} + V(\beta,\gamma) \tag{2.17}$$

where, following reference [16], the vibrational kinetic-energy operator, T_{vib}, in β and γ co-ordinates is given by:

$$T_{vib} = -\frac{\hbar^2}{2}\left[\frac{1}{B_2}\frac{\partial^2}{\partial\beta^2} + \frac{1}{B_\gamma\gamma}\frac{\partial}{\partial\gamma}\left(\gamma\frac{\partial}{\partial\gamma}\right)\right] \tag{2.18}$$

and the rotational kinetic energy is given by

$$T_{rot} = \frac{\hbar^2}{2}\left[\frac{L(L+1)-K^2}{\Im} + \frac{K^2}{\Im_\gamma}\right] \tag{2.19}$$

where L and K designate the angular momentum quantum number and its projection on the symmetry axis, respectively, while the $\Im$ designate the moments-of-inertia. The mass parameters B_2, B_γ and the potential parameters (C_β, C_γ below) can be determined by fitting to data. In a lowest order approximation, the vibrational potential energy is assumed to be quadratic about an equilibrium shape ($\beta = \beta_0, \gamma = 0$):

$$V(\beta,\gamma) = \frac{1}{2}\left[C_\beta\left(\beta-\beta_0\right) + C_\gamma\gamma^2\right] \tag{2.20}$$

The vibrational solutions to the Schrödinger equation are given by

$$\begin{aligned} E_\beta &= \hbar\omega_\beta\left(n_\beta + \frac{1}{2}\right),\ n_\beta = 0,1,2,... \\ E_\gamma &= \hbar\omega_\gamma\left(n_\gamma + \frac{1}{2}\right),\ n_\gamma = 2N + |K|/2,\quad N = 0,1,2, \end{aligned} \tag{2.21}$$

The two lowest eigenvalues of these equations (for $n_\beta = 1$ and $n_\gamma = 1$ ($K = 2$)) define the heads of the well-known β and γ-vibrational bands. A β-vibration occurs when the nucleus oscillates along the symmetry axis and the nucleus preserves its cylindrical symmetry, while for a γ-vibration, the cylindrical symmetry is violated. The two types of vibrations are illustrated in figure 2.12. The band head energies associated with β and γ vibration bands are given by $\hbar\omega_\beta$ and $\hbar\omega_\gamma$ for β and γ bands, respectively, where ω denotes the angular frequency.

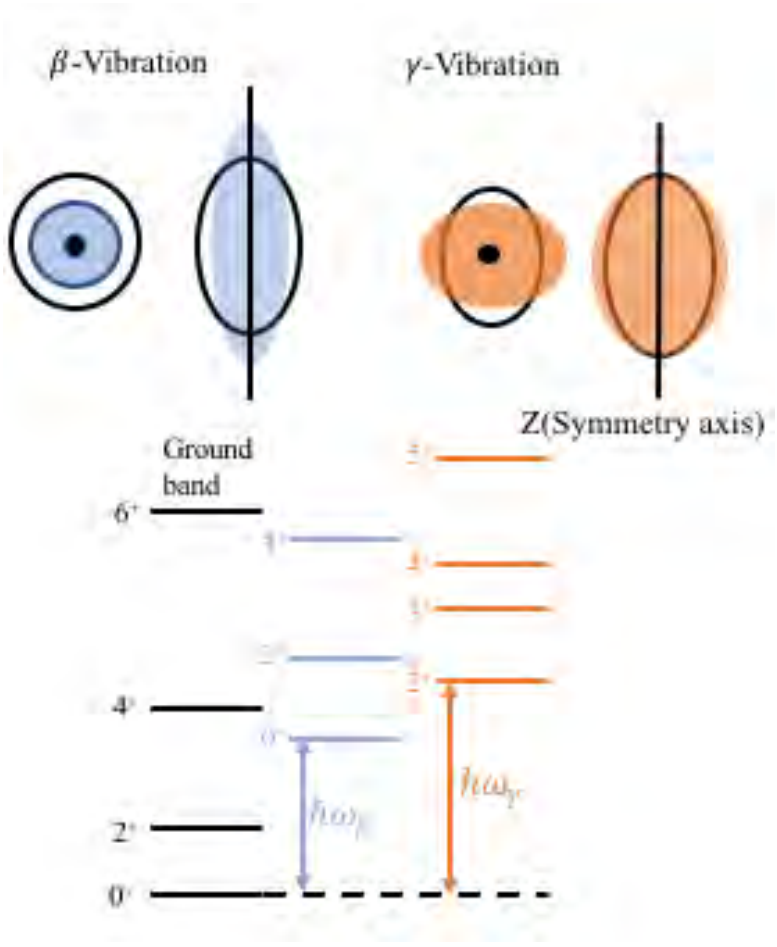

Figure 2.12. A general description of β- and γ-vibration [17].

The success of this model was demonstrated by the observation of the low-lying β and γ bands in the rear-earth region similar to the one shown in figure 2.12. However, according the P E Garrett [18], some of the 0^+ bands do not have the characteristics of the predicted β-band, inplying that other modes of excitation's contribute to their formation.

2.3.4 Potential energy surfaces and mass parameters

The simple potential energy function of equation 2.20, and illustrated in figure 2.13, requires the fitting of the parameters C_β and C_γ, and is clearly an oversimplification of the actual nuclear potential, but it has the advantage of having simple solutions. Better results could be expected if a realistic nuclear potential could be employed, albeit at the expense of solving the problem numerically. In principle one could find an energy minimum, as a function of deformation, by using a deformed shell model potential, as in the Nilsson Model, by summing the energies of all orbitals occupied, up to the Fermi surface as a function of deformation. This approach would find an energy minimum, but the total energy would be overestimated [15, 19]. A more accurate approach is the Macroscopic-Microscopic method, employing the liquid drop plus shell correction, developed by Strutinsky [20]. Here the potential energy is given principally by the

liquid drop model, to which a smoothed shell-correction, based on a deformed shell model is added.

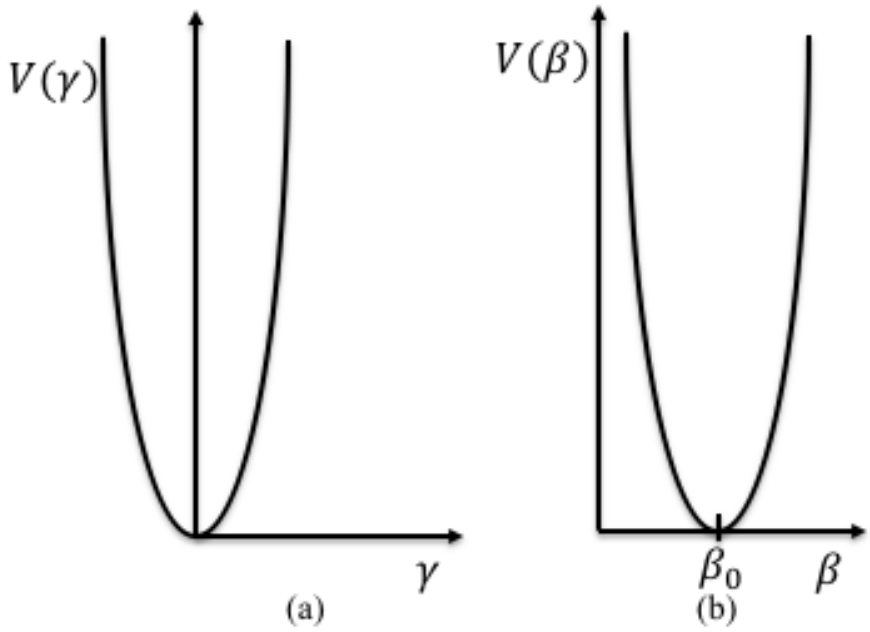

Figure 2.13. Potentials corresponding to (a) for γ and (b) for β planes of the PES shown in figure 2.15.

The Nilsson model originally employed a distorted harmonic oscillator potential, and in more recent versions, a Woods-Saxon potential. The problem with both is the lack of self-consistency - the wavefunctions of the occupied orbits do not generate the potential from which they were derived. A self-consistent, and a more fundamental approach, is to use the Hartree-Fock method [21]. Here, a self-consistent potential is generated in an iterative procedure. One begins with suitable wavefunctions (e.g. from the Harmonic Oscillator) to represent particles that interact through a microscopic force, such as the Skyrme interaction [22], and calculates new wavefunctions from which a new potential is generated. The procedure iterates until convergence.

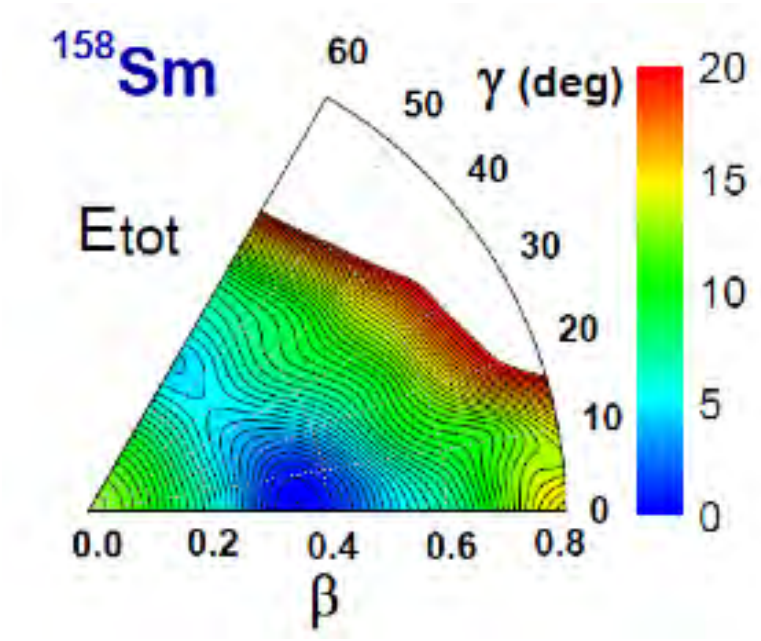

Figure 2.14. A example of potential energy surface of ^{158}Sm, where $V(\beta, \gamma)$ has been calculated using the density functional theory, the dot denote local minimum [23].

An example of a realistic PES calculated using relativistic mean field theory [23] is shown in figure 2.14, where the energy is plotted as a function of both β and γ. This surface is more complex than the simple parabolic shape represented in figure 2.13. In fact, a secondary minium is seen along the γ-direction, at $\gamma = 60°$ (corrsponding to an oblate shape).

The problem remains to calculate the inertial parameters, and the moments-of-inertia. As the nuclear moment-of-inertia is reduced by the pairing interaction, the BCS approximation is usually employed and the inertial parameters can be calculated using the cranking approach [19].

In Chapter 8, theoretical calculations performed by Tomaz Rodriguez are presented. They solve the collective Hamiltonian using the Generator Coordinate Method (GCM). The idea is to build a collective wave function $|\Psi\rangle$ out of microscopic wave functions (for instance a Slater determinant constructed for occupied single particle Nilsson or HF wave functions) $|\Phi(a)\rangle$ where a is a generalized collective coordinate such as β or γ. This is accomplished using the weight functions $f(a)$:

$$|\Psi\rangle = \int f(a)\,|\Phi(a)\rangle\,da \tag{2.22}$$

The weight function is determined using the variational principle, which leads to the *Hill-*

Wheeler-Griffin equation:

$$\int \langle \Phi(a)| H |\Phi(a')\rangle f(a')da' = E \int \langle \Phi(a) |\Phi(a')\rangle f(a')da' \tag{2.23}$$

The problem is usually solved using the Gaussian overlap approximation, in which the quantity $\langle \Phi(a) |\Phi(a')\rangle$ can be replaced by a Gaussian, which falls off as the collective coordinates differ. The full theory is beyond the scope of this dissertation, but details are presented in [24, 25]. The major advantage of the GCM is of course, that the full collective Hamiltonian is solved from a microscopic approach [15, 26].

2.4 Shape coexistence

Shape coexistence in atomic nuclei was observed nearly 63 years ago when H. Moringa [27] published a paper that interpreted the first excited states in ^{16}O as deformed, raising questions about multi-nucleon cross-shell excitations [28]. With the development of experimental techniques, it became clear that shape coexistence is a widespread phenomenon, observed in particular nuclei that exhibit eigenstates with different shapes at similar energies. It is possible to have both deformed and spherical shape in the same nucleus at a similar excitation energy. It can be characterized by the existence of two minima in the nuclear total energy surface (eg. see figure 2.15 at $\beta = 0.27$ and at 0.45). One of the two minima corresponds to the ground state and the other corresponds to a shape-coexisting structure. Two minima are shown in figure 2.15.

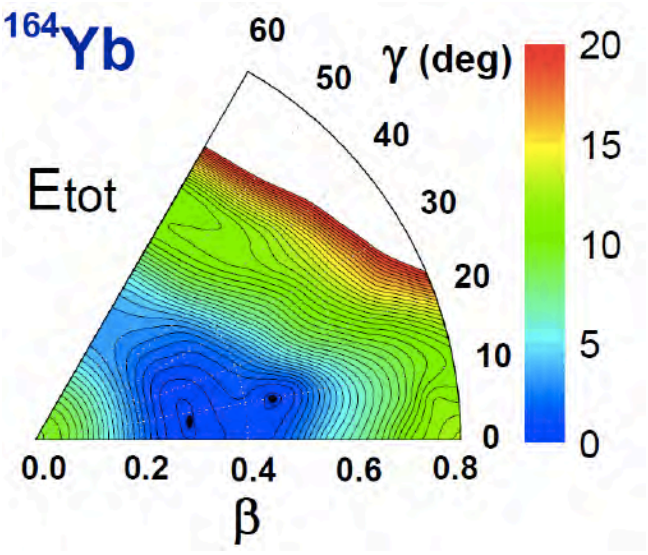

Figure 2.15. A example of potential energy surface of ^{164}Yb, where $V(\beta, \gamma)$ has been calculated using the density functional theory [23].

If the barrier between the two minima (in figure 2.16) is high, the two corresponding wave functions cannot penetrate the barrier appreciably and the wave functions remain relativity pure. Therefore, the Bohr Hamiltonian could be solved separately resulting in two set of bands. Again, if the barrier is low, the wave function penetrates the barrier and mix, displacing the levels from their unperturbed positions.

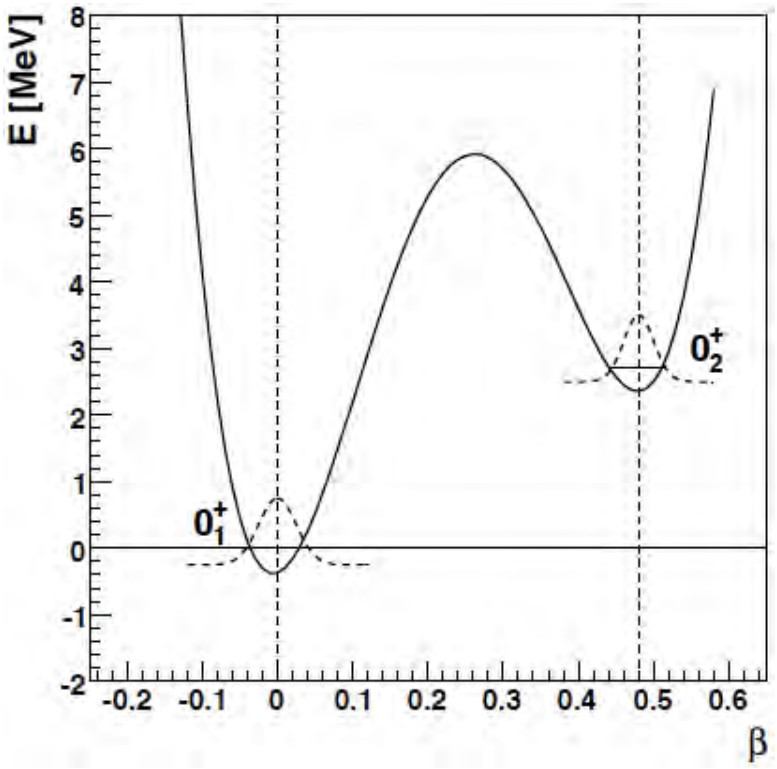

Figure 2.16. Schematic diagram showing the potential energy surface as a function of the quadrupole deformation. This illustrate the 2-level model with likely spherical and strongly deformed shape $(0_1^+, 0_2^+)$. Schematic collective wave functions are drawn with dashed lines [29, 30]

A classic example of shape coexisting structure is illustrated in figure 2.17, where rotational band is built on excited states at a closed proton shell. These Sn isotopes demonstrates the coexistence of spherical vibrational and rotational structures.

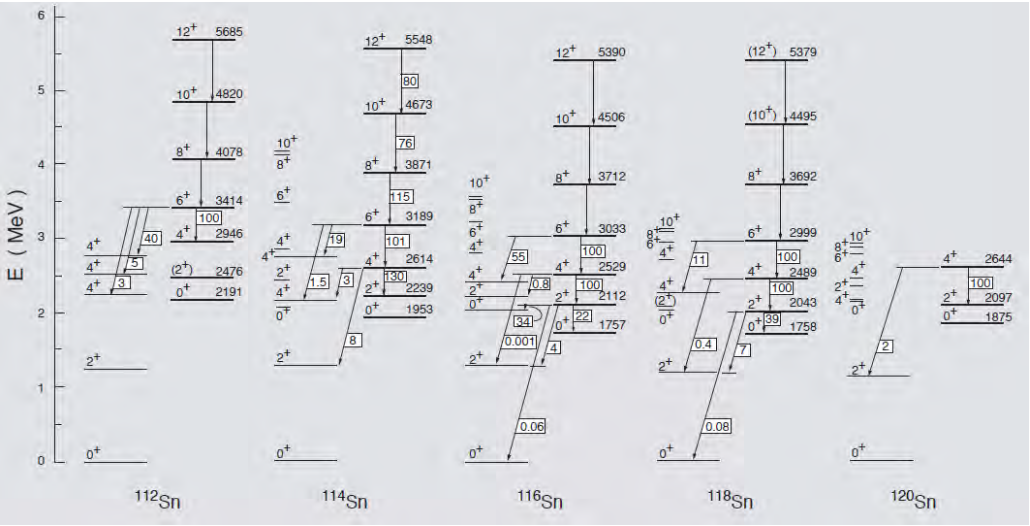

Figure 2.17. Low-lying level spectrum of the Sn isotope illustration shape coexisting structures i.e. rotational band built on-top of the 0^+ states [31].

If the barrier is too low, it results in the penetration of the barrier by the wavefunctions belonging to each well, leading to mixing of excited energy levels, for example, spherical energy states can mix with a deformed states either prolate or oblate as shown in figure 2.22. This concept will be expanded upon in section 2.5.3.

2.4.1 Intruder states

According to Federman and Pittel [32], deformation is driven by p-n interactions between valence particles (particle or hole). Therefore, the *p-n* interactions should maximize the deformation at mid-shell where the number of *p-n* interactions, given by the product of neutron and proton valence pairs, N_pN_n, is a maximum. Hence deformation is maximum at mid shells. If one shell is closed or nearly closed, deformation can still be realized by promoting particles across the shell gap, thereby increasing the number of particle and holes.

In the case of Hg isotopes, N_p =1. However, N_p can be increased by promoting a pair of protons across the Z=82 gap. Then the number of proton holes increases to 4 and the number of proton particles goes up to 2, so that the number of *valence* pairs increases from 1 to 3. This creates an alternative configuration that competes in energy with the 2-hole configuration, but has a larger deformation.

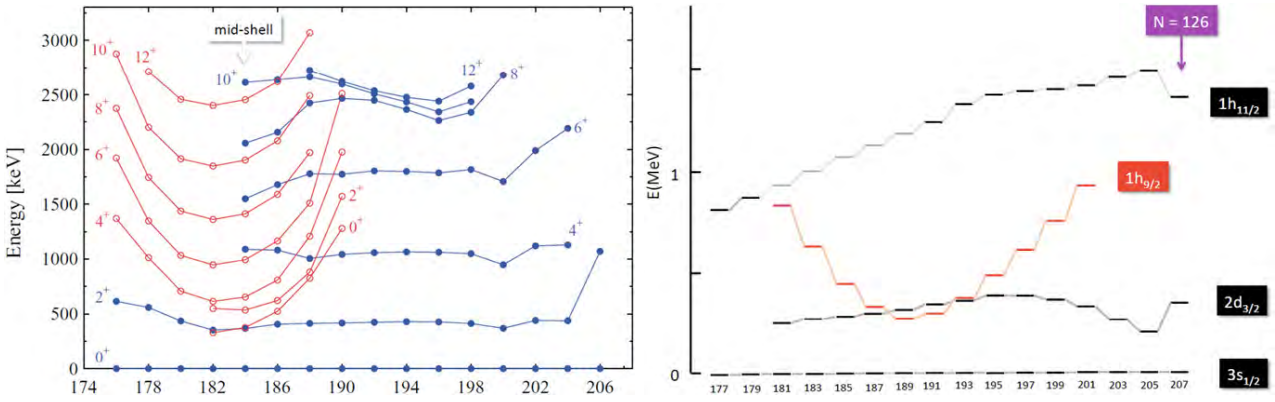

(a) . (b) .

Figure 2.18. An example of intruder states taken from Heyde *at al.* [28], where (a) shows the low lying states in even-mass Hg isotopes and (b) shows the systematics of the $1h_{9/2}$ proton intruder state in odd-mass Tl isotopes.

Because the deformed configuration is lowered in energy by the N_pN_n interactions, a state above the Z=82 gap is lowered below that gap. Hence it "intrudes" into the lower shell and configuration is often called an intruder configuration. An intruder state or configuration is a state with an intrinsic structure that differ significantly from that of the other state in same excitation energy. In the case of coexistence of spherical and deformed shapes, single-particle states based on the spherical shape and rotational band-heads due to the deformed shape appear at approximately the same energy. In the Z=82 region the $\pi h_{9/2}$ orbital has been identified with the intruder. Figure 2.18(a) shows the existence of shape coexistence in Hg isotopes. The intruder states in neutron-deficient Hg isotopes is demonstrated by the parabolic pattern of the excitation energy of the shape coexisting structure (reflecting the N_pN_n dependences). Figure 2.18(b) gives an example of the proton intruder states in Tl isotopes. The $1h_{9/2}$ proton particle state is lowered in energy and has then parabolic trend as the Hg intruder states [28].

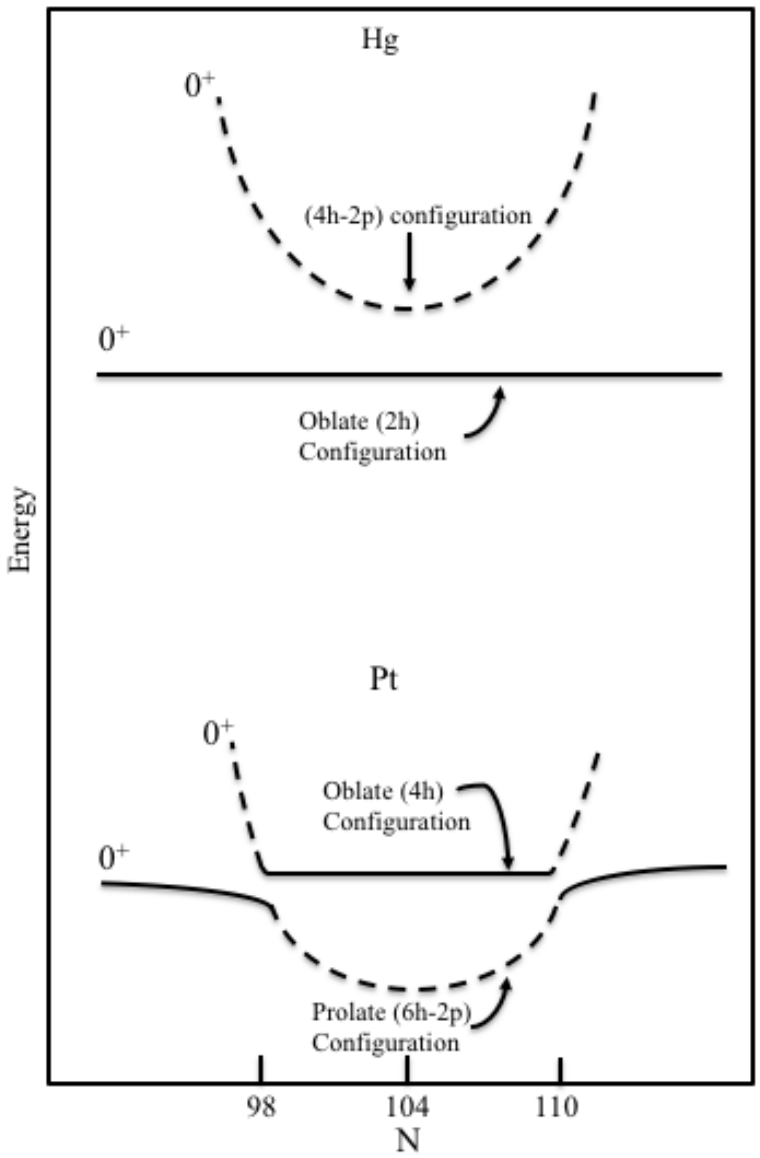

Figure 2.19. Schematic diagram illustrating energy of proton intruder configuration relative to the normal configuration in Hg and Pt isotope as a function of neutron number [33].

In figure 2.19, the excitation energy of the intruder configuration minimizes near the middle of the (N=82-126) neutron shell, the result of maximizing the number of deformation driving p-n interactions. In the Hg nuclei, the intruder configuration remains an excited band as a function of neutron number, and results in rather dramatic band-crossings of the prolate band with the less deformed ground band. In the isotopes of Pt, the removal of an extra pair of protons increases the number of attractive p-n interactions and lowers the energy of the intruder configuration, such that it becomes the ground band in the middle of the neutron shell, rising at the edges of the shell to become an excited band [33].

Figure 2.20 shows the intruder state in ^{190}Hg. This level scheme was obtained when studying the ^{190}Hg via the radioactive decay of Tl isotopes (^{190m}Tl(3.7 min) and ^{190g}Tl(2.6 min)) [34].

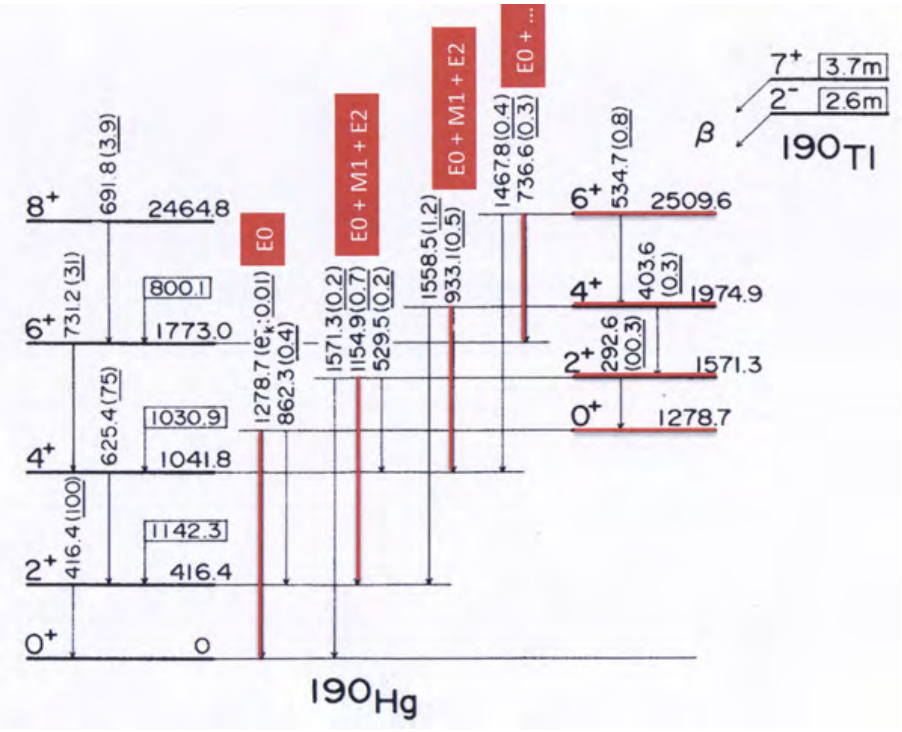

Figure 2.20. Schematic diagram showing the E0 and E0 enhanced transition between the spherically ground state and deformed intruder configuration in ^{190}Hg [34].

2.4.2 Appearance of shape coexistence in atomic nuclei

As explained in section 2.4, the essential ingredients of shape coexistence in nuclei include the occurrence of energy gaps due to spherical shells or sub-shells and the mixing of energy levels resulting from proton and neutron configurations.

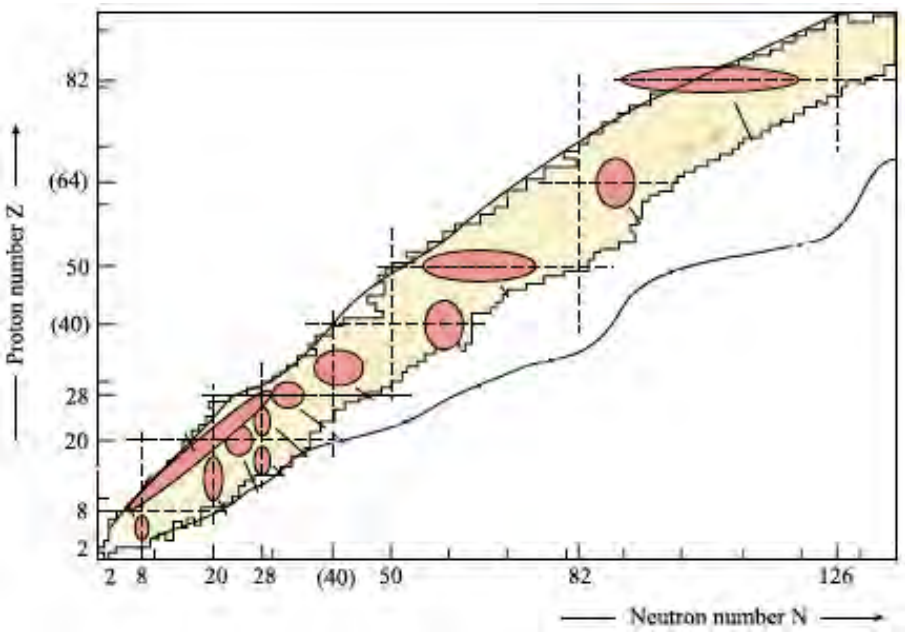

Figure 2.21. The circular path represent the main region of shape coexistence in the nuclear chat [35].

Figure 2.21 shows the region that shape coexistence will likely occur in the nuclear chart. It appears that with an exception, low-lying state 0^+ states are associated with shape coexistence. The occurrence of 0^+ states in nuclei has been the subject of many interpretations but there is no debate regarding their universal appearance as the ground state of the doubly even nuclei. This is the result of residual pairing correction which causes protons and neutrons to separately from $J = 0$ Cooper pair.

2.5 Electromagnetic properties of the models

2.5.1 Gamma decay

An unstable or excited nucleus can change into a stable system by emitting excess energy in the form of radiation such as a γ-ray photon, where the excess energy is expressed as follows:

$$E_\gamma = \Delta E - E_r \tag{2.24}$$

where ΔE $(= E_i - E_f)$ is the energy difference between the initial and final energy level and E_r is the energy of the recoiling nucleus in its final state, given by

$$E_r = \frac{(E_\gamma)^2}{2m_n c^2} \tag{2.25}$$

where m_n is the mass of the daughter nucleus. Generally, the energy of the recoiling nucleus is negligibly small and is ignored in equation 2.24. When the nucleus de-excites to a lower energy or stable state, the probability of a particular transition depends upon the quantum numbers of the state and the transition energy. There are other electromagnetic processes that compete with the emission of a γ-ray such as internal conversion, discussed in section 2.5.2, or internal pair creation. The latter process is possible for high energy transitions.

2.5.1.1 Angular momentum and parity selection rules

Electromagnetic radiation can be generated by either an oscillating charge, which causes an oscillation in the external electric field or by a varying current or magnetic moment which sets up a varying magnetic field. Radiation emitted by a changing electric field is called electric (E) radiation and when it is caused by a changing magnetic field it is called magnetic (M) radiation.

An emitted photon carries away angular momentum of magnitude given by the quantum number

L, which can only be an integer greater than zero as photons with $L = 0$ do not exist. They can be referred to as having multipolarity L. If $L = 1$ or 2 or 3... the transitions are called dipole or quadrupole or octupole .., respectively. The photon angular momentum is related to the spin of the initial and final nuclear state. Therefore, L can have any integer value between the sum and difference of the quantum number of the initial and final state shown in the following equation:

$$|I_i - I_f| \leq L \leq |I_f + I_i| \tag{2.26}$$

Transition where both the ground state and first excited state have spin-zero can still decay by internal conversion (section 2.5.2). The parity of γ-ray radiation is conserved and the parity selection rule should be obeyed. The radiation field can have even or odd parity for a given value of L, depending on whether the radiation is electric or magnetic type. The parity selection rules for γ-ray radiation are given by equation 2.27. Electric multipole are denoted by E1, E2 E3, ...EL while magnetic multipoles are denoted by M1, M2, M3, ... ML. Electric or magnetic multipoles of the same order always have opposite parities.

$$\begin{aligned} \pi(\mathrm{EL}) &= (-1)^L \qquad \text{For elcctric,} \\ \pi(\mathrm{ML}) &= (-1)^{L+1} \qquad \text{For magnetic} \end{aligned} \tag{2.27}$$

the parity selective rule can be written as:

$$\pi = \pi_i \times \pi_f \tag{2.28}$$

where L is the multipole order of the transition, I_i, π_i and I_f, π_f are the angular momentum and parities of the initial and final nuclear state, respectively. Provided equation 2.26 is obeyed two possible multipoles are generally possible and that property is called the branching ratio (λ). This property represents the fraction of nuclear that will be decay via one mode over the total number of nuclei that decay from the same state. The branching ratio of the intensity of the $E2$ stretched transition ($I \to I-2$), to the intensity of the mixed $M1/E2$ ($I \to I-1$) and it is given by:

$$\lambda = \frac{I_\lambda(E2 : I \to I-2)}{I_\lambda(M1/E2 : I \to I-1)} \tag{2.29}$$

Table 2.1 represents the possible multiporalities that can occur in a transition.

Table 2.1. The Classification of γ-transition and their possible mixtures [36].

L = | I_i - I_f |	π_f/π_i = -1		π_f/π_i = +1	
	Transition	Possible Mixture	Transition	Possible mixture
0 (0 → 0)	Forbidden		Forbidden	
0 (1/2 → 1/2)	E1		M1	
0 (1→1)	E1	M2	M1	E2
1	E1	M2	M1	E2
2	M2	E3	E2	M3
3	E3	M4	M3	E4
4	M4	E5	E4	M5
Even L (J_i or J_f = 0)	ML		EL	
Odd L (J_i or J_f = 0)	EL		ML	

2.5.1.2 Transition probabilities

The emission of γ-rays from any excited nuclear state is related to the electromagnetic interaction. The electromagnetic transition probability λ_γ, for multipole transition with multipolarity (L) is given by:

$$\lambda_\gamma(E(M)L; KI_1 \rightarrow KI_2) = \frac{8\pi(L+1)}{L\left[(2L+1)!!\right]^2} q^{2L+1} B(E(M)L; KI_1 \rightarrow KI_2) \tag{2.30}$$

where the nuclear information is obtained in the term called the reduced transition probability, $B(E(M)L; KI_1 \rightarrow KI_2)$. Most observed transitions in γ-ray spectroscopy are electric dipole (E1), electric quadropole (E2) and magnetic dipole (M1) transitions. The total transition probability for these transitions can be deduced from 2.30 and is expressed in the following:

$$\begin{aligned}
\lambda_\gamma(E1; KI_1 \rightarrow KI_2) &= 1.59 \times 10^{15} E_\gamma^3 B(E1; KI_1 \rightarrow KI_2) \\
\lambda_\gamma(E2; KI_1 \rightarrow KI_2) &= 1.22 \times 10^{9} E_\gamma^5 B(E2; KI_1 \rightarrow KI_2) \\
\lambda_\gamma(M1; KI_1 \rightarrow KI_2) &= 1.76 \times 10^{13} E_\gamma^3 B(E1; KI_1 \rightarrow KI_2)
\end{aligned} \tag{2.31}$$

where E_γ is energy in MeV, $B(E1)$ and $B(E2)$ are in units of $e^2(fm)^2$ and $e^2(fm)^4$, respectively and $B(M1)$ is in units of μ_N^2, where $\mu_N^2 = \frac{eh}{2M_e}$.

2.5.1.3 Transition probabilities in the vibration model

The radiation emitted by a free oscillations of the nuclear shape is of electric multipole type of the same multipole order, λ, as the nuclear deformation. The decay of a one-phonon to a non-phonon state, the reduced transition probability is given by the in-compressible model as [11]:

$$B(E\lambda) = \frac{3\lambda}{8\pi} Z^2 e^2 R_{av}^{2\lambda} \frac{\hbar^2}{AMR_{av}^2} \frac{1}{\hbar\omega_\lambda} \tag{2.32}$$

The collective nature of such a transition leads to a much faster decay than for a corresponding single-particle transition. For a strongly deformed nucleus, the collective transitions are of two types: vibration or rotational. While the E2 transition rotational probabilities depends on the static λ=2 deformation and become larger than in equation 2.32, those of the vibrational type remain of order of equation 2.32 [11, 37, 38].

2.5.1.4 Transition probabilities in rotational bands

Collective rotational motion leads to a large change in the electromagnetic field of the nucleus, which may result in a higher probability of γ-ray emission. Because the electric quadrupole moment measures the extent to which the nuclear charge distribution deviates from spherical symmetry, the reduced transition probability of an $E2$ transition is given by:

$$B(E2 : I_i \rightarrow I_f) = \frac{5}{16\pi} Q_0^2 |\langle I_i K_i 20 | I_f K_f \rangle|^2 \tag{2.33}$$

where Q_0 is the intrinsic quadrupole moment, K is the projection of the total angular momentum onto the symmetry axis and $|\langle I_i K_i 20 | I_f K_f \rangle|$ is a Clebsch-Gordan coefficient [27, 39]. The intrinsic quadruple moment is given by the following expression:

$$Q_0 = \frac{3}{\sqrt{5\pi}} R_{av}^2 Z \beta_2 (1 + 0.16\beta_2) \tag{2.34}$$

and the quadruple moment $Q(I)$ is related to the Q_0 by the following expression:

$$Q(I) = \frac{3K^2 - I(I+1)}{(I+1)(2I+3)} Q_0 \tag{2.35}$$

if $I = K$ in the ground state, the quadrupole moment is given by:

$$Q(I) = \frac{I(2I-1)}{(I+1)(2I+3)} Q_0 \tag{2.36}$$

The $E2$ transition probability is obtained by combining equation 2.33 and 2.34 and substituting the final product to expression that yield 2.30. Therefore, the $\lambda(E2)$ can be given by:

$$\lambda(E2) \approx 3 \times 10^{-7} E_\gamma^5 A^{4/3} \beta_2^2 Z^2 \tag{2.37}$$

where λ is given in s^{-1}. This expression is true for $K = 0, I = 2$ transitions with $I_i = I$ and $I_f = I - 2$ [15, 40].

2.5.2 Internal conversion

Internal conversion is a process that competes with γ-ray emission. The electromagnetic fields generated by the nucleus interact with an atomic electron, causing one of the inner electrons to be ejected. The electron is not created like in a β-decay process but it is an existing electron from the atomic orbitals. The energy of the ejected electron is given as:

$$E_e = E_\gamma - BE \tag{2.38}$$

where E_γ is the energy of the competing gamma ray and BE is the binding energy of the atomic electron. Equation 2.38 implies that the internal conversion process has an energy threshold equal to the binding energy of a particular shell. The emitted electron comes out with different energies depending on the shell from which it was emitted.

Conversion electrons are labeled according to the electron shell they are emitted from e.g. $K, L, M...$ These shells correspond to principal atomic quantum number $n = 1, 2, 3, ...$ The conversion electrons from the inner shell are most likely to be emitted, they are most bound which means they have lowest energy, while conversion electrons from the outer shell are observed with higher energy. The ratio of electron to γ-ray emission probability is called the internal

conversion coefficient and it given by:

$$\alpha_t = \frac{\lambda_e}{\lambda_\gamma} \tag{2.39}$$

where λ_e and λ_γ are the internal conversion and γ-ray emission decay rates, respectively. Partial internal conversion coefficients can be calculated for the individual shells from which electrons are emitted from.

$$\alpha_K = \frac{\lambda_{eK}}{\lambda_\gamma}; \quad \alpha_L = \frac{\lambda_{eL}}{\lambda_\gamma} \tag{2.40}$$

The total internal conversion coefficient (α_t) is given by the following sum:

$$\alpha_t = \alpha_K + \alpha_L + \alpha_M + ... \tag{2.41}$$

where $\alpha_L = \alpha_{L_I} + \alpha_{L_{II}} + \alpha_{L_{III}}$. The total decay probability (λ_t) and internal conversion coefficient are related according to the following expression:

$$\lambda_t = \lambda_\gamma(1 + \alpha_t) = \lambda_\gamma(1 + \alpha_K + \alpha_L + \alpha_M + ... + \alpha_\pi) \tag{2.42}$$

The non-relativistic approximations for internal conversion coefficients (for electric (E) and magnetic (M)) are given by the following equations [7, 10, 12]:

$$\alpha(EL) \cong \frac{Z^3}{n^3}\left(\frac{L}{L+1}\right)\left(\frac{e}{4\pi\varepsilon_0\hbar c}\right)^4\left(\frac{2m_e e^2}{E}\right)^{L+5/2} \tag{2.43}$$

$$\alpha(ML) \cong \frac{Z^3}{n^3}\left(\frac{e}{4\pi\varepsilon_0\hbar c}\right)^4\left(\frac{2m_e e^2}{E}\right)^{L+3/2} \tag{2.44}$$

where Z is the atomic number, n is the principal quantum number of the electron orbital, L is the multipole order of the γ-ray, m_e is the rest mass of an electron, E is the energy of the transition energy in MeV and this factor $e/4\pi\varepsilon_0\hbar c$ is the fine structure constant.

2.5.2.1 Electric Monopole (E0) Transitions

The detailed investigation of electric monopole transitions gives significant information about nuclear shapes and details of the nuclear structure[41]. The $E0$ transition occurs between levels with the same spin and parity. The $E0$ transitions are easily identified between 0^+ levels because their internal conversion lines have no corresponding γ-ray lines. In transitions between non-zero spin levels, the monopole transitions compete with γ-radiation and internal conversion of the higher order multipoles. The $E0$ transition probability is given by the following expression [42]:

$$\lambda(E0) = \frac{1}{\tau(E0)} = \lambda_{ic}(E0) + \lambda_{\pi}(E0) \tag{2.45}$$

where $\tau(E0)$ is the partial mean-life of the state for $E0$ decay, and $\lambda_{ic}(E0)$ and $\lambda_{\pi}(E0)$ are the transition decay rates probability for internal conversion electron and electron-positron pair emission, respectively. These probabilities are given by:

$$\lambda_{ic}(E0) + \lambda_{\pi}(E0) = \rho^2(E0) \times [\Omega_{ic}(E0) + \Omega_{\pi}(E0)] \tag{2.46}$$

where $\Omega_{ic}(E0)+\Omega_{\pi}(E0)$ are electric factors for internal conversion electron and electron-positron pair emission, and $\rho(E0)$ is the dimensionless monopole transition strength. These quantities are a function of atomic number, Z, and transition energy [43].

2.5.2.2 The E0 Monopole strength

The monopole transition strength contains all information about the nuclear structure related to the monopole matrix element. The matrix element of $\hat{M}(E0)$ is directly related to the mean-square charge radius. The operator is given by the following expression [44, 45]:

$$\hat{M}(E0) = \sum_k e_k r_k^2 \tag{2.47}$$

where e_k is the effective charge of the k_{th} nucleon and r_k is the position of the nucleon relative

to the centre of mass of the nucleus. The quantity $\rho(E0)$ is given by:

$$\rho(E0) = \frac{\langle f|\hat{M}(E0)|i\rangle}{eR_{av}^2} \tag{2.48}$$

so that the $E0$ transition rate can be defined as

$$\frac{1}{\tau(E0)} = \rho_{fi}^2(\Omega_K + \Omega_L + ... + \Omega_{IP}) \tag{2.49}$$

and ρ_{fi}^2 is given by:

$$\rho_{fi}^2 = \left|\frac{\langle f|\Sigma_k e_k r_k^2|i\rangle}{eR_{av}^2}\right|^2 \tag{2.50}$$

where e is the electronic charge and R_{av} is the nuclear radius given in equation 2.1. The values of ρ are usually given as $\rho^2(E) \times 10^3$ because its ranges from 10^{-3} to 10^{-1}, references usually gives it as $10^3\rho^2(E0)$. The monopole transition strength can be determined experimentally by measuring the absolute transition rate and calculating the electric factor. The reduced $E0$ transition probability $B(E0)$ can be obtained from the square of the monopole transition strength and it is given by

$$B(E0) = \rho^2(E0)e^2R_{av}^4 \tag{2.51}$$

E(0) transitions between 2^+ states can be obtained from the following expression:

$$q_K^2(E0/E2) = \frac{I_K(E0)}{I_K(E2)} \tag{2.52}$$

where $I_K(E0)$ and $I_K(E2)$ are the intensity of the $E0$ and $E2$ K-conversion electron components of the initial and final transition, respectively. The dimensionless ratio of $E0$ and $E2$ reduced

transition probabilities ($X(E0/E2)$) is defined by [42, 46]:

$$X(E0/E2) \equiv \frac{B(E0)}{B(E2)} = \frac{\rho^2(E0)e^2R_{av}^4}{B(E2)} \tag{2.53}$$

For K conversion electrons, the experimental value can be deduced from the following general formula:

$$X(E0/E2) = 2.54 \times 10^9 \times A^{4/3} \times q_K^2(E0/E2)\frac{\alpha_K(E2)}{\Omega_K(E0)}E_\gamma^5 \tag{2.54}$$

where E_γ is the $E2$ γ-ray energy in MeV, $\alpha_K(E2)$ is the K-conversion coefficient for pure a E2 transition, $\Omega_K(E0)$ is the electronic factor and $q_K^2(E0/E2)$ is given in equation 2.52. The strong presence of the $E(0)$ transitions is the indication of shape coexistence.

2.5.3 Shape mixing effect on E0 transition

The strength of the $E0$ transition depends on the mixing of the configuration with different mean-square charge radii. In such cases the observables are conversion electron lines. The challenge in measuring 0^+ state in the even-even nuclei is their low excitation energy. Shape coexistence can also be identified through nuclear deformation i.e. diagonal $E2$ matrix elements. The diagonal matrix element can be obtained by measuring γ-ray yield in multi-step Coulomb excitation. Identifying $B(E2)$ values can give signatures of shape coexisting structure but it does not distinguish between static and dynamic deformation. The $B(E2)$ values can also be determined via life-time measurement particularly Doppler line-shape broadening and fast timing. Again it can be extracted from Coulomb excitation of γ-rays [35, 44, 45]. All this information about shape coexisting states or structure plays an important role in the quest for an understanding of changes to the nuclear structure in exotic nuclei.

The mixing of two states $(0_i^+, 0_f^+)$ with different deformations can be described by a two level mixing model. Nuclei which are characterized by strong mixing will exhibit a strong $\rho^2(E0)$. This model is demonstrated in figure 2.16, which shows the schematic potential energy surface as a function of quadrupole deformation.

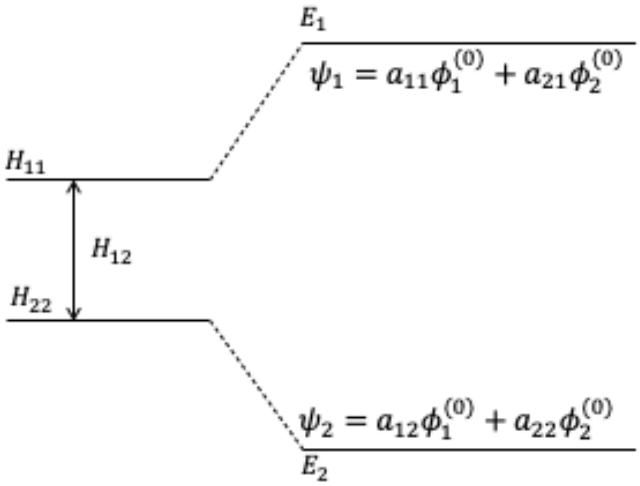

Figure 2.22. Schematic diagram representation of a two-level mixing between spherical and oblate deformed state [47].

The mixing is observed as a result of the interaction between the close-lying spherical and deformed (prolate or oblate) states of the same spin and parity. These two states get mixed via the interaction H_{12} and repel each other as shown in figure 2.22. A ground state of a spherical nucleus and a deformed 0_2^+ excited state in the unperturbed system are coupled by the mixing amplitude a_{ij}:

$$\begin{aligned} \psi_1 &= a_{11}\phi_1^{(0)} + a_{21}\phi_2^{(0)} \\ \psi_2 &= a_{12}\phi_1^{(0)} + a_{22}\phi_2^{(0)} \end{aligned} \tag{2.55}$$

The eigenvalues of the mixed levels are given by:

$$E_p = \frac{1}{2}\left\{H_{11} + H_{22} \pm \sqrt{(H_{11} - H_{22})^2 + 4H_{12}^2}\right\} \tag{2.56}$$

The monopole strength $\rho^2(E0)$ describes the overlap between the wave function of the $\langle 0_i^+|$ initial state and $|0_f^+\rangle$ excited state in the potential is given by:

$$\rho_{fi}^2(E0) = \left|\frac{\langle 0_i^+|M(E0)|0_f^+\rangle}{eR_{av}^2}\right|^2 \tag{2.57}$$

then, expanding $\langle 0_i^+|$ and $|0_f^+\rangle$ the monopole matrix element $\rho_{fi}(E0)$ can be expressed as:

$$\rho_{fi}(E0) = \frac{1}{eR_{av}^2}\Big[a_{11}b_{12}\Big(\langle 0_1^+|M(E0)|0_1^+\rangle - \langle 0_2^+|M(E0)|0_2^+\rangle\Big) + (a_{11}^2 - b_{12}^2)\langle 0_2^+|M(E0)|0_1^+\rangle\Big] \quad (2.58)$$

As shown in figure 2.22, the two states can strongly mix or repel each other. For the case of weak mixing between configuration that correspond to strongly different equilibrium shapes, the product of their amplitude is given by:

$$a_{11}b_{12} \backsimeq 0$$

which results in

$$\langle 0_2^+|M(E0)|0_1^+\rangle \backsimeq 0 \quad (2.59)$$

The wave function are localized in different potential minima with different deformation and thus

$$\rho_{fi}^2 \simeq 0. \quad (2.60)$$

The second case its where we have strong mixing and still consider that the condition of equation 2.59 is still valid, but

$$a_{11} \backsimeq -b_{12} \backsimeq \frac{1}{2} \quad (2.61)$$

Then the general results of equation 2.58 is approximated to be:

$$\rho_{fi}(E0) = \frac{1}{2}\Big[\langle 0_1^+|M(E0)|0_1^+\rangle - \langle 0_2^+|M(E0)|0_2^+\rangle\Big]\frac{1}{eR_{av}^2} \quad (2.62)$$

The E0 transition strength is proportional to the difference in mean square charge radius of the interacting levels, and is a fingerprint of shape coexistence [44, 45, 48].

Chapter 3

Systematics of Ru isotopes

3.1 The search for spherical vibrators

In the mid-nineties, Kern and coworkers [4] performed a dedicated search for examples of nuclei that could be classified as ideal spherical vibrators, or in the language of the IBA [49, 50], as U(5) candidates. As shown in Figure 1.4, taken from Kern *et al.* [4], the best candidates were found close to the $Z = 50$ closed shell, chiefly in Cd isotopes but also in isotopes of Te, Pd, Ru and Mo.

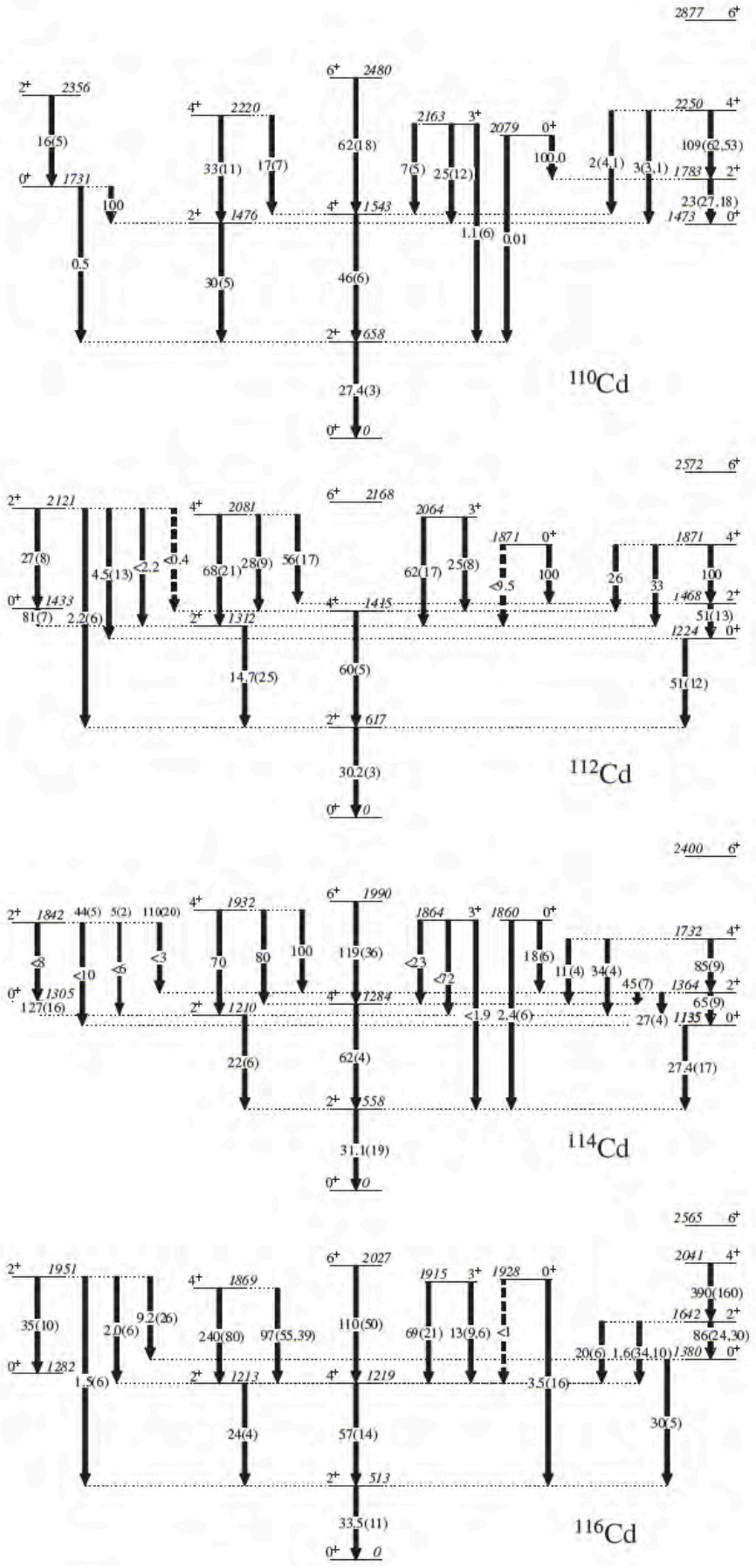

Figure 3.1. Partial level scheme of even-even $^{110-116}$Cd isotopes showing the vibrational state. The numbers in the transitions show the B(E) values in W.u., levels energies are in MeV, spin and parities are shown [51].

The low-spin level schemes of the Cd isotopes, shown in Figure 3.1, are a case in point. As discussed in Chapter 2, they presented "text-book" level schemes expected of a vibrational structure - a 2_1^+ level corresponding to the first quadrupole phonon, a $0^+, 2^+, 4^+$ multiplet corresponding to the coupling of two different angular momenta centred at twice the energy of the first phonon, and the $0^+, 2^+, 3^+, 4^+, 6^+$ members of the three phonon triplet. However, a close examination of the $B(E2)$ values from the excited states revealed stark departures from vibrational expectations [51].

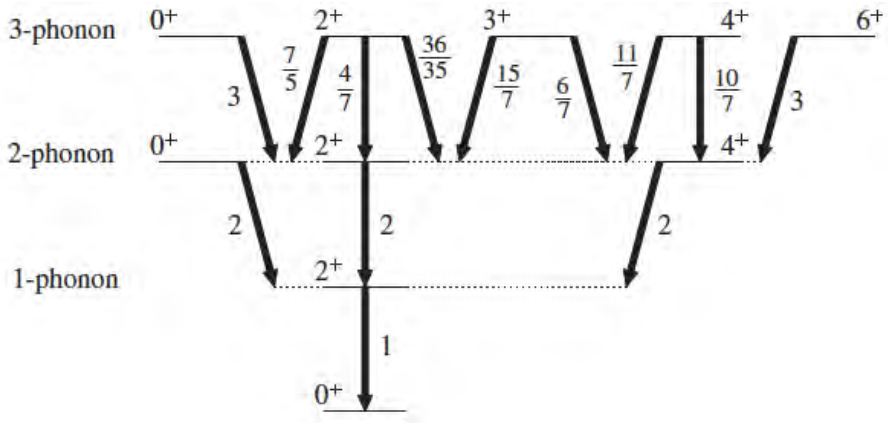

Figure 3.2. B(E2) values, relative to the B(E2; $2_1^+ \rightarrow 0_+^+$) value, expected for a quadrupole harmonic vibrator [51]

As summarized in figure 3.2, the $B(E2)$ values for the transition from a two-phonon state to the one-phonon state should be twice that of the one-phonon state to the ground state:

$$B(E2; 0_2^+, 2_2^+, 4_1^+ \rightarrow 2_1^+) = 2B(E2; 2_1^+ \rightarrow 0_1^+) \tag{3.1}$$

While this relation holds across the Cd isotopes for the $B(E2; 4_1^+ \rightarrow 2_1^+)$ compared to the $B(E2; 2_1^+ \rightarrow 0_1^+)$, it breaks down for the $B(E2; 2_2^+ \rightarrow 2_1^+)$ compared to the $B(E2; 2_1^+ \rightarrow 0_1^+)$ and breaks down badly for the $B(E2; 0_2^+ \rightarrow 2_1^+)$ compared to the $B(E2; 2_1^+ \rightarrow 0_1^+)$, see Figure 3.1. However, in addition to the vibrational levels, further band-like structures are observed in the Cd isotopes, which correspond to a shape coexisting (2p-4h) intruder structures [52]. These are shown at right in the level schemes of Figure 3.1. These levels may mix with the "vibrational" levels and distort the expected pattern of decays, or $B(E2)$ strengths from the vibrational candidates. Indeed. complete mixing between the intruder and vibrational levels could explain for example, the near vanishing of the decay from the 0_s^+ to the one-phonon 2_1^+ level in $^{110-116}$Cd [51, 52]. However, anomalies remained across the chain of isotopes [4] which could only be explained by a rather contrived, chance mixing of levels, making the vibrational interpretation improbable.

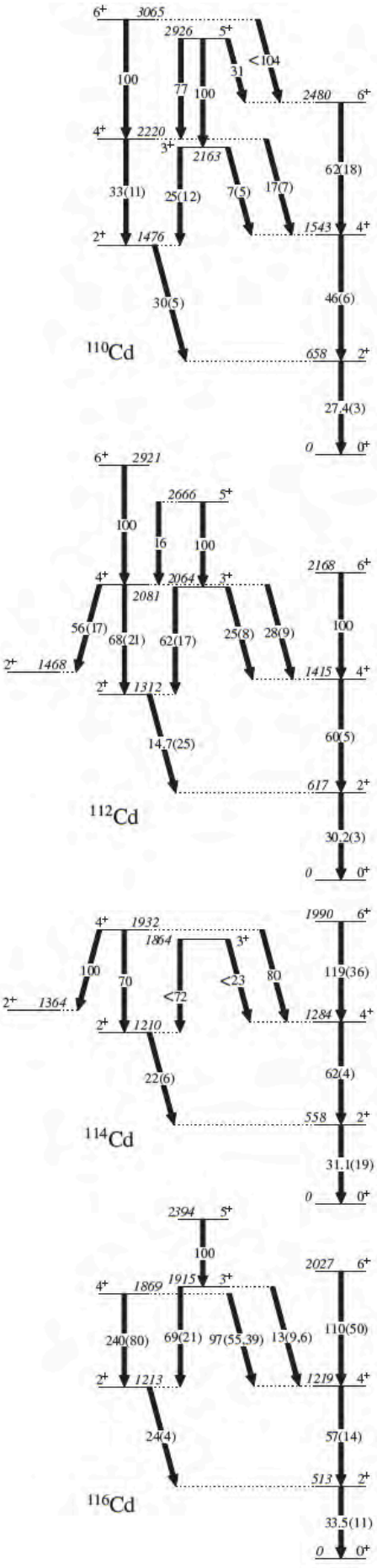

Figure 3.3. Suggested rearrangement of the low-lying levels in the $^{110-116}$Cd isotopes into band structures [51].

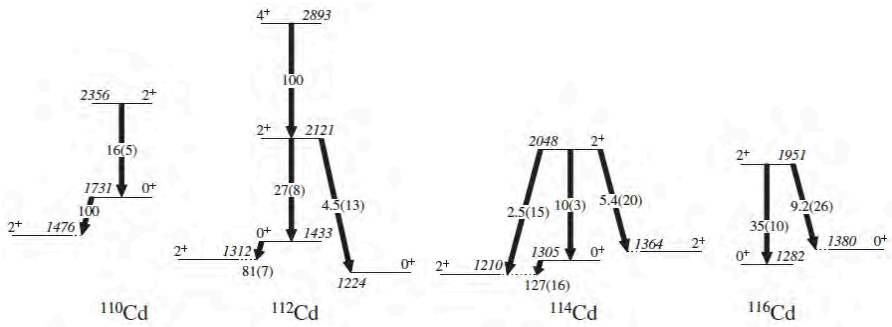

Figure 3.4. Proposed new bands, based on the 0_3^+ states in $^{110-114}$Cd and the 0_2^+ state in ^{116}Cd. Diagonal arrows to the right are transitions to the deformed intruder band [51].

Indeed the Cd isotopes have been re-interpreted as γ-soft rotors [5, 51]. In figure 3.3 and 3.4, the "vibrational" levels of the Cd isotopes have been rearranged into rotational bands; the levels are now divided into a ground band, an additonal band based on excited 0^+ states and a "$K = 2$ γ-band". The large splitting of the odd and even spins of the latter band is indicative of softness in the potential energy surface along the γ-plane.

3.2 Systematics of Ru isotopes

An updated survey [5] for possible spherical vibrators, taking account of the increase in data since the survey of Kern *et al.* [4], found that most of the original candidates could be excluded. Now only the Ruthenium isotopes, ^{98,100}Ru, survived as amongst the possible remaining candidates. The low-lying level structure of the Ruthenium isotopes is shown in figure 3.5. They show similarities to spherical harmonic vibrators (see figure 2.10), especially in ^{98,100}Ru. In ^{98}Ru the relationship of equation 3.1 for a spherical vibrator holds approximately true. However, as the mass of the Ru isotopes increases, the $2_1^+ \rightarrow 0_1^+$energy decreases and the $E(4^+)/E(2^+)$ ratio increases, indicating increasing deformation and collectivity. This interpretation is also supported by the increasing values of B$(E2; 2 \rightarrow 0)$ with increasing A.

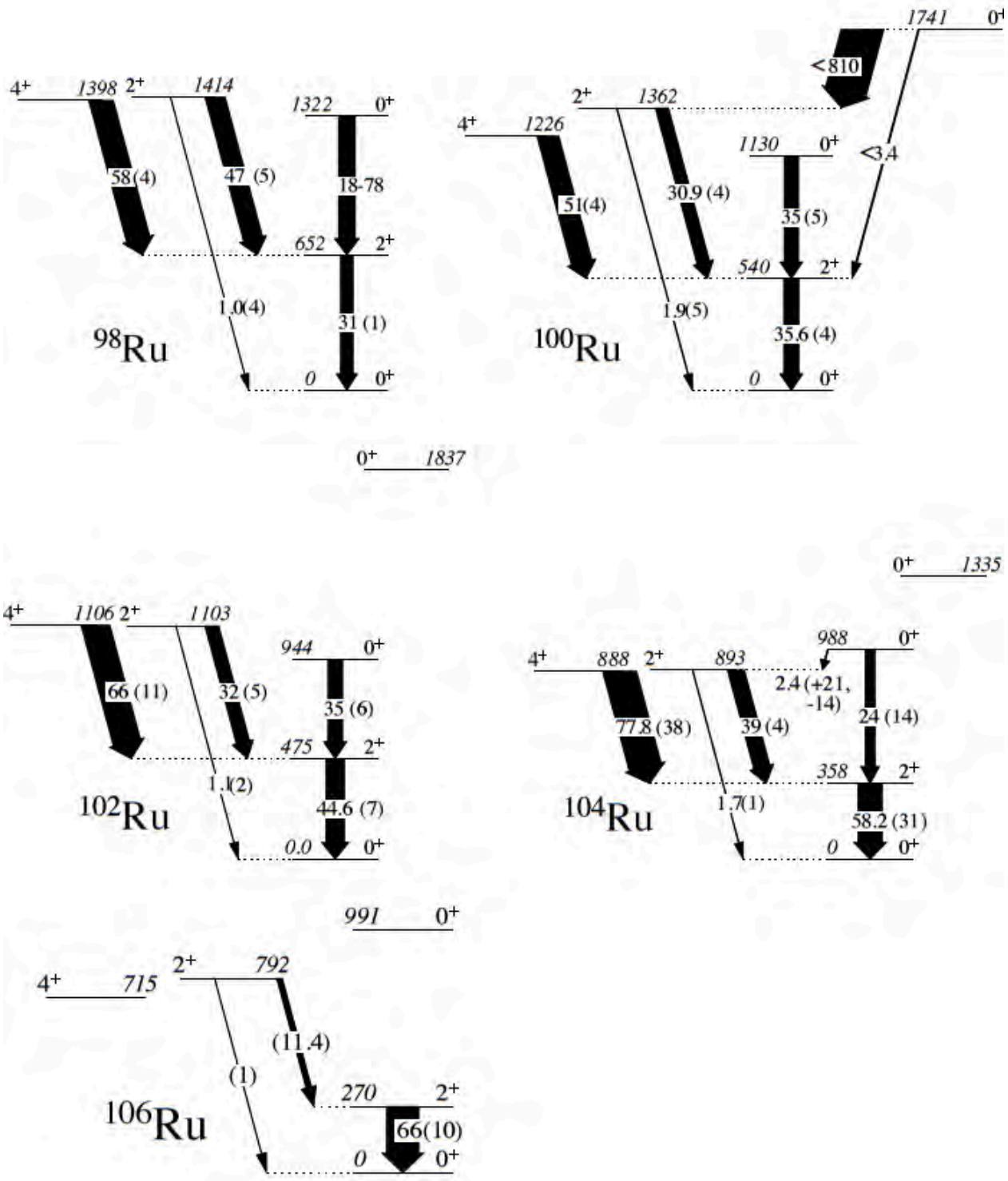

Figure 3.5. Low-lying levels in $^{98-106}$Ru. The arrows represents the B(E2) transitions and they are labelled in W. u. with the uncertainties immediately following in parentheses. The B(E2) data for ^{98}Ru and ^{104}Ru are taken from [53] and [13], respectively.

Indeed, the measured quadrupole moments of the 2_1^+ states, shown in Figure 3.6, confirm the picture of increasing deformation with neutron number. At ^{104}Ru the Coulomb excitation study by Srebrny *et al.* [53] found that the ground state band has a large triaxial deformation with $\beta_0 \approx 0.28$ and $\gamma_0 \approx 25°$.

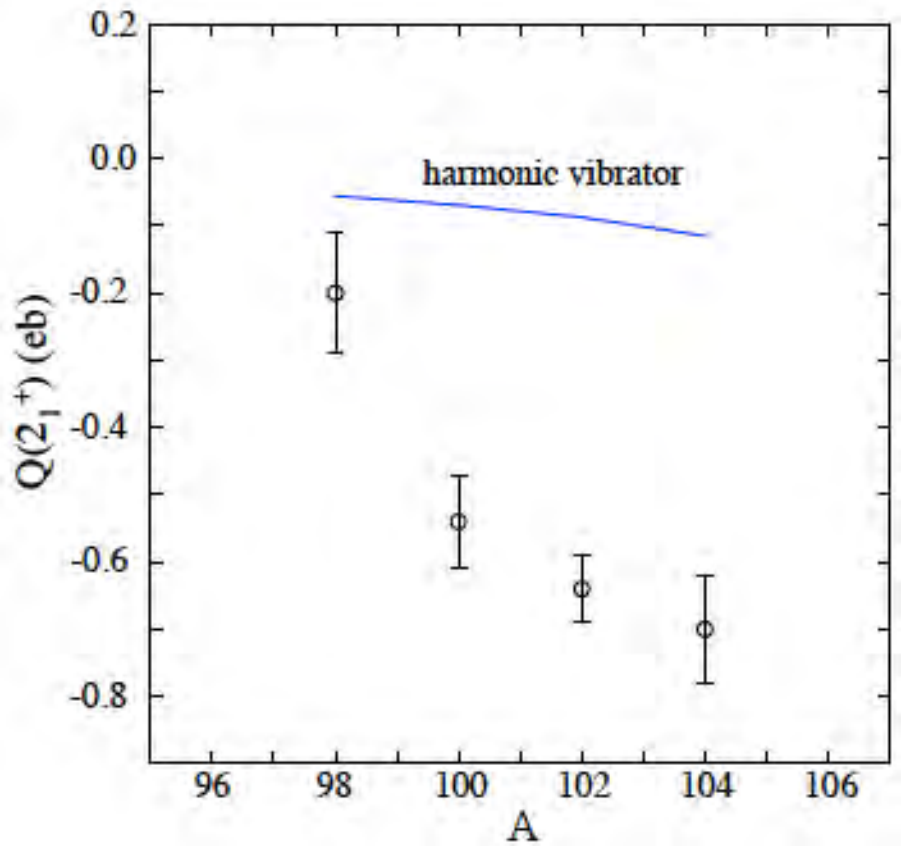

Figure 3.6. Quadrupole moments for the 2_1^+ states in the stable even-even Ru isotopes, taken [13]. Blue line: the Q(2_1^+) predicted for a harmonic vibrator to second order in the expansion for the quadrupole moment.

The transition from spherical vibrational structure to a deformed structure has been modelled in a simple shape-coexistence interpretation by Urban *et al.* [54]. The light Ru isotopes lie between two regions of shape-coexistence - the Cd isotopes discussed above, and the Sr/Zr region at lower values of Z [35], but evidence for intruder configurations in the light Ru isotopes is sparse. Nevertheless Urban *et al.* [54] proposed a two-configuration mixing-model which is shown schematically in figure 3.7. At neutron number 50, the energy separation between the 0_1^+ state and 2_1^+ state, and the 2_1^+ state and 0_2^+ state, are approximately equal, as in a vibrational scheme. The ground state configuration at $N = 50$ would be spherical, and the 0_2^+ level a 2-phonon state. Using the 2_1^+ state as reference, the systematics with N suggest that the two configurations would cross near ^{102}Ru, see figure 3.7. Because ^{104}Ru is well deformed, the second assumption was that the two phonon configuration would gradually evolve with neutron number to become a deformed configuration. The minimum separation of the configurations, near $N = 57$, implied an interaction strength of 400 keV in this simple model.

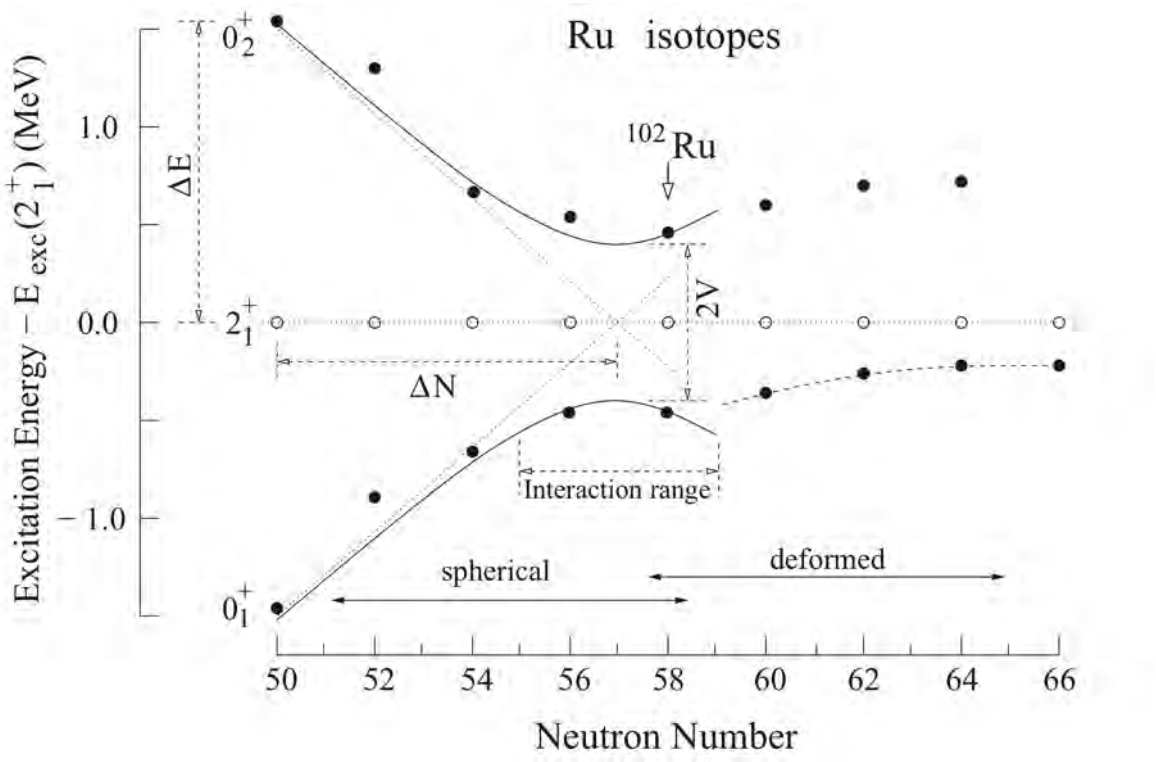

Figure 3.7. Two-level mixing calculation represented by solid line. The position of 0_1^+ and 0_2^+ level (full dots) relative to the 2_1^+ phonon excitation (open dots). Figure taken from [54].

More sophisticated models have been used to interpret the low-lying states in Ru isotopes [55, 56, 57, 58]. Abusara *et al.* [57] performed a systematic theoretical study of the shapes of Ru and Mo isotopes using the self-consistent mean-field (SCMF) approximation based on the Gogny-GIM energy density function (EDF) [56], the PES using the Skyrme HF+BC [21] and relativistic mean field (RMF) with BCS pairing [59]. They found no evidence of shape-coexistence except for ^{104}Ru; in general the PES's were γ-soft. Only ^{96}Ru could be described as having a spherical PES, while for ^{98}Ru, the PES while minimizing near $\beta_2 = 0.2$, was soft towards sphericity and increasing γ-deformation.

The spectroscopic data for ^{98}Ru, such as the level spacings and the small value of the quadrupole moment of the 2_1^+ state in ^{98}Ru (see figure 3.6) support the picture of a near spherical nucleus. While Kern *et. al.* [4] had suggested that the energy reproduction of the 2_2^+ level was poorly characterized, and an early determination of the collectivity in ^{98}Ru of the 4_1^+ level revealed a rather curious situation with the B(E2; $4_1^+ \rightarrow 2_1^+$) value smaller than the B(E2; $2_1^+ \rightarrow 0_1^+$) value, a recent lifetime measurement of the 4_1^+ level in ^{98}Ru [60] resolved this confusing situation, with the result that the B(E2; $4_1^+ \rightarrow 2_1^+$) is a factor of 1.86(16) that of the $2_1^+ \rightarrow 0_1^+$ transition, close to the expected factor of 2. The B(E2; $0_2^+ \rightarrow 2_1^+$) value, unfortunately, has a rather large uncertainly, resulting from the unknown signs of matrix elements in competing population pathways in the Coulomb excitation [61], but shows enhancement in its value.

At higher excitation energies, the low-spin structure of ^{98}Ru was investigated by Cakirli *et al.*

[62] using the ^{96}Mo(α,2n) reaction, Their work concluded that none of the known states could be identified as having three-phonon nature in an anharmonic vibrator description. This only left open the possibility of a maximum of a two-phonon description. An alternative is that the low-spin structure of ^{98}Ru could rather be interpreted in terms of shape-coexisting structures or rotational bands as was done for example, in the Cd isotopes or heavier Ru isotopes. This would need a good understanding of the spins, parities and transitions connecting the low-spin levels in the nucleus.

Indeed the ^{97}Mo(^{3}He,2n) reaction has been utilized to observe states up to spin 10 [63, 64, 65] with a thorough spectroscopic analysis. A number of new levels were observed, in addition to transitions between states known previously. A partial level scheme is shown in 3.8.

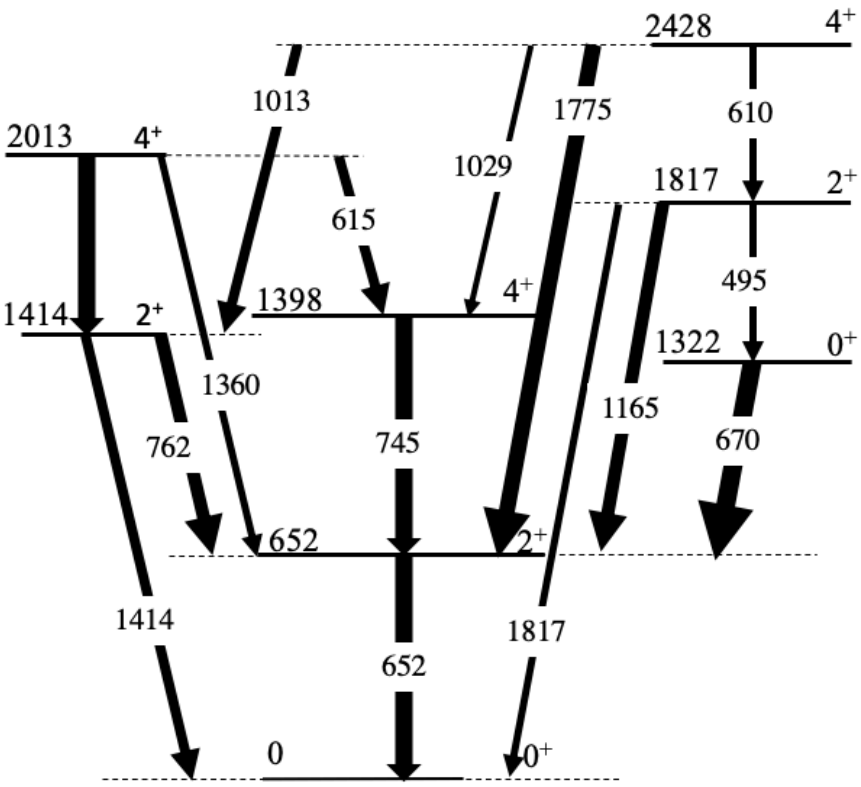

Figure 3.8. Partial level scheme of ^{98}Ru observed in the decay of ^{98}Rh.

Cakirli *et al.* [62] assigned possible spin values of 0^+ and 2^+ to the 1817 keV level, as they could not confirm the existence of an 1817 keV γ-ray transition to the ground state. This transition was observed by Giannatiempo *et al.* [66], who proposed a spin-parity of $2^+$to the 1817 keV level. The level is fed by a 610 keV γ-ray transition from a level at 2428 keV, assigned by both Cakirli *et al.* [62] and Giannatiempo *et al.* [66] as a 2^+ state. A level at 2013 keV had a firm assignment of $I^\pi = 3^+$. However, their data still left the precise nature of the 0_2^+ state open to alternative explanations. For example, the possibility that it is the head of a shape-coexisting intruder configuration, or the head of a rotational band, as in the case in the heavier Ruthenium isotopes, remained an open question. Furthermore, there were no assignments of

additional excited 0^+ states in ^{98}Ru beyond the 0_2^+ level. Thus knowledge of the excited level and decay scheme of ^{98}Ru was inadequate to make any firm conclusions about its structure. Should shape-coexistence play a role in ^{98}Ru, the presence of $E0$ transitions would be an ideal way to establish shape coexisting structures and might be expected to be present in ^{98}Ru to some degree.

The structural behaviour of ^{98}Ru and ^{100}Ru have been investigated extensively in references [54, 57, 62, 66, 67, 68, 69, 70, 71, 72, 73, 74], which explore proprieties of this nucleus at low-spin. With the possibility of observing an intruder-free vibrational nucleus, the low-lying structure of ^{100}Ru was studied by Genilloud *et al.* using the reactions ^{100}Ru(n,n'γ) [73], ^{99}Ru(n, γ), and ^{98}Mo(α,2nγ) [68]. Genilloud *et al.* [73] came to the conclusion that a pure U(5) description was not appropriate and had to break U(5) by adding (rotational) SU(3) terms to the IBA Hamiltonian. Konstantinopoulos *et al.* [75] considered ^{100}Ru as a possible E(5) [76, 77] candidate, based on the yrast-band energies, but the B(E2) values did not display the increasing trend predicted.

Although ^{100}Ru would not appear to be a good vibrational nucleus, and the spectroscopy of ^{100}Ru appeared to be in a much better state of knowledge than ^{98}Ru, a closer examination of figure 3.5 immediately reveals that many crucial low-energy decay branches are still missing, for example, the decay of the 2_2^+ level to the 0_2^+ level had not been observed nor an upper limit established. Additionally, there is only one E0 observed, with a $\rho^2(E0)$ value of 0.011$\pm$ 0.002 for the $0_2^+ \rightarrow 0_1^+$ transition.

Thus this work has focused on the study of both ^{98}Ru and ^{100}Ru, with the data for ^{98}Ru to be analyzed by Prof. P Garrett, and that for ^{100}Ru, to be analyzed by the present author. Both nuclei would be studied using β-decay, to observe electron and γ-ray transitions.

Chapter 4

The concept of β-decay

4.1 Introduction

This work is motivated by studying properties of Ruthenium isotopes. To achieved this goal, the β-decay technique is employed because of its importance to populate low-spin states. Again, it is also motivated by the long-term desire to study short-lived nuclei in the near future in the LERIB facility of iThemba LABS. Therefore, this chapter will cover the concept of β-decay spectroscopy in atomic nuclei.

4.2 The concept of β-decay

The basic process of beta decay involves the conversion of a neutron into a proton or a proton into a neutron. In these processes, both Z and N change by one unit in a nucleus, while the total mass number A (= Z + N) always remains constant. Beta-minus decay occurs in the neutron-rich region of the nuclear chart while β^+-decay or EC occurs in the proton-rich of the nuclear chart. Figure 4.1 shows the nuclear chart with various dominant modes of decay. On the nuclear chart, the black squares represent the stable nuclide's, while blue and red squares represents unstable nuclei that decay via β^- and β^+ or EC, respectively, while yellow squares show nuclei that decay via α-decay, the emission of the helium ($^4_2$He) nuclide. The β-decay processes can occur in the following way:

$\diamondsuit$ β^- **decay**

The process of β^- decay involves the emission of an electron (e^-) and anti-neutrino ($\overline{\nu}$), which can be represented as follows:

$$n \rightarrow p^+ + e^- + \overline{\nu}$$

The unstable atom ($^{A}_{Z}X_{N}$) undergoes β^{-} decay to a daughter atom where a neutron is converted into proton and an electron and anti-neutrino are emitted:

$$^{A}_{Z}X_{N} \rightarrow {}^{A}_{Z+1}Y_{N-1} + e^{-} + \overline{\nu} \tag{4.1}$$

The energy release from the above decay process can be expressed in terms of the atomic mass difference as follows

$$Q_{\beta^-} = [m(^{A}_{Z}X_{N}) - m(^{A}_{Z+1}Y_{N-1})]c^2 \tag{4.2}$$

♢ β^{+} **decay**

The process of β^{+} decay involves the emission of a positron (e^{+}) and a neutrino (ν), which can be represented as:

$$p^{+} \rightarrow n + e^{+} + \nu$$

The unstable atom ($^{A}_{Z}X_{N}$) undergoes β^{+} decay to a daughter atom where a proton is converted into neutron with a positron and a neutrino being emitted.

$$^{A}_{Z}X_{N} \rightarrow {}^{A}_{Z-1}Y_{N+1} + e^{+} + \nu \tag{4.3}$$

The energy released from the above decay process can also be expressed in terms of atomic mass difference as follows:

$$Q_{\beta^+} = [m(^{A}_{Z}X_{N}) - m(^{A}_{Z-1}Y_{N+1})]c^2 - 2m_e c^2 \tag{4.4}$$

♢ **Electron Capture (EC)**

In electron capture, an atomic electron, mostly from the K- or L-shell, is absorbed in the nucleus. In order to fill the resulting vacancy, electrons rearrange in the atomic shells and characteristic X-rays are emitted.

$$p + e^- \Rightarrow n + \nu$$

$$^{A}_{Z}X_N \quad + \quad e^- \quad \Rightarrow \quad ^{A}_{Z-1}Y_{N+1} \quad + \quad \nu \tag{4.5}$$

The energy released in the EC decay process can be expressed in terms of atomic masses as follows:

$$Q_{EC} = [m(^{A}_{Z}X_N) - m(^{A}_{Z-1}Y_{N+1})]c^2 \tag{4.6}$$

The decay of an unstable parent nucleus via β^+ and EC decay yields the same daughter nucleus and the difference between the Q value for these decay processes is given by

$$Q_{EC} - Q_{\beta^+} \approx 2m_e c^2 = 1.022MeV \tag{4.7}$$

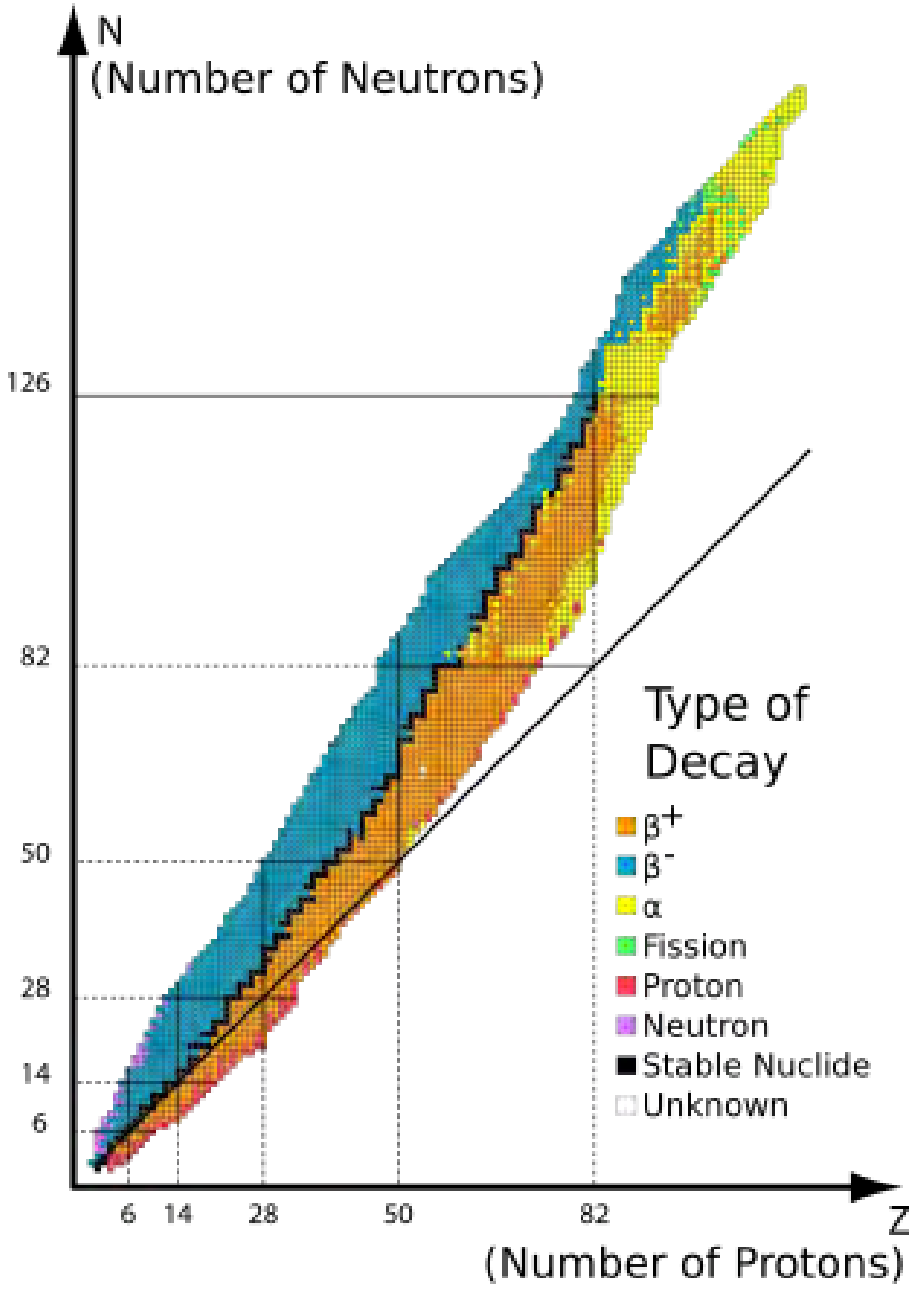

Figure 4.1. Nuclear chart showing different modes of decay [78].

4.2.1 Fermi Theory of β-decay

The feature of β-decay can be obtained from the basic expression for the transition probability caused by an interaction that is weak compared with the interaction that forms the quasi-stationary states. This is true for β-decay because the characteristic half-lifes are typically of the order of seconds or longer compared to nuclear system times which are typically 10^{-9}s. In this process an electron and a neutrino are created and do not exist inside the nuclear system. Beta-decay corresponds to a transition of the nuclear system between two discrete energy states i.e initial and final. The final energy states may be a ground state or an excited state of the daughter nucleus. Excited states of the daughter nucleus either decay by internal

conversion (section 2.5.2) or γ-ray (section 2.5.1) emission. As discussed in section 4.2, the energy released can be expressed in terms of their atomic mass difference, and it is called the Q-value. This energy represents the kinetic energy shared between the β-particle, the neutrino and the daughter nucleus. This gives rise to a continuous energy distribution of emitted β-particles with a typical shape similar to figure 4.2, where the end-point energy represents the maximum energy a β-particle can have.

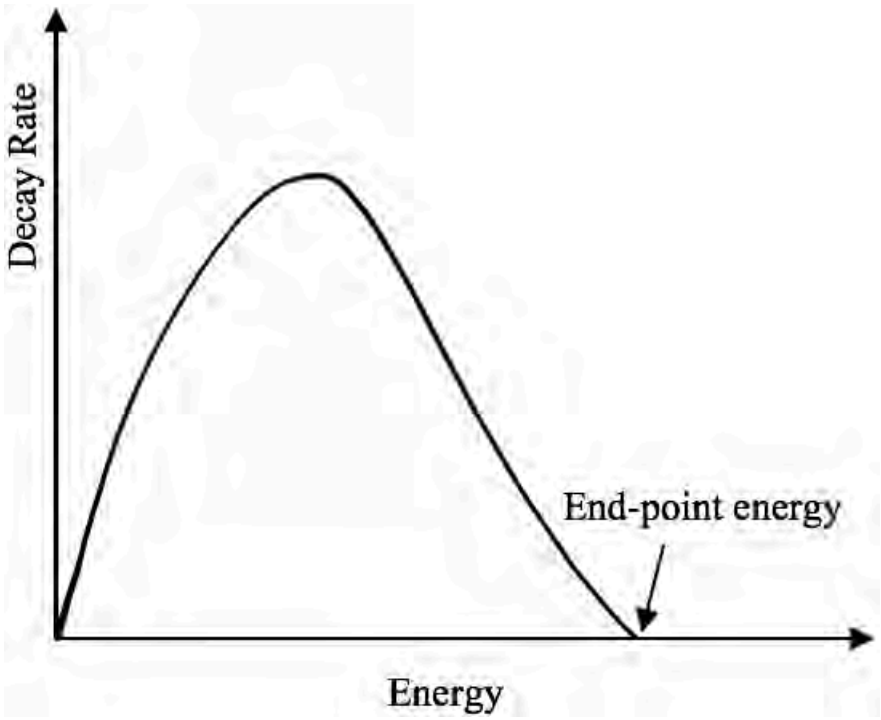

Figure 4.2. A schematic representation of the β-particle energy distribution [7].

Fermi successfully developed the theory of β-decay based on the Pauli neutrino hypothesis. The probability of a transition between two nuclear states in β-decay is given by the total decay rate (λ) as follows:

$$\lambda = \frac{g^2 m_e^5 c^4 |M_{fi}|^2}{2\pi\hbar^7} f(Z, E_0) \tag{4.8}$$

where $g = 8.8 \times 10^{-5}$ MeV·fm^3 is known as the β-decay strength constant, E_0 is the maximum total energy, m_e is the electron rest mass energy, c is the speed of light, $\hbar$ is the Plank's constant, $|M_{fi}|$ is the reduced matrix element for the transition between the initial and final states and the $f(Z, E_0)$ is known as the Fermi integral. This integral has been tabulated for values of Z and E_0 and it integrates over all values of momentum p_e of the emitted electron. It is given in

the following expression:

$$f(Z, E_e^{max}) = \frac{1}{(m_e c)^3 (m_e c^2)^2} \int_0^{p_{max}} F(Z, p_e) p_e^2 (E_0 - E_e)^2 dp_e \tag{4.9}$$

where $E_e (= \sqrt{p^2c^2 + m_e^2c^4} + m_e c^2)$ is the kinetic energy of an electron in relativistic terms and $F(Z, p_e)$ is known as the Fermi function which accounts for the influence of the nuclear Coulomb field. Since $\lambda = \frac{LN2}{t_{1/2}}$ where $t_{1/2}$ is the half life of the β-decaying nucleus of interest, equation 4.9 can be expressed as follows:

$$ft_{1/2} = LN2 \frac{2\pi^3 \hbar^7 c^3}{g^2 m_e^5 c^4 |M_{fi}|^2} \tag{4.10}$$

where $ft_{1/2}$ is known as the *comparative half-life* or simply the *ft value* and it gives a way to compare the β-decaying probabilities in different nuclei. As shown in equation 4.8, the decay rate depends on Z and E_0, and this dependence is also incorporated to f. This means that the differences in the *ft values* must be due to difference in the nuclear matrix element, hence differences in nuclear wave functions.

Electrons and neutrinos are fermions and they have an intrinsic spin $s = \frac{1}{2}\hbar$. If we consider the coupling between the two particles, we can have two possibilities, either the spins are parallel or anti-parallel. Therefore, the total spin is given by $S = s_e + s_\nu$, where s_e and s_ν is an intrinsic spin for electron and neutrino, respectively. If the coupling between the electron and neutrino is anti-parallel, the decay is called a **Fermi (F) decay** and it has a total spin $S = 0$. If the coupling between the electron and the neutrino is parallel, the decay is called a **Gamow-Teller (GT) decay** and it has the total spin $S = 1$.

4.2.2 Allowed and forbidden β-decay

Since electrons and neutrinos are created during the β-decay process, they do not carry any orbital angular momentum and the only change in angular momentum of the nucleus must result from the intrinsic spin of both particles. The most probable β-decay transition is called the *allowed* transition; it occurs when the electron and neutrino carry orbital angular momentum $l = 0$ or 1. For a Fermi decay, there is no change in the nuclear spin, thus $\Delta I = |I_i - I_f| = 0$

If the electron and neutrino satisfy the GT-decay, they carry a total angular momentum of one unit, and thus I_i and I_f must be coupled through a vector of length 1; $I_i = I_f + 1$. This is possible only if $\Delta I = 0$ or 1, except for I_i=0 and I_f=0 in which case only the Fermi transition

can contribute.

If the electron and neutrino carry no orbital angular momentum, then the parities of the initial and final states must be identical because the parity associated with orbital angular momentum l is given by $(-1)^l$. Therefore, the selection rule for all the *allowed* β-decay transition is given by

$$\Delta I = 0, 1 \qquad \Delta\pi(\text{parity change}) = \text{No} \tag{4.11}$$

In a case where both Fermi and Gamow-Teller selection rules are satisfied, the transition is referred to as a mixed transition. The exact proportions of F and GT are determined by the initial and final wave functions. Decays which are less probable than the *allowed* decay are called *forbidden* decays and generally have longer half-lives. However, if the *allowed* matrix element vanishes, the *forbidden* decays are the only ones that can occur. The most favorable forbidden decay is when the initial and final states have opposite parities, hence the selection rule for *allowed* decay is violated. To accomplish the change in parity the electron and neutrino must be emitted with an odd value of the orbital angular momentum relative to the nucleus. Table 4.1 presents the β-decay processes and their *ft* values.

If the *forbidden* decay has orbital angular momentum, $l = 1$, the decay is called a *first-forbidden* decay. Like the *allowed* decay, electron and neutrino spins can be coupled anti-parallel or parallel resulting in Fermi (S=0) or Gamow-Teller (S=1) decay, respectively. For Fermi type decay with $l = 1$, a total angular momentum of one unit is carried by the β-decay so that ΔI = 0, or 1. For Gamow-Teller decay with $l = 1$, it gives the 0,1 or 2 units of angular momentum, which results in ΔI= 0,1 or 2. Therefore, the selection rule for *first-forbidden* decay is given by:

$$\Delta I = 0, 1, 2 \qquad \Delta\pi \text{ (parity change)} = \text{Yes} \tag{4.12}$$

Transitions with $\Delta I \geq 2$ but without any change in parity, are not endorsed by either the *allowed* or *first-forbidden* selection rules. Transitions with $l = 2$ β emission are known as *second-forbidden* decays. For S=0 or 1 to $l = 2$ the nuclear spin can be changed by any amount from $\Delta I = 0$ to $\Delta I = 3$. Cases like $\Delta I = 0$ or 1 fall within the selection rules of the *allowed* decays and the contribution of the *second-forbidden* decay is negligibly small [7]. Therefore,

the selection rules for *second-forbidden* decay is given by:

$$\Delta I = 2, 3 \qquad \Delta\pi \text{ (parity change)} = \text{No} \tag{4.13}$$

The higher the order of forbiddenness the more unlikely the decay, which means nuclei prefer to decay via *allowed* or *first-forbidden* decays. Table 4.1 represents the types of β-decay transitions.

Type	Order of forbiddenness	ΔL	$\pi_f\pi_i$	log ft
Super-Allowed		0	+1	3.48 - 3.5
Allowed		0,+1	+1	3.5 - 12.5
Forbidden unique	1	$\pm$2	-1	5.1- 17
	2	$\pm$3	+1	11 - 15.5
	3	$\pm$4	-1	$>$ 17.6
	4	$\pm$5	+1	
	(ΔL $-$1) nth	$>$1	(-1)$^{(L-1)}$	
Forbidden	1	0, $\pm$1	-1	
	2	$\pm$2	+1	
	3	$\pm$3	-1	
	4	$\pm$ 4	+1	
	(ΔL $-$1) nth	$>$1	(-1)$^{\Delta L}$	

Table 4.1. Categorization of β-transition types [36].

Chapter 5

Design of the Tape Station

5.1 Motivation for tape station

iThemba LABS is developing a radioactive-ion beam facility that will be in operation in the near future. This facility will be realized by producing fission fragments when a uranium carbide target is bombarded by protons. Many of the produced fission fragments are short-lived, and they β-decay to daughters and grand-daughters until they reach a stable nucleus. With a measurement setup such as AFRODITE (AFrican Omni-purpose Detector for Innovative TEchniques) array [79] of HPGe detector at iThemba LABS, it is difficult to study the β-decay of these fission fragments because of the background radioactivity created by their daughters.

The build-up of radioactivity from the decay of grand-daughters reduces the experimental sensitivity by increasing the level of background radiation. To address the problem of radioactivity created by daughters, a device such as a tape station is used. It is used to transport the activity to and away from the site of the detectors. After the activity from the nucleus of interest has been observed for a determined period, the tape moves the activity away from the measurement position and stores it in a shielded area. The production of activity for this type of measurement is discussed in section 5.1.1.

5.1.1 Source of activity in β-decay measurement

To successfully perform β-decay measurements and to demonstrate the capabilities of the tape station, radioactive nuclei are required. These nuclei are artificially produced in the laboratory, often in radioactive-ion beam (section 1.2) facilities. However, at the time of this work, radioactive-ion beams were not available at iThemba LABS. Therefore, another method of producing radioactive nuclei had to be used. In this case, fusion-evaporation reactions provide a source of recoiling radioactive atoms that could be implanted on the tape.

In fusion-evaporation reactions, two nuclei are fused to form a compound nucleus which decays by first emitting nucleons (proton or neutrons) until the energy is not enough to emit more nucleons. Then the compound nucleus can decay either by emitting γ-rays before it reaches either the ground state or a long-lived state. These states decay by undergoing successive β-decays while emitting γ-rays and conversion electron until a stable nucleus is reached. More details about fusion evaporation reactions can be found in these references [80, 81, 82, 83]

5.2 Description of the tape station

Tape station systems are used for the collection and counting of short-lived radioactive nuclei, often at radioactive-ion beam facilities. There are two types of tape station configurations. The first configuration is where the implantation point is different from the measuring point. The implanted activity is transported to the measuring site as shown in figure 5.1(a). However, this configuration has limitations when it comes to nuclei with half-lives shorter than the transportation time, because they decay before reaching the detection site. In these cases the tape station is limited by the speed of operation, therefore another configuration must be used. The second type is where the implantation point is the same as the measuring point, as shown in figure 5.1(b). In this configuration, no time is lost in transporting the activity to the detectors, the decay of the radio-nuclide of interest is measured and thereafter, it is transported away from the site of the detectors before the activity of the grand-daughters builds-up.

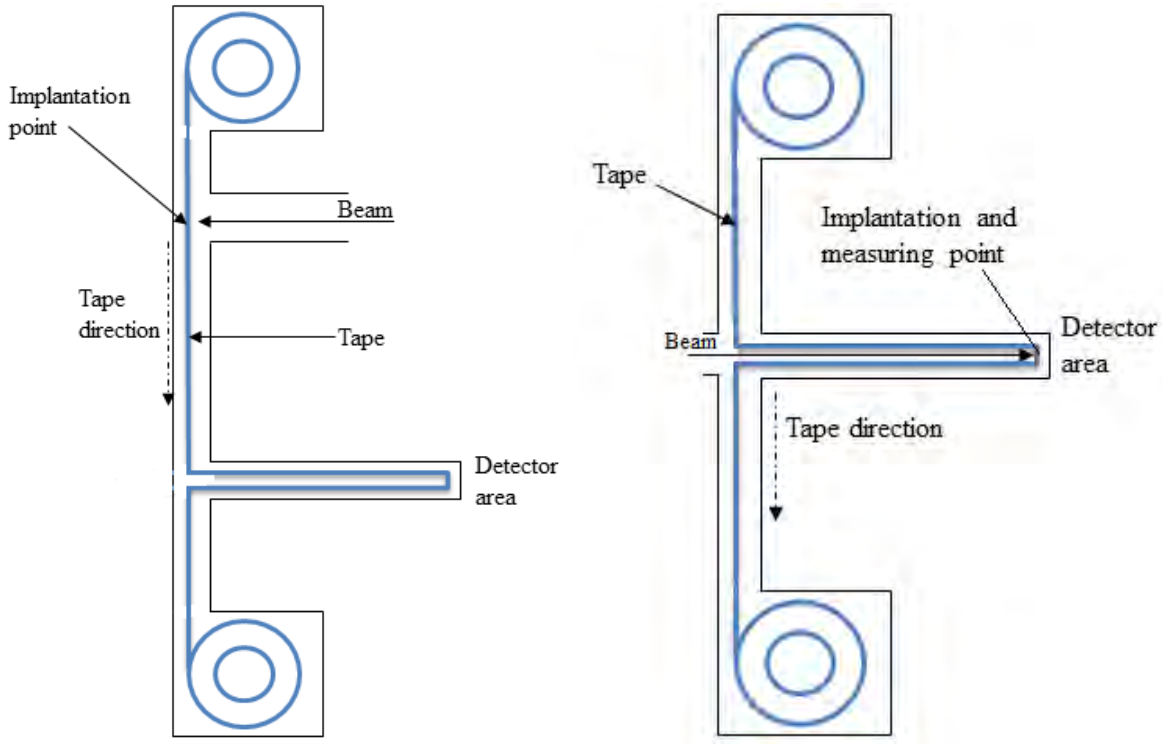

(a) . (b) .

Figure 5.1. Schematic representation of different designs of tape stations where (a) show the measuring at different spot while implantation at other spot and (b) shows measuring at the implantation point.

5.3 Review of the tape station systems

At the beginning of the project we visited overseas laboratories to see first hand, the operation different tape stations, in particular BEDO (section 5.3.3) and TATRA (section 5.3.4, figure 5.5(b)); the latter also in an experiment at ISOLDE (section 5.3.1, figure 5.2). These visits were aimed at getting as much information as possible about the advantages and disadvantages of different configurations of such devices. We also performed a survey (section 5.3) of different tape stations used in radioactive-ion beam facilities around the globe, to make an informed decision about our tape station design.

Tape stations used in different radioactive-ion beam facilities are distinct from each other. Their mechanical properties are different, but they all transport radioactivity to and away from the sight of the detectors. The following section discusses tape-stations used in some leading radioactive-ion beam facilities.

5.3.1 Tape stations at ISOLDE and SPIRAL II

This fast tape station was designed and developed at the Institute Pluridisciplinaire Hubert Curien (IPHC) Institute of Strasbourg to be deployed at ISOLDE, CERN [84] and SPIRAL II, GANIL [84, 85]. For this tape station, radioactive-ions are implanted at one spot and the tape is moved at high speed to the measuring site. This system can accommodate multiple measuring points equipped with dedicated counters as shown in figure 5.2(a). The tape transport system is kept under vacuum separately from the beam line by its vacuum pumps. This system consists of three fast motors, one for each spool and one at the central capstan. The capstan motor controls the tape movement while the spool motors are used to keep constant tension on the tape [84, 86].

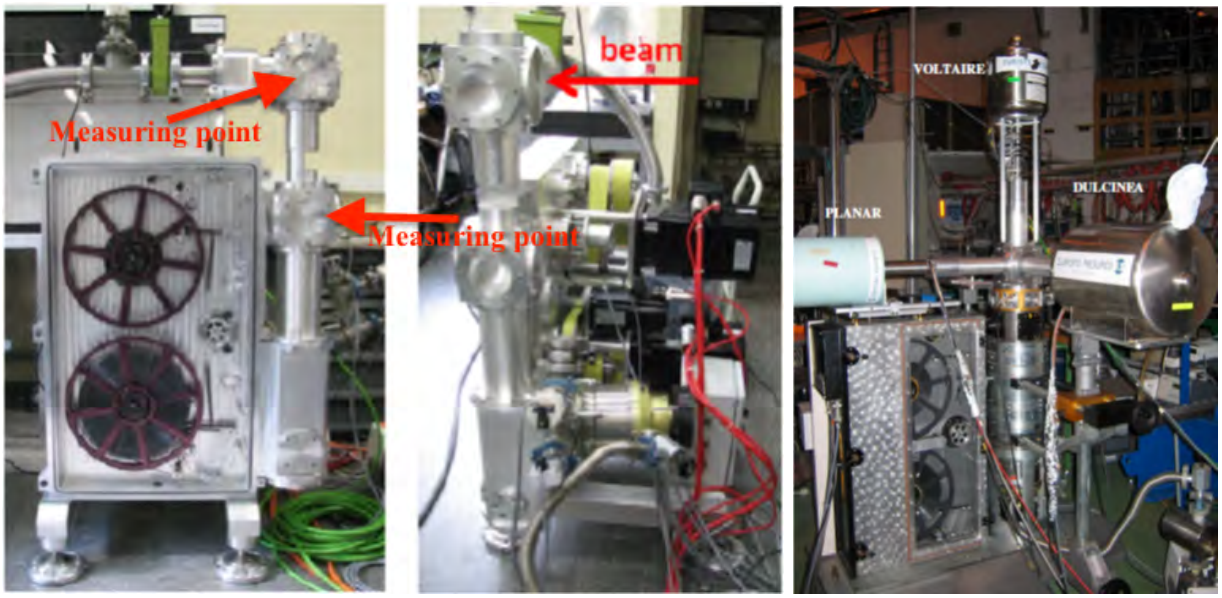

(a) (b)

Figure 5.2. Tape station used at ISOLDE (b) [84] and (a) SPIRAL II [86] designed at IPHC institute Strasbourg [86].

With this device, the collected source can be 50 cm away from the implantation point and it only takes 120 ms to transport the implanted activity. The implantation to measurement distance can be adjusted according to the aim of the planned experiments. However, at rather high speeds (> 5 m/s) the performance of the system strongly depends on the geometry of the tape path. The tape used in this system is aluminized Mylar of 55 μm thickness with a 0.08 μm thick aluminium coating on one side. The tape is 12,7 mm wide and the reels can accommodate up-to one kilometre of tape [86]. The disadvantage of this system is that the tape overshoots during deceleration, and during acceleration the pitch roller (the small wheel that pushes the tape against the capstan) opens-up, causing the tape to slip out of the capstan and pulleys. Lastly, the tape looses tension at high speed [84].

5.3.2 Tape station at HRBF and TRIUMF

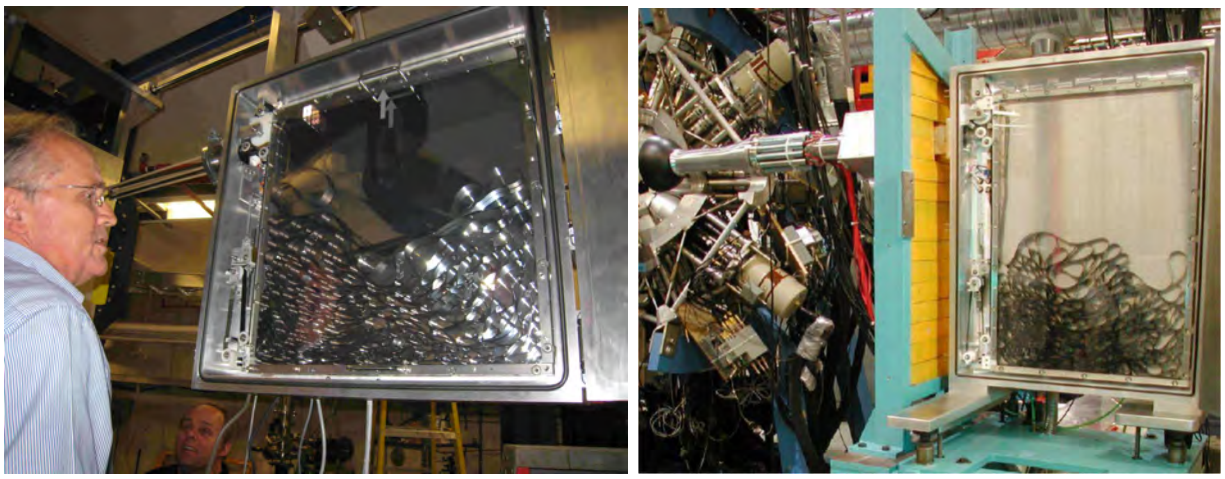

(a) (b) .

Figure 5.3. Tape station designed by E F Zganjar (shown in figure 5.3(a)) where the tape is only under tension external to the device, (a) HRBF Moving Tape Collector (MTC) [87] and (b) the tape station couple to the 8π spectrometer at ISAC, TRIUMF [88].

The Holifield Radioactive Beam Facility (HRBF) at Oak Ridge National Laboratory has built a tape station and is referred to as a Moving Tape Collector (MTC) 5.3(a). In this system, a radioactive-ion beam is implanted at the measuring point before the activity is moved away from the sight of the detectors. This system is unique because the tape is not under tension, it is contained loose in a cassette. That means the inertia of only a few centimeters of tape must be overcome in both acceleration and deceleration. The same design was also adopted by ISAC (Isotope Separator and ACcelerator) facility at TRIUMF [88]. The tape transport system was installed on the 8π spectrometer where the radioactive beam is deposited at the center of the array, and then the tape is moved away and stored behind a lead shielding wall to suppress long-lived daughter activities as shown in figure 5.3(b). The bulk of the tape is contained loosely in a cassette as shown in figure 5.3 and can adjust itself between the moves of the external part of the tape. The cassette can accommodate 92 m (300 feet) of tape and it can have a velocity up-to 3000 RPM depending on the experimental details.

5.3.3 BEDO tape station

At IPN-Orsay, a tape station known as BEDO (BEta Decay studies at Orsay) has been developed. In this system, the implantation point is the same as the measuring point, see figure 5.4(a). The nuclei of interest are implanted onto a 12 mm wide aluminized Mylar tape. The tape cassette is located above the detection system as shown in figure 5.4. As the tape goes down it interrupts the beam where radioactive nuclei of interest are implanted and different

nuclear properties are measured, thereafter it runs a bit further down and turns-up again, ending in the second reel far away from the implantation point. The whole system is kept under the same vacuum as the beam line. The implanted radioactive nuclei undergo β-decay creating daughter nuclei. To obtain a clean spectrum (meaning not polluted by the γ-rays from the daughter nuclei) the tape is moved in cycles so that the implantation position changes and the previous one is far enough not to contribute as a background radiation source. The average time required for one tape move is 2 sec. The tape movement is set and controlled with an automatic system.

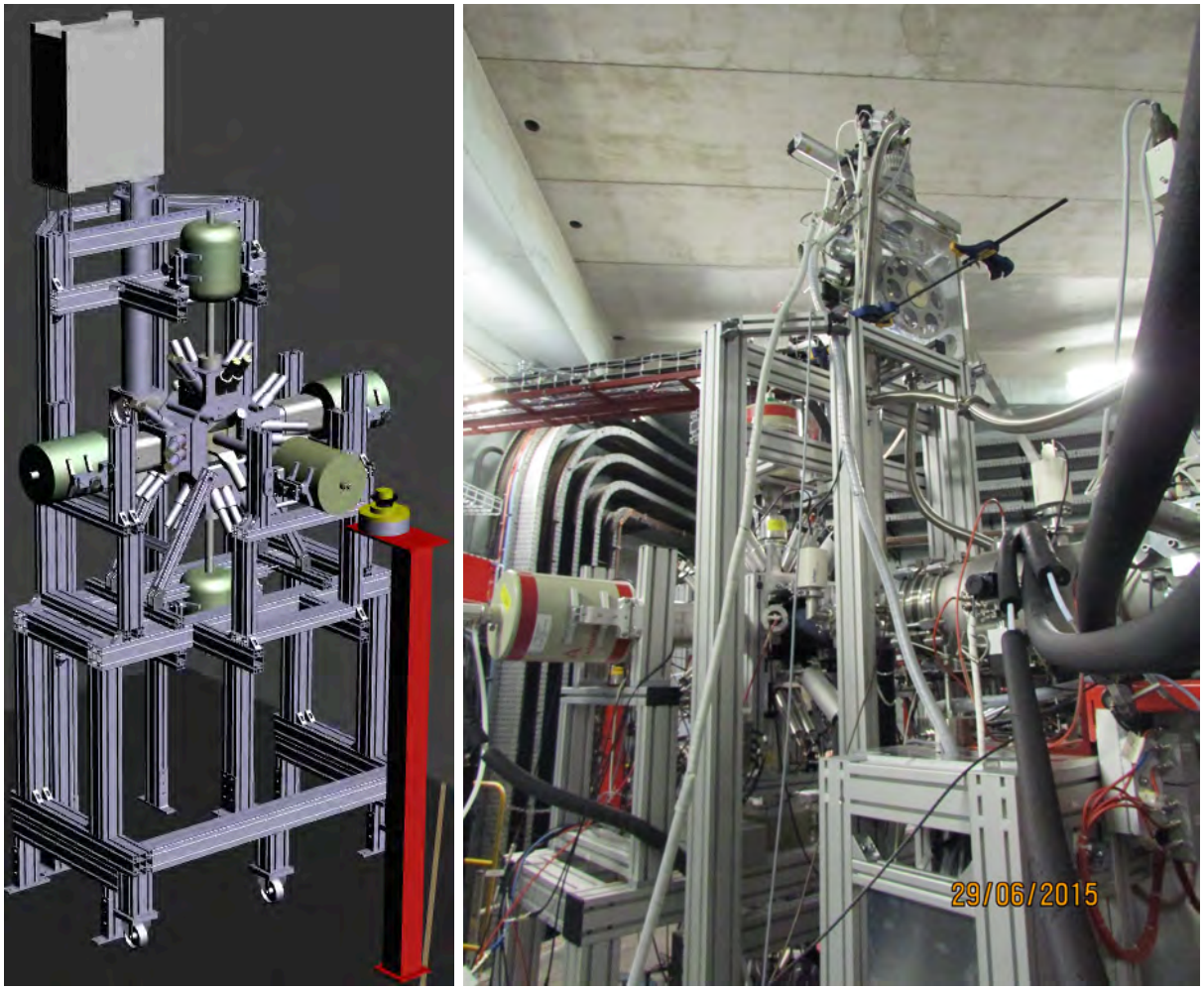

(a) . (b) .

Figure 5.4. BEta Decay studies at Orsay (BEDO) tape station, (a) CAD drawing of the BEDO tape station, (b) photograph of the BEDO tape station connected to beam line at Orsay

The BEDO system can accommodate up-to one kilometer of tape. Due to the mechanical design of this system, the speed is limited to one meter per second. At high operational speed the tape overshoots during deceleration.

5.3.4 UNISOR Moving Tape Collector and TATRA

These tape systems are based on the 8-track cartridge [89, 90] which was used for music in the early 1960's. It contains a single spool and it can only play 8-tracks, hence the name 8-track. The first concept was successfully used at the UNISOR (UNiversity Isotope Separator at Oak Ridge) facility at the Oak Ridge National Laboratory, and is shown in figure 5.5(a). Due to the success of this design, three systems were built. These systems utilized an endless continuous loop carried by a single reel. The tape is pulled from the center of the reel, passes into the system and winds back to the outside of the same reel. The first design was portable with the dimensions 25 cm x 15 cm x 6 cm and could accommodate 117 m of tape [91]. Due to the compact design of this system, the transportation time was 0.5 second over a distance of 15 cm. The UNISOR tape station used the recording tape coated with graphite on the reverse side and for experimental purposes that coating was also used to read the beam current [91].

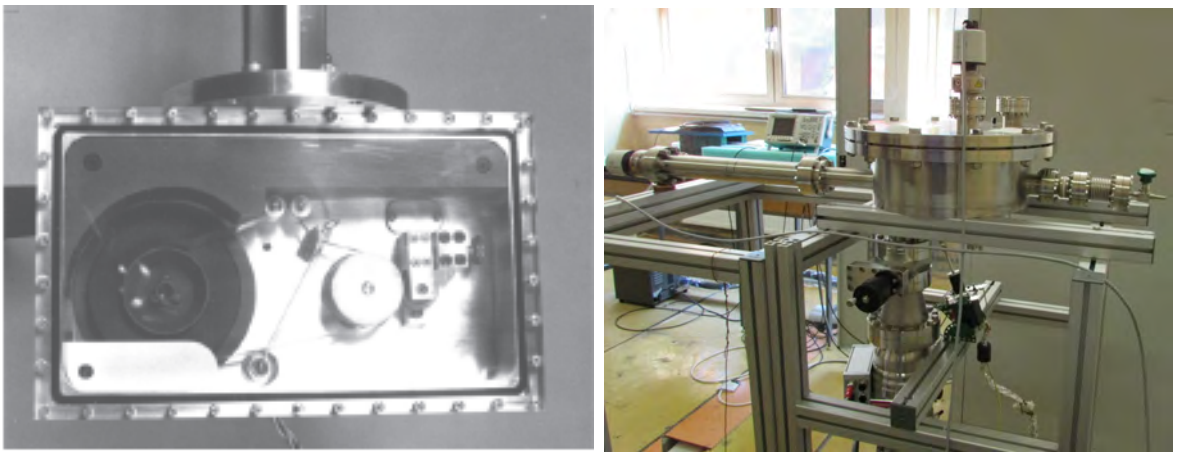

(a) (b)

Figure 5.5. Single spool tape station, (a) UNISOR moving tape collector [34, 91, 92], (b) TATRA tape station [93].

However, on the TATRA (TApe TRAnsportation) system (shown in figure 5.5(b) [93]) the plastic tape was replaced with an amorphous metallic alloy tape. The metallic tape was prepared by rapid quenching (106 K/s) of a molten $Fe_{30}Ni_{46}Cr_2Mo_2Si_5B_{15}$ alloy [93]. The tape properties are suitable to be used during physics experiments as it is difficult to stretch during operation compared to plastic tapes, does not undergo corrosion and it can be used in a high vacuum environment. Nevertheless, it can be easily torn, and thus needs to be handled with care. The tape has a width of 6 mm, similar to that of the original 8-track, and the reel can only accommodate 25 m of tape. Because the tape is metallic and the reel carrying the tape is stainless steel, a tape longer than 25 m becomes too heavy and can easily tear during acceleration. The system can be operated up to a speed of 1 m/s [93].

5.3.5 The single spool concept

The advantage of an 8-track system is that it is a single spool that moves in one direction, continuously. The tape is pulled from the center of the reel while tape is taken-up on the outside of the reel as shown in figure 5.6. The design is mechanically simple and easy to implement. Due to the time constraints of my studies, this design was more feasible than all the other designs reviewed. However, this design has its short-comings. The major one being that it cannot have a long tape length due to the difference in radius of the center and outer reel of the tape.

Figure 5.6. Mechanical design of the 8-track cartridge illustrating the inner and outer radius. It also demonstrates how the tape slides against itself [94].

Each wrapping of the tape must decrease in length by a certain amount compared to the next outer wrap. This is accomplished by sliding the same amount relative to the previous layer. The original tape used on the 8-track hub uses a special lubricant, but once the tape loses the lubricant it binds up and jams. The tape on the spool has to be kept loose because its slides against itself. A system with the ideal length of tape can reproduce the distance to an accuracy

better than ±1 mm.

5.3.6 Review Outcome

All the tape stations reviewed are distinct from each other and have their advantages and disadvantages. For example, TATRA only used 6 mm wide tape and hold less tape compared to other systems because of the heavy nature of its tape. Again, the advantage of the TATRA tape is that it is robust to stretching, it does not stretch during operation compared to plastic tapes. The ISOLDE and SPIRAL2 (5.2) tape station is the state-of-the-art system but comes at a heavy price (70 keuro: 2008 [86]). It is a fast system dedicated in probing radio-nuclides with shorter half-lives (in the range of milliseconds). The BEDO (5.4) is a very good system but it is mechanically complicated as it uses three stepper motors.

5.4 iThemba LABS tape station

The iThembs LABS tape station is based on the UNISOR/TATRA design, section 5.3.4. This design was chosen because it is not complicated mechanically, and uses a single stepper motor, taking advantage of the single continuous loop. The advantage of the single spool is that it is a continuous system that does not need to be rewound after a certain period. This means that there will be no beam time lost during measurement(s) due to tape rewind. Our tape station could not use the same tape dimensions to that used at UNISOR/TATRA, as it would use 12 mm wide tape, see figure 5.10 and 5.11.

This design can not handle high-speed operation (more than 1 m/s) because the tape either loses or gain tension and overshoots. Therefore, speed optimization needs to occur well in advance to determine the limits. The tape join should be smooth to avoid adding different friction when the tape is sliding. For the iThemba LABS tape station, adhesive filament tape was used to join the tape because it has high tensile strength. Unsatisfactory tape joints cause the system not to lose position accuracy and it can also cause the tape to jam.

5.4.1 Design of the Tape station

The tape station should be able to catch recoiling nuclei produced by fusion-evaporation reactions (5.1.1) and transport the activity to the measuring site. The whole tape station assembly can be attached to a standard beam line (100 mm in diameter). A 3D model of the system is shown in figure 5.7. This tape system consists of the three chambers, namely: an implantation chamber, a motor drive chamber and a measuring chamber. These chambers are connected by 100 mm diameter stainless steel beam pipe.

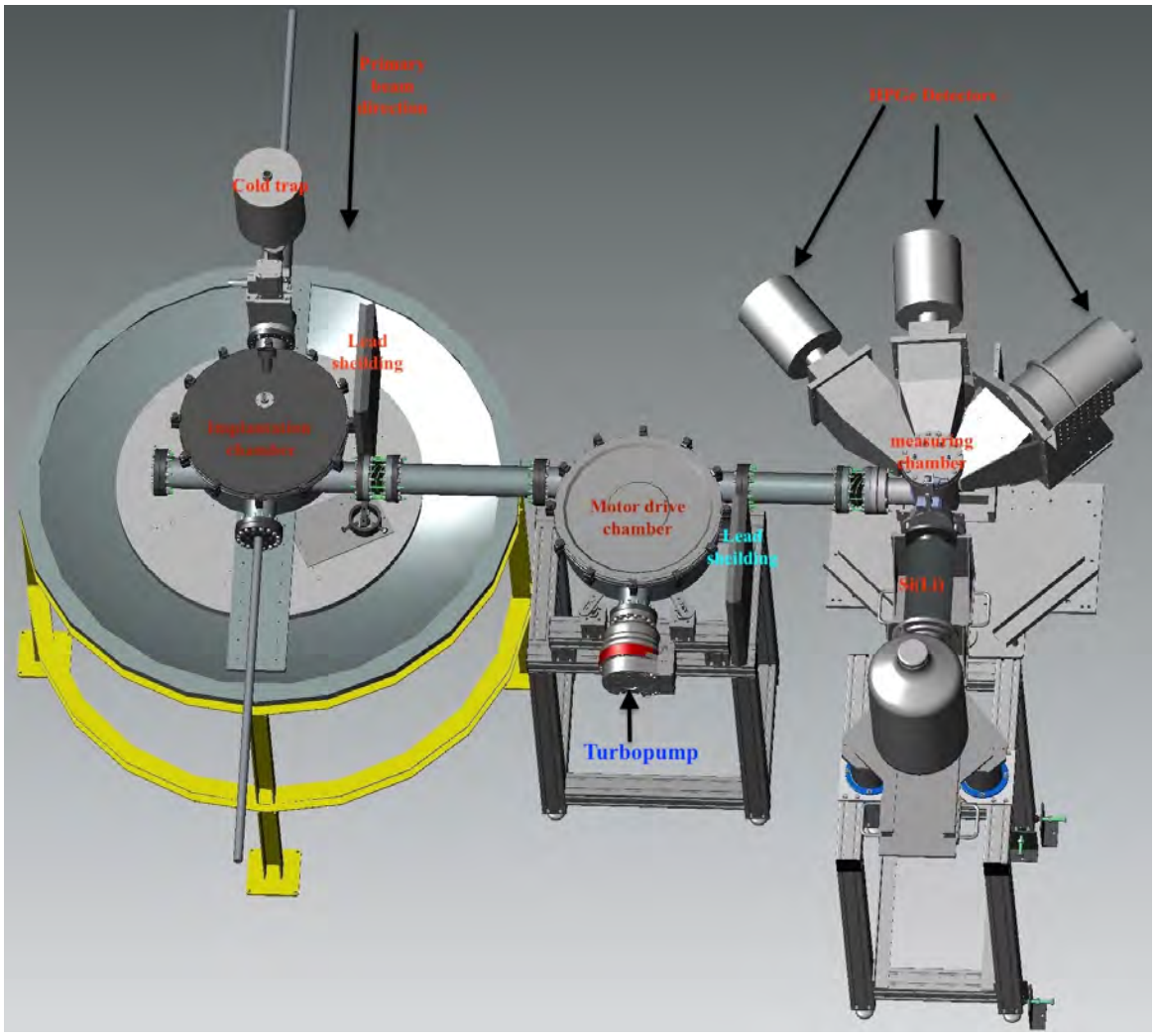

Figure 5.7. The schematic 3D model of the complete tape station setup, showing from left to right: the implantation chamber, tape driver chamber and measuring chamber surrounded by clover detectors.

These three chambers house different components of the tape station. The motor drive chamber houses the drive mechanism, the implantation chamber houses the implantation components while the measuring chamber house the Si(Li) detector and plastic scintillator. The reaction occurs at the implantation chamber where the recoils are implanted on the tape. The point of implantation is shown on the schematic of the tape station illustrated in figure 5.8. The capstan then drives the tape in a clockwise direction to transport the implanted activity to the measuring position, shown in figure 5.8.

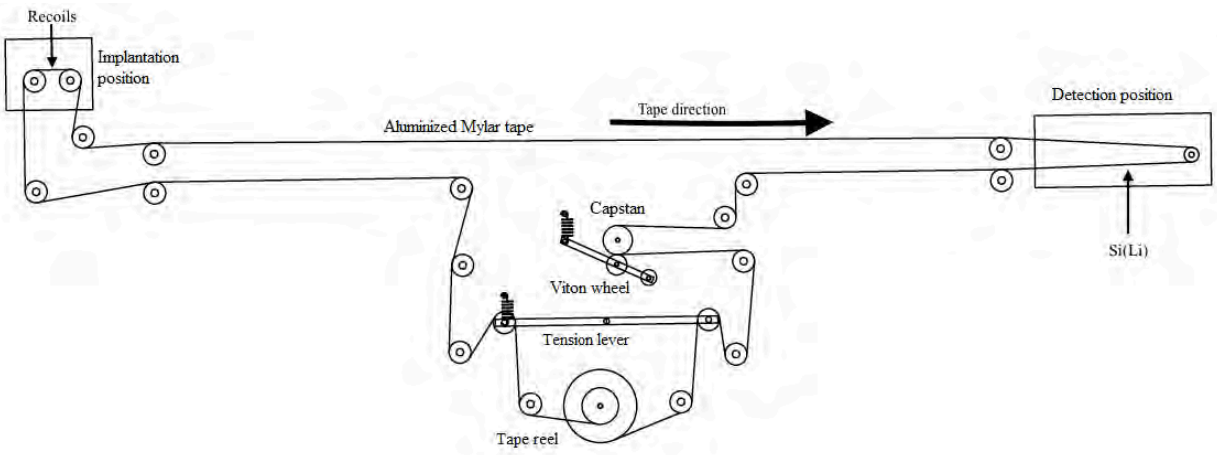

Figure 5.8. A schematic diagram of the installed tape station. The recoils are deposited on the tape in the implantation position. Thereafter transported to the detection position via the tape motion in clockwise direction. The capstan drives the tape.

The tape is driven by a stepper motor located outside the motor drive chamber as shown in figure 5.9. The stepper motor is mounted underneath the chamber and it is connected to the capstan that drives the tape via a ferromagnetic coupler. The stepper motor used in this system is a Hybrid 86S124-3508A [95]. The motor is electrically isolated from the motor drive chamber by using Vesconite spacers.

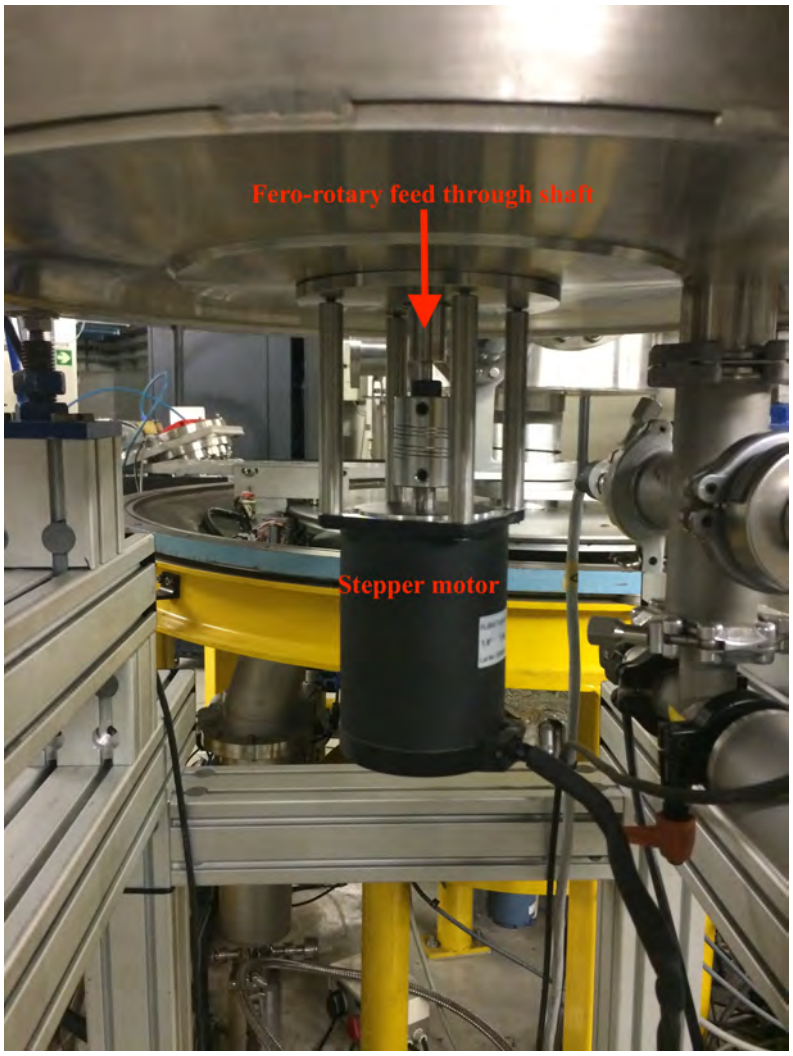

Figure 5.9. Stepper motor connected to the motor driver chamber via Fero-rotary feed through shaft.

The motor drive chamber is the heart of this tape station and has a diameter of 500 mm and height of 150 mm. The chamber internals are accessed through the top-lid of the cylinder and are shown in figure 5.10.

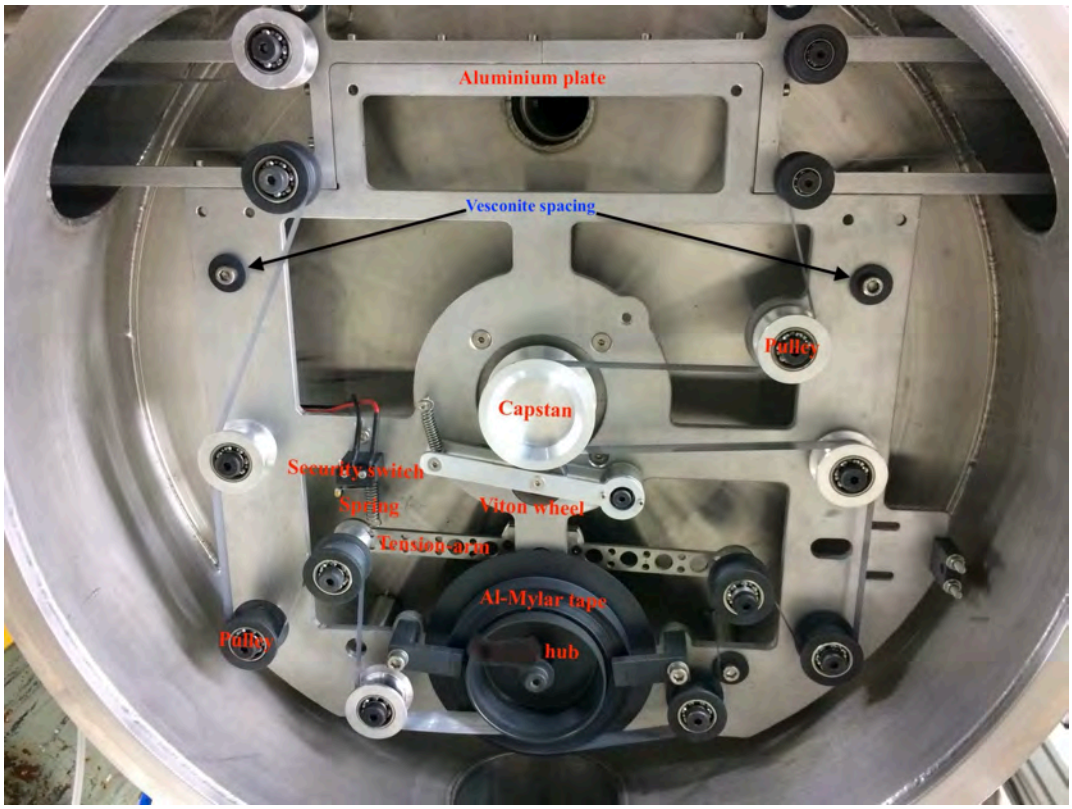

Figure 5.10. Internals of the system in the motor driver chamber. A hub with tape, capstan, some pulleys and safety switch.

This chamber houses the capstan which drives the tape, a Viton wheel which clamps the tape to the capstan to create friction, a hub which stores the tape, and a tension-arm which acts as a shock-absorber for the tape system. The tension-arm is connected to a spring that is located close to a mechanical switch. If the tape breaks or loses tension, the spring will pull the arm towards the switch and stop the system. The internal structure of the drive mechanism is supported by an aluminium plate inside the motor driver chamber. The aluminium plate extends on either side of the motor drive chamber into the connecting beam pipes. This allows the tape to navigate around the pulleys on a stable horizontal platform. The tape is electrically isolated from the motor drive chamber via Vesconite spacing between the plate and supporting rods, see figure 5.10.

The system draws inspiration from the 8-track hub which accommodates 6 mm wide tape. It was scaled-up for this experiment to work with 12 mm wide tape as shown in figure 5.11(b) The scaled-up hub (figure 5.11(b) is made of Vesconite, which has a low friction coefficient of 0.08, which is less than that of bronze or nylon [96].

(a)

(b)

Figure 5.11. This shows the original design of the (a) 8-track hub which uses 6 mm wide tape and (b) the design used in this study.

The scaled hub can not work with any tape thickness because the tape comes out on a spool at an angle as shown in figure 5.6. To address this problem, different tape thicknesses were tested and the system only accepted a tape with a minimum thickness of 50 μm. However, this thickness tape only lasted for short periods of time before it broke.

We could not source any tape thickness between 51 and 90 μm. Therefore, the tape used in this system is an aluminized Mylar (ES301955 Polyethylene terephthalate Metallised Film Polyester, PET, PETP) with thickness of 100 μm and it was obtained from GOODFELLOW [97]. The thickness of the aluminum is 0.03 μm while the Mylar is 99.97 μm. The aluminium side of the tape is used to collect nuclei. The spool is large enough to accommodate 50 m of tape, see figure 5.11(b).

The implantation chamber houses the Faraday cup (used to stop the beam and to read the

beam current), ruby (used for beam focusing), target (for radioactive ion production) and the tape to collect the recoils. The beam hits the target, thereby producing radioactive nuclei that fly, generally, in the direction of the beam. Because of neutron evaporation and scattering in the target, the recoils develop a transverse component to their momentum, which allows a sizable fraction of the recoils to bypass the Faraday cup and be implanted in the tape. The implantation chamber internals used for beam alignment are shown in figure 5.12. The comprehensive figures showing the implantation chamber with different internals used in all the experiments performed are shown is section 6.29 and 6.40.

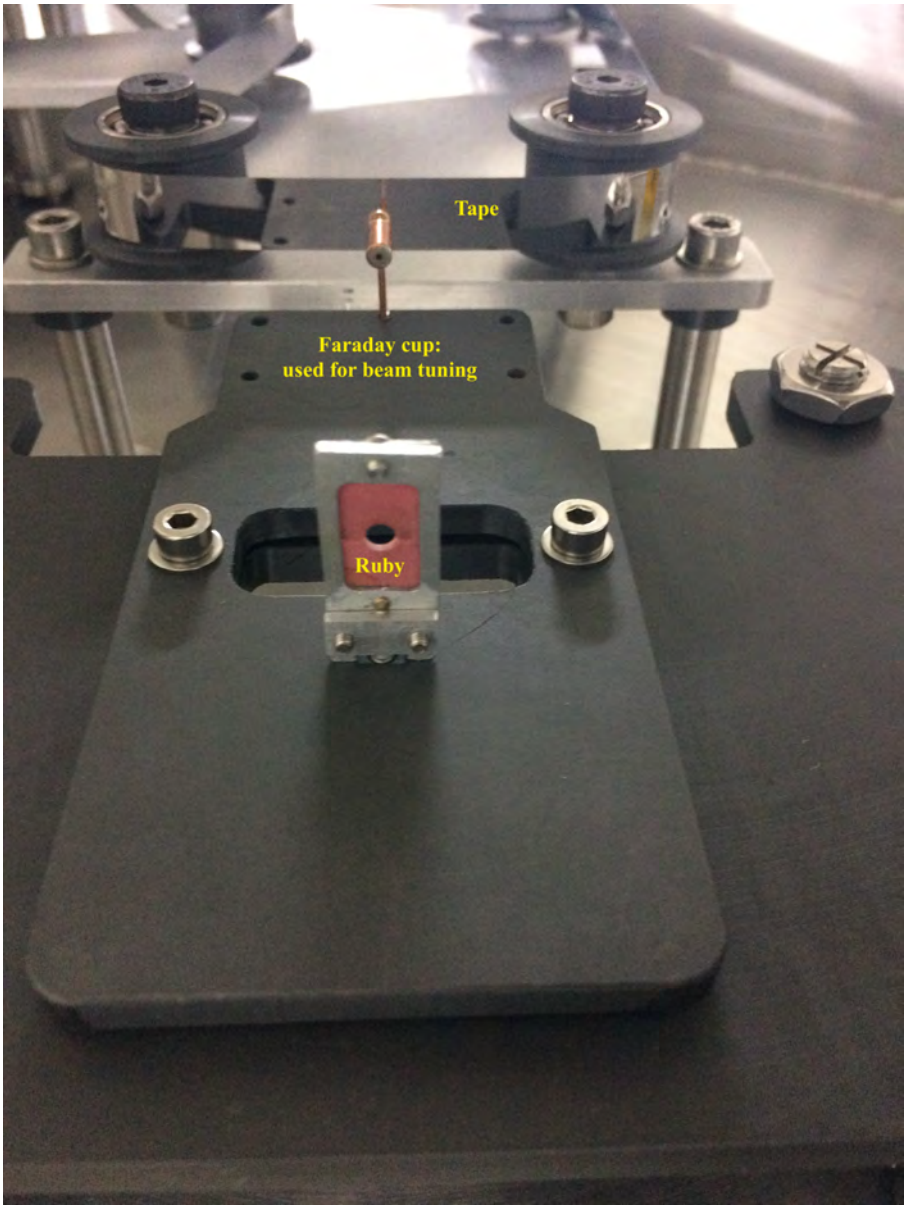

Figure 5.12. Implantation chamber internals used during beam tuning. The target ladder is attached on the top-lid cover of the chamber and it is located behind the ruby.

The measuring chamber completes the system. It houses the plastic scintillator for β-particle detection and it is connected to another chamber that houses a Si(Li) detector (see section 6.5) to detect conversion electrons while surrounded by HPGe γ-ray detectors. The measuring

chamber allows the Si(Li) and plastic scintillator to be brought into proximity to the tape, more detail about the measuring chamber is shown in chapter 6, section 6.3.3, figure 6.9 and figure 6.31. After counting for a given period of time, the tape will be moved again and the old transported activity will be stored on the hub. The distance from the implantation point to measuring position is 2.3 m and the total length of the tape used in this experiment is 50 m, giving about more than 191 movements before the first implantation spot can come back to the reaction position. The motor drive chamber and implantation chamber are shielded by 30×30 cm block of lead shielding as shown in figure 5.7. The movement between implantation to the detection point has been reproduced to a mean square accuracy of less than ± 0.1 mm. However, the transport speed is limited to 1 m/s due to tape stretching during start and stop cycles that results to tape breakages and overshooting.

Lastly, the tape system operates under high vacuum, $\approx 1.6 \times 10^{-6}$ mbar achieved by pumping on the system through a motor drive chamber with 300 *l/s* turbopump, see figure 5.7. This high vacuum is achieved before opening the valve connecting the system to the beam line.

5.5 Driver control mechanism

5.5.1 Beckhoff EtherCAT

The tape station is controlled by Beckhoff EtherCAT (Ethernet for Control Automation Technology) modules. EtherCAT is a real-time bus system that is based on the Ethernet technology i.e. it is an Ethernet field-bus system [98]. The Beckhoff EtherCAT modules used to drive the tape station are shown in figure 5.13, and comprise of a coupler, stepper motor controller, digital input and digital output. These modules are powered by a 24 V power supply while the stepper motor is powered by a 48 V power supply. The coupler is connected to a computer via a standard Ethernet connection.

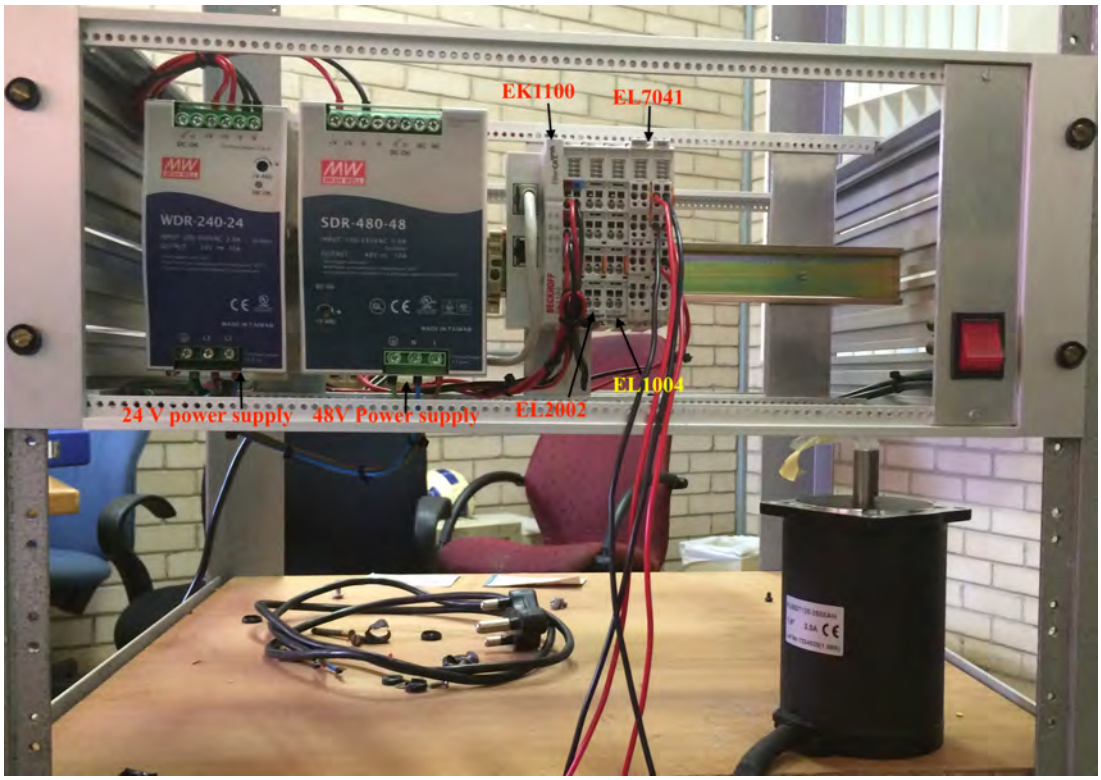

Figure 5.13. The Beckhoff modules used to drive the tape station.

The Beckhoff modules are connected together by using the spring contacts located on the inside-edges of each module as shown in figure 5.14. Any station that uses Beckhoff modules, will have a EK1100 coupler module or similar for communication. The six spring contact shown in figure 5.14 of the K-bus deal with the transfer of data and supply of the Bus terminal electronics.

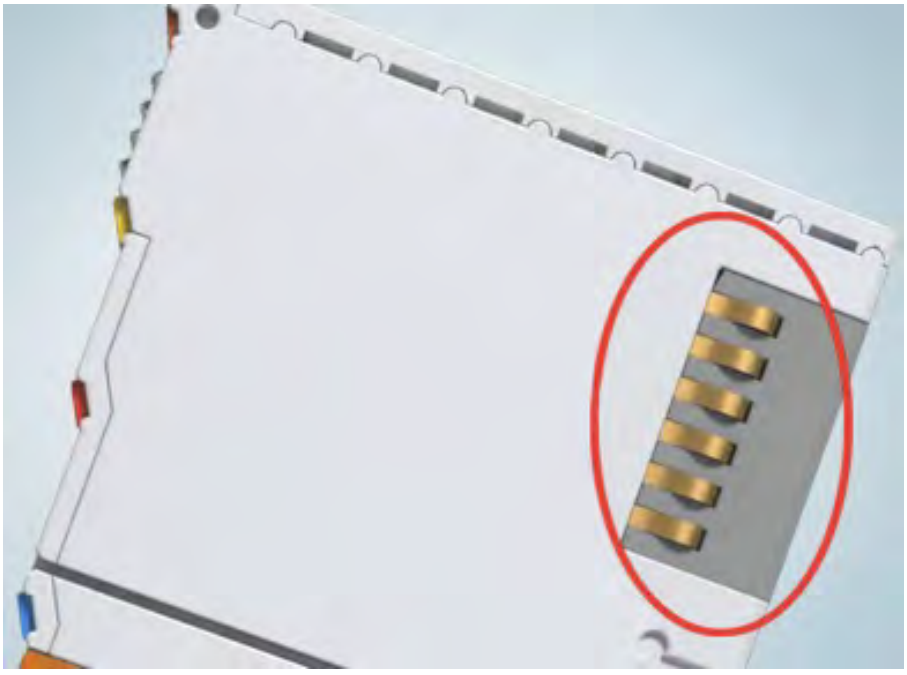

Figure 5.14. This image illustrate the pin connection of the Beckhoff modules [99].

These modules are explained in detail below;

EK1100 Bus Coupler

The EtherCAT Coupler connects the EtherCAT terminals e.g. EL1004, EL2002, and EL7401, with a E-bus communication (system that transfers data between components) to an EtherCAT network. Then the EtherCAT coverts the telegrams (coded pulse of electric current) from the Ethernet 100BASE-TX to E-bus signals. The main function of the coupler is that it supplies the connected terminal with vital E-bus current for communication. The coupler can supply a maximum of 5V/2A [99].

EL1004 Digital input

The digital input terminal acquires binary control signals from the process level and transmits them in an electrically isolated form to the higher-level automation device. To monitor the system, the signal from the security switch (see figure 5.10) of the system was connected to this module. The signal state is indicated by an LED for each channel connected [100].

EL2002 Digital output

The EL2002 digital output terminals connect the binary control signals from the automation device (beam deflector signal) onto the actuators at the process level with electrical isolation [101]. This module was used to send the signal out during tape movements and the signal output is indicated by an LED for each channel connected [102].

EL7041 Stepper motor control

The EL7041 EtherCAT Terminal is used to control stepper motor with medium performance ranges. The EL7401 can achieve a peak current of 5 A, which can generate an impressive torque of 5 Nm in conjunction with a stepper motor. It can supply a voltage of up to 50 V_{DC} which enables high speed with good torque operations. This terminal has an integrated incremental encoder interface for connecting all driver cables. The standard stepper motor with 1.8^{o} angle operates smoothly and can be set up to 12800 electronic positions per turn. The EL7041 terminal supports 2-phase stepper motors. The 4-wired motor are basically 2-phase motor with separate winding ends. The stepper motor used to drive the tape station is a 4-wired type, meaning it provides four output wires to connect to the motor controller terminal. The 4 wires carry the 4-phases of the stepper motor. The parameters of the stepper motor can be easily adjusted in the EL7401 terminal by changing a few parameters. Usually the stepper

motor operates at 200 steps per revolution but higher precision can be achieved by using 64-fold micro stepping through a software setting. This ensures that the rotor jerk is avoided and the rotor no longer tends to oscillate around each indexing position [103].

5.6 Operation characteristics

The software package Control System Studios(CSS) [98, 104] was used to develop the Graphical User Interface (GUI) for controlling the tape station. With our GUI, we can easily specify our desired implantation time, monitor the velocity of the stepper motor, transport times and acceleration. The CSS application calls EPICS (Experimental Physics and Industrial Control System) [105] commands to send out communication with the connected device. EPICS is the set of open-source tools, libraries and application developed collaboratively and used worldwide to create distributed soft real-time control systems for scientific instruments such as particles accelerators, telescopes, and other large scientific experiments [105]. iThemba LABS has developed templates that were added on the EPICS data base compatible with all the Beckhoff EtherCAT modules.

However, we can not use general EPICS code because it is intended to run stepper motors on the beam lines so for this purpose a Python code was developed to drive the stepper motor using the general EPICS code. With our Python code we could easily specify distance accurately as well as our desired speed, see appendix C for Python code. Figure 5.15 shows the GUI application that was developed to drive the tape station.

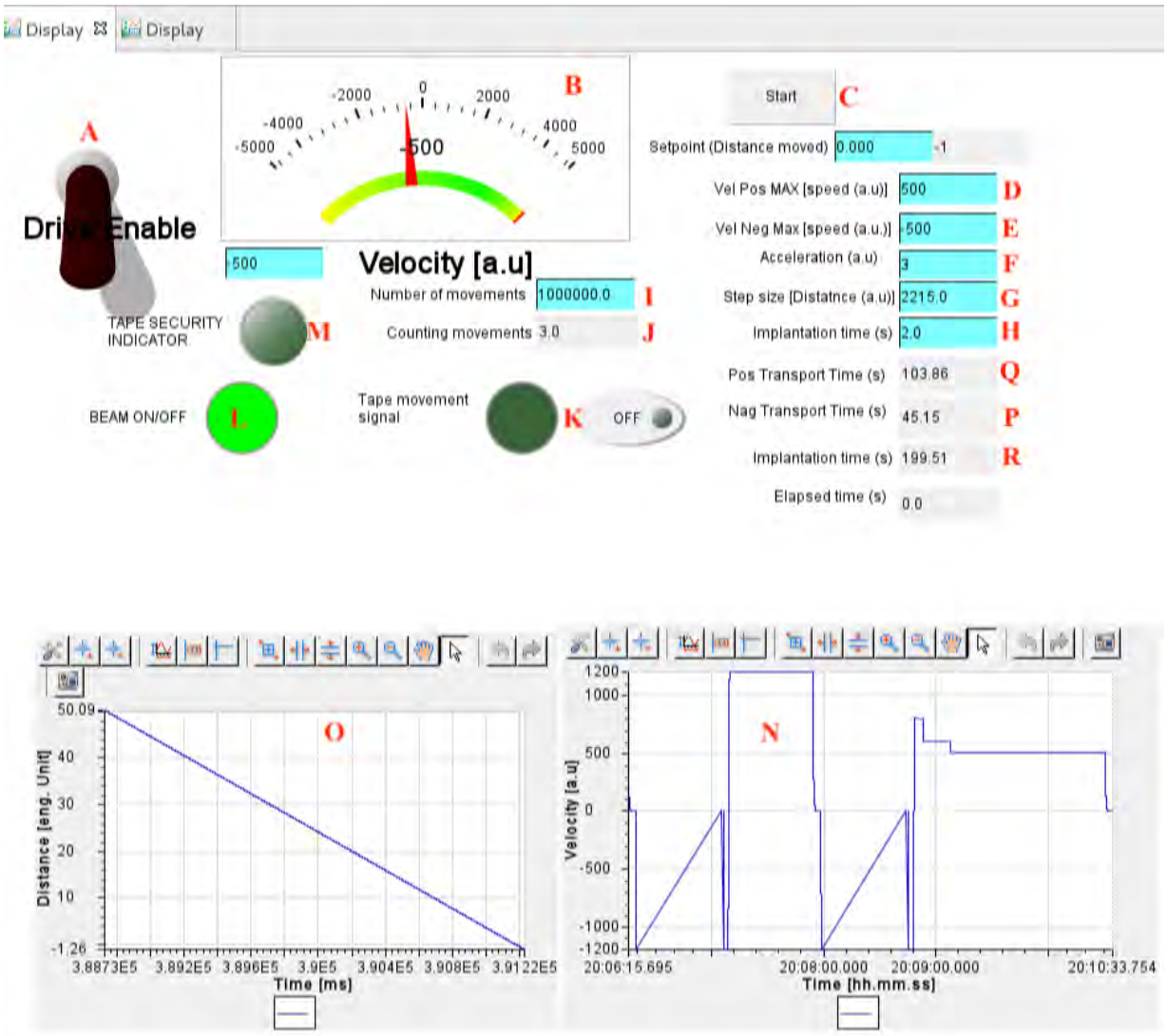

Figure 5.15. The GUI showing the parameters of the tape station. Red letters are used to describe individual function of the tape station.

All the components of the GUI are described below:

♢ A: The Driver Enable switch which turns the stepper motor on or off.

♢ B: Indicates the velocity of the stepper motor in both negative and positive directions.

♢ C: Is the start button. It initiates the whole program before the driver enable can be engaged.

♢ D: Is the speed setting for positive velocity defined later in this section.

♢ E: Is the input for negative maximum velocity.

♢ F: Is the input for acceleration.

♢ G: Is the input for the distance from implantation to measuring site.

♢ H: Is the input for the implantation time.

♢ I: Is the input for the desired number of movements.

♢ J: Counts the number of tape movements for a single implantation.

♢ K: This bulb illuminates if there is any tape movement. It indicates that the tape is moving and sends a signal to data acquisition system (Pixie16).

♢ L: This bulb illuminates if the beam is on target and turns off if there is no beam or the beam is deflected. An automated system was developed to switch the beam on and off during the implantation and transportation.

♢ M: This bulb indicates the security status of the tape system. The bulb should remain green all the time. Otherwise if it turn red, it means the tape is broken and drive enable is switched-off.

♢ N: Is the velocity versus time graph showing the motion of the tape.

♢ O: Is the distance versus time graph showing the motion of the tape.

♢ P: The system calculates the time lost during positive movements and displays it in the text widget.

♢ Q: The system calculates the time lost during negative movements and displays it here (if the fast version is used, Q = 0).

♢ R: The system counts the implantation time and displays it in the text widget.

NB: Positive means moving from the implantation site to the measuring site. Negative means transporting from measuring site to the implantation site. Negative only occurs when the spool is not used.

The GUI shown in figure 5.15 has a drive enable toggle which turns on or off the EL7041 module, and hence the stepper motor. On the GUI one can specify the number of movements the tape should make to determine the distance travelled by the tape at the end experiment. Two graphs from left to right at the bottom of the GUI show the distance-time graph and velocity-time graph during the motion of the tape.

The tension-arm, shown in figure 5.10, is connected to a soft spring which allows the arm to control the tension on the tape. The spring is tightened underneath the mechanical switch that acts as the security/safety system for the tape station. When the tape looses tension, the spring pulls the arm in the direction of the switch and closes the switch (see figure 5.10 or 6.46). Once the switch is closed, it sends a signal to one of the Beckhoff modules to shut down the operation of the system. On the GUI, the tape security indicator (letter M) will turn red

to indicate that the tape has lost tension or is broken. To fix the tape, we have to stop the experiment and break the vacuum.

To ensure that the tape is not irradiated during transportation, the beam is deflected away. The beam deflection is an automated system which gets information when the tape is moving and when it stops. The beam ON/OFF indicator (letter L) will turn green when the beam is ON-target and it will turn OFF when the beam is deflected away. During the movement, the tape movement signal (letter K) will turn-ON to indicate that the tape is moving, hence the motor is spinning.

The stepper motor is a brushless DC electric motor that divides a revolution into a number of equal steps. A full revolution consists of 200 steps, thus each step turns the shaft only 1.8^o. Several step ranges are selected in the software: 1000, 2000, 4000,6000, 8000, 16000, or 32000 steps/sec. The velocity of the stepper motor v_{step} is set by a 16 bit signed integer with values from -32768 to 32767. Thus, the actual angular velocity (ω) of the motor is given by

$$\omega = \frac{v_{step}}{32768} \times \frac{\text{range}}{200} \tag{5.1}$$

e.g. if $v_{step} = 1000$ and the range = 2000, then $\omega = 0.305$ rev/s. Since the capstan has a radius of 0,024 m, this corresponds to a tape speed of 0.046 m/s. Furthermore, if the range is = 2000 full steps/s, the maximum angular velocity, ω_{max} would be 10 revolutions/s. The speed of the stepper motor is given in the following table:

v_{steps}	ω (rev/s)	v (m/s)	ω (RPM)
1	0,0003052	4,602E-05	0,01831
100	0,03052	0,004602	1,831
400	0,1221	0,01841	7,324
800	0,2441	0,03681	14,65
1000	0,30521	0,04602	18,31
1500	0,4578	0,06903	27,47
2000	0,6104	0,0920	36,62
2500	0,7629	0,1151	45,78
3500	1,068	0,1611	64,09
4000	1,221	0,1841	73,24
5500	1,6785	0,2531	100,71

Table 5.1. Typical values for velocity of the stepper motor for relatively less aggressive (slow) acceleration, range = 2000.

If the settings are changed on the EtherCAT e.g. a higher base frequency is chosen, one can achieve faster velocity. If the range in equation 5.1 is 8000 full steps/s, then $\omega_{max} = 40$ revolutions/s. This means that the v_{steps} has a different meaning. The values in table 5.1 are

changed to be those in table 5.2:

v_{steps}	ω (rev/s)	v (m/s)	ω (RPM)
1	0,001221	0,0001841	0,07324
100	0,1221	0,01841	7,324
400	0,4883	0,07363	29,30
800	0,9766	0,1473	58,60
1000	1,2207	0,1841	73,24
1500	1,831	0,2761	109,9
2000	2,441	0,3682	146,5
2500	3,052	0,4602	183,1
3500	4,272	0,6443	256,4
4000	4,883	0,7363	293,0
5500	6,713	1,012	402,8

Table 5.2. Typical values for velocity of the stepper motor for fast acceleration, range = 8000.

Chapter 6

Commissioning test of the Tape Station

6.1 Introduction

This chapter discusses the commissioning of the tape station and its experimental setup which was assembled in the A-line vault. The detection system consisted of different types detectors. An array of HPGe detectors was assembled and will be discussed in section 6.3.1. The Si(Li) detector and plastic scintillator will be discussed in section 6.3.2.3 and 6.3.3, respectively. The acquisition system used to collect data and analysis methods are discussed as well. Two experiments were performed using the tape station and they are presented in section 6.7 and 6.8. Outcomes of the two experiments are discussed in section 6.7.1 and chapter 7.

6.2 Experimental Setup

Figures 6.1(a) and 6.1(b) show the complete experimental setup used to perform all measurements that will be presented in this work. The setup is composed of the array of clover detectors, a plastic scintillator, tape station and Si(Li) detector. The implantation chamber is connected to the beam line through a cold trap to reduce contamination from hydrocarbon in the beam line.

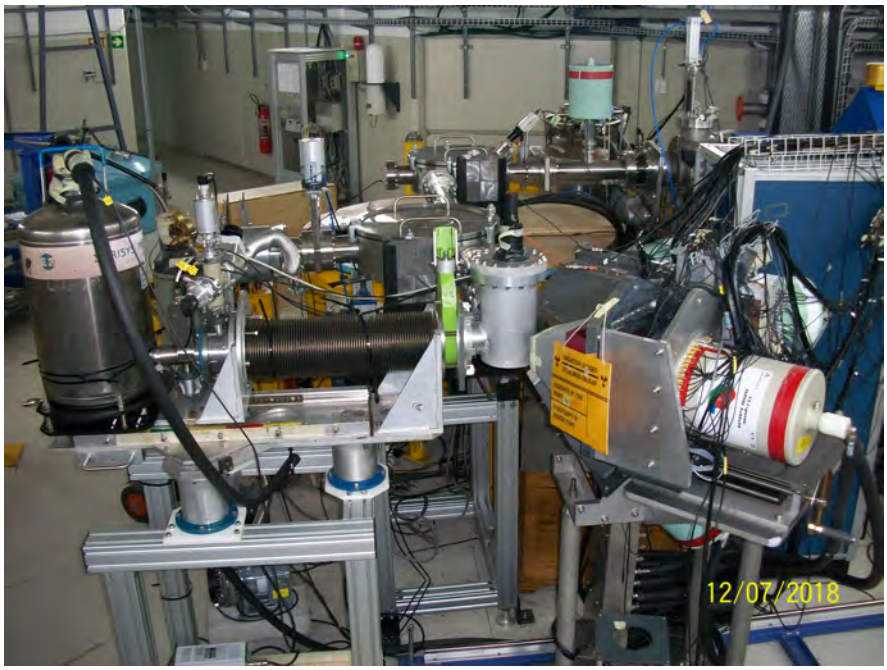

(a)

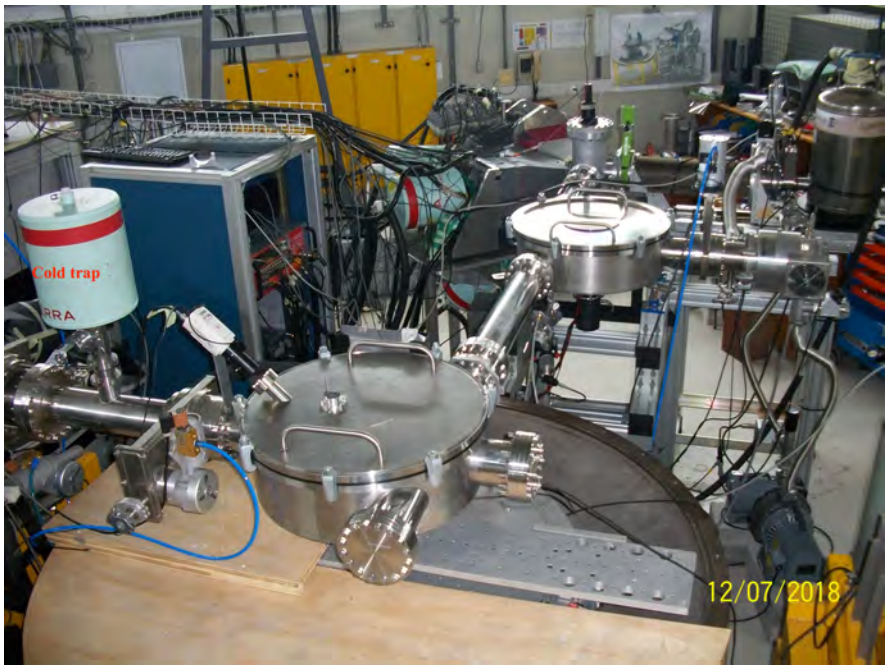

(b)

Figure 6.1. Complete experimental setup showing the top view of all three chambers for the tape station and all detectors used to collect data with (a) showing the view from the measuring chamber side and (b) is showing the view from the implantation chamber side

6.3 Detectors

The implanted activity was transported to the detection site where the decay would be observed by different sets of detectors. The array consists of germanium clover detectors for γ-ray detection, a plastic scintillator for β-particle detection and a Si(Li) for conversion electron

detection. All these detectors are discussed in detail in the following sections.

6.3.1 A-line Mini-Array

For this particular study, a mini-array was designed, developed, and installed on the A-line vault, labelled A in figure 1.1. At iThemba LABS the experimental vaults are labelled alphabetically and previously the A-line was used for scattering chamber experiments [106]. The top of the scattering chamber was removed to accommodate the tape station.

The γ-ray array comprised of three germanium clover detectors plus one segmented clover detector [107]. The segmented clover detector and clover1 and clover2 were placed on the same horizontal platform at angles: $45°, 80°$ and $135°$, respectively, with respect to the beam pipe of the tape station. Clover3 was placed at $45°$ facing the source from below as shown in figure 6.2.

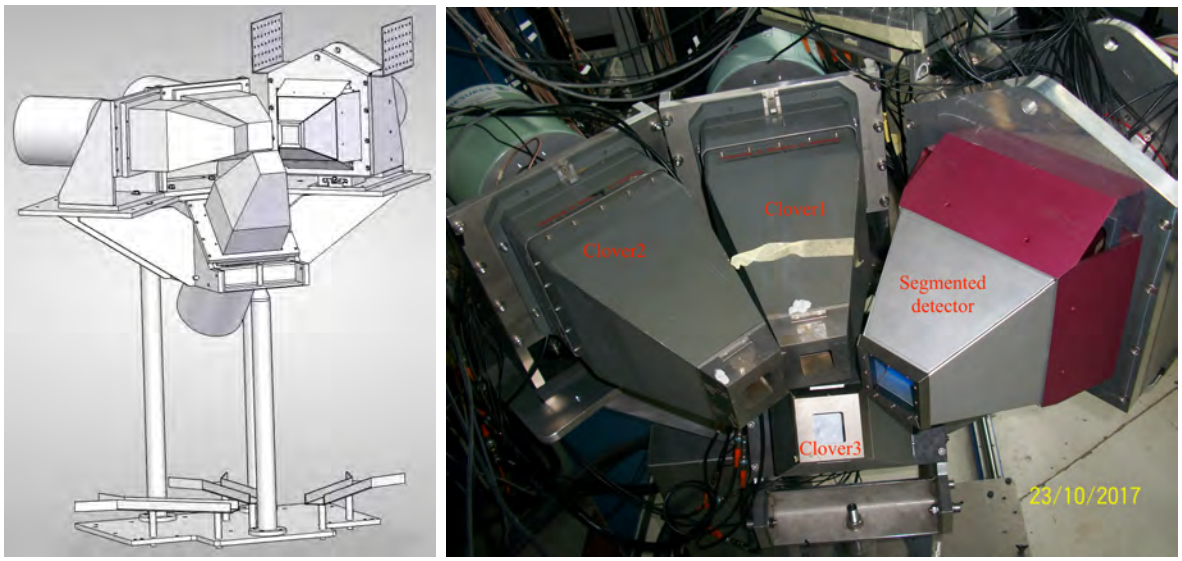

(a) (b)

Figure 6.2. Detector Array developed for the tape station where (a) shows the schematic design of the array used in this experiment and it comprises of three clover detector and one segmented detectors and (b) the photograph showing the detector array.

6.3.2 Semiconductor detectors

Solid semiconductor radiation detectors are widely used in research, especially in physics experiments where accurate measurement of energy is indispensable. A γ-ray detector usually consists of a crystal of either silicon (Si) or germanium (Ge) material. The transfer of radiation energy to the crystal material creates many electron-hole (e-h) pairs. Both electrons and holes are mobile in the conduction band and they can only move in a determined speed when an electric field is applied. When electrons and holes move within the semiconductor material they

can either arrive at their respective electrodes where the end-result will be a pulse of charge proportional to the energy deposited in the crystal, or they can be trapped in impurities in the crystal lattice. The average energy required to create an e-h pairs in the semiconductor is about 3.6 eV for Si and 3 eV for Ge. Hence, many more e-h pair are created per MeV in Ge. However, the signal is still small and further post-amplification is imperative [7, 10, 108].

	Silicon	Germanium
Atomic number Z	14	32
Mass number A	28.09	75.59
Density ($g.cm^{-3}$)	2.33	5.33
Energy gap (eV)	1.17	0.75
Electron mobility ($cm^2V^{-1}s^{-1}$)		
300K	1350	3900
77K	21000	36000
Hole mobility ($cm^2V^{-1}s^{-1}$)		
300K	480	1900
77K	1100	42000
Energy /e-h pair (eV)	3.62 (at 300K)	2.96 (at 77K)

Table 6.1. Physical properties of Silicon and Germanium material [10].

Both Ge and Si form solid crystals in which the valance electrons form a covalent bond with neighbouring atoms. Compared to the energy of the band gap of an insulator (5 eV) the energy of the bandgap of a semiconductor is only 1 eV. Because of the small energy gap of semiconductors, thermal excitation of electrons across the bandgap into the conduction band is possible at room temperature. To control electrical conductivity, a small amount of material (impurities) called dopants are added. In this process of doping, atoms with 3 or 5 valence electrons are introduced to the lattice structure. Conductivity can be provided by either n-type (electron) or p-type (holes). For n-type doping means that replacing the Ge or Si atoms with an atom that has 5 valence electrons and leave one valence electron without a partner. Since the added impurities donate one valence electron to the lattice, it is referred to as donor. For p-type doping means introducing an atom (group 3) with 3 valence electron to the lattice structure. This atom will provide a covalent bond for all Ge or Si electrons and leave one valence electron without a partner. This type is referred to as an acceptor [108].

The electron-hole pair is created when the radiation enters the depletion region (net zero charge region). The applied high voltage creates an electric field across the depletion region. Any γ-rays that enter the detector interact with the material of the detector through three processes: the photoelectric effect, Compton scattering, and pair production [7, 12]. The interaction produces electron-hole pairs in this region. These detectors are operated with a high reverse bias voltage (1000-3000V). This has two effects on the detector: firstly, increasing the electric field in the depletion region makes charge collection more efficient. Secondly, increasing the dimension of the depletion region, thereby increasing the sensitive volume of the detector by

forcing more carriers to drift from one type of material to the other.

The most common manufacturing procedure for Ge and Si detectors begins when a sample of p-type material is diffused into the surface concentration of donor states atoms, usually Li, thereby creating a thin a n-type region. When the reverse bias voltage is applied and at a slightly elevated temperature the donor states atoms (Li) drift into a p-type region, therefore creating a large depletion region. These detectors are usually known as lithium drifted Ge or Si detectors Ge(Li) or Si(Li). To prevent Li from drifting, the Ge(Li) or Si(Li) detector must be kept cold at all the times when the bias voltage is applied, otherwise the Li will drift out of the lattice structure in the depletion region and destroy the detector. Keeping the detector cold also reduces the thermal excitation of electrons across the energy gap, thereby reducing electronic noise. Large-volume high purity germanium (HPGe) detectors have become available, owing to advances in the technique of refining the Ge crystal. These detectors do not need to be kept at 77K but must be operated at 77K to keep the noise level at a minimum.

6.3.2.1 High-Purity Germanium-Clover detector

Gamma-ray spectroscopy uses high-resolution germanium detectors often surrounded by Compton suppression shields to improve the peak-to-total ratio. A picture of a clover detector is shown in figure 6.3. A clover detector consists of four separate HPGe crystals which are arranged about 0.2 mm apart. The crystals inside the cryostat have the dimension: 70 mm in length, 50 mm in diameter, 36 tapering length, and 41 mm front width. They are packed as shown in figure 6.4. Each crystal has its own electronics to ensure that it is used as an independent detector. To maximize the performance of the detector and to reduce the leakage current, each detector is filled with liquid nitrogen (LN_2). The detector was collected to an automated filling system which fills the Dewar of the detector at a determined interval.

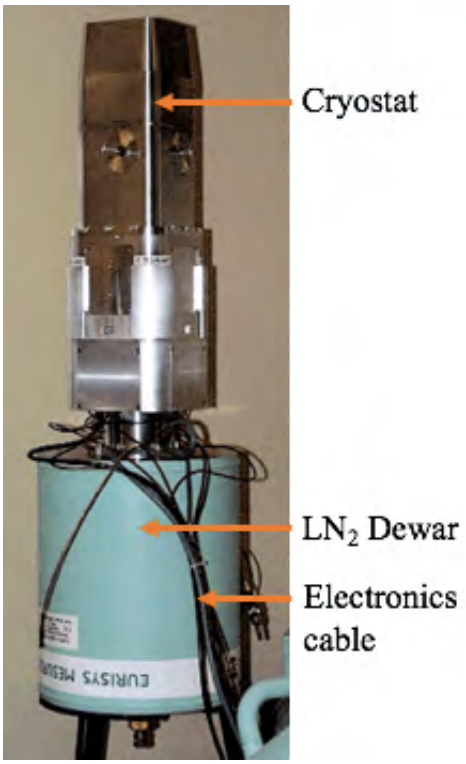

Figure 6.3. The picture of a clover detector without Compton suppression shield,usually called naked clover, showing the tapered cryostat, cylindrical Dewar for LN_2 and electronics cable.

An advantage of using this type of detector is the enhancement of the peak-to-total ratio by applying the add-back method. When a γ-ray Compton scatters from one crystal to another crystal, the energy deposited in the first crystal can be added to the energy deposited on the second crystal to sum-up and recover the total energy of the γ-ray.

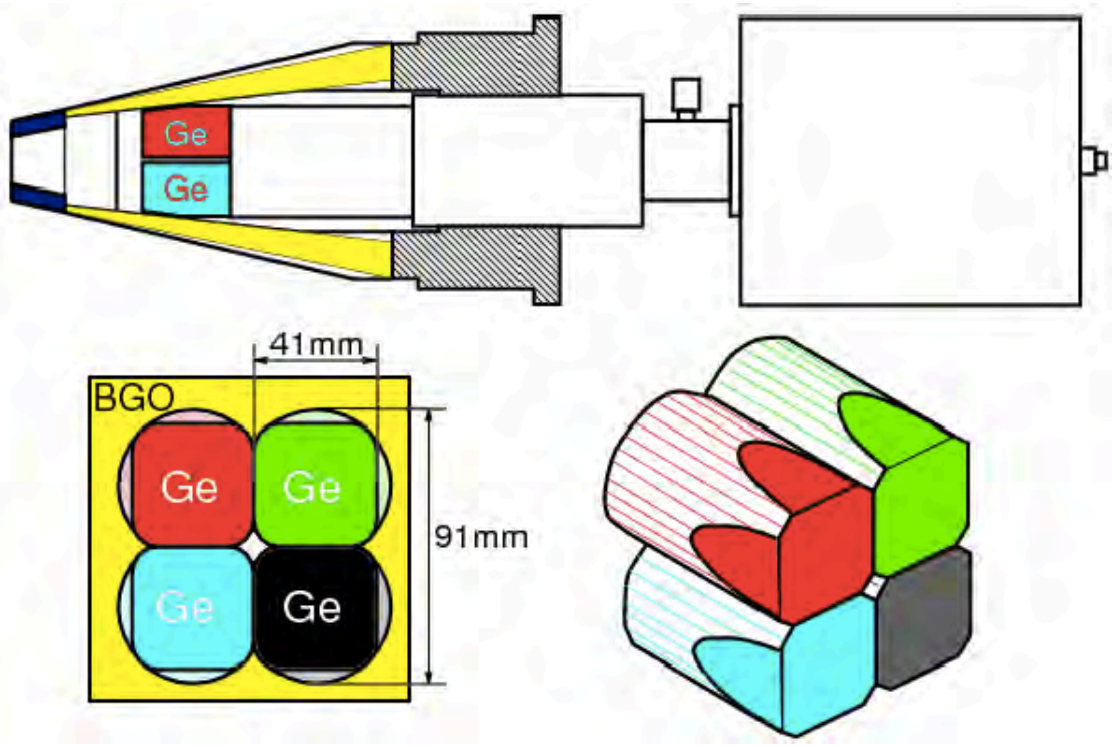

Figure 6.4. A schematic representation of the Ge-clover detector covered with Compton suppression shield. The crystals are shown in different colors with their dimensions.

Here are the specification of the clover detector:

♢ Distance from the crystal surface to the target center: D_{tc} = 196 mm

♢ Distance from the detector end-cap to the crystal surface: D_{ec} = 20 mm

♢ Total opening angle:$\Theta = 23.2^{o}$

♢ Solid angle per detector: Ge = 1.34% of the 4π (for a 0.2 mm distance between crystals)

♢ Photo-peak efficiency for 1.33 MeV: $\epsilon_{ph}\Omega_{\mathrm{Ge}}$= 17.8 $\times 10^{4}$

♢ Add-back factor for 1.33 MeV: 1.56

♢ Peak-to-total ratio for 1.33 MeV: $(\mathrm{P/T})_{\mathrm{Ge}} = 0.30$

6.3.2.2 Compton Suppression Shield

The main goal of the Compton suppression shield is to reduce the background caused by scattered γ-rays. If a γ-ray is Compton scattered out of the detector it does not deposit all of its energy in the detector. That which remains forms a background on the lower energy side of the photo-peak. A typical naked clover (figure 6.3) will give a spectrum where the photo-peak comprises only of 20% of the counts in the spectrum, while the remaining 80% is a continuous

background of low energy. For this reason, a clover detector is surrounded by another detector, called a suppression shield. The suppression shield is made of Bismuth Germanate: ($Bi_4Ge_3O_{12}$) which is abbreviated as BGO. BGO is a scintillator detector with good time response and because of Bi has a high Z, it has a high γ-ray detection efficiency. If a γ- ray is detected by both detectors within a specified time window, the γ-ray is treated as a scattered event and it is discarded. The front of the BGO is covered with a heavy collimator (material with high Z, e.g. Tungsten) to prevent γ-rays from directly interacting the BGO material.

To check whether the Compton suppression is working, a γ-ray source is used to compare the number of counts in a photo-peak versus the total counts in the whole spectrum, known as the peak-to-total(P/T) ratio. A Compton suppressed clover detector at iThemba LABS has a typical P/T ratio of about 50%.

6.3.2.3 Silicon Lithium drifted detector

The Silicon Lithium Si(Li) drifted detector used in this experiment was 5 mm thick with an active area of 300 mm^2. The detector is thick enough to stop electrons with a kinetic energy up to 2.1 MeV. The front face of the detector is coated with a very thin gold layer of roughly 20 to 40 $\mu g/cm^2$ thickness. The cross-sectional view of the detector is shown in figure 6.5(a) and it illustrates all the connections of the detector. The Si(Li) used in this work is shown in figure 6.5(b). This detector was manufactured by Mirion industries [109].

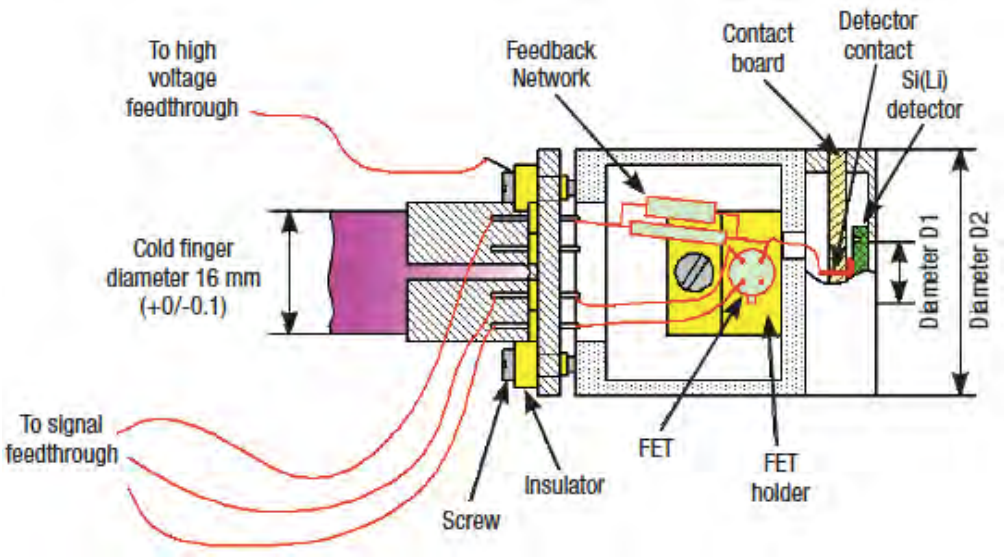

(a)

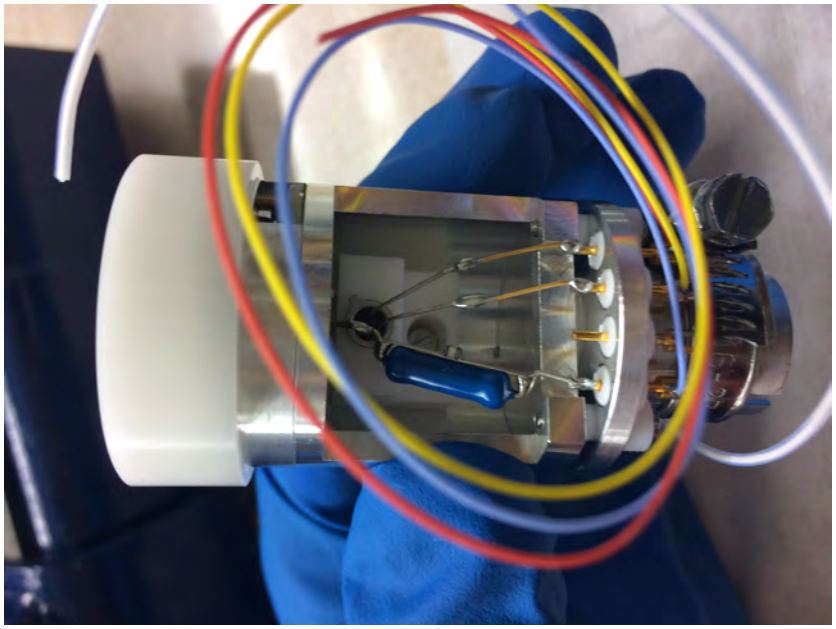

(b)

Figure 6.5. Si(Li) detector showing cable connections, where (a) shows the cross-sectional view of the detector [110] and (b) shows the photograph of the Si(Li) detector. The active end of the detector (left) is protected by a plastic cap.

The Si(Li) detector is operated at liquid nitrogen temperatures (77K) and this has a couple of benefits, firstly, to improve energy resolution and secondly, to prevent the drifting of Li atoms. The FET pre-amplifier is located in the cold section of the detector while the remaining charge sensitive pre-amplifier is located outside of the vacuum chamber at atmospheric pressure. The pre-amplifier is model PSC 761-R and figure 6.6(a) shows how it is mounted on the chamber. Figure 6.6(b) illustrates the connection of the Si(Li) detector to the cold finger. The cold finger is a copper rod connected to the LN_2 Dewar.

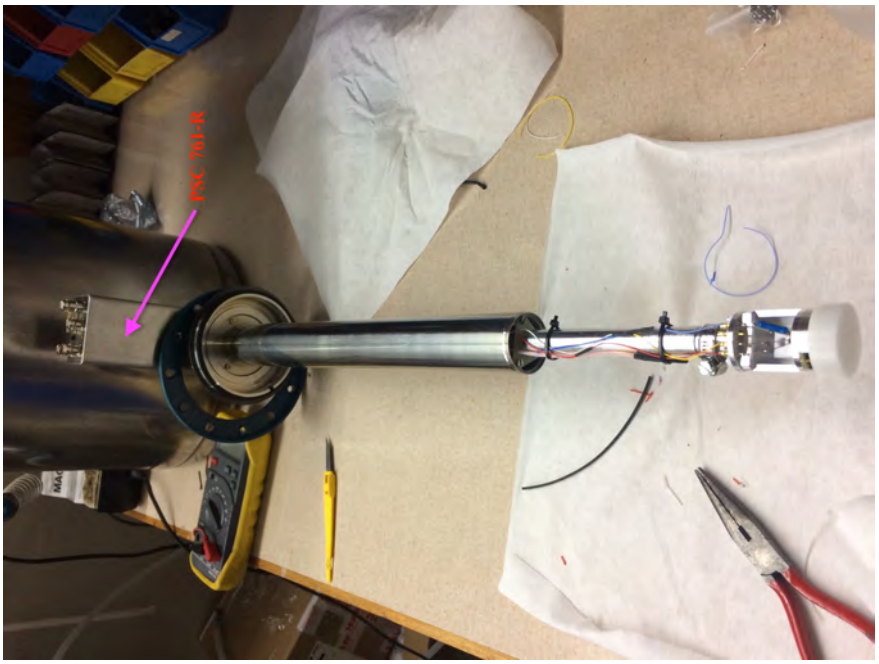

(a)

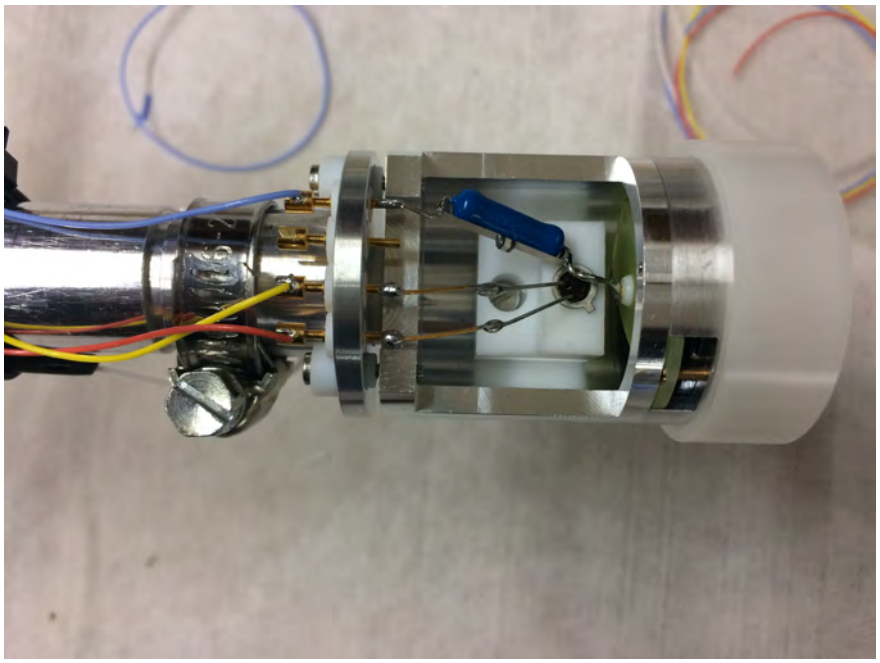

(b)

Figure 6.6. Details of the Si(Li) detector mounted on the cold-finger, where (a) shows the Si(Li) detector mounted at tip of the cold finger and (b) show the photograph of the Si(Li) detector mounted on the cold finger. The white cap protects the surface of the Si(Li) detector against any kind of vapour condensation when it is not in use.

The cryostat used in this work was donated to iThemba LABS by Herbet Hübel from the University of Bonn. The cryostat was refurbished and used to cool the Si(Li) detector. The cryostat as manufactured by EURISYS and it has the correct dimensions to house the Si(Li) detector and the PSC-761-R pre-amplifier. To avoid any residual gas from sticking on the surface of the detector, the detector is only cooled when the vacuum pressure has reached

at-least 4×10^{-6} mbar or better. The Si(Li) detector is kept in a separate vacuum chamber from the tape station. This allows opening the side of the tape station while keeping the Si(Li) detector cold. The cold finger and the bellows allow the Si(Li) detector to be retracted into its vacuum chamber behind the valve that can be closed (as shown in figure 6.7).

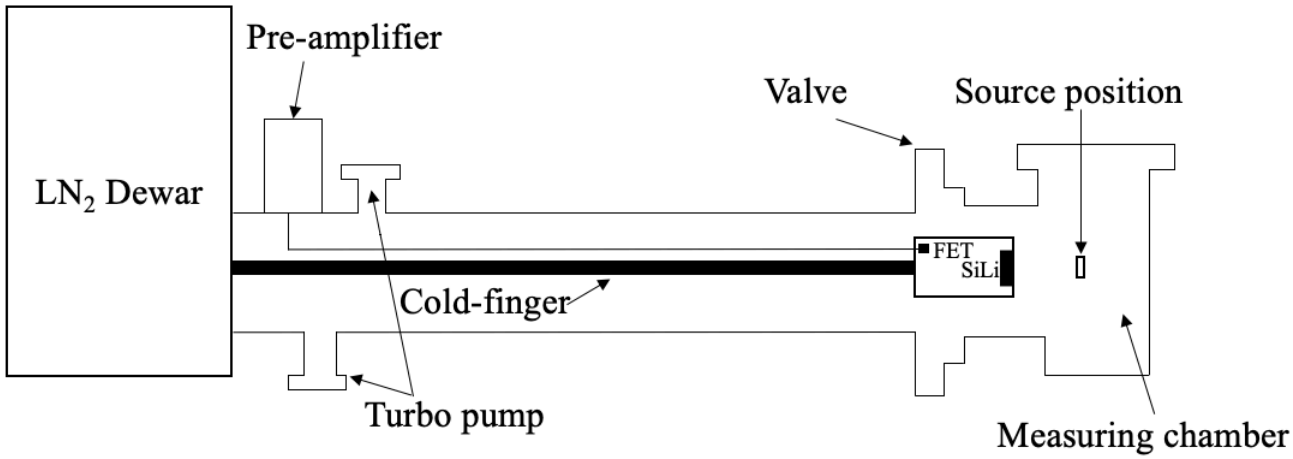

(a)

(b)

Figure 6.7. The complete assembly of the Si(Li) detector connected to the measuring chamber, where (a) is a schematic diagram showing the Si(Li) detector connected to the cold finger and a cyostat and (b) is a photo of the cryostat coupled to the measuring chamber.

6.3.3 Plastic scintillator

A plastic scintillator was used to detect β-particles following the β-decay of the implanted sample. The plastic scintillator used in this experiment was BC 404 [111, 112] 40×45 mm^2 and 5 mm thick. The plastic scintillator was coupled to a light guide as shown in figure 6.8(a) and 6.8(b). A 15 cm long Lucite light guide transferred light to the Photo-Multiplier Tube (PMT) located outside of the vacuum chamber. The plastic scintillator is wrapped with a thin aluminized Mylar that acts as a diffuse reflecting surface while the light guide was wrapped with aluminum foil to prevent light from escaping [88]. The construction of the whole plastic scintillator detector is shown in figure 6.8.

The PMT tube used in this work is a H6533 [113] manufactured by Hamamatsu. The PMT is 1200 mm long with a diameter of 31 mm and the active area has a dimension of 26 mm. The PMT has two cables, one cable for the output signal and the other for high voltage. The PMT can be biased up to voltage of -2500 V with a leakage current of 0.250 A.

(a) (b)

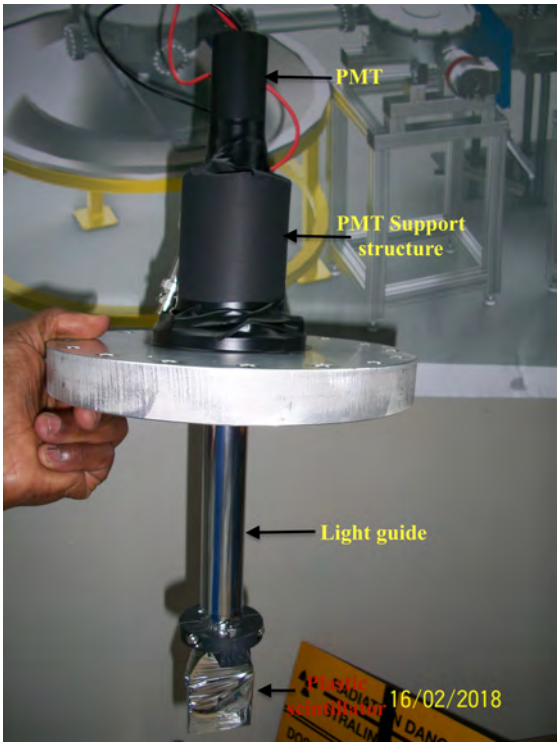

(c)

Figure 6.8. Construction of the plastic scintillator detector. where (a) show the plastic Scintillator couple to the light guide, (b) the plastic scintillator couple to the light guide which join the photomultiplier tube located outside the vacuum chamber. Both plastic scintillator and light guide are wrapped with aluminised Mylar to prevent light from escaping and (c) the complete construction of the plastic scintillator. The light guide is glued to photomultiplier tube which is located outside vacuum.

The activity implanted on the tape (or target transporter, see section of 6.8), is transported to the measuring chamber where the implanted spot stops in front of the Si(Li) and plastic scintillator detector. The position of the plastic scintillator inside the measuring chamber is

shown in figure 6.9, in between the tape (purple). It is shown in green while the light guide shown in transparent gray. The plastic scintillator detector, Si(Li) detector, and the tape are all in the same horizontal plane.

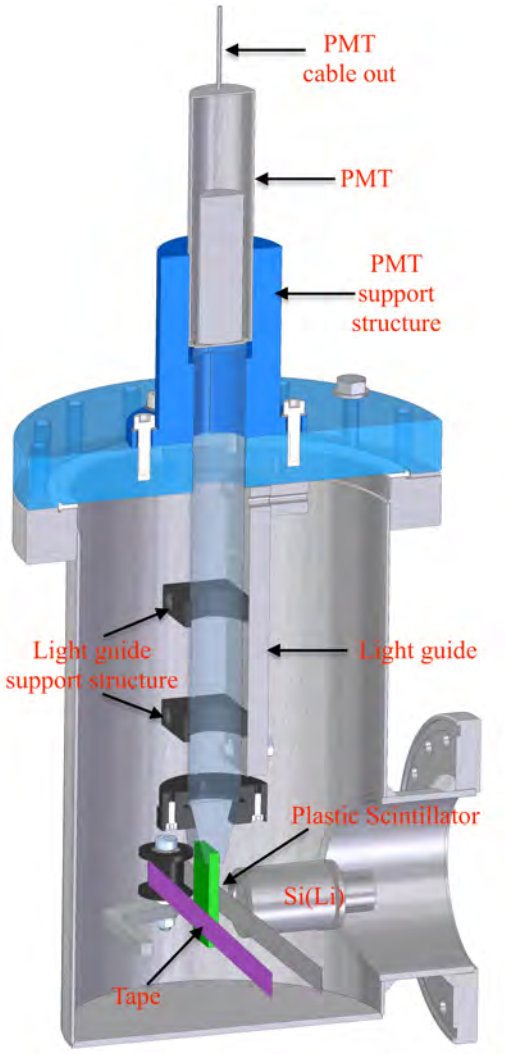

Figure 6.9. A cross-sectional view of the measuring chamber displaying the plastic scintillator detector mounted on the lid that covers the measuring chamber, the Si(Li) detector and the tape. The plastic scintillator tape is shown in green, the tape in purple color and the Si(Li) in metallic grey.

6.4 Data Analysis

6.4.1 Data acquisition

The data acquisition system used to collect data is the Total Data Readout (TDR) system. This acquisition system is being used for nuclear physics experiments at iThemba LABS, especially in the AFRODITE array spectrometer. This system uses the XIA Pixie-16 modules [114]. The signals from individual crystals of the detectors are directly connected to Pixie-16 modules,

described in 6.4.1.1.

The tape movement signal from Beckhoff module (EL2002) is converted from a digital signal to analogue signal that mimics a Ge detector signal before being fed into a Pixie-16 module. When the tape moves, it sends the movement signal to the acquisition system to mark when the new sample arrives. A schematic representation of the data acquisition used in the experiment is shown in figure 6.10.

The Beckhoff module produces a +24V logic signal. This logic signal is converted to TTL logic and then into a NIM logic signal in the TTL to NIM level adapter, before being passed to the quad discriminator. This signal is used to trigger the pulser.

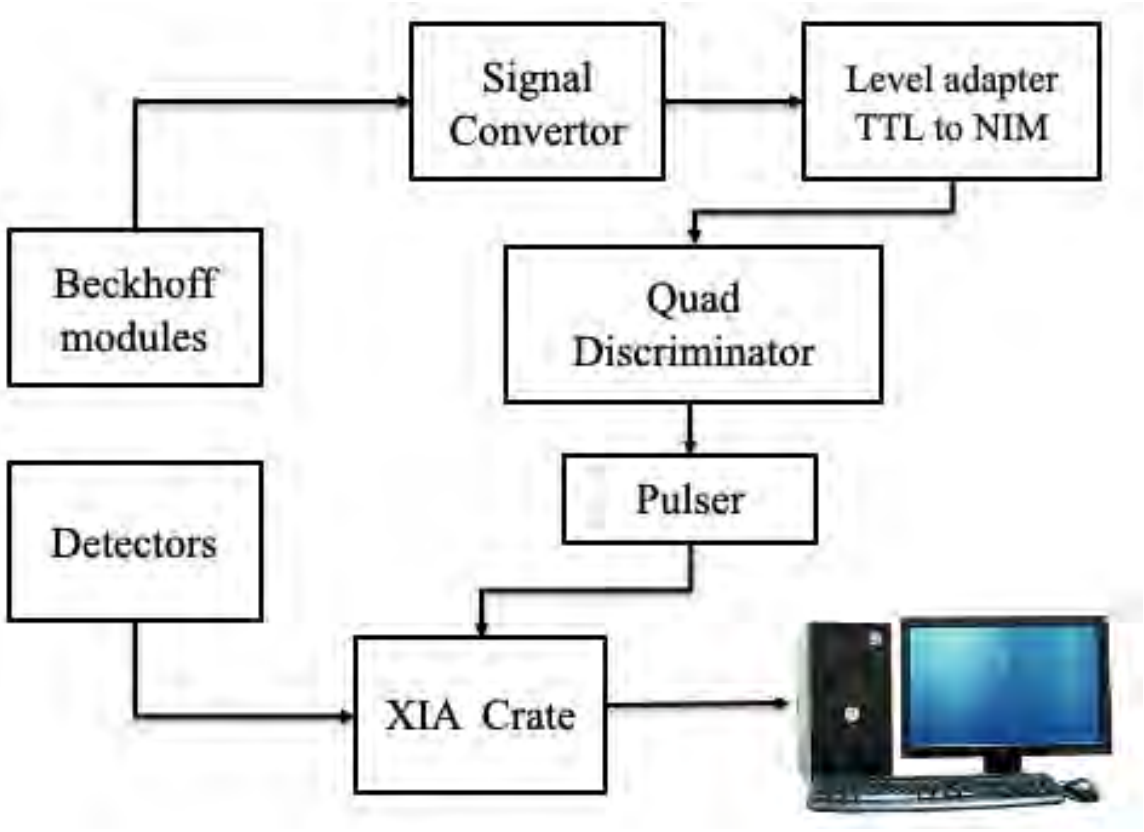

Figure 6.10. A schematic diagram of the data acquisition system. The signal from the Beckhoff module was converted to an analogue signal for the DAQ.

6.4.1.1 PIXIE-16 Theory of Operation

Pixie-16 card is a 16 channel unit designed for γ-ray spectroscopy and waveform capturing that is capable of measuring both the amplitude and shape of pulses in nuclear spectroscopy applications. It incorporates five functional building blocks, namely: analog signal conditioning, real-time processing unit, digital signal processing, PCI interface and trigger interface. More details about these functions is given in [114, 115].

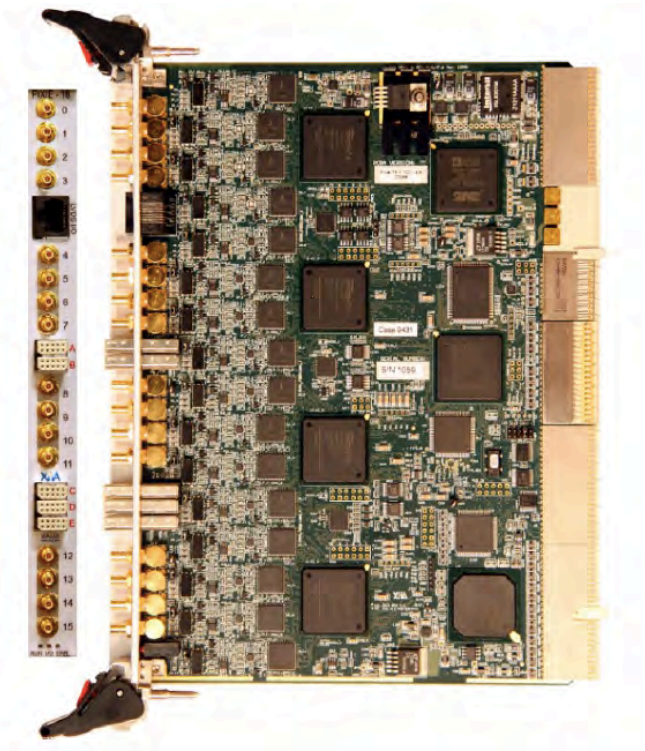

Figure 6.11. Front and side view of the Pixie-16 module [115].

The user can adjust certain parameters, see figure 6.16, through the user interface. The Pixie-16 accepts signals from radiation detectors. The incoming signals are digitized by the 12-bit 100 MSPS ADCs. Waveforms of up to 100 μs in length for each event can be stored in a FIFO. These waveforms are available for onboard pulse shape analysis. Waveforms, timestamps, and the results of the pulse shape analysis can be read out by the system for further off-line processing [114].

The HPGe detector are operated with charge sensitive preamplifier as shown in figure 6.12(a). The Detector (D) is biased with Voltage (V) connected to the input of the preamplifier (A) which has feedback capacitor (C_f) and feedback resistor (R_f).

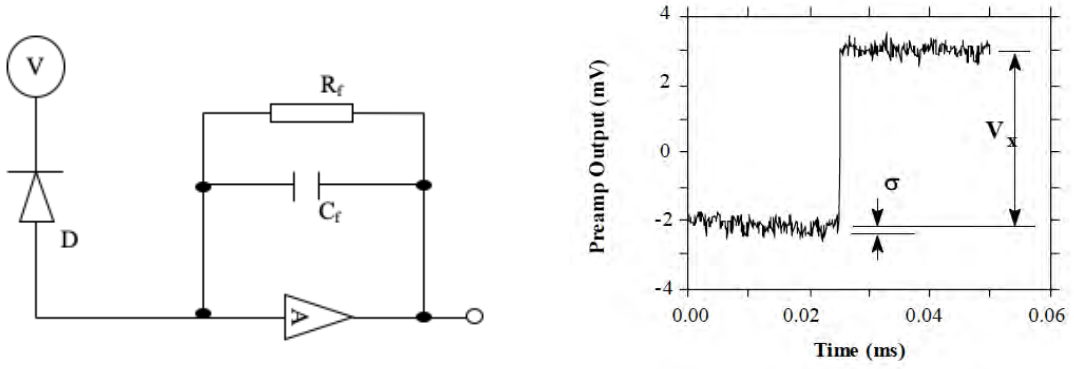

(a) (b)

Figure 6.12. Figure (a) show the charge sensitive preamplifier with RC feedback and (b) the output on absorption of an γ-ray. Figure taken from [114].

When a γ-ray of energy E_x is absorbed in the detector (D), the output of the preamplifier is shown in figure 6.12(b) as the step of the amplitude V_x. The absorbed γ-ray releases an electric charge given by:

$$Q_x = \frac{E_x}{\epsilon} \tag{6.1}$$

where ϵ is the material constant. When Q_x is integrated onto C_f it gives:

$$V_x = \frac{Q_x}{C_f} = \frac{E_x}{\epsilon C_f} \tag{6.2}$$

Equation 6.2 means that measuring the E_x of the γ-ray requires the measurement of the voltage step V_x in the present of amplifier noise σ as shown in figure 6.12(b).

The recorded data is filtered and the signal is digitized so it is no longer continuous, but it is a string of discrete values as shown in figure 6.13. To determine V_x in any data set, an average over the points before each step is taken and then it is subtracted from the value of the average over the points after the step. As shown in figure 6.13 averages are computed over Length (L) and Gap (G) region. The differences in this value is the measurement of V_x and it can be calculated as:

$$V_{x,k} = -\sum_{i(before)} W_i V_i + \sum_{i(after)} W_i V_i \tag{6.3}$$

where W_i and V_i are weighs and V_i are sample voltages which determine the computed average.

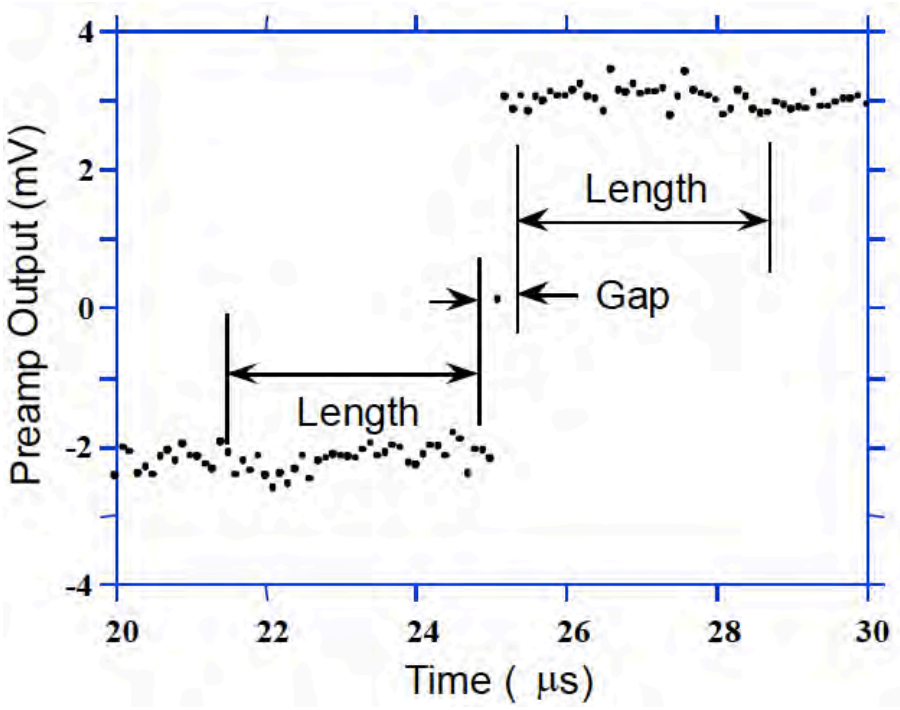

Figure 6.13. Data Digitalization on Pixie-16 [115].

Different filters are used for weighting values. When larger weighting values are used for the region close to the step and smaller values are used for the data away from the step, and equation 6.3 produces cusp-like filters. When weighing values are constant, it produces triangular or trapezoidal filters.

The Pixie-16 is optimized for high speed operation. It implements a fixed length filter with all W_i values equal to unity and therefore computes the sum for each new signal value of k. The equation for this process is given as:

$$LV_{x,k} = \sum_{i=kL-G+1}^{k-L-G} V_i + \sum_{i=k-L+1}^{k} V_i \tag{6.4}$$

The factor L multiplying $V_{x,k}$ arises because the sum of the weights is not normalized.

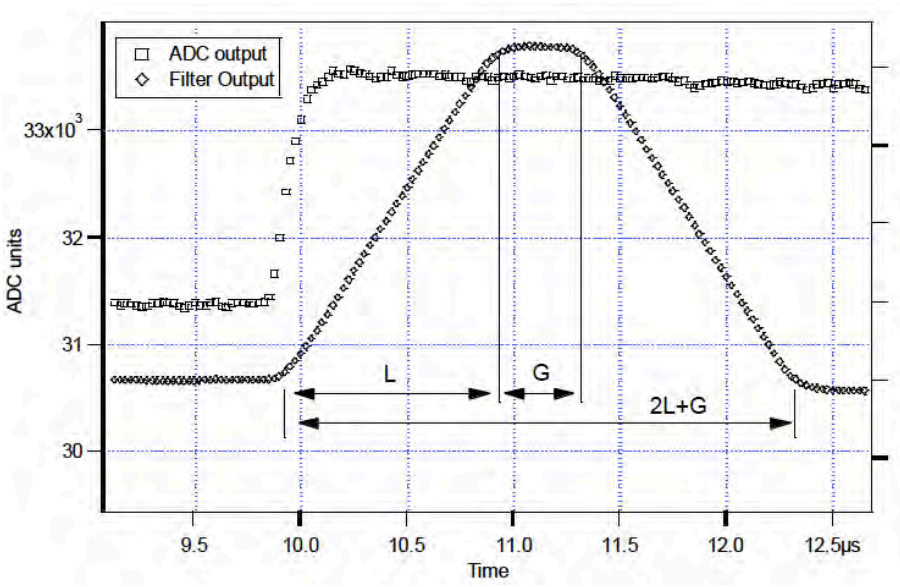

Figure 6.14. Trapezoidal filtering of a preamplifier step [115].

A trapezoidal filter is implemented in Pixie-16 modules according to equation 6.4 and it shown in figure 6.14. The result of this filter with L=1μs and G=0.4 μs to a γ-ray event is shown in 6.14. The filter output is trapezoidal in shape and has a rise time equal to L, a flat-top equal to G, and a symmetrical fall time equal to L. The base width, which is a first-order measure of the filters noise reduction properties, is $2L$+G [115].

Shown in figure 6.15 is the event over a longer time interval and how the filter is used to treat the preamplifier noise in the presence of γ-ray pulse. The effect of a filter reduces the amplitude of the fluctuation and reduces its high-frequency content. This region establishes the level from which γ-ray peak with amplitude V_x is to be measured and it is referred to as the baseline. The fluctuations in the baseline are called the electric noise and it has a standard deviation σ_e and it depends on the rise time of the filter used.

The γ-ray peak contribute an additional noise which arises from statistical fluctuations in the amount of charge Q_x produced when the γ-ray is absorbed in the detector. The total noise σ_t when measuring V_x is given by:

$$\sigma_t = \sqrt{\sigma_e^2 + \sigma_f^2} \tag{6.5}$$

where σ_f is a property of the detector material.

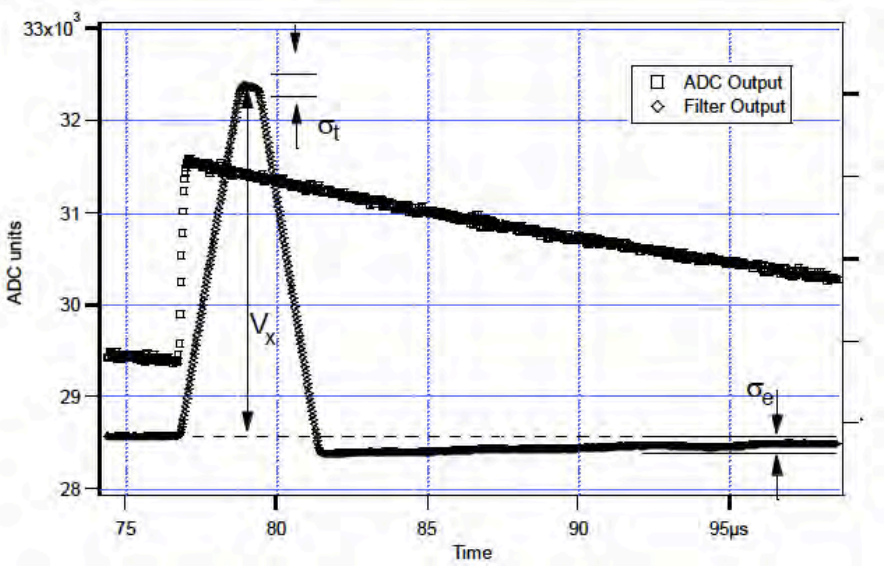

Figure 6.15. The baseline noise and the effect of the preamplifier decay time in a γ-ray event [115].

When the RC-type preamplifier is used, figure 6.12(a), the slope of the preamplifier is rarely zero because every step decays exponentially back to the DC level of the preamplifier, this is indicated in figure 6.15. The baselines can be mapped back to the DC level by using the decay constant τ. As a result, the γ-ray energy can be precisely determined even if the pulse sits on the falling slope of a previous pulse. The value of τ is the characteristic of the preamplifier, hence the detector. The τ is determined by the user, host software and downloaded to the module in a window similar to figure 6.16.

6.4.1.2 Digital Data Acquisition Systems (DDAS) setup

There are two distinct processes for digital data acquisition. Firstly, it has a front-end system consisting of XIA crate and Pixie-16 modules connected to a server PC. The server PC hosts and runs the acquisition for data collection. Secondly, it has a control part on the server PC running the merge, filter, event-building, on-line sorting, storage, and GUI. Data are read from the merger, and output to Tape Server. The Tape Server receives and stores data locally, either on a disc, USB, network, Tape, etc [81, 116]. The stored data can be sorted with MTsort [117], with the following input handlers; EUROGAMONLINETS for on-line sorting and EUROGAMDISC for off-line sorting [116, 118].

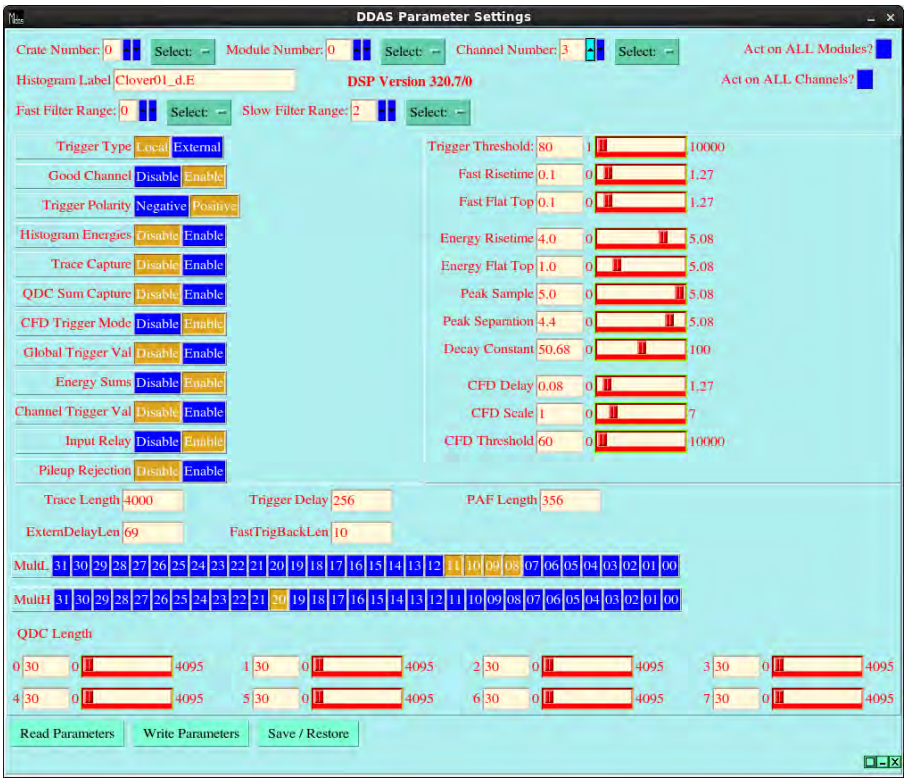

Figure 6.16. A DDAS window showing different parameters used to optimize the system for better energy resolution for individual detector.

Figure 6.16 shows the parameters of the DDAS system ..... those discussed in the previous section, used to optimized individual crystal of the clover detector, plastic scintillator, and Si(Li) detector. More information can be obtained from the XIA user manual [114]. Since a clover detector has four crystals which can be treated as individual detectors, parameters for each crystal can be optimized for better energy resolution using a window similar to 6.16. The collected data was stored on a hard disk and sorted later with MTSort. MIDAS software is a user-oriented digital interface system for data acquisition and experiment control [116]. This acquisition system was used to collect data during experiments.

6.4.2 Energy Calibration

6.4.2.1 Clover Detector

Energy calibration was performed with the following sources: ^{152}Eu, ^{133}Ba and ^{56}Co. Cobalt-56 was used for high energy γ-rays, while ^{133}Ba was used to get a good turn-over point on the efficiency curve and for low energy γ-rays. The sources were individually placed at the center of the array at the same position as the transported activity. Data were collected in hourly intervals and saved on a hard-disk for further analyses.

The RadWare [119] software package was used to fit the spectra and to determine the centroid

of each photo-peak for all three radioactive sources. RadWare has built-in commands for energy calibration which are "ca", "ca3" and "ca4". By using either one of these commands on the individual spectrum, it can automatically fit the entire spectrum and calculate the energy calibration coefficients. However, the "ca" command requires the source file (.sou) which contains standard γ-ray energies and intensities of all the individual radioactive sources. RadWare performs calibrations using linear or quadratic fits in the form of the following equation.

$$E = a_0 + a_1 x + a_2 x^2 \tag{6.6}$$

where x is the channel number, and (a_0, a_1, a_2) are the energy calibration coefficients. These coefficients are needed for each individual crystal of all the clover detectors. The coefficients were then used in the sorting code to gain match the collected data during the experiments and off-line. Using the gain matching coefficients, the following spectrum 6.17 was obtained with a ^{133}Ba radioactive source.

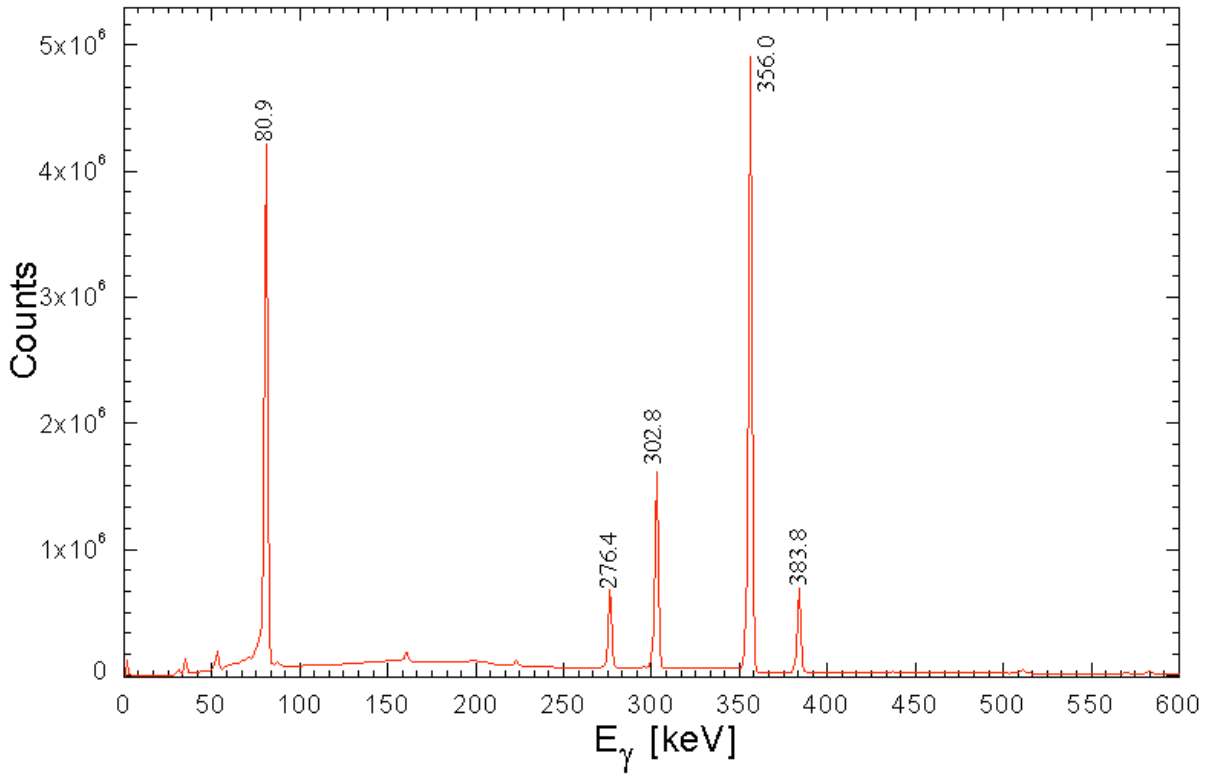

Figure 6.17. The gain matched calibrated spectrum obtained with ^{133}Ba radioactive source.

The following spectrum 6.18 was obtained with a ^{152}Eu radioactive source.

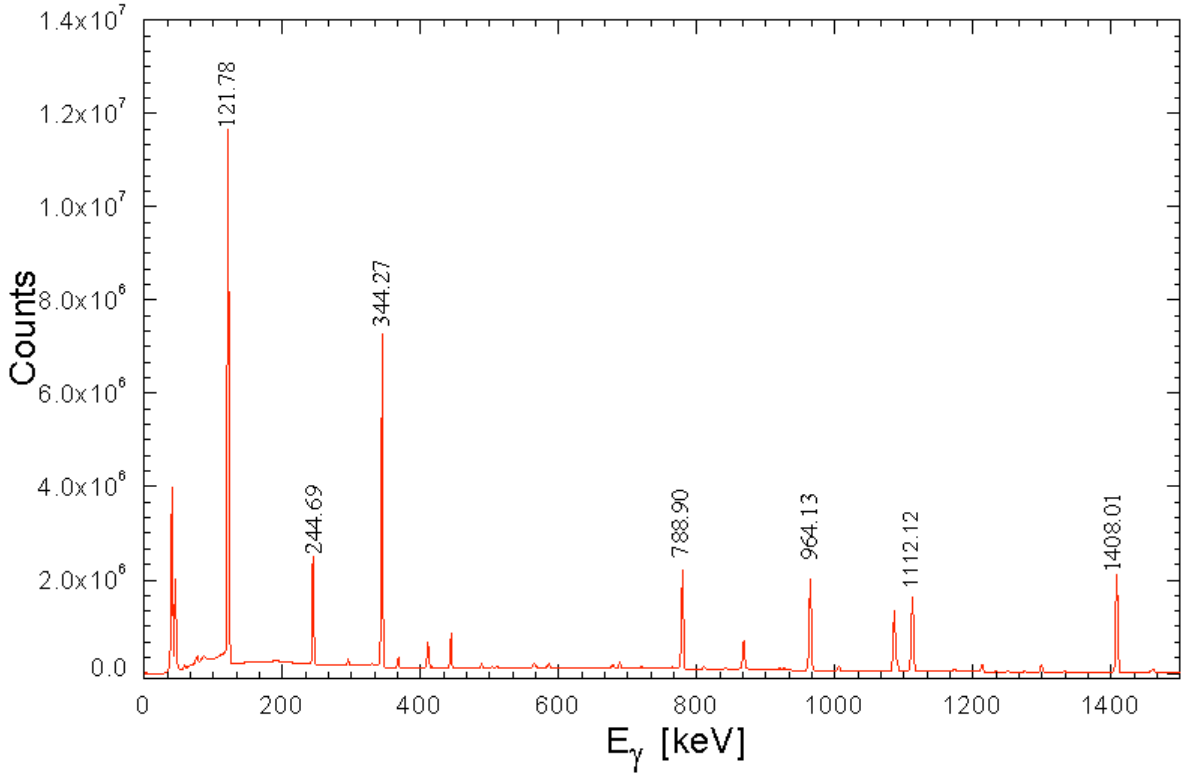

Figure 6.18. The gain matched calibrated spectrum obtained with ^{152}Eu radioactive source.

The following spectrum was obtained from ^{56}Co radioactive source. This source was produced at the iThemba LABS radioisotope department and it consists of ^{57}Co and ^{58}Co impurities or contaminants. However, it was still considered fine for energy and efficiency calibration.

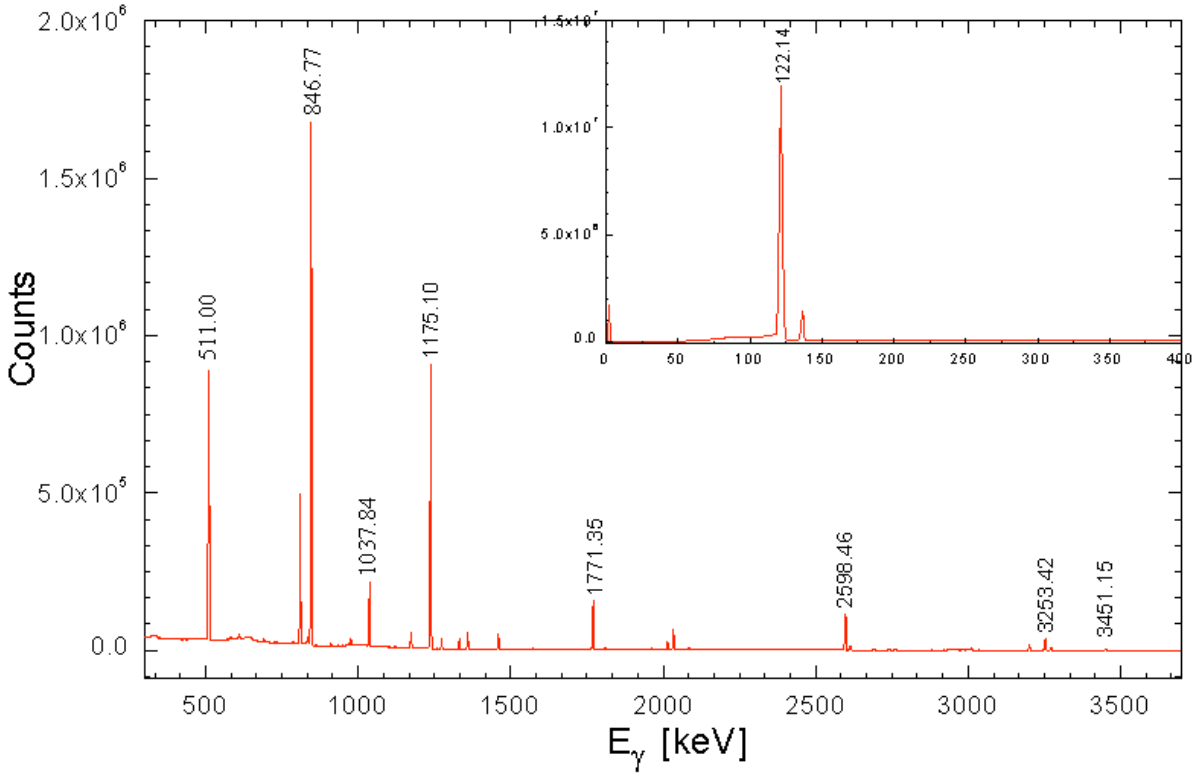

Figure 6.19. The typical calibrated spectrum obtained with ^{56}Co radioactive source.

6.4.2.2 Si(Li) detector

The Si(Li) detector was calibrated by using a ^{207}Bi electron source mounted on the tape and facing the Si(Li) detector in the same position as the transported activity. Figure 6.20 shows ^{207}Bi calibration spectrum obtained with the Si(Li) detector. The tail on the low energy side of each photo-peak is due to some fraction of electron energy lost in the source and it means that they do not deposit all their total kinetic energy [30].

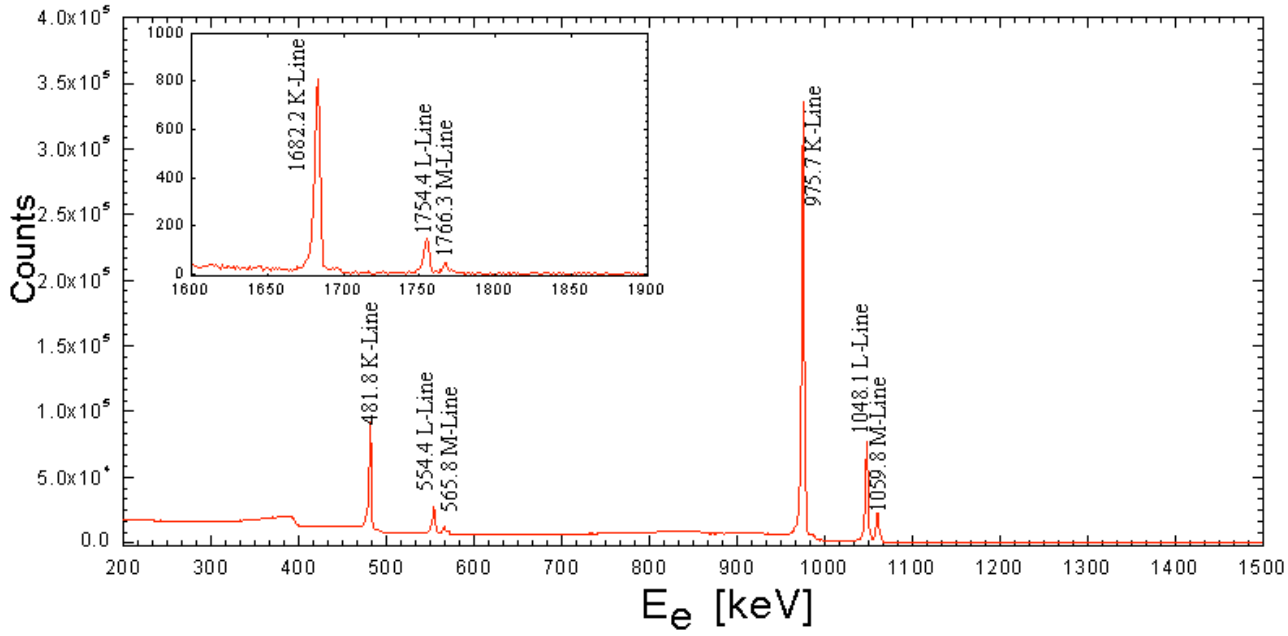

Figure 6.20. The typical conversion electron spectrum obtained using a ^{207}Bi radioactive source.

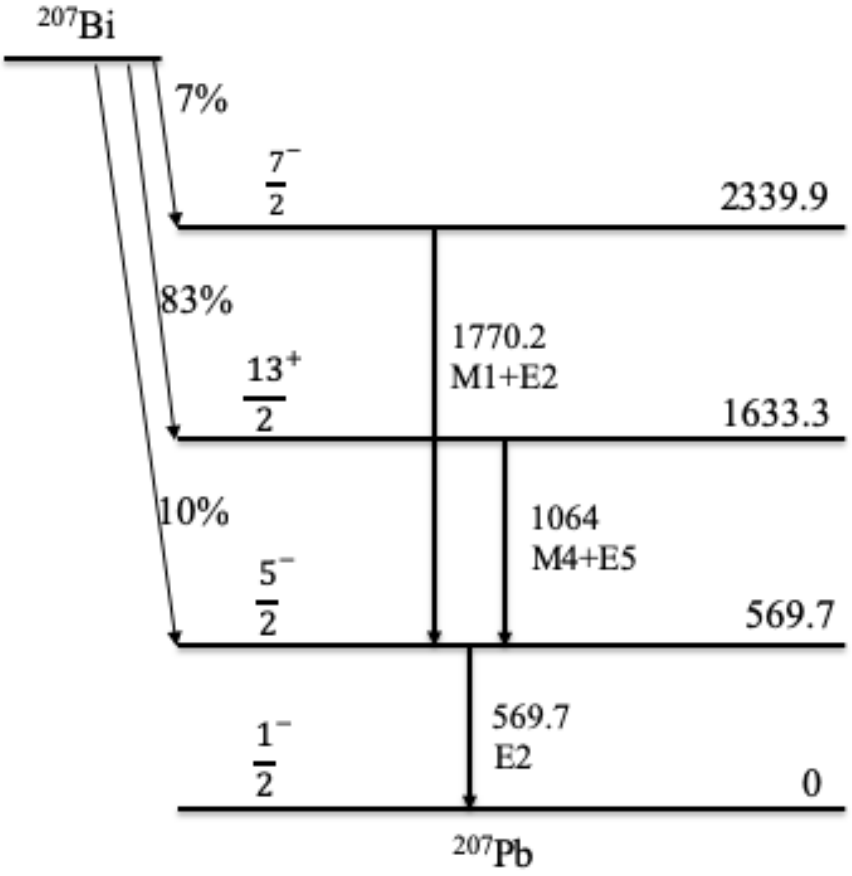

Figure 6.21. The ^{207}Pb level scheme as a result of ^{207}Bi electron capture [13].

E_γ [keV]	I_γ [%]	E_e [keV]	Shell	I_e [%]
		481.7	K	1.515
569.7	97.76	554.4	L	0.438
		565.8	M	0.147
		975.7	K	7.03
1063.7	74.6	1048.1	L	1.843
		1059.8	M	0.545
		1682.2	K	0.024
1770.2	6.87	1754.4	L	0.0034
		1766.3	M	0.0009

Table 6.2. This table shows ^{207}Bi electron line intensities and their coincidence γ-ray [30].

All electron lines from the three transitions were resolved. Figure 6.20 shows the K, L, and M conversion electrons from the three strong transitions of ^{207}Bi i.e 569.7 keV, 1063.7 keV and 1770.2 keV.

6.4.3 Efficiency Calibration

6.4.3.1 Clover Detector

The Efficiency calibration measurement for the A-line mini-array (section 6.3.1) was performed at the end of the experiment by using ^{133}Ba, ^{152}Eu and ^{57}Co radioactive sources which were mounted at the same position as the transported activity. The data were recorded and sorted off-line by using the MTSort program [117].

The efficiency curve was obtained by using the RadWare EFFIT program [119]. This program requires input (.sin) and source (.sou) files which define energies and intensities of the selected photo-peak energies. The EFFIT program uses different parametrizations to define efficiency for low and high energies. For low energies, the efficiency is given by:

$$log(eff) = A + B \times log\left(\frac{E_\gamma}{E_1}\right) + C \times log\left(\frac{E_\gamma}{E_1}\right)^2 \tag{6.7}$$

while for high energy the efficiency is given by:

$$log(eff) = D + E \times log\left(\frac{E_\gamma}{E_2}\right) + F \times log\left(\frac{E_\gamma}{E_2}\right)^2 \tag{6.8}$$

where E_γ is the γ-ray energy and E_1 and E_2 are constant with values of 100 keV and 1 MeV, respectively. A, B, C are parameters defining the efficiency at low energies while D, E, F are parameters defining the efficiency at high energies. The complete function for efficiency is given by:

$$eff = exp((A + Bx + Cx^2)^{-G} + (D + Ey + Fy^2)^{-G})^{G^{-1}} \tag{6.9}$$

where x and y are given by the following equations:

$$x = log\left(\frac{E_\gamma}{E_1}\right), \qquad y = log\left(\frac{E_\gamma}{E_2}\right) \tag{6.10}$$

G is the interaction parameter between the low and high energy region, the larger the value of G the sharper low energy the turn over and vice verse. Figure 6.22 was obtained when fitting equation 6.10. This represents the relative efficiency of the entire array of three clover detectors plus one segmented detector.

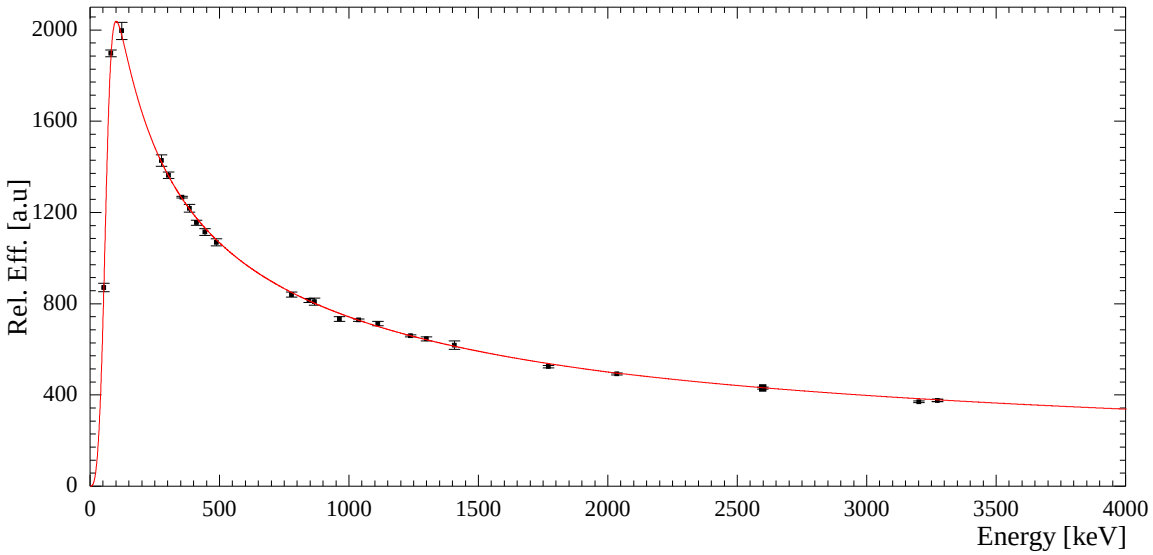

Figure 6.22. The relative efficiency of three clover detectors plus one tigress detectors measured with ^{133}Ba, ^{152}Eu and ^{57}Co radioactive source mounted on implanted position.

The maximum detection efficiency occurs near 120 keV for all the detectors. Thereafter it decreases monotonically with an increase in energy as shown in figure 6.22. This decrease in efficiency is caused by a decrease in cross-section of both the photoelectric effect and Compton scattering as a function of γ-ray energy [82].

6.5 Data Analysis Method

6.5.1 Coincidence matrix

Following the β-decay measurement, a large data set was collected and stored on the hard-disk to be sorted off-line. An MTsort [117] code was used to sort this data set into matrices compatible with Radware software [119]. A matrix is a two dimensional ($E_{\gamma 1}$, $E_{\gamma 2}$) energy histogram with the energy of one photon on one axis and the energy of a coincidence photon on the other axis. An example of a γ-ray level scheme is illustrated in figure 6.23. When a gate is set around an energy γ_1, a coincidence γ-ray spectrum is formed (e.g a spectrum showing γ_2, γ_3 and γ_4) and when another gate is set on γ_2 a γ-ray spectrum consisting of only γ_1 will be formed. Using these coincidence relationships, a level scheme can be constructed.

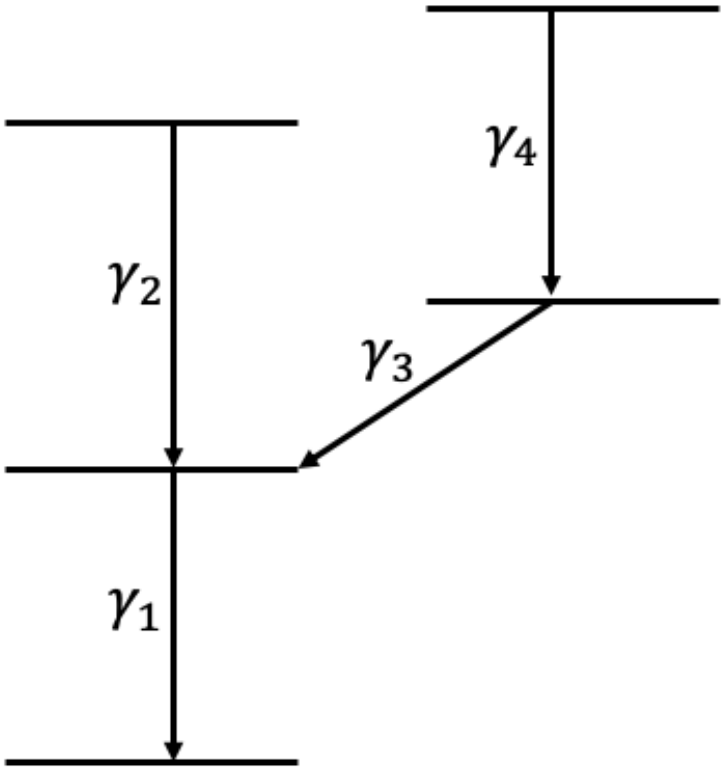

Figure 6.23. A typical level scheme illustration coincidence γ-rays.

The MTSort code uses the calibration coefficients obtained when calibrating the detectors (section 6.4.2) to gain match the detector to the same dispersion. Different matrices were created: a γ-γ matrix, a Si(Li)-γ matrix, and a plastic scintillator gated-γ-γ matrix. After creating all these matrices, it was necessary to convert the two-dimensional spectra into a format compatible with RadWare for further analyses, using the eg2rad program. The converted matrices had a dimension of 4096×4096 channels and a dispersion of 1 keV/ch for all the clover detectors. The γ-γ matrix was used to construct the level scheme, plastic scintillator gated-γ-γ matrix as a background reduced matrix and the Si(Li)-γ matrix for conversion electrons in coincidence with γ-rays. A typical example of the two-dimensional γ-γ matrix is shown in figure 6.24.

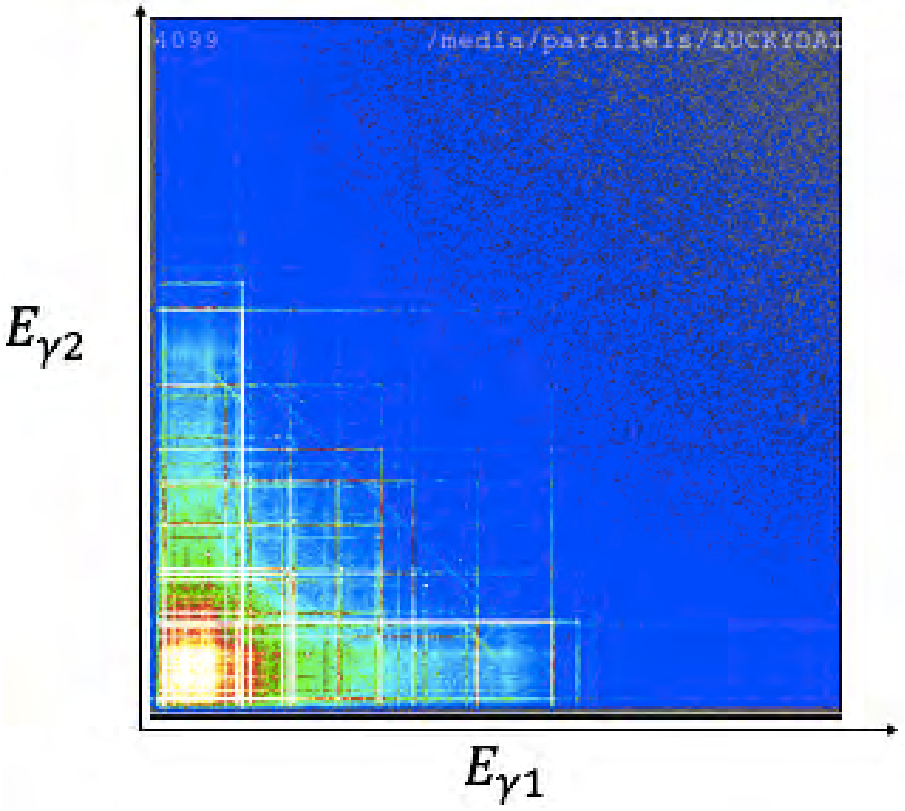

Figure 6.24. A γ-γ correlation matrix of ^{162}Yb. The orange color correspond to γ-rays with high intensity while cyan color correspond to γ-rays with low energy.

6.5.2 γ-γ coincidence and construction of the level scheme

A γ-γ coincidence means a simultaneous detection of two γ-rays by the detector array within a specified time window, usually called a coincidence window. This method makes it possible to determine whether the detected γ-rays are from the same source or not. If they are from the same source and detected within this time window, those γ-rays are referred to as in "prompt coincidence". A typical time window is shown in the time difference spectrum shown in figure 6.25. Events or γ-rays detected outside this time window are called random events and they contribute to background in the spectrum. The random events increase with an increase in the width of this time gate but if the time gate is too narrow, it cuts-off true events. Therefore a compromise in determining the correct time gate could be used. Our times gate shown in 6.25 cuts out low energy x-rays to reduces randoms.

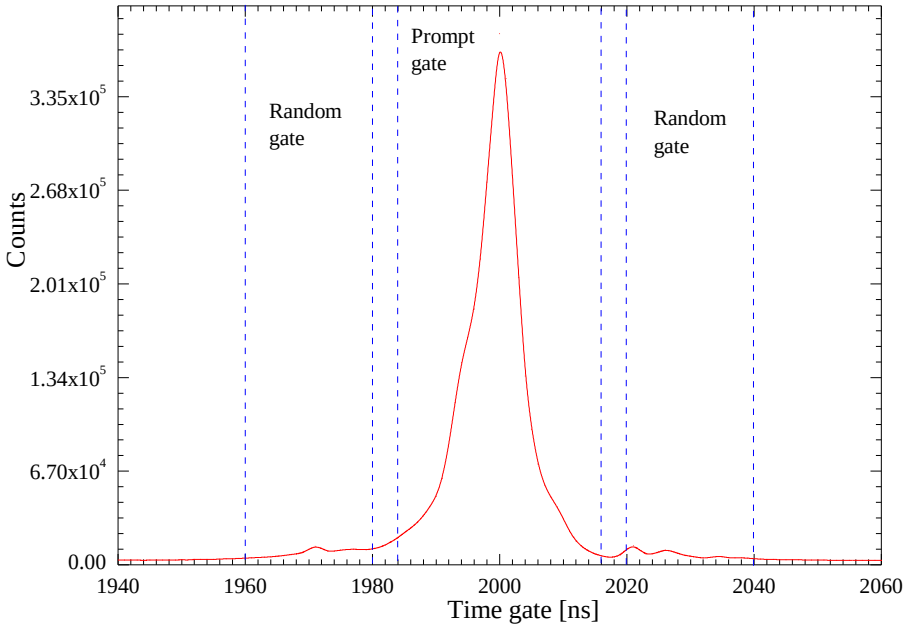

Figure 6.25. Time difference spectrum, good events occurs within the selected time gate.

As random events also occur within the prompt window, it is better to do a random subtraction of these events before creating a matrix that will be used to build a level scheme. In this case, three different matrices were created within the sorting code, one matrix within the correct time gate (prompt gate) and two with gates on either side of the time gate (random gate). Each matrix created on either side of the time gate contains prompt and randoms. To get a matrix with a random subtracted event, the following equation was used:

$$RS_m = TG_m - k(LR_m + RR_m) \tag{6.11}$$

where RS_m is called Random Subtracted matrix, TG_m is Time Gated matrix, LR_m is Left Random matrix, RR_m is Right Random matrix and k is is coefficient given by the following equation:

$$k = \frac{x}{y + z} \tag{6.12}$$

where x is the number of channels in the time gate window and y, z are the number of channels on either side of the time gated spectrum. The random subtracted matrix was then used to construct the level scheme using the RadWare program called ESCL8R [120]. ESCL8R program needs the following files to build the level scheme: Energy calibration (.aca file) of the detectors, Efficiency calibration (.aef file) file of the detector, random subtracted γ-γ matrix (.m4b format), either x or y projection spectrum of the matrix (.spe file) and a background spectrum (created

by drawing the background on the projection spectrum using the sc command in gf3) (.spe file) [119].

6.6 Transition Intensities

For all the measured γ-rays, their intensity can be calculated by the following equation:

$$I_\gamma = \frac{A}{\epsilon} \tag{6.13}$$

where A is the area under the single peak, and ϵ is the efficiency of the detector as explained in section 6.4.3.1. The intensity uncertainty measurement was calculated using

$$\Delta I = I \times \sqrt{\left(\frac{\Delta A}{A}\right)^2 + \left(\frac{\Delta \epsilon}{\epsilon}\right)^2} \tag{6.14}$$

The area and uncertainty in the area of the peak was obtained by fitting each peak in the singles spectrum using the Radware program gf3. The relative efficiency of the detector for each γ-ray was obtained from the spectrum 6.22 using the programs EFFIT and gf3. The intensity and the uncertainty of all the γ-rays were normalized using the intensity of the strong peak, e.g.540 keV for ^{100}Ru. The total intensity (I_t) is given by:

$$I_t = I_\gamma(1+\alpha) = \frac{A}{\epsilon}(1+\alpha) \tag{6.15}$$

where α is the internal conversion coefficient [7] and it is given by

$$\alpha = \frac{I_e}{I_\gamma} \tag{6.16}$$

The internal conversion coefficient gives the probability of electron emission relative to γ-ray emission (for more see section 2.5.2).

6.7 Experimental details

6.7.1 Study of ^{162}Yb

The test run to demonstrate the proof of principle and obtain credible results with the tape station was to study ^{162}Yb from the decay of ^{162}Lu. Radioactive nuclei of ^{162}Yb were produced in the ^{147}Sm(^{19}F, 4n) reaction. More details about this experiment are shown in table 6.3. This was a perfect nucleus because it would not require a tape station to be operated at too high speed because it has a half-life of 1.37 minutes.

6.7.1.1 FLUKA Simulation

The design of the internals of the implantation chamber draws inspiration from the Yale tape collector setup [121]. In the Yale setup, the beam was stopped by the 3 mm gold plug after interacting with the target. A similar setup was designed for this measurement where the Faraday cup was used to stop the beam before hitting the tape. A schematic diagram illustrating the position of the Faraday cup is shown in figure 6.26. In figure 6.26, the beam interacts with the target and produces recoiling compound nuclei that fly in the general direction of the beam. To optimize the thickness of the target and estimate the implantation efficiency, the FLUKA simulation package was used.

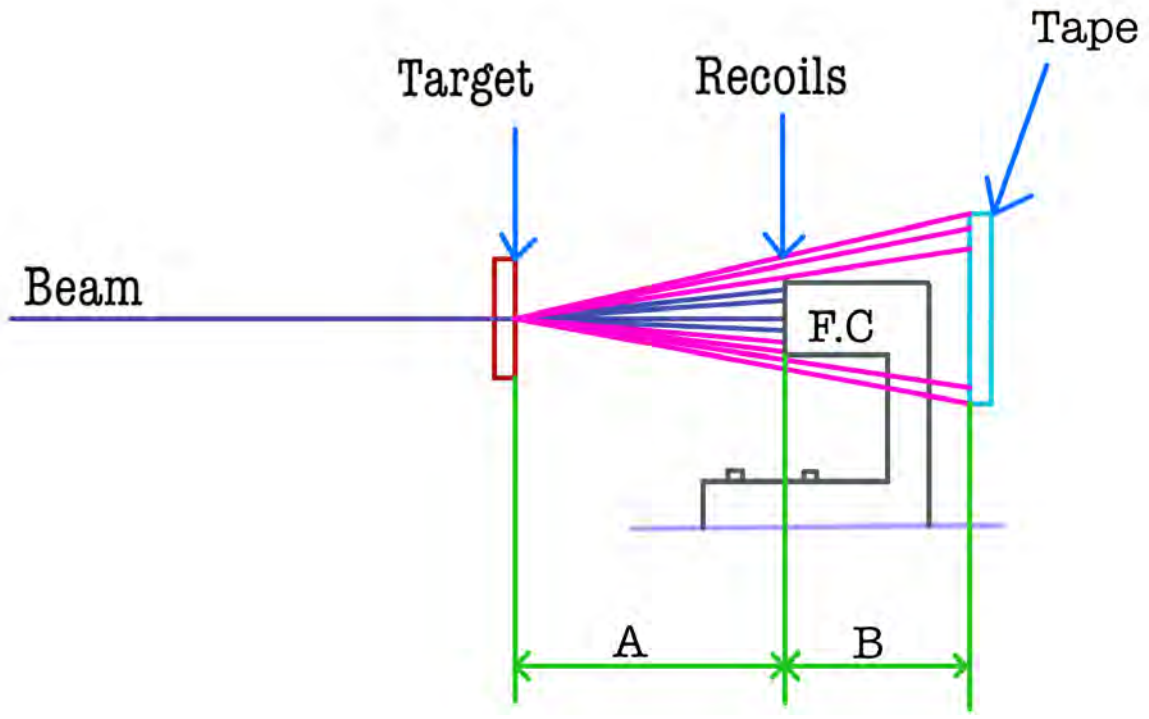

Figure 6.26. This figure illustrates the optimization of the Faraday cup (FC). The position and thickness of the Faraday cup was optimized by using FLUKA calculation. Recoils are indicated by the pink lines.

The size and position with respect to the tape (and the target) of the Faraday cup was optimized to increase the collection efficiency, while minimizing that the beam that reaches the tape. This was also needed to reduced unwanted reactions on the tape.

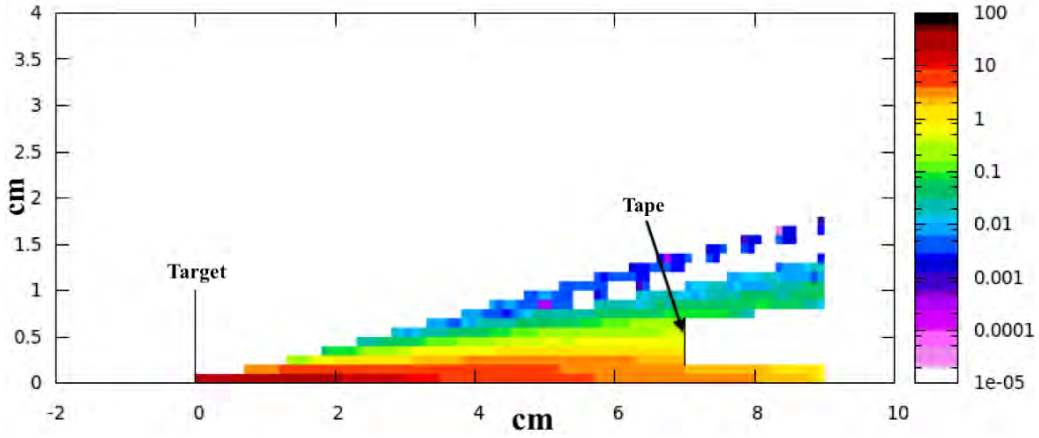

(a)

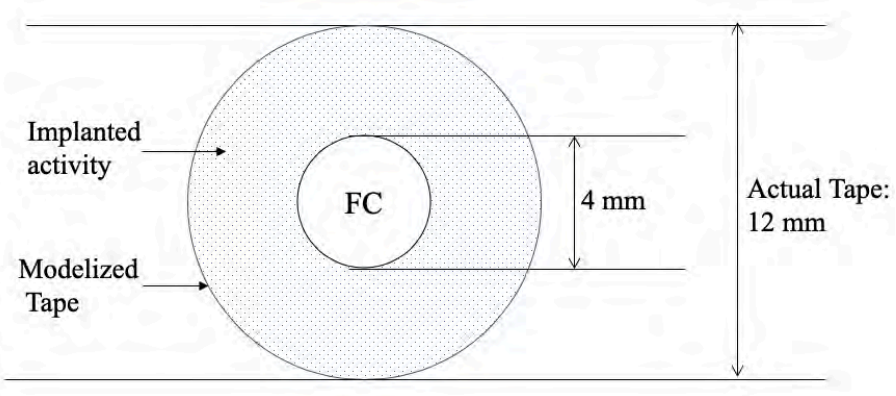

(b)

Figure 6.27. The optimization of the recoils collection using the FLUKA simulation. (a) recoils implanted on the tape and (b) modelling of the Faraday Cup (FC) in th FLUKA simulation.

Figure 6.27(a) shows the calculated distribution of the recoils emerging from the target. In figure 6.27(a), the target position is modelled at 0 cm while the tape is further back at 7 cm. For computational ease, the Faraday cup was modelled as a hole in the tape, as shown in figure 6.27(b) and the tape modelled as a concentric disk. With this calculation, the size and position of the Faraday cup to be used in this experiment was deduced.

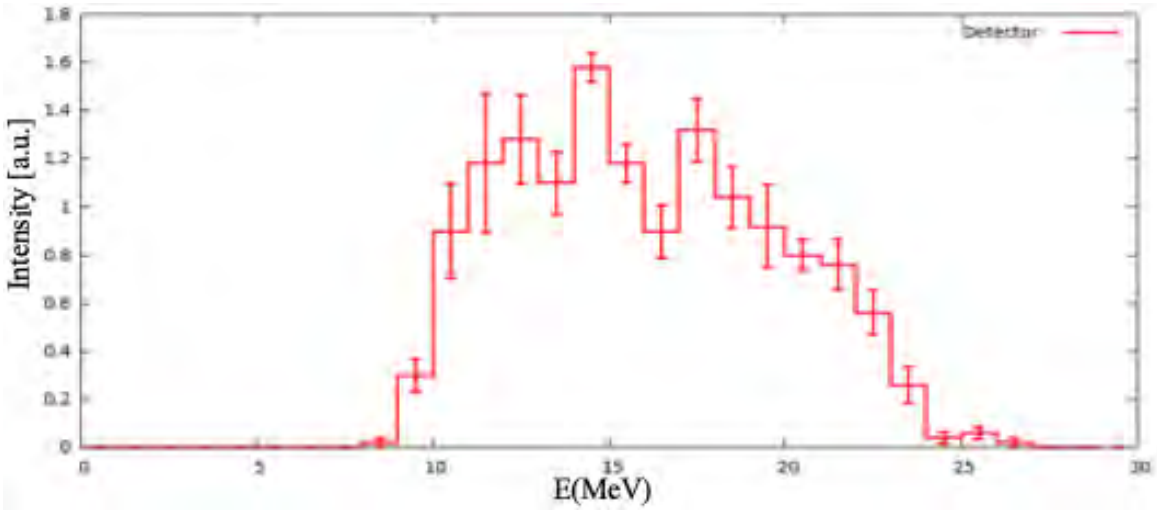

(a)

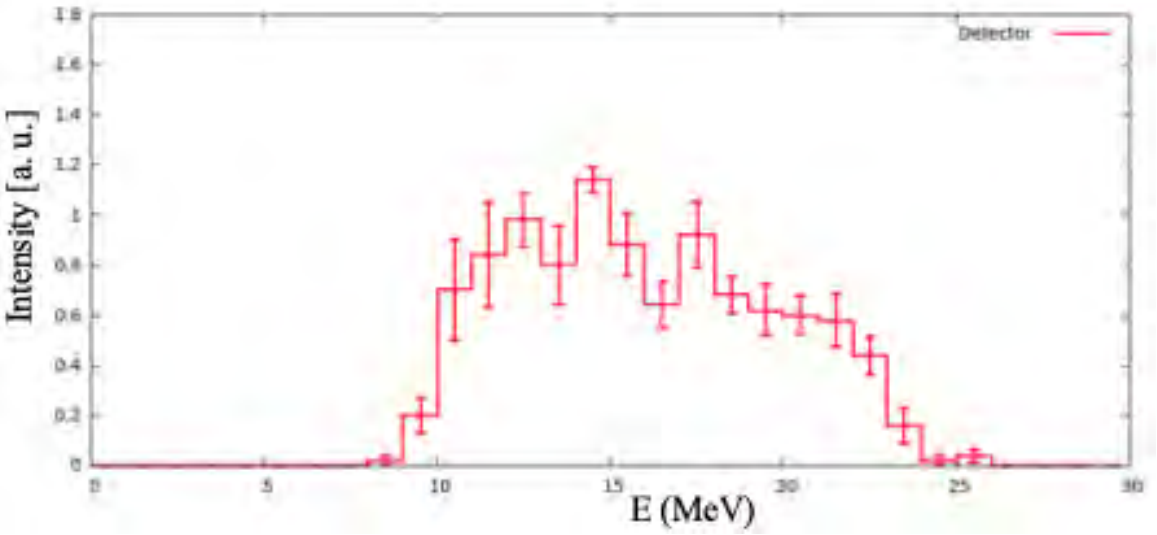

(b)

Figure 6.28. The demonstration of the recoils leaving and hitting the tape (a) is the energy distribution of recoils leaving the target and (b) is the distribution of recoil reaching the tape.

Figure 6.28(a) shows the calculated energy spectrum of recoils emerging from the target, while 6.28(b) shows the spectrum of recoils hitting the annular disk, that represents the tape. The ratio of the areas gives the collection efficiency of $\approxeq$ 70%.

6.7.1.2 ^{162}Yb Experimental details

Figure 6.29 shows the internals of the implantation chamber used for ^{162}Yb experiment. The ruby was used to focus the beam through the target and onto the Faraday cup. The Faraday cup was used to stop the beam before the tape and to read the beam current. The two magnetic poles were used to bend the electrons scattered off the cup into a circular orbits so they return to the Faraday Cup and get collected.

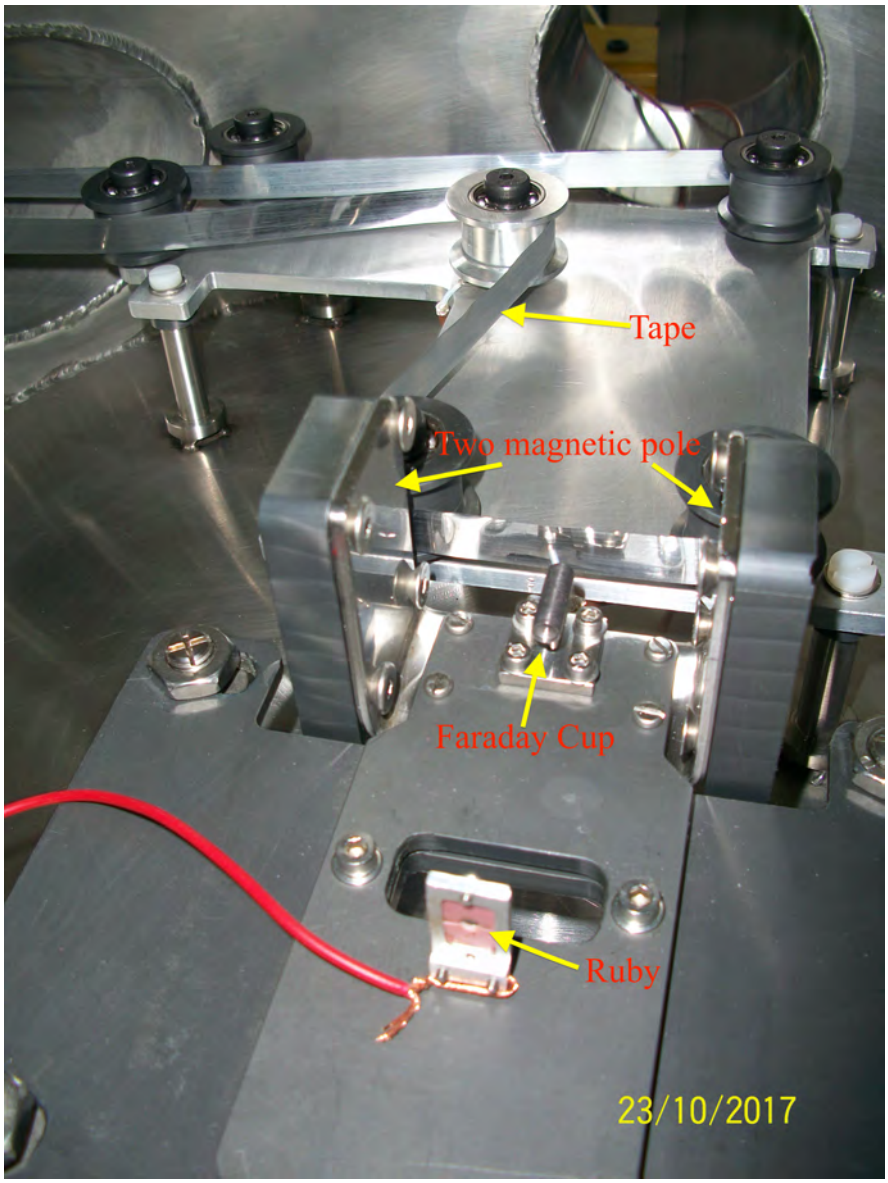

Figure 6.29. This image showing the Ruby, Faraday cup and the tape located behind the Faraday cup.

A 95 MeV ^{19}F beam was delivered by the K=200 Separated Sector Cyclotron (SSC) and bombarded a 2 mg/cm^2 ^{147}Sm target. The target was placed 5 mm behind the ruby. The Faraday Cup was a 4 mm diameter tantalum cylinder located 7 cm away from the target and 2 mm in front of the tape. To reduce the solid angle shadowed by the cup, and have high collection efficiency on the tape, the Faraday Cup was place closed to the tape.

The recoils were collected/deposited onto a 12 mm wide aluminized Mylar tape and thereafter transported to the measuring site. An automated system was developed to deflect the beam during transportation. Figure 6.30 shows a schematic diagram illustrating the beam deflection and transportation time. This process repeated for the whole measurement.

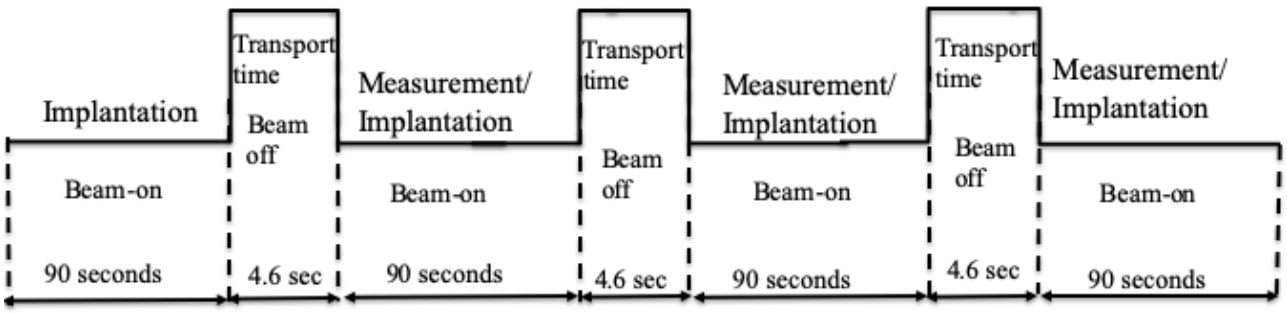

Figure 6.30. The cycle illustration of beam on/off and measurement using the tape station

The implanted activity of ^{162}Yb was transported to the measuring chamber, where nuclear decay by the emission of β-particles, followed by the emission of γ-rays and conversion electrons was recorded. The implanted point on the tape stops in front of the Si(Li) detector as shown in figure 6.31 with the activity facing the Si(Li) detector. The Si(Li) detector can be moved closer or away from the tape as required.

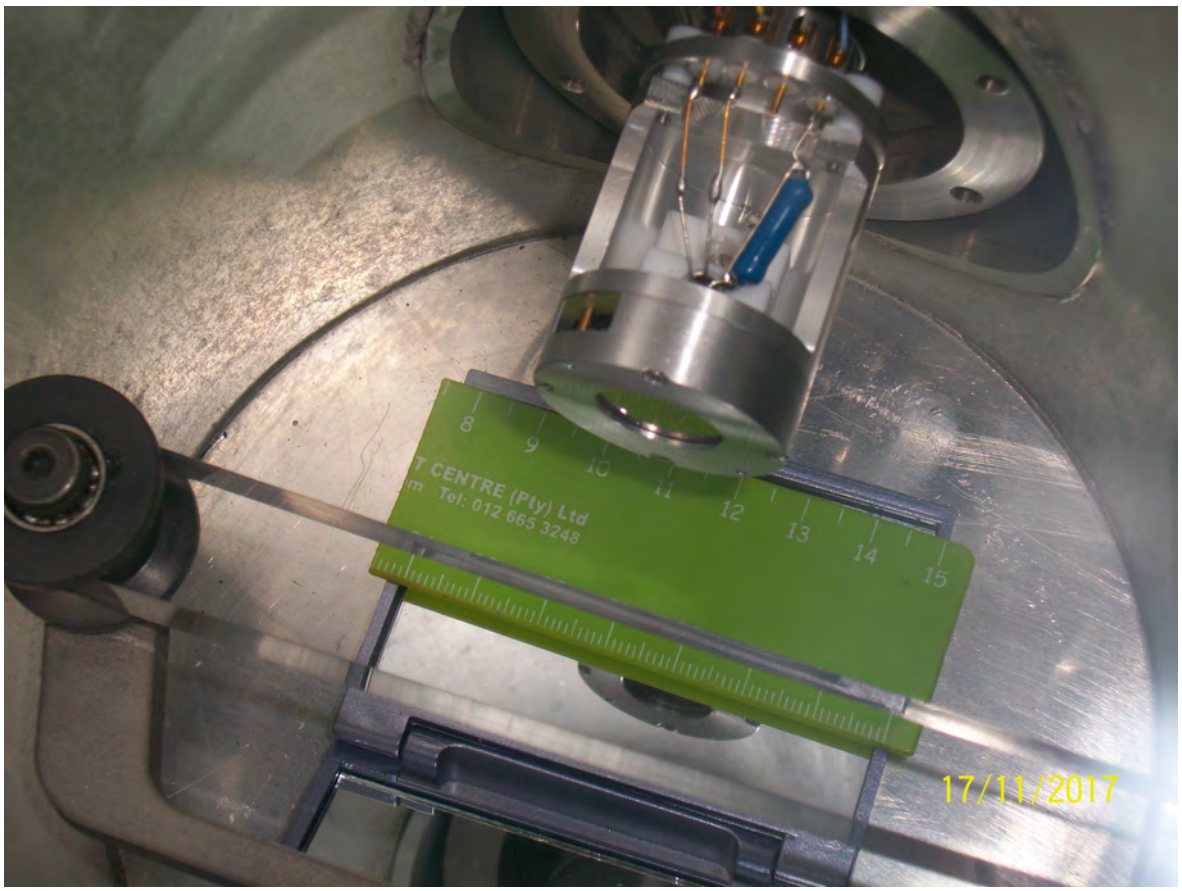

Figure 6.31. Si(Li) detector facing the implanted side of the tape.

The following table summarized the conditions used for this measurement:

Table 6.3. ^{162}Yb experimental details.

Primary beam	^{19}F
Beam energy	95 MeV
Beam current	22 - 40 nA
Target nucleus	^{147}Sm
Target thickness	2 mg/cm^2
Clover position	45°, 95°,135°
Si(Li) position	90^o with respect tape
Plastic scintillator position	90° with respect to the target
Implantation time	90 seconds
Transport time	4.6 seconds
Counting time	90 seconds

6.7.2 Results and Outcomes

This section presents the experimental results obtained from β-decay measurement of ^{162}Yb. More than 1.3×10^9 γ-γ events and $2.3{\times}10^7$ Si(Li) counts were recorded during this measurements and analyzed off-line for the nucleus of interest. These results are compared to the previous measurements of ^{162}Yb, especially the experiment performed at Yale University with their tape collector [121] and some conclusions are drawn about this result. This experiment demonstrated the working operation of the tape station.

6.7.2.1 Previously observed ^{162}Yb Level Scheme

The low-lying energy levels in ^{162}Yb had been studied previously with the Yale tape collector [121]. Figures 6.32 show the partial level scheme of ^{162}Yb isotopes of McCutchan *et al.* [121]. The level transition and energies are given in keV.

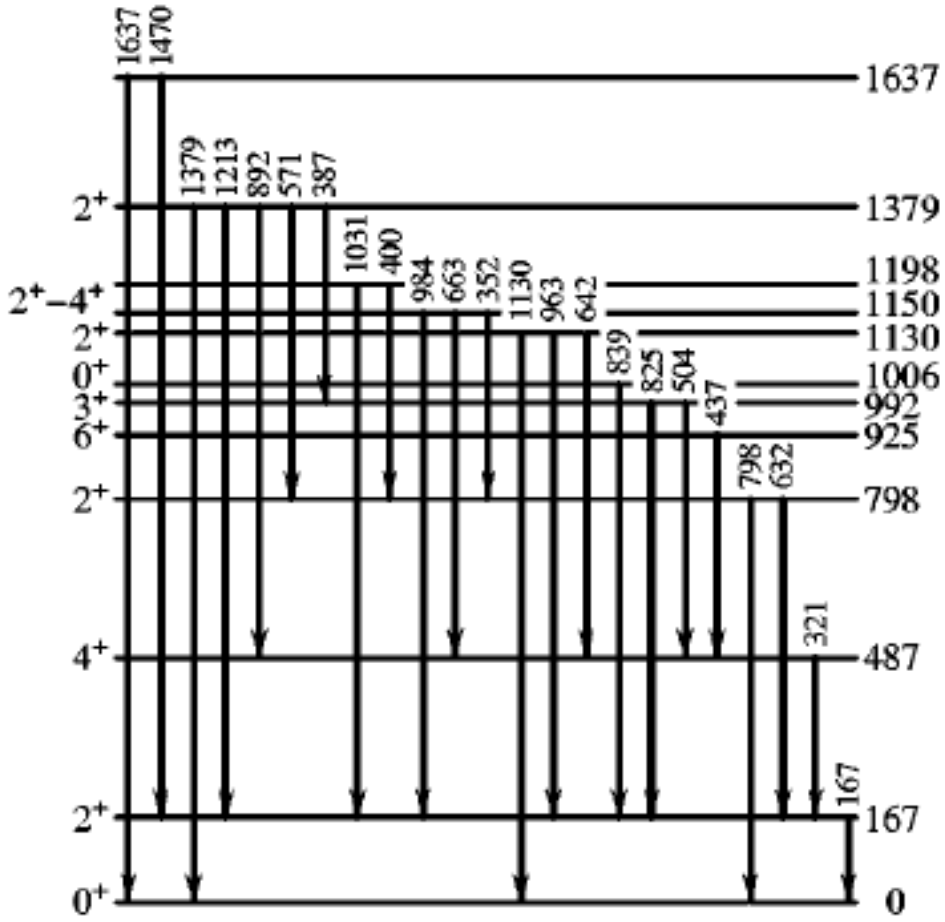

Figure 6.32. Partial level scheme of ^{162}Yb, from previews work done at Wright Nuclear Structure Laboratory. In total Yale observed nn'γ of which most where observed in this measurement [121].

6.7.2.2 Observed γ-ray and level scheme

Low-lying energy levels of ^{162}Yb were observed in the present work. The singles energy spectrum of all γ-rays observed during the measurement is shown in figure 6.33. This spectrum also contains contaminants from the room background, like ^{40}K from the walls, and ^{60}Co from activated steel material of the scattering chamber [106]. Tape station was installed on the beam line that was used for scattering chamber experiments [106], and the vault contains a lot of steel. As a result, we could not avoid detecting ^{60}Co contaminates. Other contaminants are the result of the beam hitting the tape and causing a reaction.

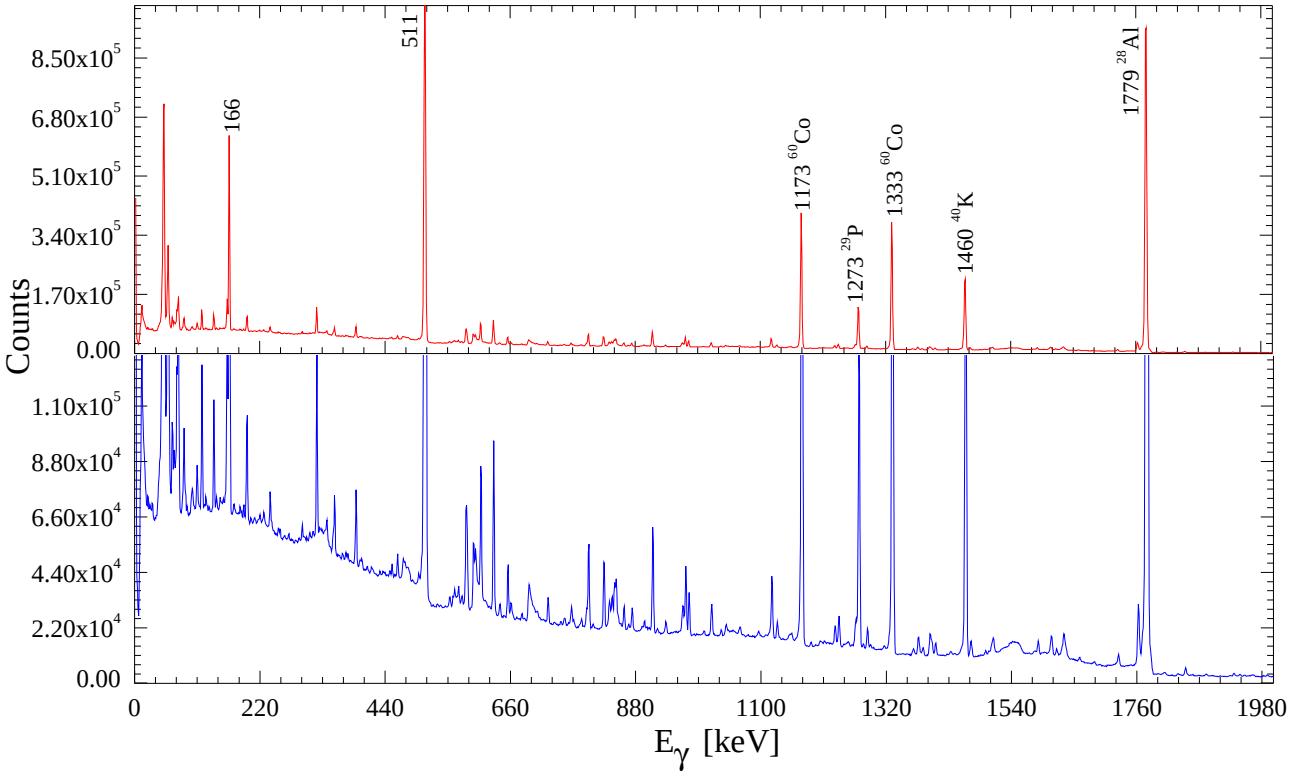

Figure 6.33. The total singles spectrum obtained from this measurement. The bottom panel (blue) has an expanded y-scale to illustrate the peaks that are located at "grass-level", nearly all of which are in ^{162}Yb.

The contaminants in figure 6.33 are clearly visible. To clean the spectrum, the plastic scintillator detector was used. Thereafter, a plastic scintillator-γ-γ matrix was created. Gating on the β-particle reduces room background but fails to reduce the background caused by beam hitting the tape. A total projection spectrum obtained after using the plastic scintillator is shown in figure 6.34.

The recoils were implanted on the *Al*-side of the tape. However, the beam was not properly tuned to be deposited in the Faraday cup, a fraction of the beam hit the tape which created reactions with ^{12}C and ^{16}O, hence producing an unavoidable background. The two huge peaks in figure 6.34 come from ^{29}P and ^{28}Al as a result of beam hitting the tape, shown in the following reactions:

$$^{19}F +^{12} C =^{31} P =^{28} Al + 2pn$$
$$=^{29} P + 2n$$

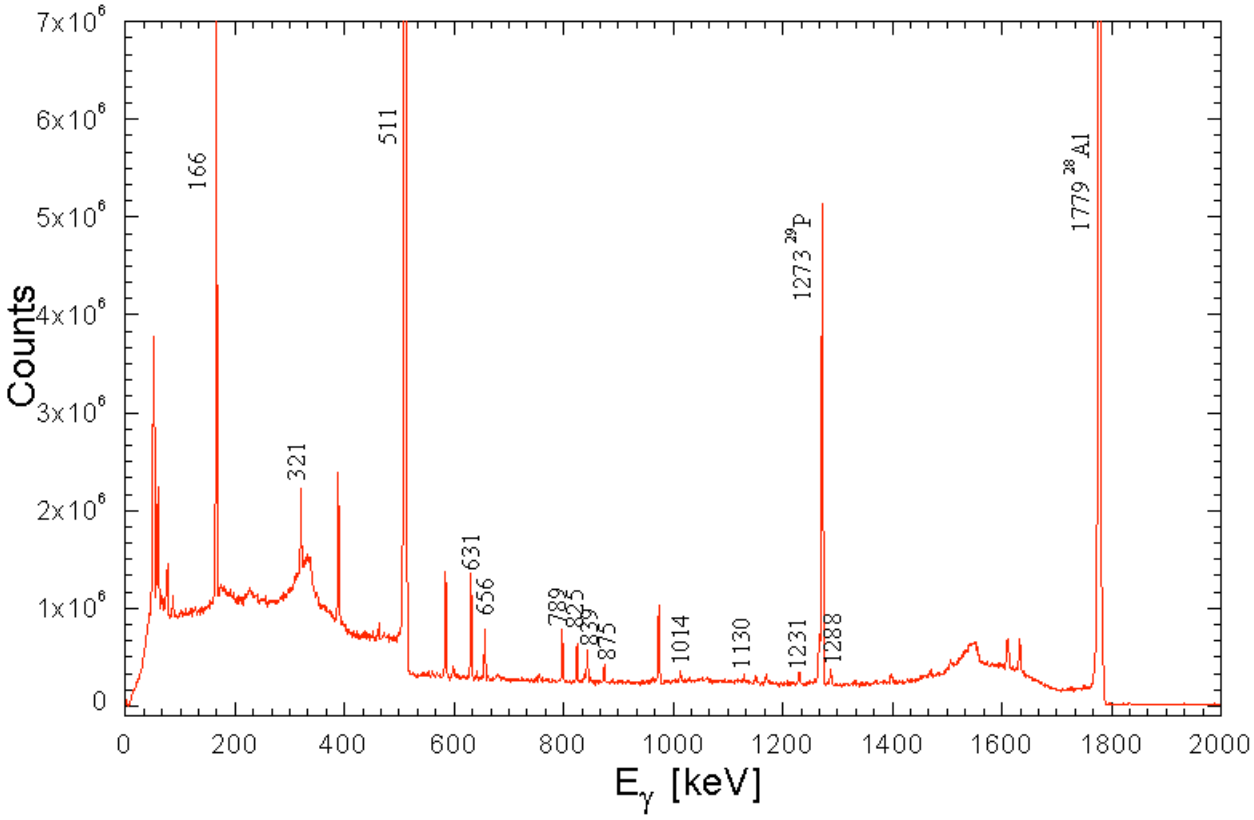

Figure 6.34. The total projection spectrum obtained from 2D γ-γ matrix after gating with the plastic scintillator to reduce background.

The γ-γ matrix was created. This coincidence condition managed to suppresses most of the random events from ^{40}K, ^{60}Co, ^{29}P, and ^{28}Al. The γ-γ total projection spectrum is shown in figure 6.35. This method managed to reduce the intensity of the contaminants from being dominants to grass-level.

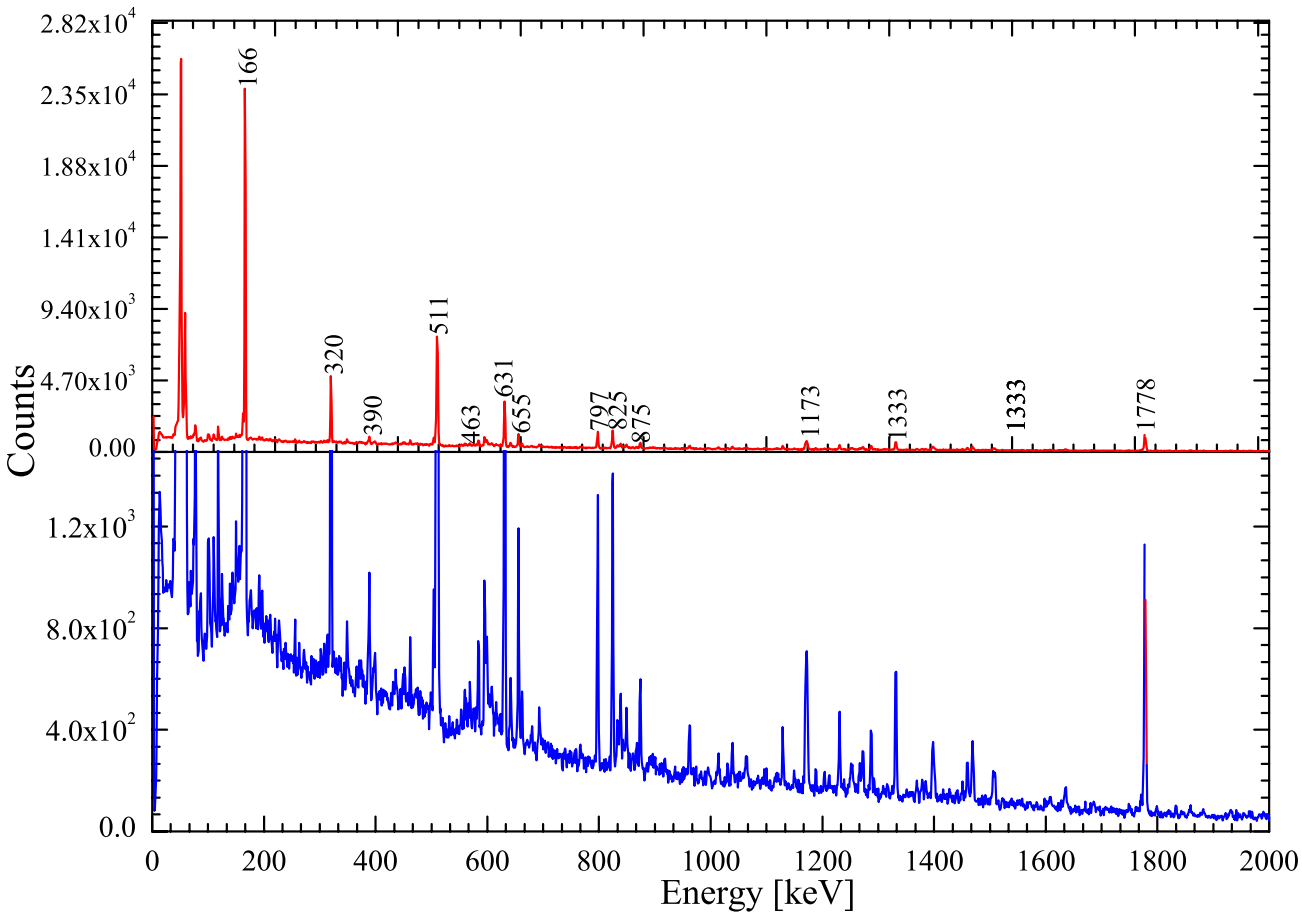

Figure 6.35. Total projection of γ-γ matrix. The bottom panel (blue) has an expanded y-scale to illustrate the peaks that are located at "grass-level."

A gate was set on the strongest transition of ^{162}Yb, $2^+ \rightarrow 0^+$ (166 keV), and the spectrum showing γ-rays in coincidence with 166 keV is shown in figure 6.36.

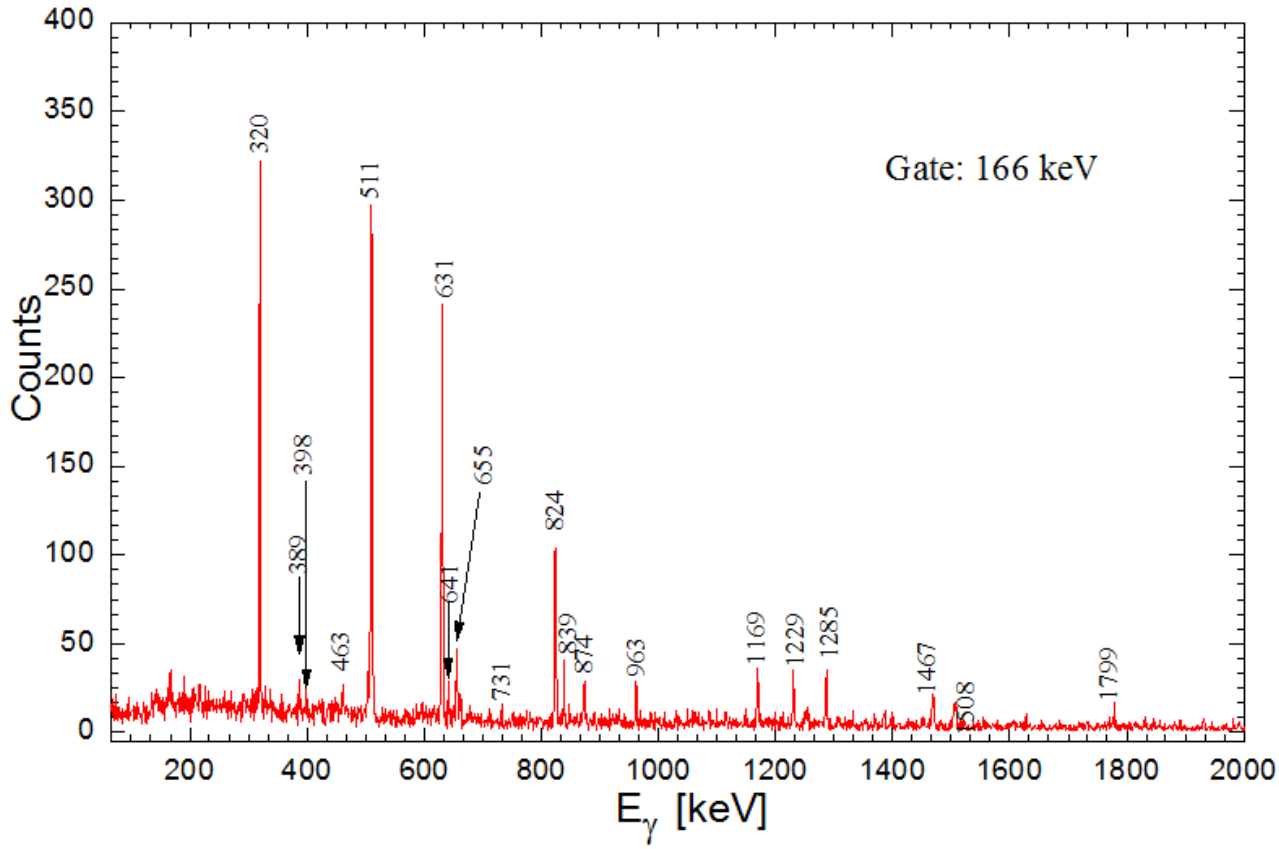

Figure 6.36. ^{162}Yb spectrum obtained after gating from 166 keV line.

The γ-γ matrix was used to build the level scheme shown in figure 6.37. The observed low-lying transitions and levels are indicated by solid lines while spins and parities are indicated on the left of the level. The observed transitions were positioned in the level scheme based on coincidence relationships and intensity arguments. In the singles spectrum, figure 6.33, all the γ-rays observed by McCutchan *et al.* [121] could also be seen.

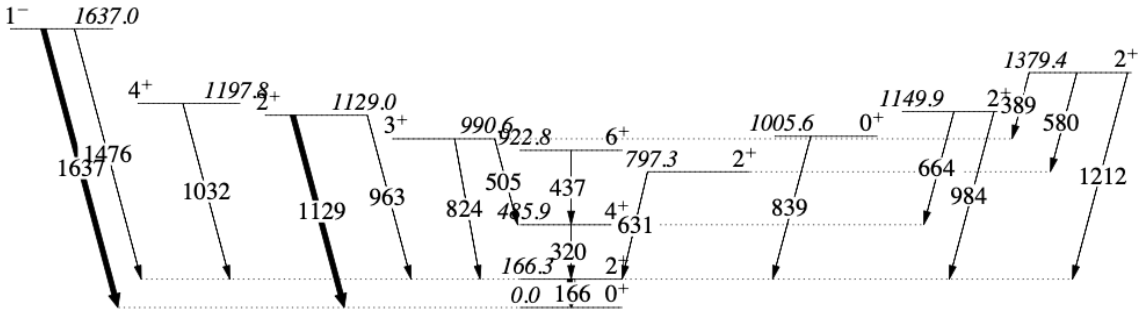

Figure 6.37. The constructed level scheme of ^{162}Yb using the collected data.

6.7.2.3 Conversion electron analysis

Figure 6.38 shows the conversion electrons observed in the measurement. Conversion electrons were observed from strong transitions of ^{162}Yb, especially the 166 keV ($2^+ \rightarrow 0^+$), 319 keV (4^+

$\rightarrow 2^+$), 656 keV ($2^+ \rightarrow 2^+$), and 827 keV ($3^+ \rightarrow 2^+$) transitions. However, due to the beam hitting the tape a huge background was detected, and it was later learned that the Si(Li) was sensitive to noise caused when the stepper motor was energized.

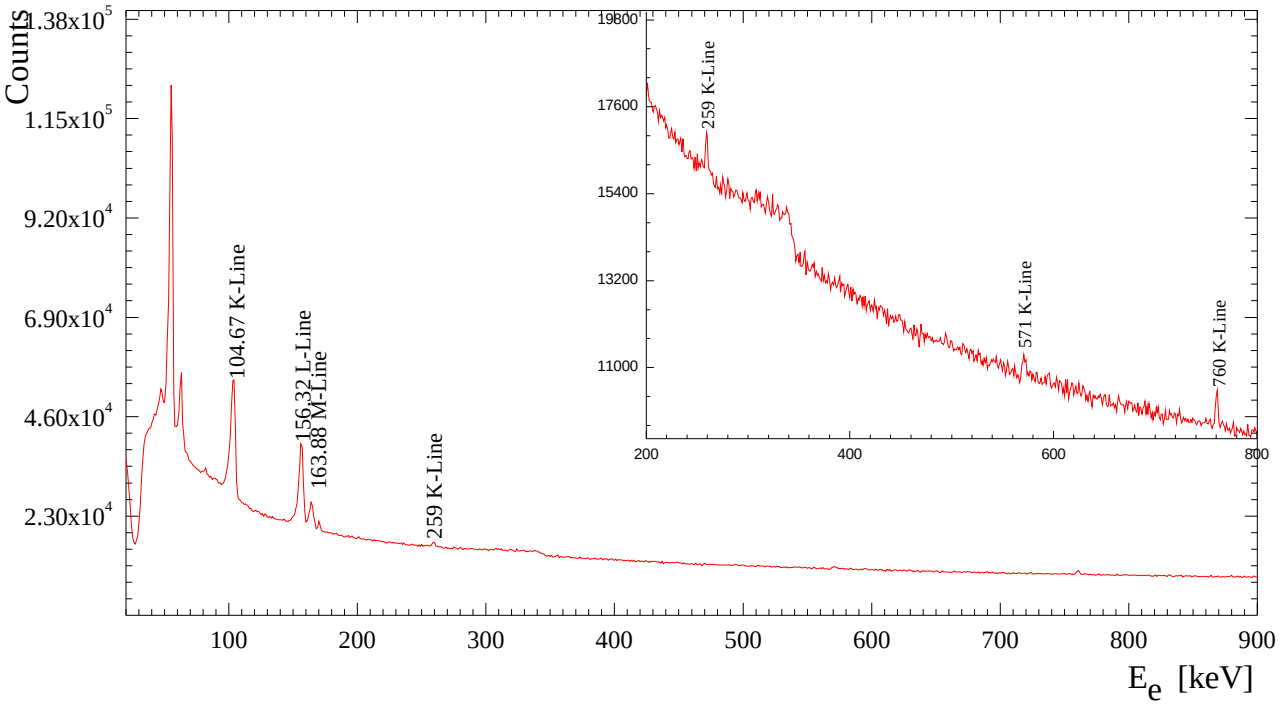

Figure 6.38. Ungated conversion electron spectrum of ^{162}Yb.

Figure 6.39 shows conversion electron lines obtained after using the plastic scintillator to create a γ- Si(Li) matrix. The conversion electrons from the ($2^+ \rightarrow 0^+$) transition were observed, while the $4^+ \rightarrow 2^+$ was obscured by the Compton edge of the 511 keV γ-ray. Again, the 760 K-line conversion electron was observed. However, we could not avoid background from the Compton edge of the strong γ-ray lines such as 511 keV and 1779 keV. The Compton edge affected the sensitivity of our measurement.

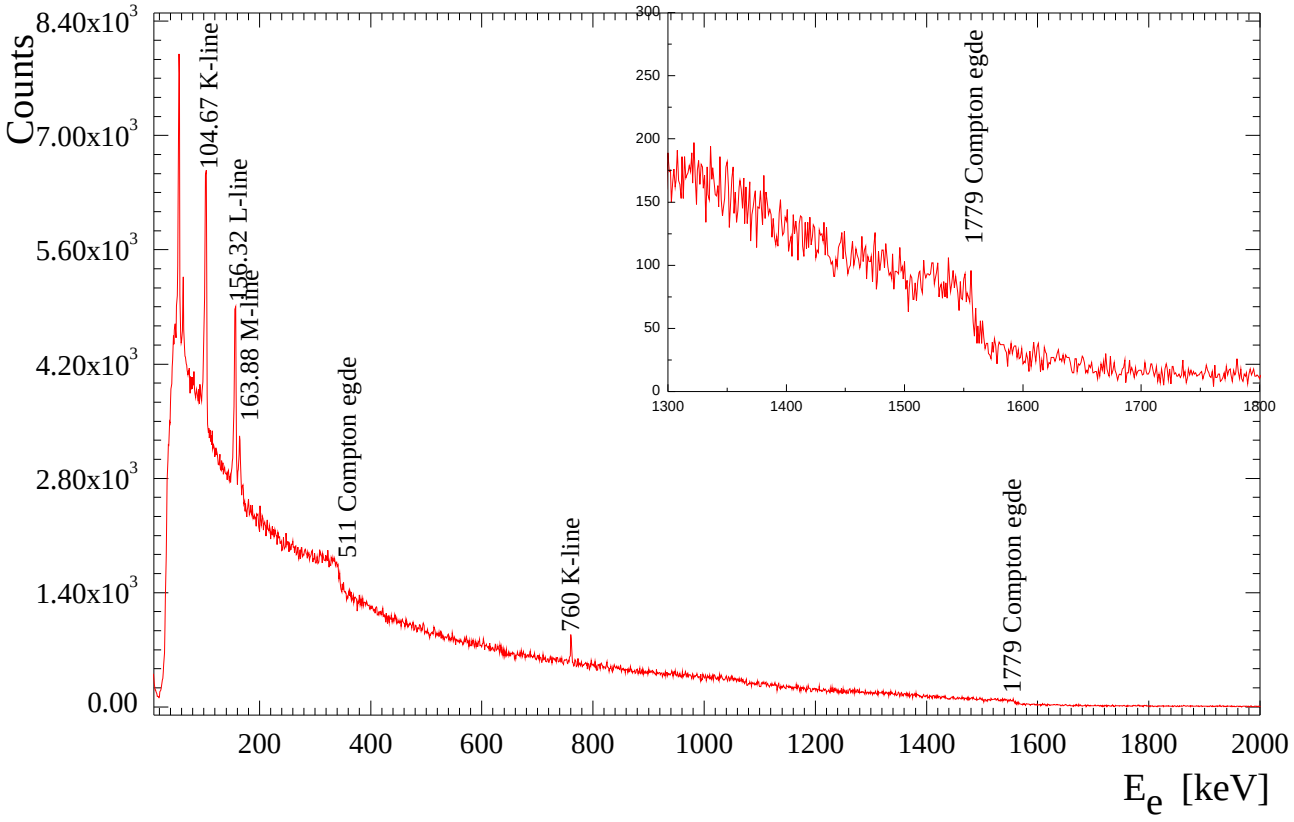

Figure 6.39. Plastic scintilator gated conversion electron spectrum ^{162}Yb.

Table 6.4 shows the observed conversion electron (C.E.) in this measurement.

Table 6.4. Observed conversion electron from the decay of ^{162}Yb

C.E. E_e [keV]	Shell	E_γ[keV]	Parent Nucleus
104.67	K	166.71	^{162}Yb
156.32	L	166.71	^{162}Yb
163.88	M	166.71	^{162}Yb
259.40	K	320.60	^{162}Yb
571.10	K	631.63	^{162}Yb
760.52	K	825.29	^{162}Yb

6.8 Study of Ru isotopes

The study of the ^{98,100}Ru isotopes differed as these nuclei have a longer half-lives and they both β-decay to a stable nucleus. Therefore, this measurement did not require a fast transport system similar to the first experiment 6.7.1, because a long β-decay chain back to stability would not be observed. To have maximum collection efficiency for this particular measurement, a thick target was used to trap the recoiling nucleus within the target, thereafter transporting the target slowly to the detection site. Hence, the tape station was modified to meet the

requirement of this particular study i.e. to directly transport the target from the reaction site to the measuring site.

6.8.1 ^{98,100}Ru Experimental details

Figure 6.40 shows the modified internals of the implantation chamber used in ^{89}Ru and ^{100}Ru experiments. Figure 6.40 shows the ruby, target transporter holding a real target, Faraday cup, and two magnetic poles.

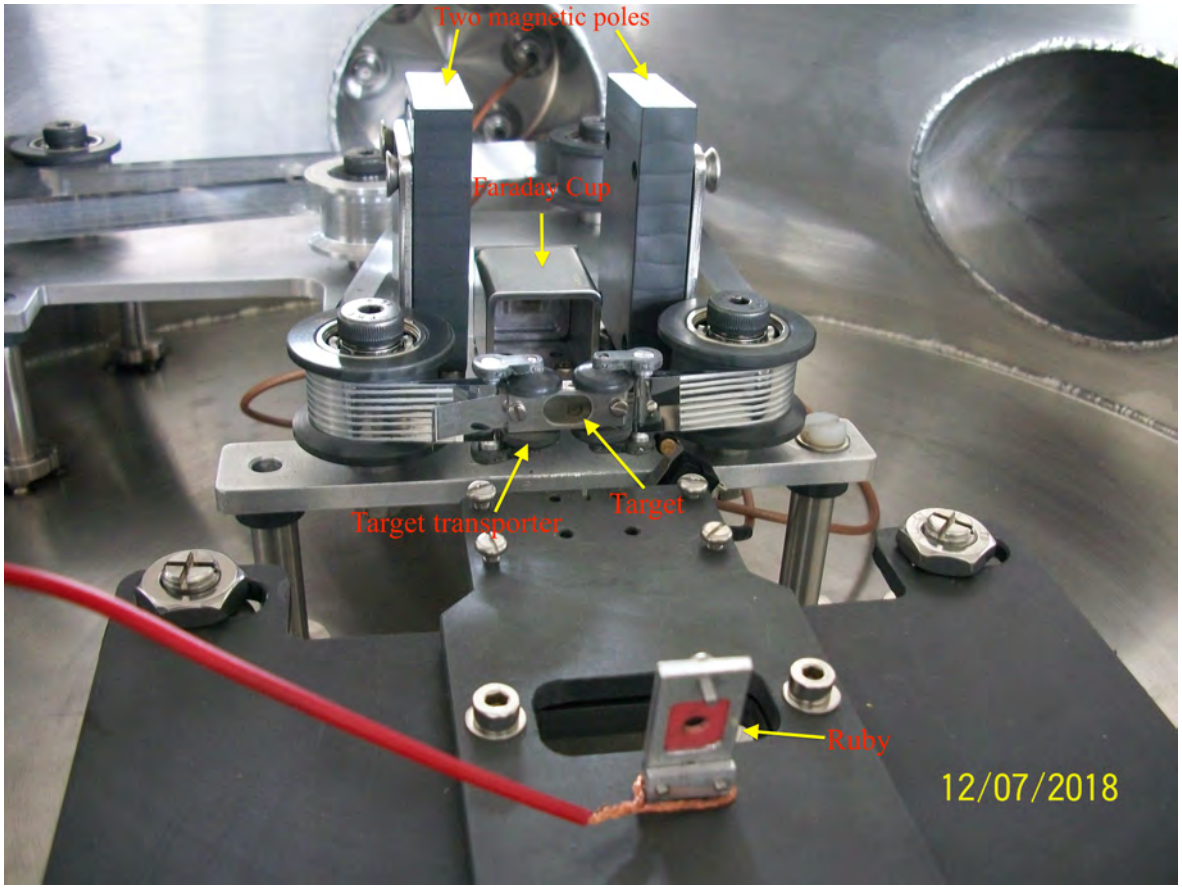

Figure 6.40. This image shows the internals of the implantation chamber. Target transporter with the target, Ruby for beam focusing and Faraday cup which was used as beam stopper.

The two isotopes of ruthenium were produced using the ^{89}Y(^{12}C, 3n)^{98}Rh and ^{89}Y(^{14}N, p2n)^{100}Rh (and ^{89}Y(^{14}N, 3n)^{100}Pd) reactions. In the latter reaction, ^{100}Pd has half-life of 3.63 days and it decays to ^{100}Rh which eventually decays to ^{100}Ru. As a result, the final irradiation of the target was for 6 hours, after which counting continued for a week, see table 6.5. The beam energy used to bombard the target was 45 MeV and 47 MeV, respectively. The beams (^{12}C and ^{14}N) were delivered by K=200 Separated Sector Cyclotron (SSC) and used to bombard 3.5 mg/cm^2 ^{89}Y target. The target was mounted on the target transport as shown in figure 6.40. After the beam passes through the target, it was collected by the Faraday cup placed behind the target. The material used to make the new Faraday cup and the target holder is tanta-

lum (to reduce neutron activation). An automated system was developed to switch the beam off during transportation and measuring time. The schematic diagram illustrating the beam on/off period, measurement time and transportation times are shown in figure 6.41. Table 6.5 summarizes the details for this experiment, identified by unique code PR294. Ruthenium-100 has two isomers, hence two measurement times were used shown in table 6.5.

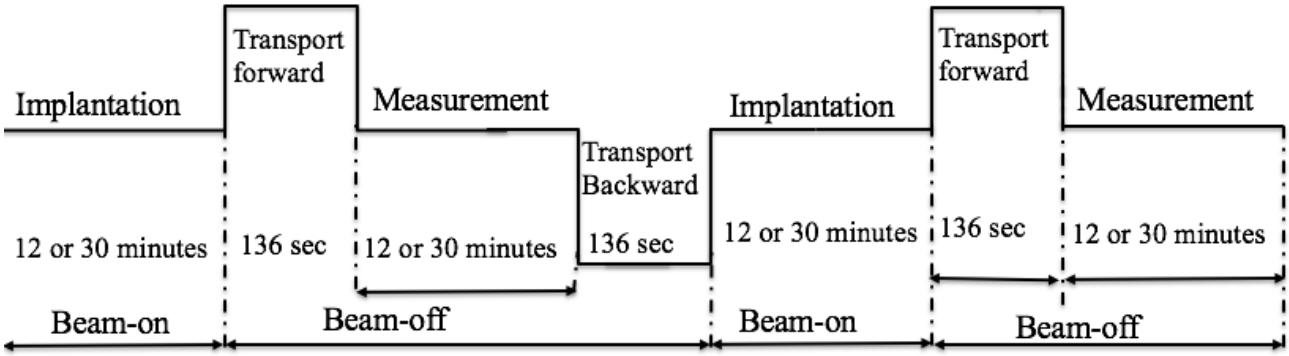

Figure 6.41. An illustration of the beam on/off and transportation timing used for ^{100}Ru measurement.

Table 6.5. ^{98,100}Ru experimental information. * ^{100}Ru has two β decay levels with different half-life. * Counting at the end of the measurement.

	Weekend one (^{98}Ru)	Weekend two (^{100}Ru)
Beam or Projectile	^{12}C	^{14}N
Beam energy	45 MeV	47 MeV
Beam current	10 - 40 nA	22 - 40 nA
Target nucleus	^{89}Y	^{89}Y
Target thickness	3.5 mg/cm^2	3.5 mg/cm^2
Clover position	45°, 95°,135°	45°, 95°,135°
SiLi position	90° with respect target	90° with respect target
Plastic scintillator position	90° with respect to the target	90° with respect to the target
Implantation time	5 and 18 minutes	12 and 30 minutes, 6 hours
Transport time	136 seconds to and from	136 sec to and from
Counting time	5 and 18 minutes	*12 and 30 minutes and *1 week

6.8.2 Target transporter

A truck shown in figure 6.42, was designed to transport the target from the reaction site to the detection site. The target is transported slowly to the detection chamber to count the activity created for a certain period and then moved back to the reaction position to be bombarded by the beam again. The truck profile and dimension was designed to fit that of the pulleys during transportation. It consists of four small wheels to prevent the target from touching the pulleys during movement. The tape is connected around two aluminium pins on either side of the target

transporter in a wrist-watch-like configuration. Light materials were used to manufacture this design (Al and Vesconite) to avoid sagging and to have smooth transportation.

Figure 6.42. Target transporter.

The target transporter is flexible and it can easily navigate over the pulleys without breaking the target. The flexibility was tested by using a thin target. Figure 6.43(a) shows the target transporter connected to the tape and figure 6.43(b) shows the target transporter navigating around the pulleys with a thin dummy target.

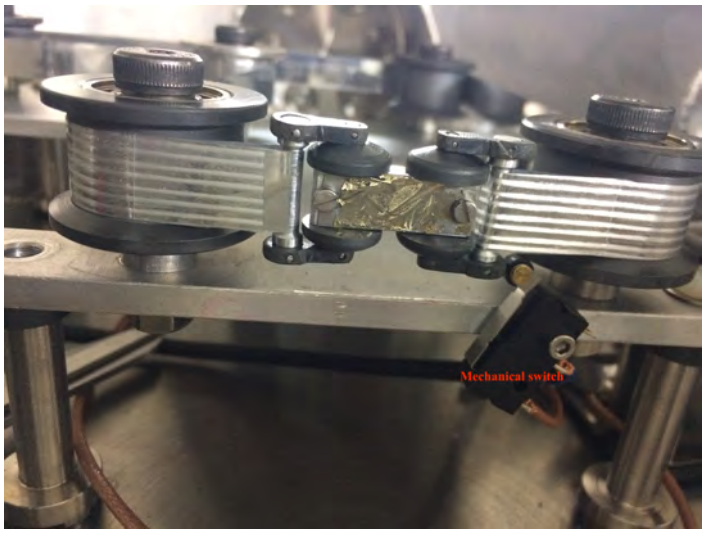

(a)

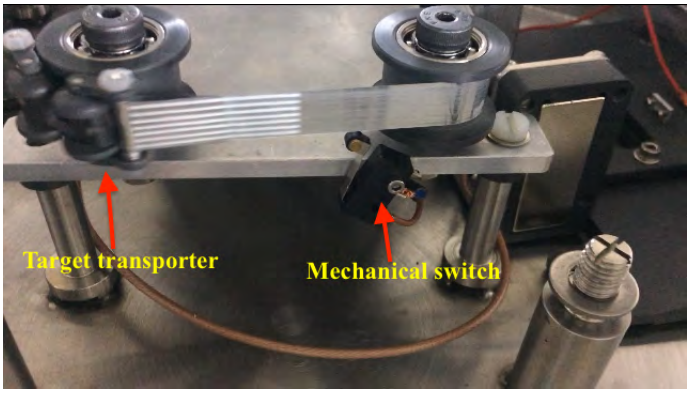

(b)

Figure 6.43. This figure demonstrates the flexibility of the target transporter as it navigates around the pulleys without damaging the target. Figure (a) shows how the target transporter connected to the tape, with target facing the beam direction. NB: test target 1 mg/cm^2 thickness. (b) shows the target transporter navigating around the pulleys.

A mechanical switch, shown in figure 6.43, was also added to make sure that the target transporter always stopped at the same reaction position. If the program miss-counts the number of steps when moving back to the reaction position, the system will stop moving when the target transporter hits the switch. The switch will then reset the number of steps moved to make sure that the target transporter always moves the same number of steps when transporting the target to the detection site.

The target stays in the detection site for a specified time before returning to the reaction site for activation or bombardment. On the detection site, the target faces the Si(Li) detector as shown in figure 6.44.

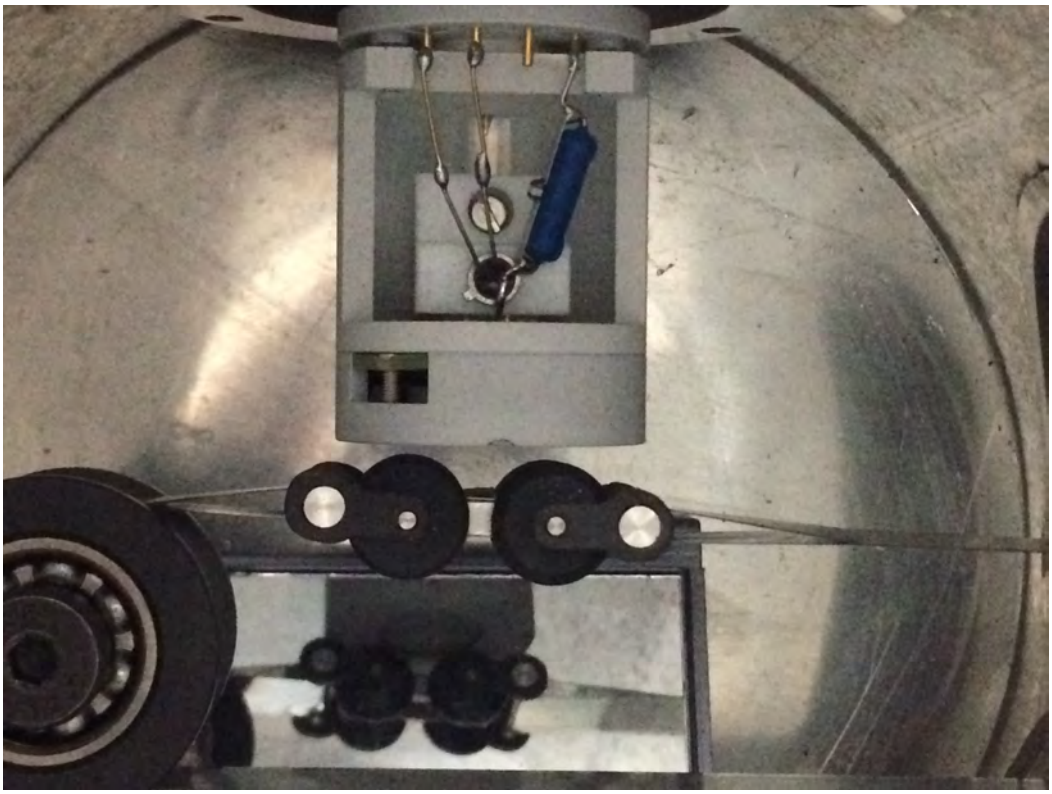

Figure 6.44. Target transporter with the target facing the Si(Li) detector.

6.8.3 Motor drive internals

Figure 6.45 shows the skeleton of the tape station in this new configuration. It consists of the aluminized Mylar tape and the target transporter which is connected to the tape. This configuration makes it easy to transport the whole target to the detection site.

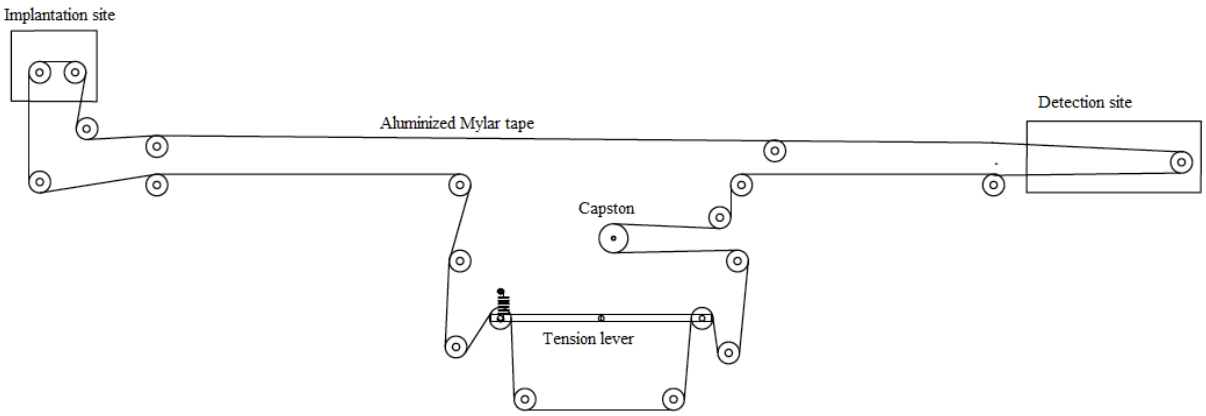

Figure 6.45. The schematic system illustrating the tape station. The target transporter is mounted on the tape. After counting for a while, the target is transported back to be bombarded with beam.

Figure 6.46 shows the new configuration of the drive internals in the motor drive chamber.

The spools was removed because there was no excess tape needed. In this configuration, the capstan is used to drive the tape and two Viton wheels were added to make sure that there is no slippage during acceleration in both directions.

Figure 6.46. This picture shows the internals of the tape station.

Chapter 7

Experimental Results: ^{98,100}Ru

7.1 Introduction

This chapter presents experimental results on ^{100}Ru and ^{98}Ru that were obtained from the ^{89}Y(^{14}N, p2n)^{100}Rh (and ^{89}Y(^{14}N, 3n)^{100}Pd) and ^{89}Y(^{12}C, 3n)^{98}Rh reactions, respectively. The ^{98}Ru experimental data was analyzed by Prof. P.E. Garrett and his team, while I analyzed ^{100}Ru. More than 2×10^9 γ-γ events and 2.6×10^8 Si(Li) counts were recorded during this measurement and used in the off-line analysis for ^{100}Ru. The collected data were converted into RadWare format and a γ-γ coincidence matrix was created and used to build the level scheme. We first present the previous obtained level scheme of ^{100}Ru.

7.2 The β^+ decay of ^{100}Rh to ^{100}Ru

The ^{100}Rh nucleus β^+-decays from two levels with half-lives of 4.6 minutes and 20 hour 8 minutes. Both of these states were populated in this measurement. The previous β^+-decay level schemes of these states are shown in figure 7.1, 7.2,7.3, 7.4 and 7.5, respectively, taken from [67].

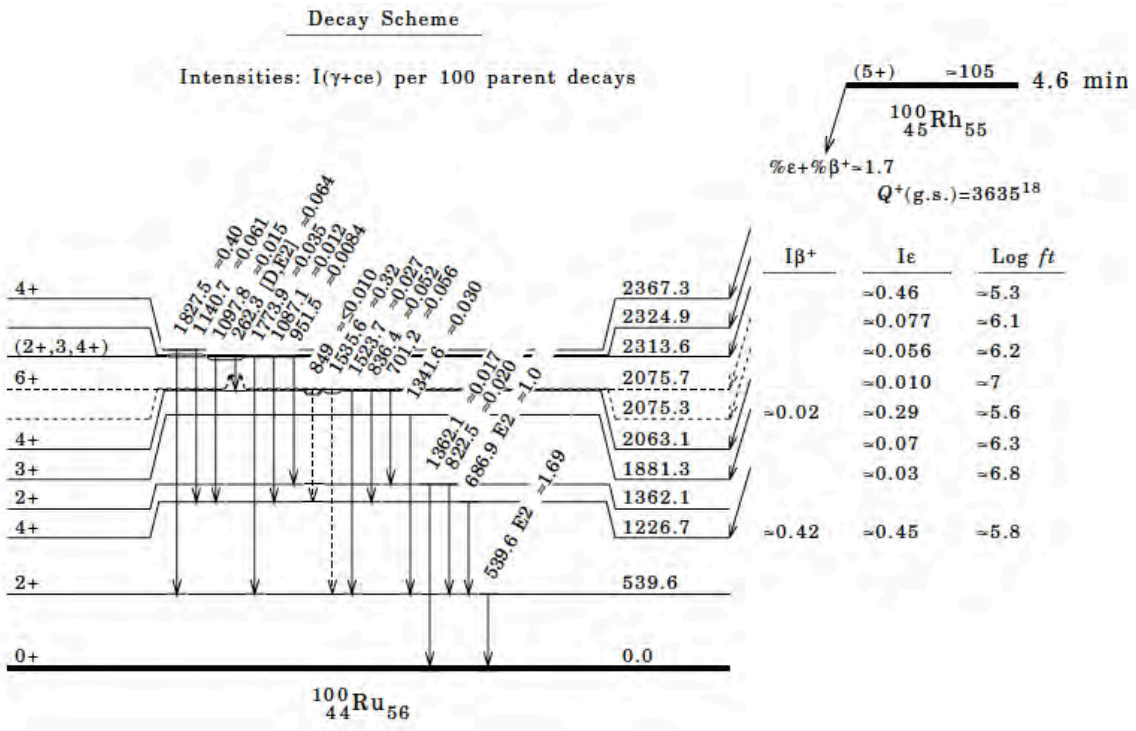

Figure 7.1. The β^+ decay scheme of ^{100}Rh (4.6 min) decaying to ^{100}Ru. The level scheme was obtained from the nuclear data sheets [67]

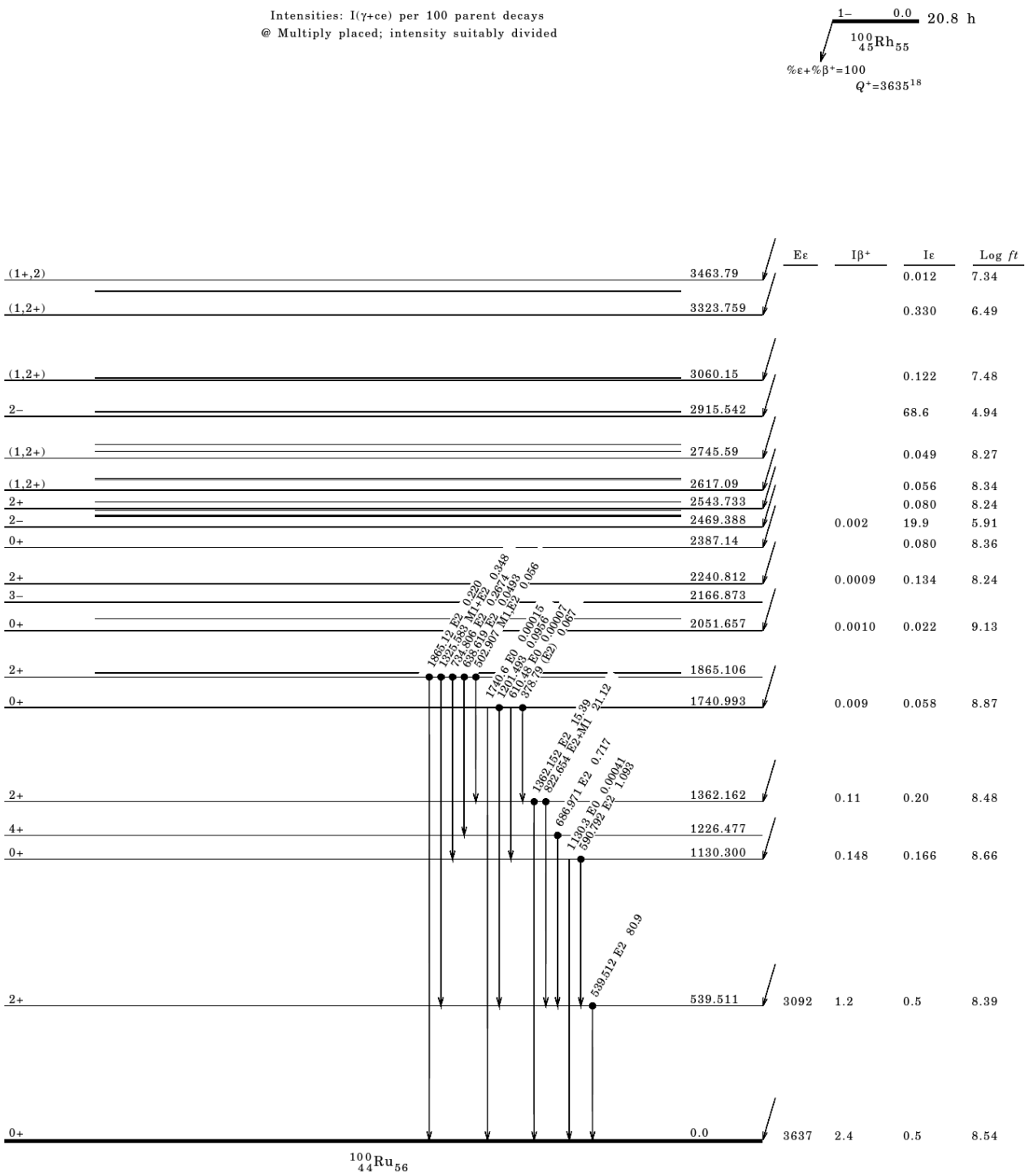

Figure 7.2. Portion of ^{100}Ru level scheme obtained from the nuclear data sheet [67].

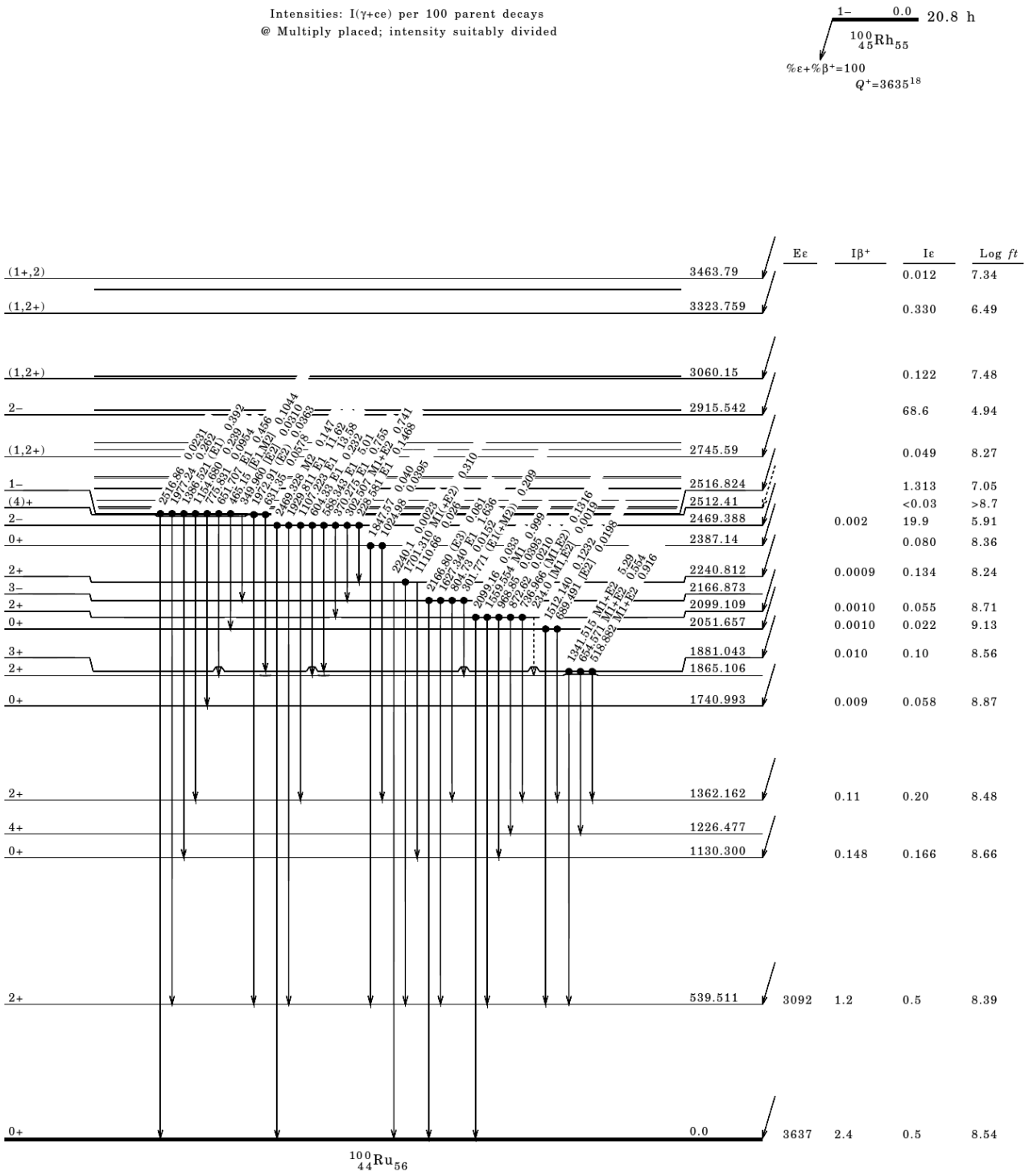

Figure 7.3. Portion of ^{100}Ru level scheme obtained from the Nuclear Data Sheets [67].

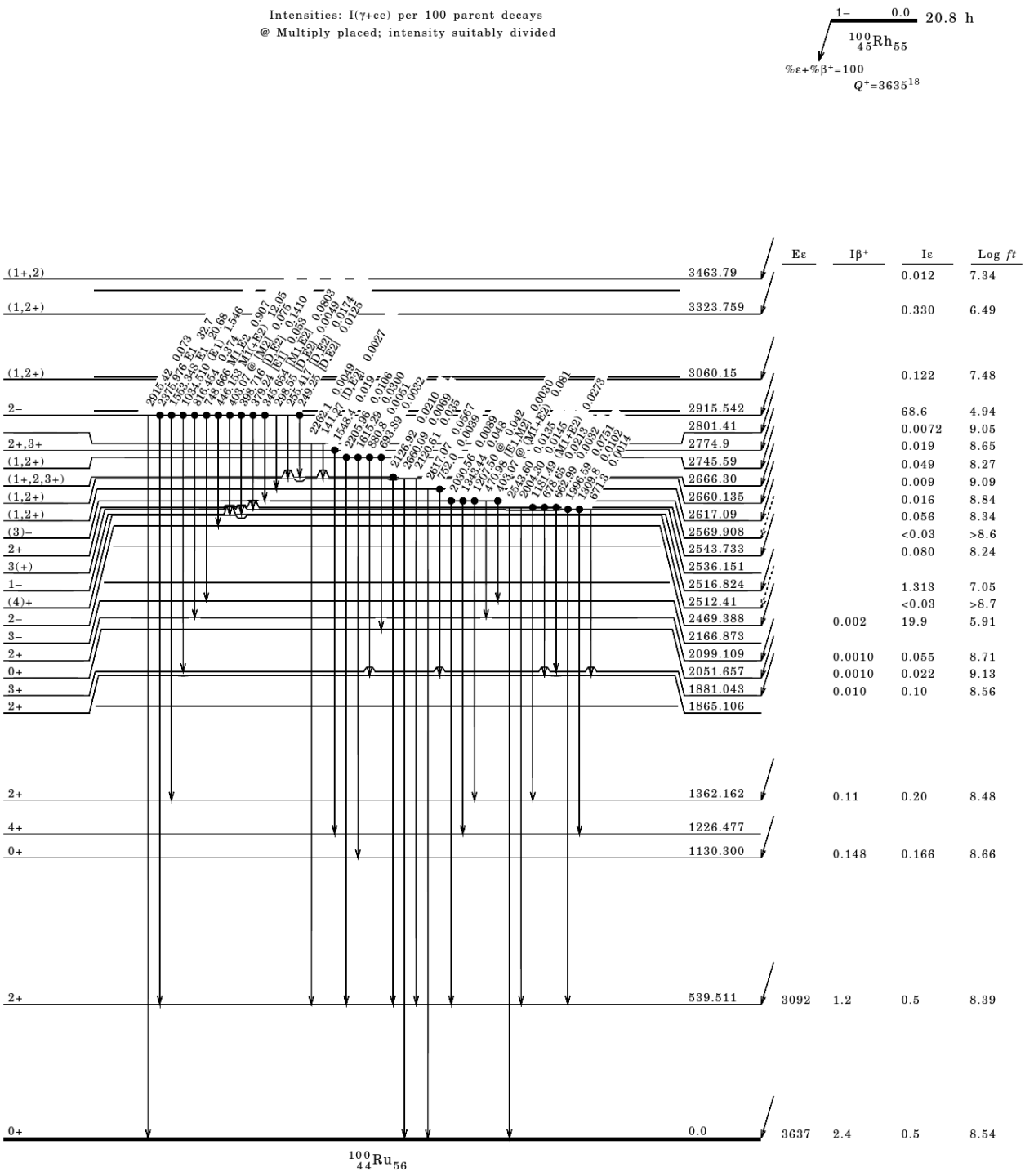

Figure 7.4. Portion of ^{100}Ru level scheme obtained from the Nuclear Data Sheets [67].

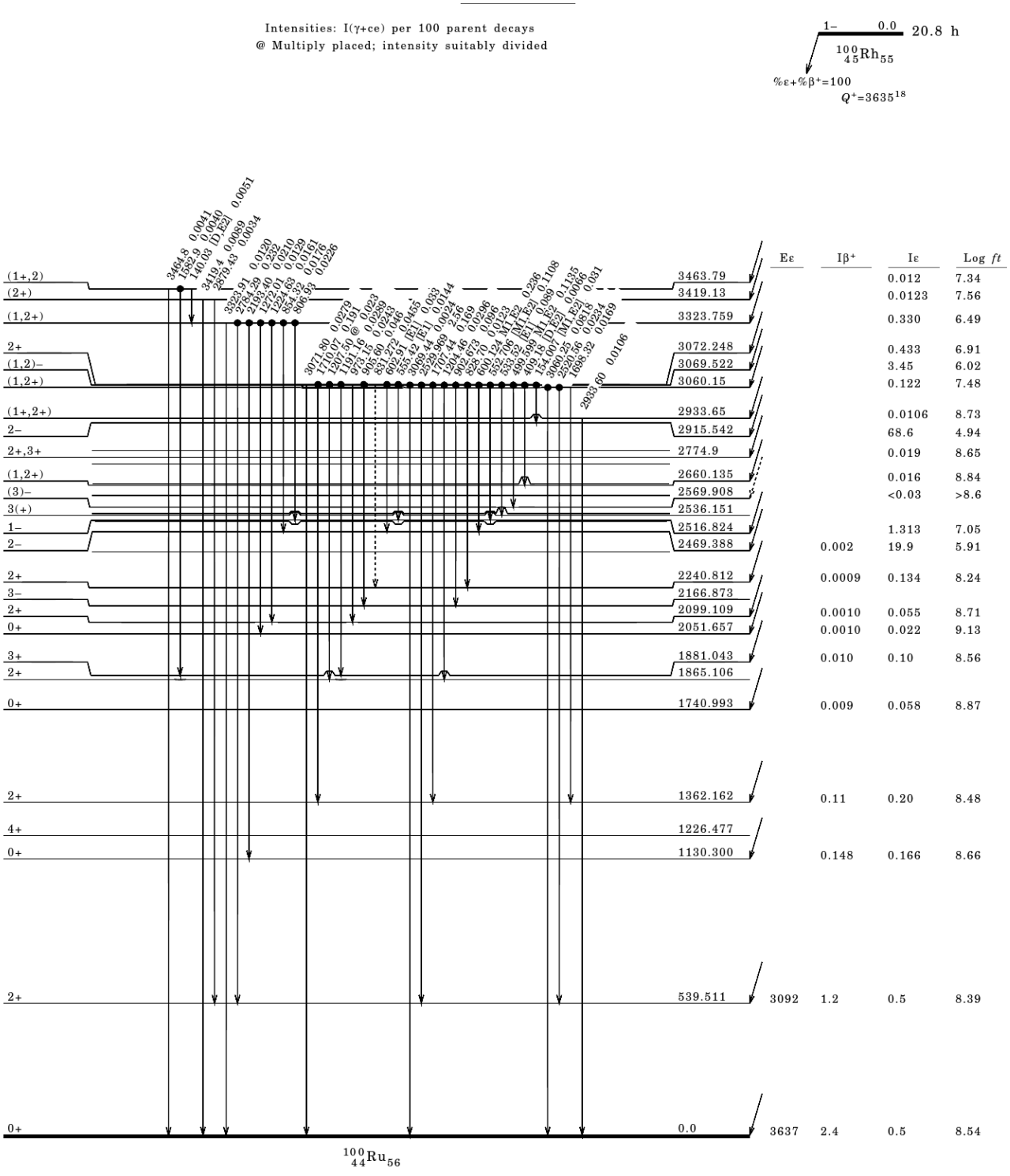

Figure 7.5. The final portion of the β^+ decay scheme of ^{100}Rh (20.8 h) decaying to ^{100}Ru. These level scheme were taken from the Nuclear Data Sheets [67]

7.3 ^{100}Ru Spectrum Analyses

The data recorded in the different counting times (corresponding to the two isomers) were sorted separately, but were later combined to increase coincidence statistics. The spectrum containing all singles γ-rays observed is shown in figure 7.6 and 7.7. This spectrum contains also γ-rays from other reaction channels populated when a ^{89}Y target is bombarded by a ^{14}N beam.

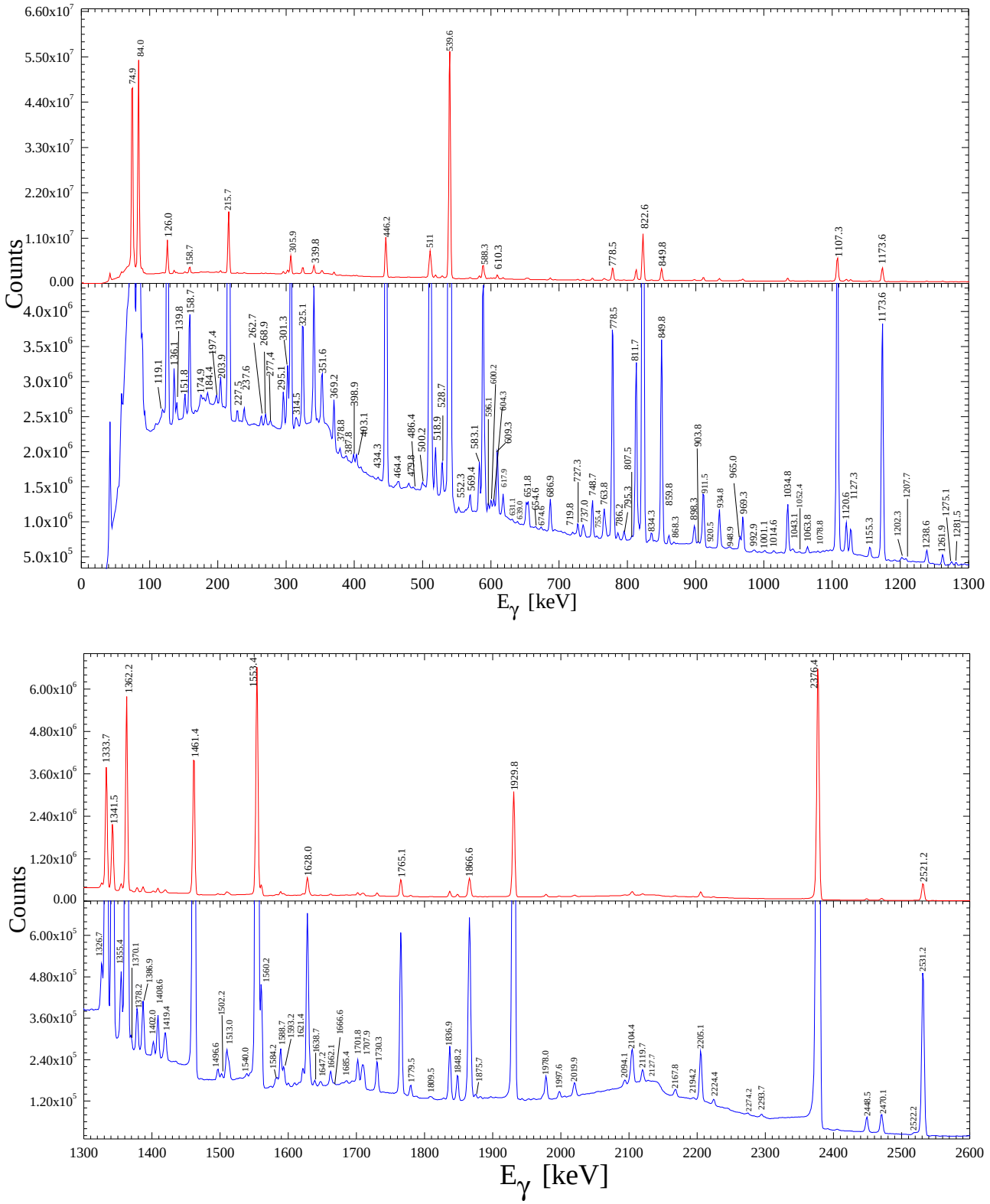

Figure 7.6. Portion of the total singles spectrum obtained in this measurement. The bottom panel (blue) has an expanded y-scale to illustrate the peaks that are located at "grass-level."

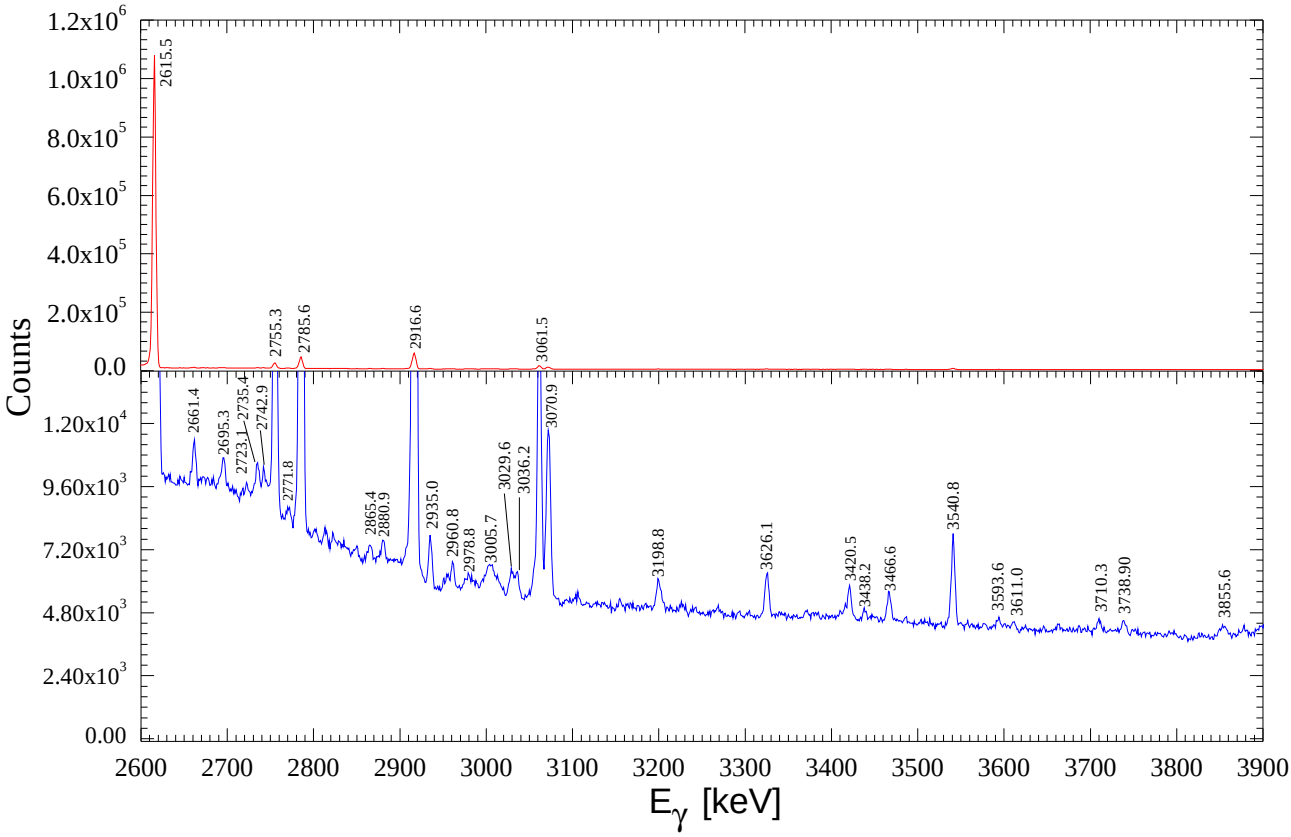

Figure 7.7. The final portion of the total singles spectrum obtained in this measurement. The bottom panel (blue) has an expanded y-scale to illustrate the peaks that are located at "grass-level."

7.3.1 ^{100}Ru Spectrum Analysis

A γ-γ matrix was created by following the steps discussed in section 6.5.2. Figure 7.8 shows the total energy projection from the 2D γ-γ matrix.

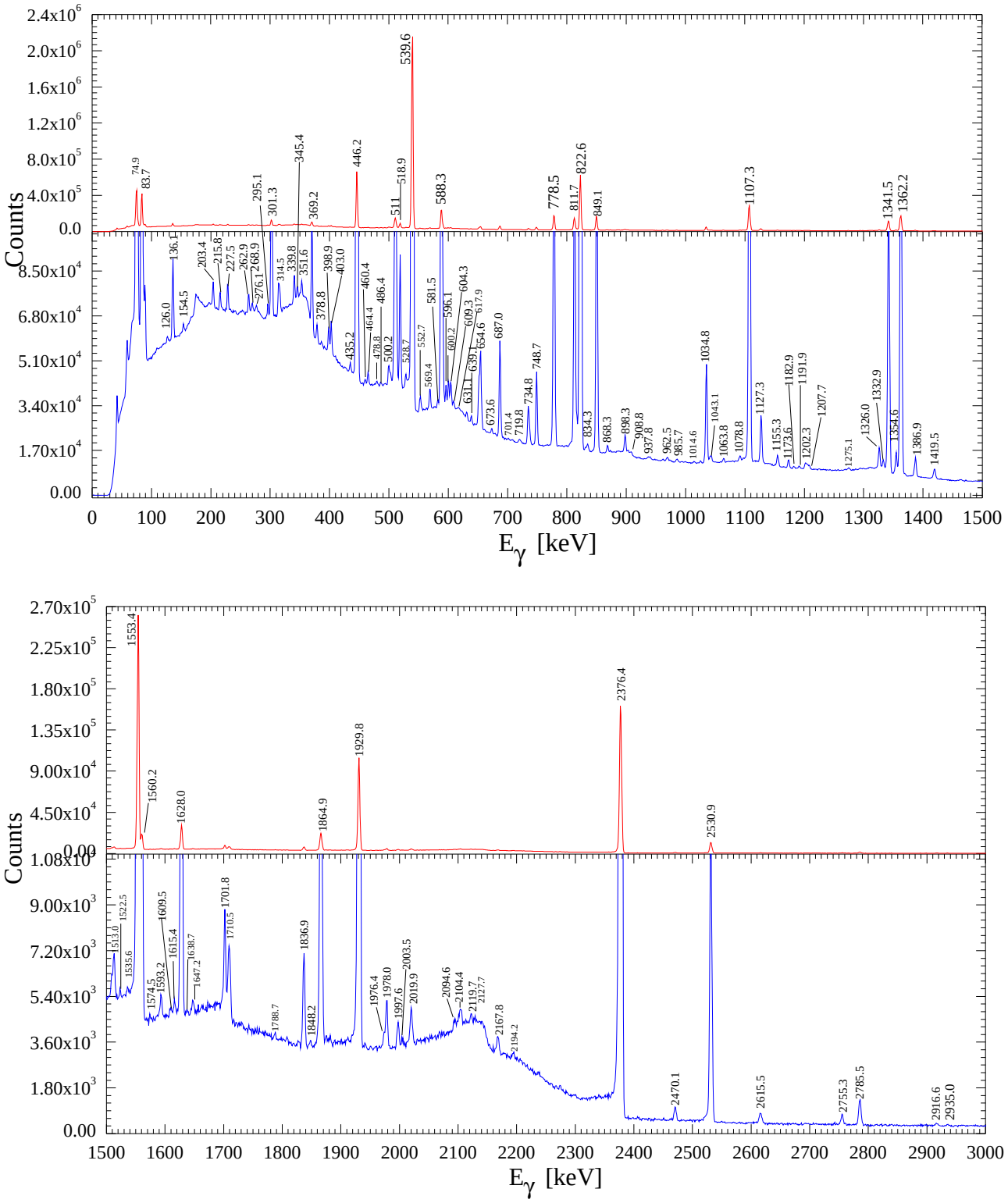

Figure 7.8. The total projection spectrum obtained from 2D γ-γ-matrix. The bottom panel (blue) has an expanded y-scale to illustrate γ-rays located at "grass-level."

Using the γ-γ matrix and gating on the strongest transition of ^{100}Ru, the 540 keV $2^+ \rightarrow 0^+$ transition, the spectrum shown in figure 7.9 was obtained, and it confirms the same γ-rays seen earlier [73, 122].

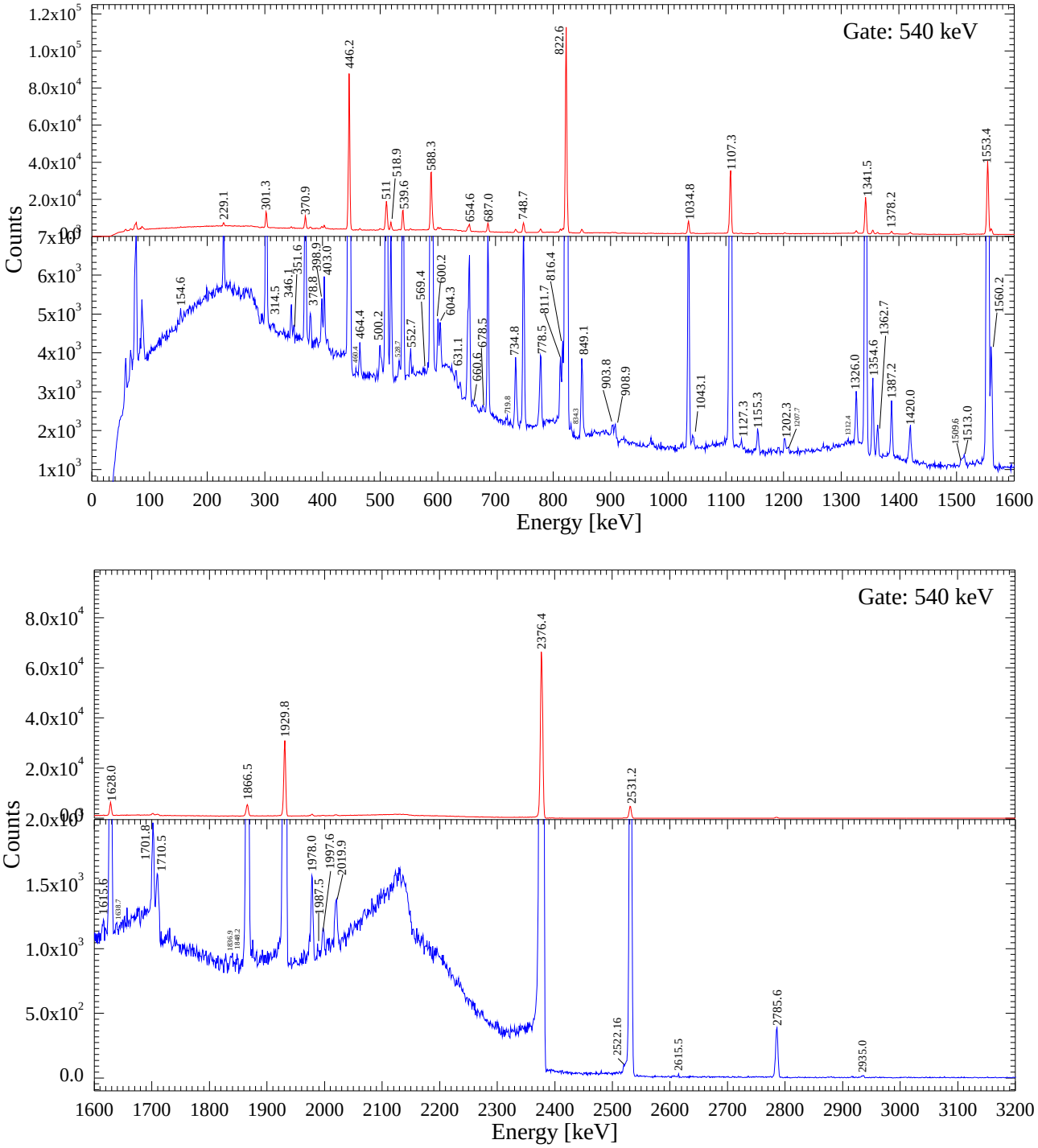

Figure 7.9. Coincidence spectrum obtained by gating on the 540 keV γ-ray. The bottom panel (blue) has an expanded y-scale to illustrate γ-rays located at "grass-level".

A gate was set on the γ-γ-coincidence matrix on the $2^+ \rightarrow 2^+$ transition at 823 keV to obtain the spectrum shown in figure 7.10. The spectrum confirms the γ-rays observed by Garabed Kenchians [74].

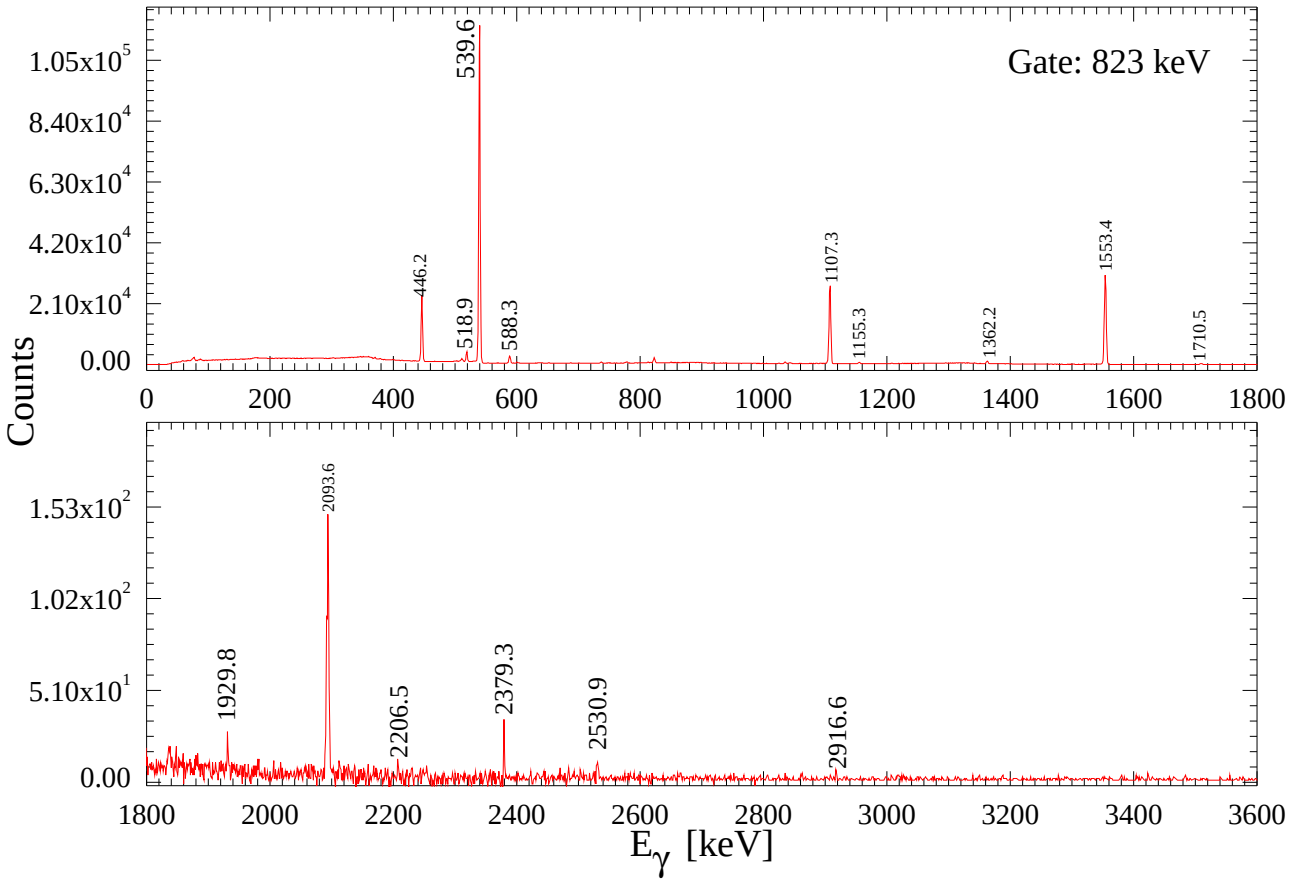

Figure 7.10. Coincidence spectrum obtained by gating on the 823 keV γ-ray.

In search of new γ-rays, another gate was set on the $2^- \rightarrow 2^+$ transition (446.2 keV) the resulting spectrum in shown in figure 7.11. These results only confirmed the previous studies of ^{100}Ru, as no new low-lying γ-rays are observed.

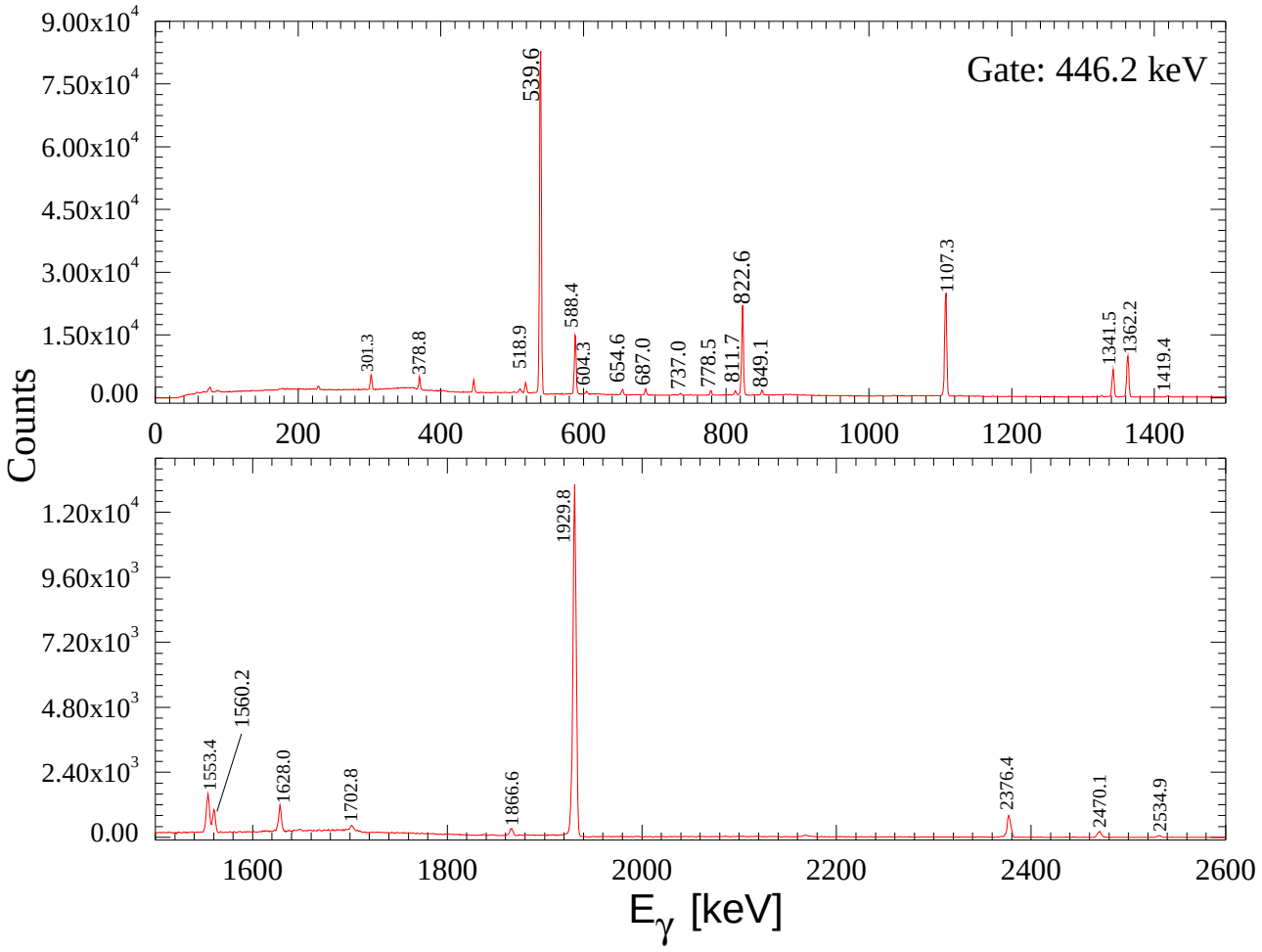

Figure 7.11. Coincidence spectrum obtained by gating on the 446.2 keV γ-ray.

7.4 Level Scheme of ^{100}Ru

The γ-γ matrix was used to build the level scheme of ^{100}Ru. Figure 7.12 and 7.13 shows the fully developed level scheme of ^{100}Ru deduced from this work and it was constructed from the analysis of both γ-γ coincidences matrix and γ-ray singles. The spin assignments were taken from [67, 68].

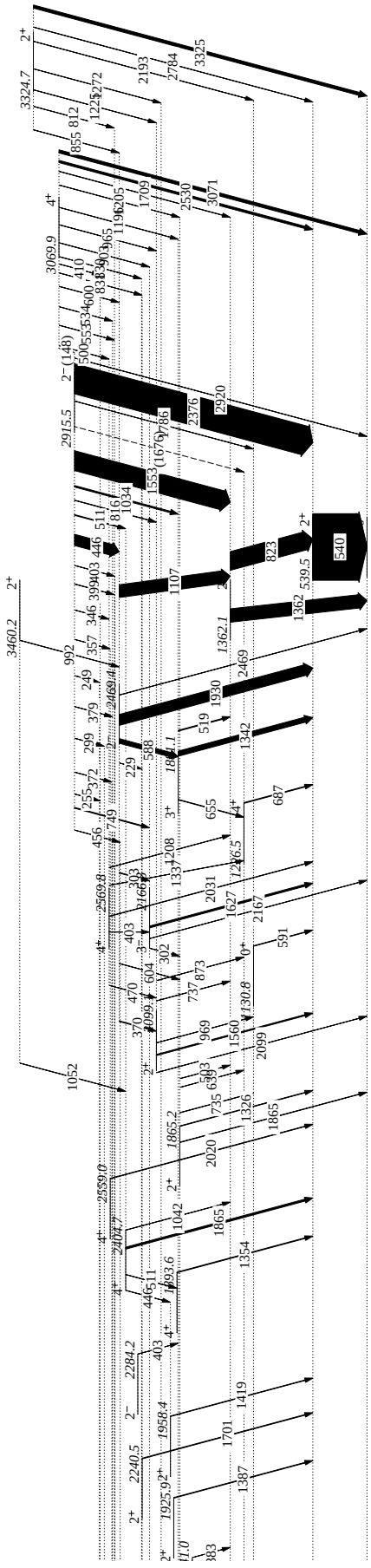

Figure 7.12. Constructed level scheme of ^{100}Ru. Thickness of transition arrows indicates their intensities. The spin assignment was taken from [67, 68].

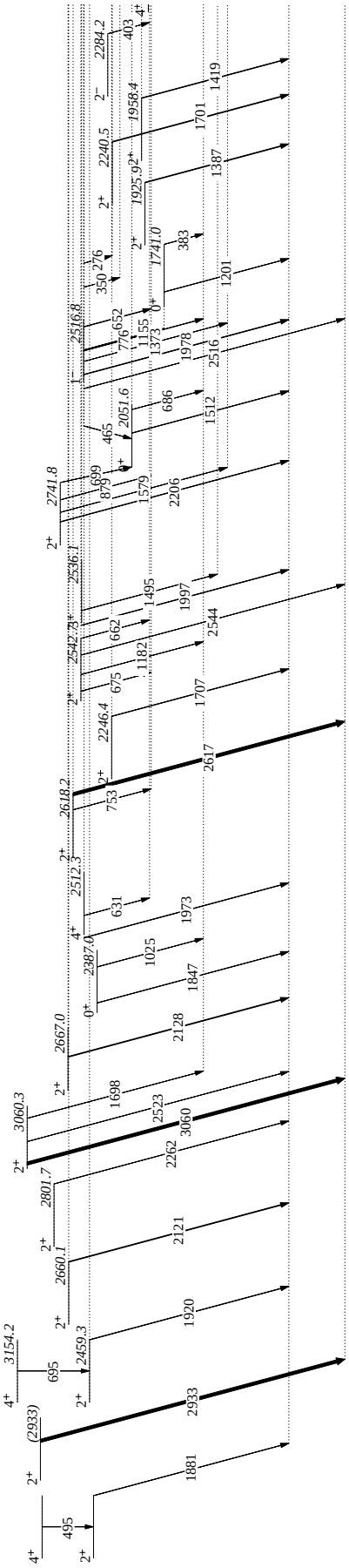

Figure 7.13. Constructed level scheme of ^{100}Ru. Thickness of transition arrows indicates their intensities. The spin assignment was taken from [67, 68].

The β-decay measurement only populates low spin states to a certain energy, and if a particular nucleus has been intensively studied, like ^{100}Ru, see figure 7.1 to 7.5, it is difficult to observe new γ-rays. We could not add more to the available data but we populated all the previously observed levels and γ-rays seen in figure 7.1 to 7.5 and in reference [68, 73]. For example, figure 7.9, 7.10, 7.11 gated on the 540 keV, 822 keV, and 446 keV transitions, respectively, show no new lines. Figure 7.14 shows a partial level scheme of ^{100}Ru demonstrating the states relevant to the vibrational structure as shown in section 2.3.2, figure 2.10, which shows the first, and second phonon states and the ground-, β- and γ-bands, as will be discussed.

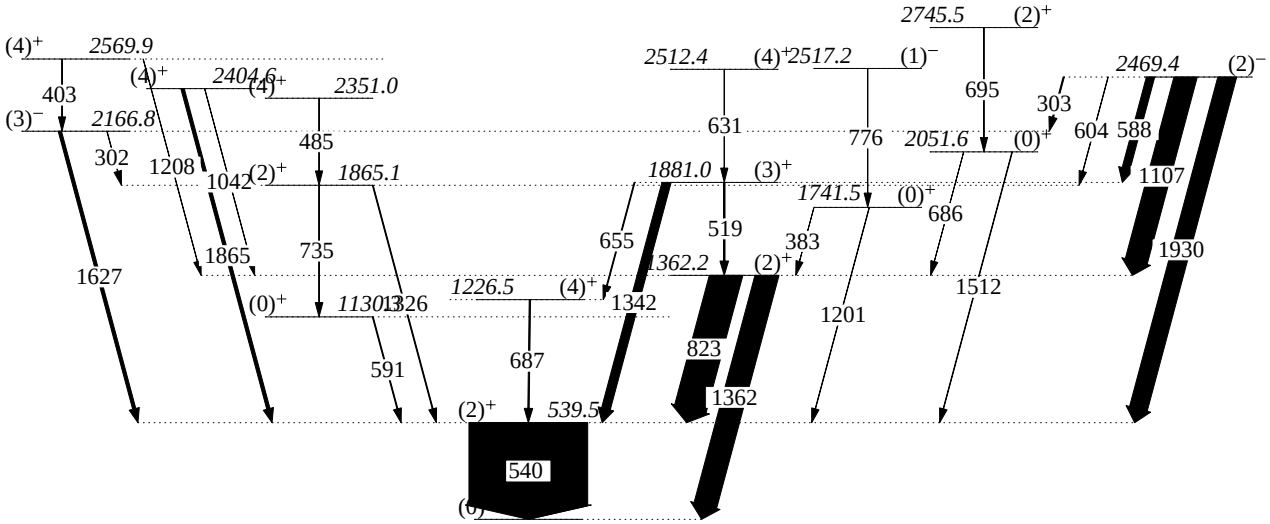

Figure 7.14. Partial level scheme of ^{100}Ru obtained from the β-decay of ^{100}Rh. The full level scheme is shown in figure 7.12 and 7.13.

7.5 Conversion Electron Analysis

This section presents conversion electrons observed in this measurement. Conversion electrons from other strong reaction channels were also observed and "usually" they came from the $2^+ \rightarrow 0^+$ transitions.

7.5.1 Observed Conversion electrons

Figure 7.15 shows the singles conversion electron spectrum obtained in this measurement. The conversion electrons come from all reaction channels open in this measurement, and mostly only K and L electron lines were observed.

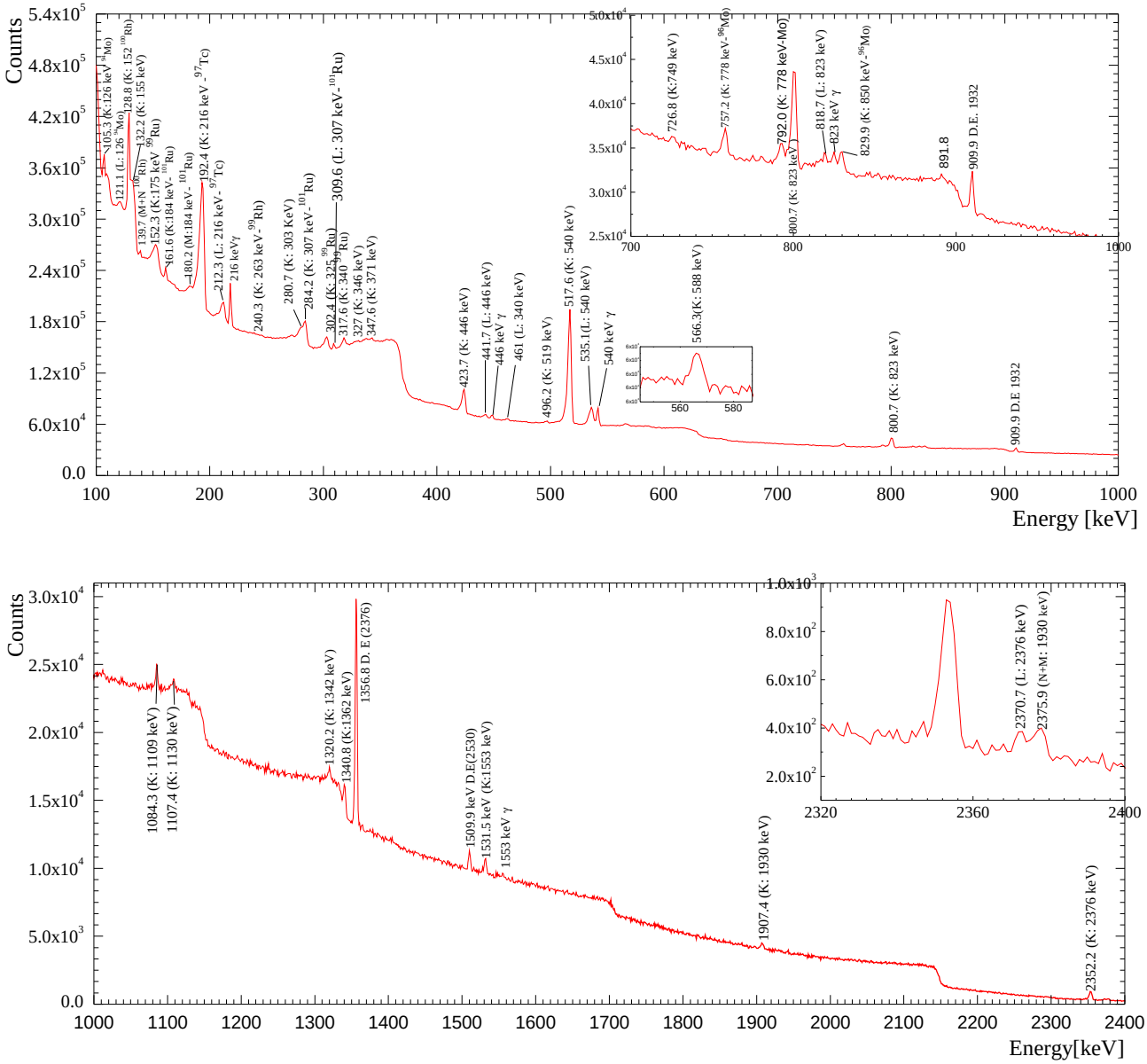

Figure 7.15. Observed conversion electrons in ^{100}Ru measurement. The label D.E. indicates the Double Escape peak of the 2376-keV, $2^- \rightarrow 2_1^+$ γ transition.

The large background in figure 7.15 is due to the presence of the β^+-particles in the Si(Li) detector, as well as Compton-scattered γ-rays and noise from the stepper motor. The label D.E. peak in figure 7.15 indicates the Double Escape peak of the 2376-keV, $2^- \rightarrow 2_1^+$ and 1931 keV, $2^- \rightarrow 2_1^+$ γ-transition [123]. Table 7.1 lists the observed conversion electrons visible in figure 7.15 from the ^{100}Ru measurement. Conversion electrons from other reaction channels were observed as well, such as ^{96}Mo, ^{97}Tc, ^{99}Ru, ^{99}Rh, and ^{101}Ru.

Table 7.1. Conversion electron (C.E.) observed in figure 7.15.

C.E. E_{CE} [keV]	Shell	E_γ [keV]	Parent Nucleus
105.3	K	125.8	^{95}Mo
121.1	L	125.8	^{95}Mo
128.8	K	151.8	^{100}Rh
132.2	K	154.0	^{100}Ru
139.7	M+N	151.8	^{100}Rh
152.3	K	175.4	^{99}Ru
161.6	K	179.6	^{101}Ru
180.2	K	184.1	^{101}Ru
192.4	K	215.7	^{97}Tc
212.3	L	215.7	^{97}Tc
240.3	K	263.6	^{99}Rh
280.7	K	302.4	^{100}Ru
284.2	K	306.9	^{101}Ru
302.4	K	325.2	^{101}Ru
309.6	L	306.9	^{101}Ru
317.6	K	340.8	^{99}Ru
327.4	K	345.6	^{100}Ru
347.6	K	370.3	^{100}Ru
423.7	K	446.2	^{100}Ru
441.7	L	446.2	^{100}Ru
461.3	L	470.9	^{100}Ru
496.2	K	518.9	^{100}Ru
517.6	K	539.6	^{100}Ru
535.1	L	539.6	^{100}Ru
566.3	K	588.3	^{100}Ru
588.3	K	610.3	^{100}Ru
726.8	K	748.7	^{100}Ru
757.2	K	778.5	^{96}Mo
791.8	K	810.3	^{96}Mo
800.7	K	822.6	^{100}Ru
818.7	L	822.6	^{100}Ru
829.1	K	849.8	^{96}Mo
1084.3	K	1107.3	^{100}Ru
1107.4	K	1130.2	^{100}Ru
1320.6	K	1341.5	^{100}Ru
1340.8	K	1362.2	^{100}Ru
1531.5	K	1553.4	^{100}Ru
1907.4	K	1929.8	^{100}Ru
2352.2	K	2376.3	^{100}Ru
2370.7	L	2376.3	^{100}Ru
2375.9	(N+M)	2376.3	^{100}Ru

7.5.2 Extraction of Internal Conversion Coefficients

The Internal Conversion Coefficient (ICC) is the ratio of electron emission rate to γ-ray emission rate. Therefore, the ICC is calculated as follows:

$$\alpha_{exp} = \frac{N_e}{N_\gamma} \cdot \frac{\varepsilon_\gamma}{\varepsilon_e} \tag{7.1}$$

where N_e and N_γ are the number of detected conversion electrons and γ-rays, respectively, while $\frac{\varepsilon_e}{\varepsilon_\gamma}$ is the relative efficiency deduced in section 7.5.3. The ICC depends on a number of multiple factors such as the multipole order of the transition, electric or magnetic nature of the transition, transition energy, and the Z of the nucleus in which the transition occurs, the shell or sub-shell from which the electron is ejected.

7.5.3 Efficiency calibration of the Si(Li) Detector

The internal efficiency calibration of the Si(Li) detector was performed during data analysis. An internal efficiency calibration of the Si(Li) detector was deduced by using known E1 and E2 transitions in the present study, and then combined with ^{207}Bi source data. The following γ-ray lines were used for internal calibration 539.5 keV (E2), 588.3 keV (E1), 1107.3 keV (E1), 1929.8 keV (E1) and 2376,3 keV (E1) from ^{100}Ru and the strongest of ^{207}Bi : 569.7 keV, 1063.7 keV and 1770.2 keV. The relative efficiency curve for the Si(Li) detector shown in figure 7.16, was deduced by using the know α_K conversion coefficients obtained from BRICC [124, 125].

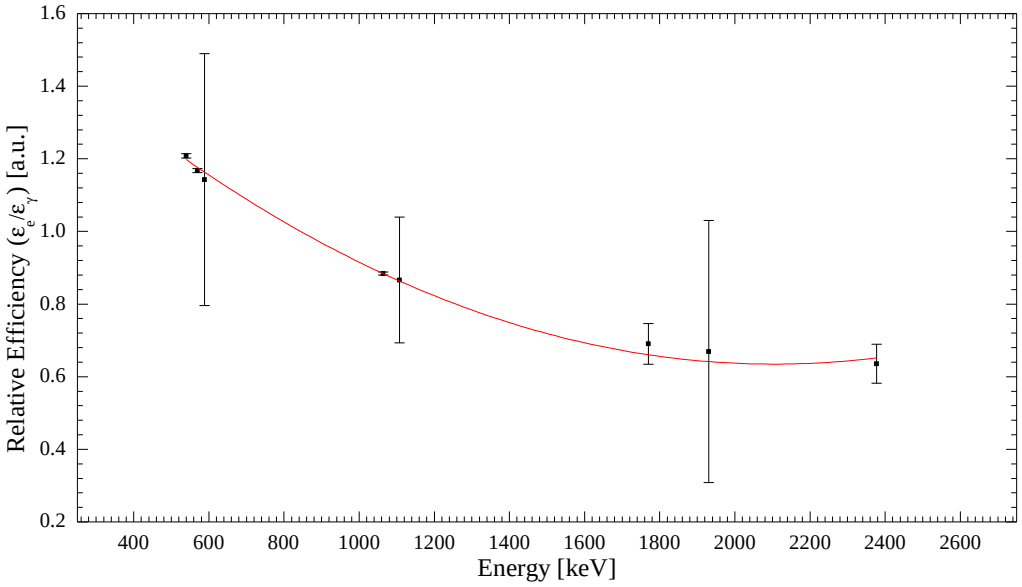

Figure 7.16. Relative Efficiency extracted for the Si(Li) data using results from known E1and E2 transitions from ^{100}Ru and ^{207}Bi.

7.5.3.1 ICC

Clearly observed conversion electrons in ^{100}Ru are shown in figure 7.15 were used to extract ICC's. Only K-conversion electrons were used for ICC calculations because they were well-resolved from other multipolaliry conversion electrons and γ-rays. The measured ICC's for ^{100}Ru are presented in table 7.2 where they are compared with the theoretical ICC from BRICC [124]. Measured ICCs are usually used to determine transition multipolarities and thereafter deduce the spin and parity of the state involved [126]. However, since no new γ-ray(s) were observed in ^{100}Ru, only a comparison is made.

Table 7.2. Measured Internal Conversion Coefficient for K transition, $M\lambda$ is the multipolarity of the transition taken from [13], * conversion electron were used for calibration in section 7.5.3.

E_γ [keV]	E_{CE} [keV]	Measured ICC[10^{-3}]	BRICC [10^{-3}]			$I_i^\pi \rightarrow I_f^\pi$	Assignment
			M1	E2	E1		
446.2	423.7	5.39(9)	5.37	6.53	1.95	$2^- \rightarrow 2^-$	M1
518.9	496.2	4.07(5)	3.75	4.19	1.36	$3^+ \rightarrow 2^+$	E2
*539.6	517.7	3.72(6)	3.39	3.72	1.23	$2^+ \rightarrow 0^+$	E2
*588.3	566.3	1.01(4)	2.78	2.93	1.01	$2^- \rightarrow 3^+$	E1
748.7	725,8	1,53(12)	1.59	1.55	0.59	$2^- \rightarrow 3^-$	M1/E2
822.6	800.7	1.17(4)	1.29	1.22	0.49	$2^+ \rightarrow 2^+$	E2
*1107.3	1084.3	0.28(7)	0.68	0.62	0.28	$2^- \rightarrow 2^+$	E1
1342.5	1320.6	0.41(14)	0.45	0.41	0.19	$3^+ \rightarrow 2^+$	M1/E2
1362.2	1340.8	0.34(5)	0.43	0.40	0.19	$2^+ \rightarrow 0^+$	E2
1553.4	1531.5	0.12(7)	0.33	0.31	0.15	$2^- \rightarrow 2^+$	E1
*1929.8	1907.4	0.11(11)	0.22	0.20	0.11	$2^- \rightarrow 2^+$	E1
*2376.3	2352.2	0.08(10)	0.14	0.14	0.08	$2^- \rightarrow 2^+$	E1

To make sure that all peaks were accounted for in ^{100}Ru data set, a Si(Li)-clover matrix was created, i.e conversion electron-γ-ray matrix. Thereafter, a gate was set on particular γ-rays or conversion electron transitions. For example, a gate was set on the 517 keV conversion electron, and the coincident γ-ray spectrum is shown in figure 7.17.

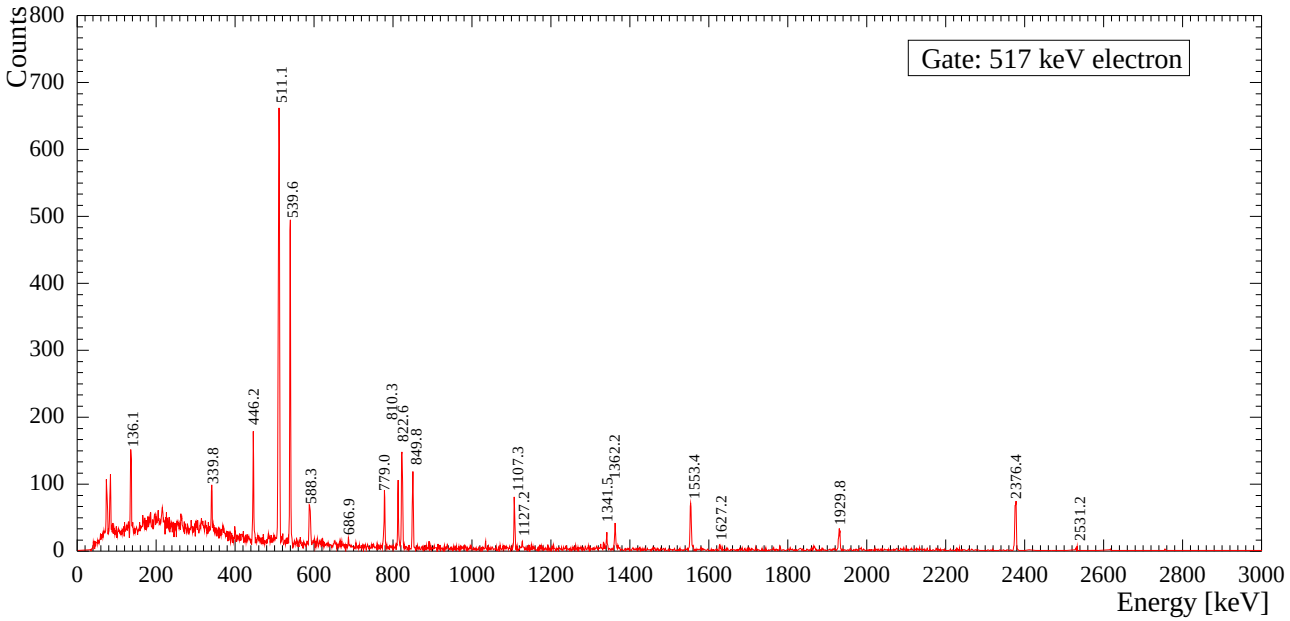

Figure 7.17. Gamma-ray spectrum obtained when gating on the 517 keV K-electron.

The most dominant peak in figure 7.17 is the 511 keV line coming from annihilation process, and 540 keV γ-ray ($2^+ \rightarrow 0^+$). To obtain the 517 keV conversion electron spectrum, a gate was set on a γ-ray feeding the 540 keV transition i.e. 823 keV γ-ray, and figure 7.18 was obtained.

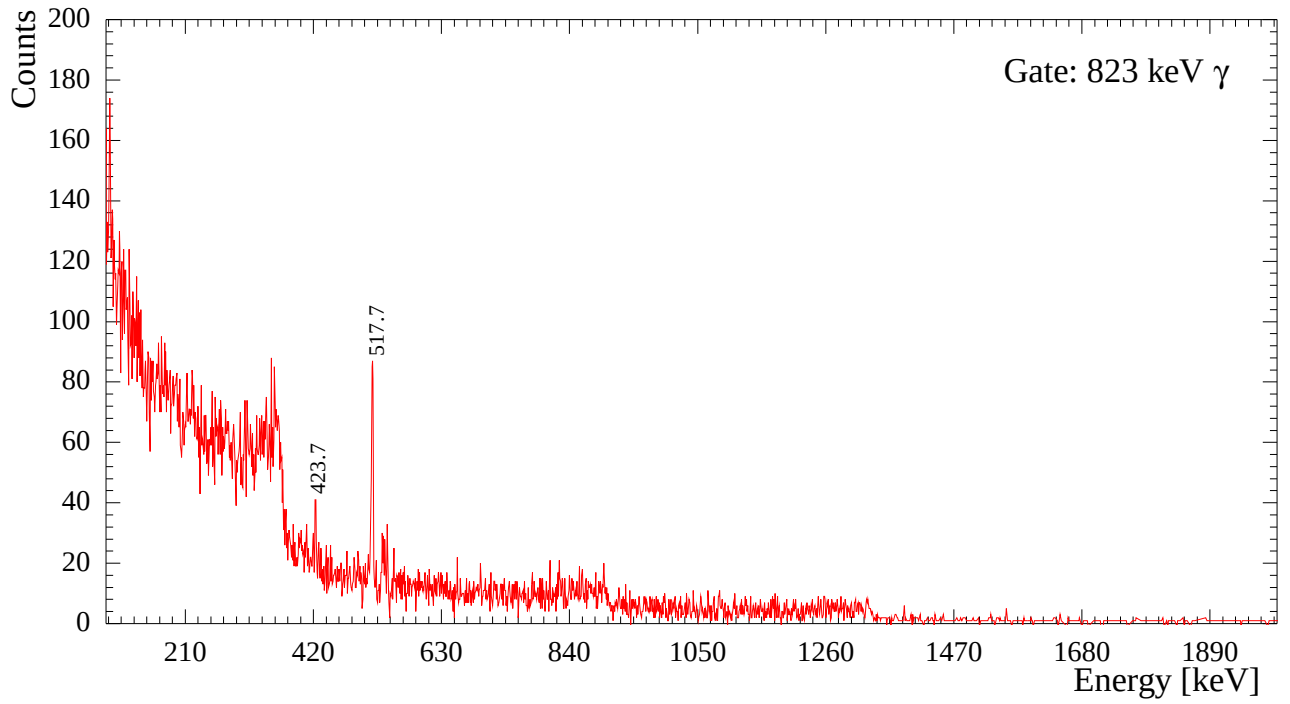

Figure 7.18. Conversion electron spectrum obtained when gating on the 823 keV γ-ray.

In figure 7.18, these visible conversion electrons come from the γ-rays: 446 keV (K: 423.3) and

540 keV (K: 517 keV). Gating on the $2^+ \rightarrow 0^+$ γ-ray transition 540 keV, conversion electrons associated with γ-rays feeding the 2^+ level are observed. Figure 7.19 shows the observed conversion electrons. These conversion electrons are associated with the γ-rays: 446 keV (K: 422.7), 823 keV (800.7 keV) and the 1356.3 keV γ-ray, the double escape peak from the 2376 keV transition.

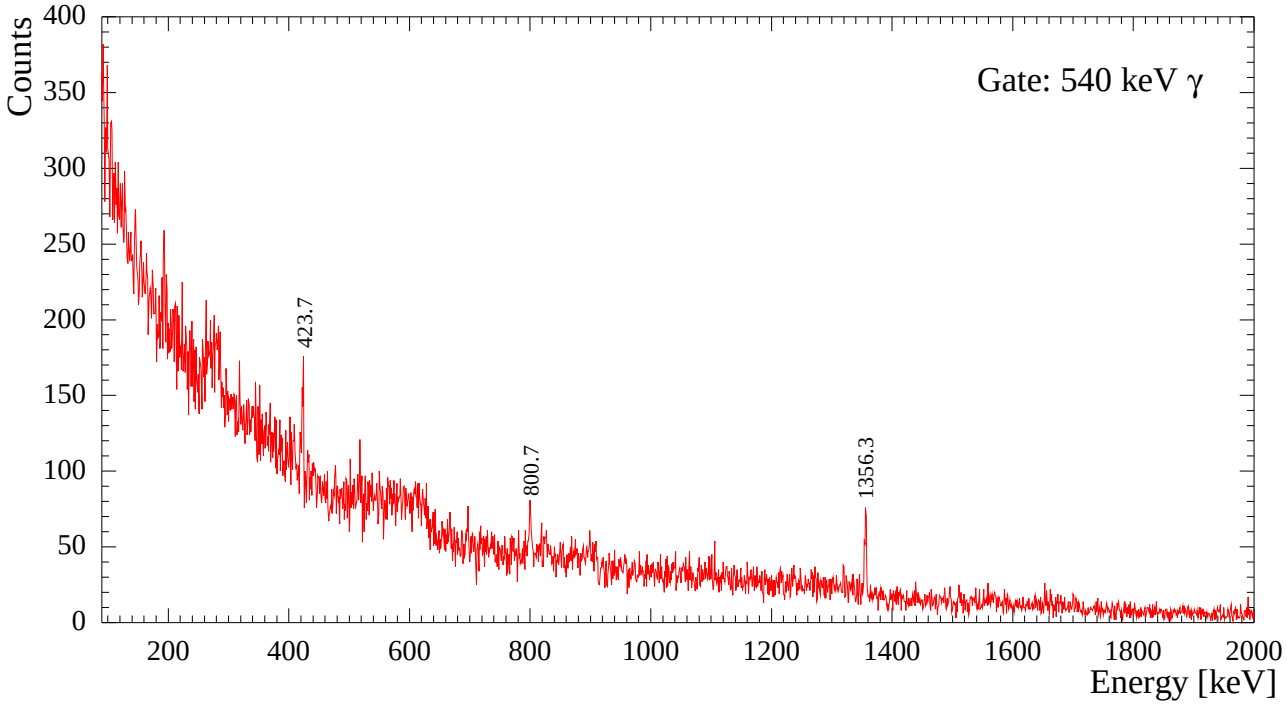

Figure 7.19. Conversion electron spectrum obtained when gating on the 540 keV γ-ray.

A gate was set on the 591 keV γ-ray to search for the conversion electrons associated with transitions feeding the 0_2^+ level. The resulting spectrum is shown in figure 7.20.

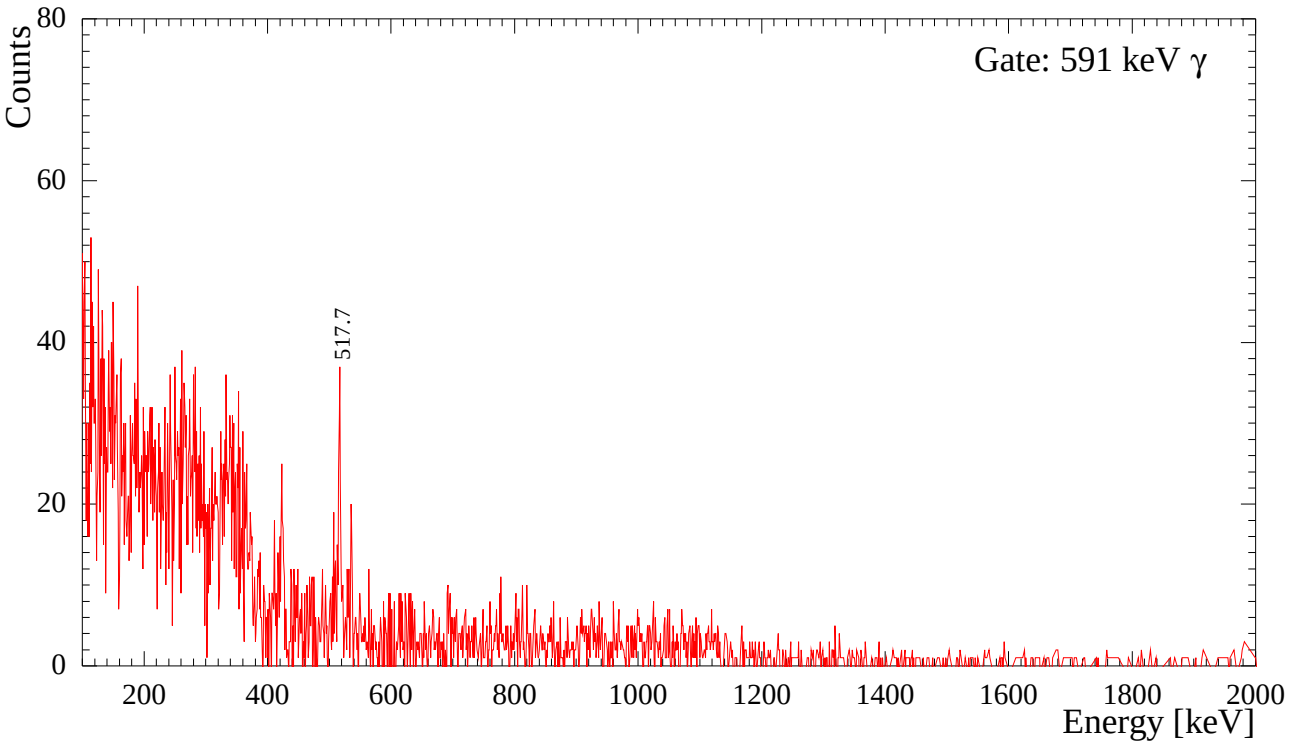

Figure 7.20. Conversion electron spectrum obtained by gating on the 591 keV transition on the conversion electron-γ-rays matrix.

In figure 7.20, only the conversion electron peak arising from the 540 keV (K: 517 keV) γ-ray is visible.

7.5.4 Observed E0 component in ^{100}Ru

Figure 7.21(a) shows the level scheme illustrating the decay of the $0_2^+ \rightarrow 0_1^+$ E0 transition in ^{100}Ru. This transition has been observed in singles spectrum in this measurement and can be seen in figure 7.21(b), an expanded portion of figure 7.15. The 1108 keV peak corresponds to the 1130 keV $0_2^+ \rightarrow 0_1^+$ transition. Also present in the spectrum are the 1085 keV and 1104 keV K and L electron from the 1107 keV $2^- \rightarrow 2^+$ transition. The binding energy of the K-shell electron is 22.12 keV.

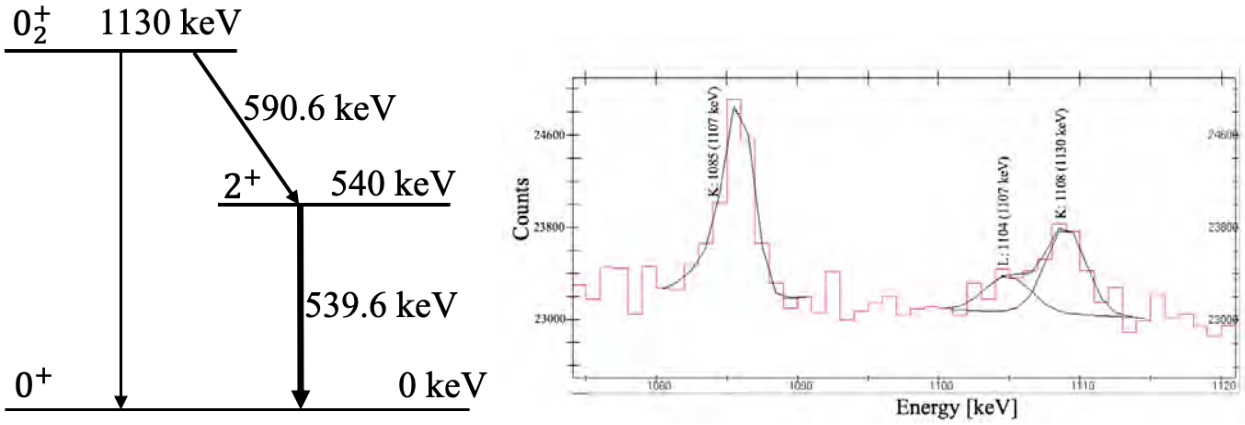

(a) (b)

Figure 7.21. The observed E0 transition in this measurement. The 1108 keV: $0_2^+ \rightarrow 0_1^+$ conversion electron is observed.

The monopole transition strength can be determined experimentally by measuring the absolute transition rate and calculating the electric factor according to using equation 2.45 and 2.46 and it can be rearranged and written as:

$$\rho^2(E0) = \frac{I_{eK}(E0)}{I_{eK}(E2)} \frac{\lambda_\gamma(E2)\alpha_K(E2)}{\Omega} \tag{7.2}$$

where $I_{eK}(E0)$ and $I_{eK}(E2)$ indicates the electron intensity of the E(0) and (1130.2 keV) and E2 (590.6 keV) transitions, respectively, $\alpha_K(E2)$ is the conversion coefficient, Ω is the electronic factor taken from BRICC [124] and $\lambda_\gamma(E2)$ is absolute transition probability. The λ_γ(E2) is deduced by using the adopted value of the half-life (8.2 ps) of the 1130 keV level [42]. To determine $I_{eK}(E0)$,the spectrum displayed in figure 7.21(b) was fitted with two peak as shown. However, the Si(Li) detector directly faced the source of activity as shown in figure 6.44, which resulted in γ-rays depositing their energy in the detector, notably for strong γ-ray transition.

The characteristic of electron lines is the tail on the low energy side of the peak. The γ-ray lines were easily identified on the Si(Li) spectrum because they do not possess the tails. For example, the 540 keV γ-ray is labelled in figure 7.15. Unfortunately, in the figure 7.21(b) the two peaks obscure an important contribution from the 1107 keV γ-ray. This contribution was estimated from the ratio of γ-ray counts in the Si(Li) spectrum (figure 7.15) to the singles γ-ray spectrum (figure 7.6 and 7.7) of the 823 keV and 1553 keV γ-ray, interpolated for the 1107 keV γ-ray. After subtracting this contribution, a value of $\rho(E0)$ 0.17 $\pm$0.04 is deduced, agree with a value from Kibédi and Spear [42], of $\rho(E0)$= 0.10$\pm$0.02

7.6 ^{98}Ru experiment results

This section presents experimental results obtained from the ^{89}Y(^{12}C, 3n)^{98}Rh experiment, analyzed by Professor P. E. Garrett and his team. The level scheme is shown in figure 7.22, where new transitions are highlighted in red.

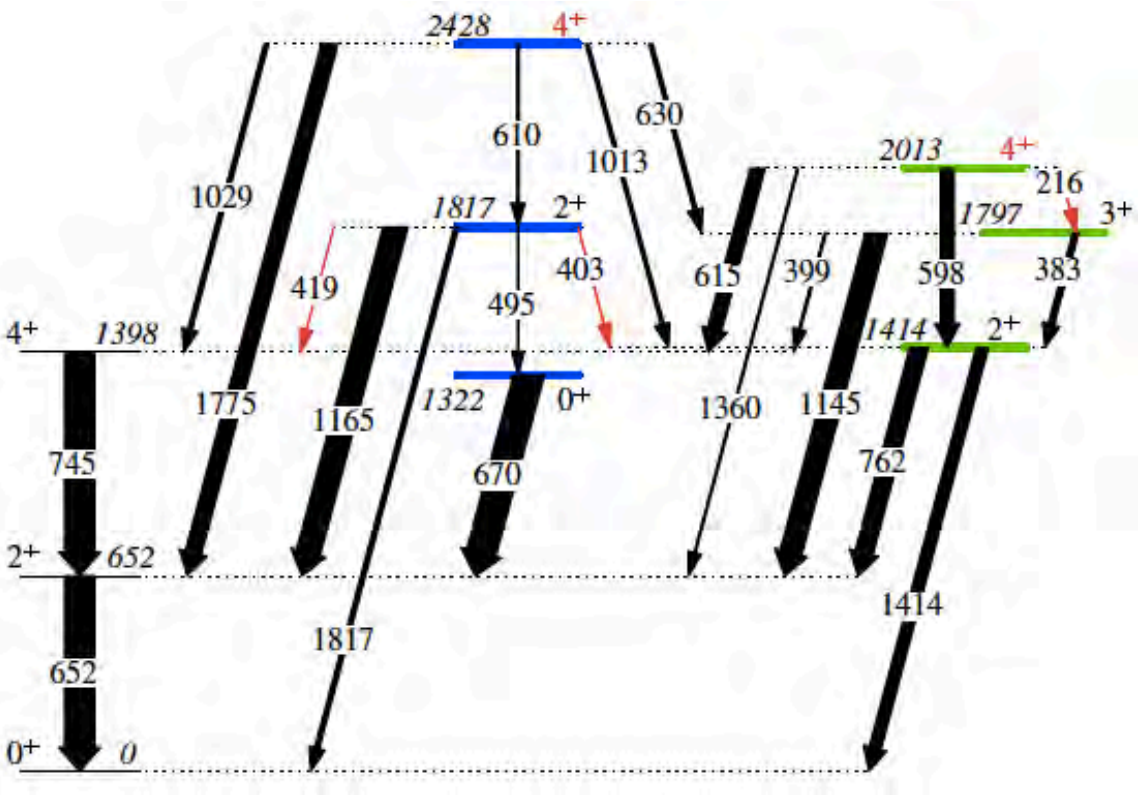

Figure 7.22. Partial level scheme of ^{98}Ru displaying the 0_2^+ and the γ band assigned in the present work. New γ-rays are highlighted in red. The transitions are labelled with their energies in keV, and the widths of the arrows are proportional to the measured branching ratios [127].

Figure 7.23 shows the portion of the spectrum obtained from the γ-γ coincidences that confirms the placement of the 495 keV transition [66] decaying from the 2_3^+ level, at 1817 keV to the 0_2^+ state at 1322 keV, and also a newly observed 419 keV γ-ray decaying from the 2_3^+ level, to the 4_1^+ state.

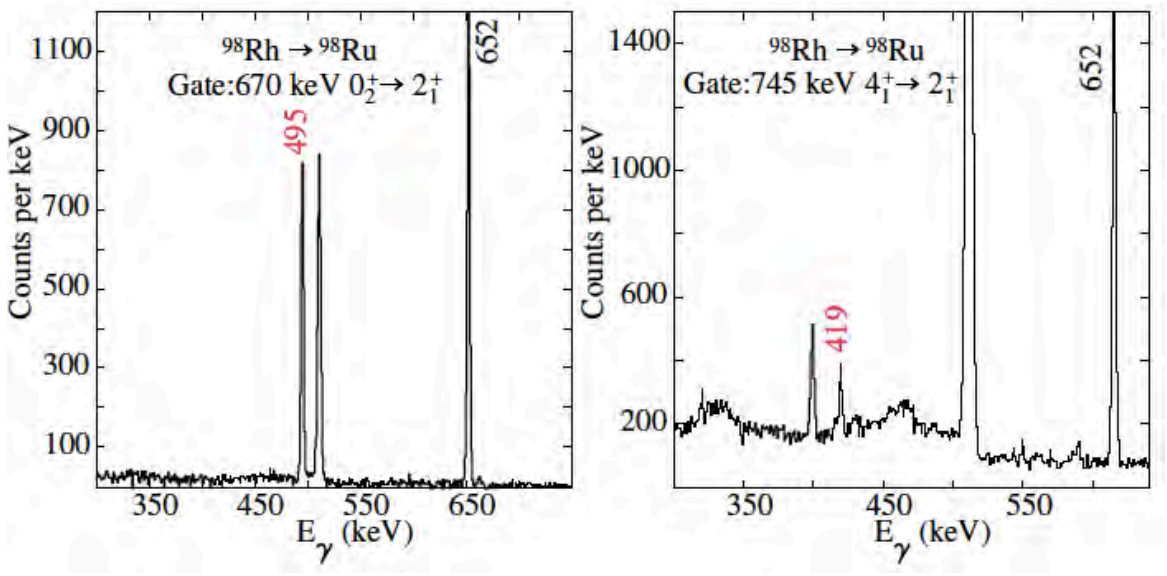

Figure 7.23. Spectrum showing newly observed γ-rays for ^{98}Ru in the present data. Gating placed on the 670 keV γ-ray decay (left) from the 0_2^+ state, confirms the placement of the 495 keV γ-ray by [66] as the $2_3^+ \rightarrow 0_2^+$ transition, and on the 745 keV $4_1^+ \rightarrow 2_1^+$ γ-ray decay on the right, indicating the newly assigned 419 keV $2_3^+ \rightarrow 4_1^+$ γ-ray transition [127, 128].

Figure 7.24(a) shows the portion of the spectrum of γ-rays in coincidence with the 762 keV $2_2^+ \rightarrow 2_1^+$ γ-ray indicating the presence of the newly observed 403 keV γ-ray depopulating the 1817 keV level, as shown in the partial level scheme in figure 7.22. With the observed γ-ray transition to the $0_{1,2}^+$ and 4_1^+ levels, the spin and parity of the 1817 keV state assigned in reference [66] as the 2_3^+ level, is confirmed. Another newly observed γ-ray is shown in figure 7.24(b), the 216 keV γ-ray is observed from the decay 2013 keV level as shown in the level scheme in figure 7.22.

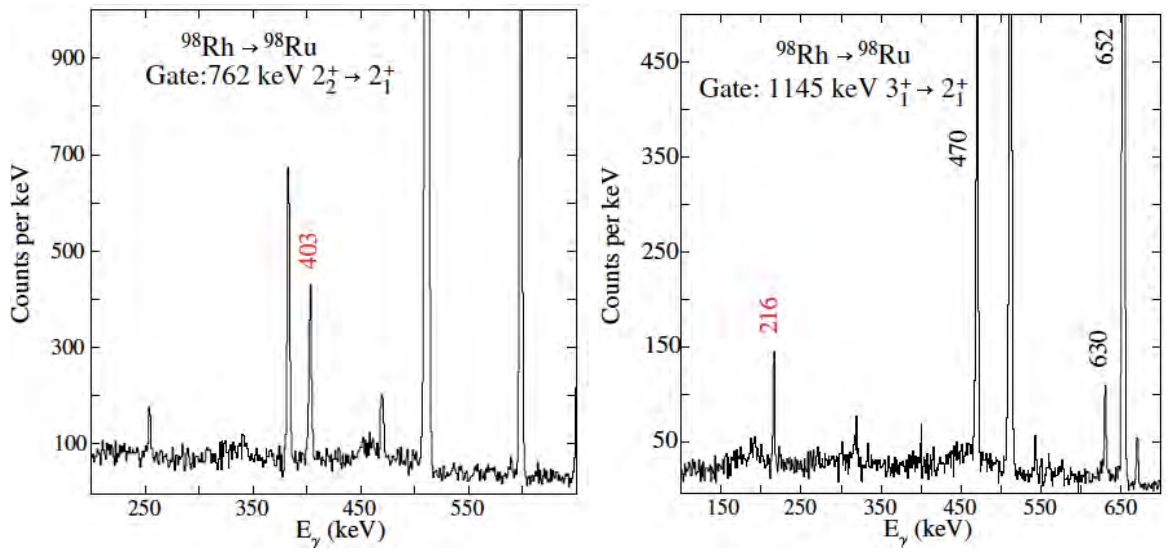

(a) (b)

Figure 7.24. Spectrum showing newly observed γ-rays in ^{98}Ru measurement. Spectrum (a) was created with a gate placed on the 762 keV $2_2^+ \rightarrow 2_1^+$ transition. The newly-observed 403 keV γ-ray from the 2_3^+ level is indicated. While spectrum (b) is the result from a coincidence condition with the 1145 keV $3_1^+ \rightarrow 2_1^+$ γ-ray, with the newly observed 216 keV γ-ray placed as the 2013 keV $4^+ \rightarrow$ keV 1797 3_1^+ transition [127, 128].

The spin of the 2013 and 2428 keV levels were determined in the another complimentary experiment: ^{100}Ru(p,t) two-neutron-transfer reaction [127, 128]. With the new spin assignments, the level scheme displayed in figure 7.22 strongly suggests the presence of a band based on the 0_2^+ level at 1322 keV, and also a γ-band based on the 2_2^+ level at 1414 keV. (We use the label "γ-band" to indicate the $\Delta I = 1$ sequence built on the 2^+ state, irrespective of its underlying character.) The key to these suggested bands are the re-assignments of the spins of the 2428-keV and 2013-keV levels to 4^+.

Chapter 8

Interpretation of the experimental results

8.1 Introduction

This chapter interprets results of the two experiments that were performed, ^{98}Ru and ^{100}Ru, from the β-decay of ^{98}Rh and ^{100}Rh, respectively. To make a good assessment of the collected data at low-excitation energy with the predicted theory, it was essential that no levels were missed during analysis.

The new spin assignments of 4^+ to the 2428 keV and 2013 keV levels of ^{98}Ru, allow the level scheme (figure 8.1) to be displayed in a way that strongly suggests the presence of a band based on the 0_2^+ level at 1322 keV, and also a band based on the 2_2^+ level at 1414 keV. Shown in figure 3.5 are the level schemes of $^{96-106}$Ru, arranged as 0_1^+ , 0_2^+ , and γ-bands. It can be seen that the newly assigned band structures in ^{98}Ru fit into the systematics well. The bands display a very smooth evolution as a function of neutron number, with the maximal staggering of the γ-band observed in ^{100}Ru [128]. The 5_1^+ state in ^{98}Ru was too weakly populated in the present experiment to permit observation of its in-band decay, and thus its assignment is based only on the energy systematics.

Another way to present the energy systematics is on a plot of Energy (less a rigid-rotor reference) vs spin, as is done in figure 8.2 below.

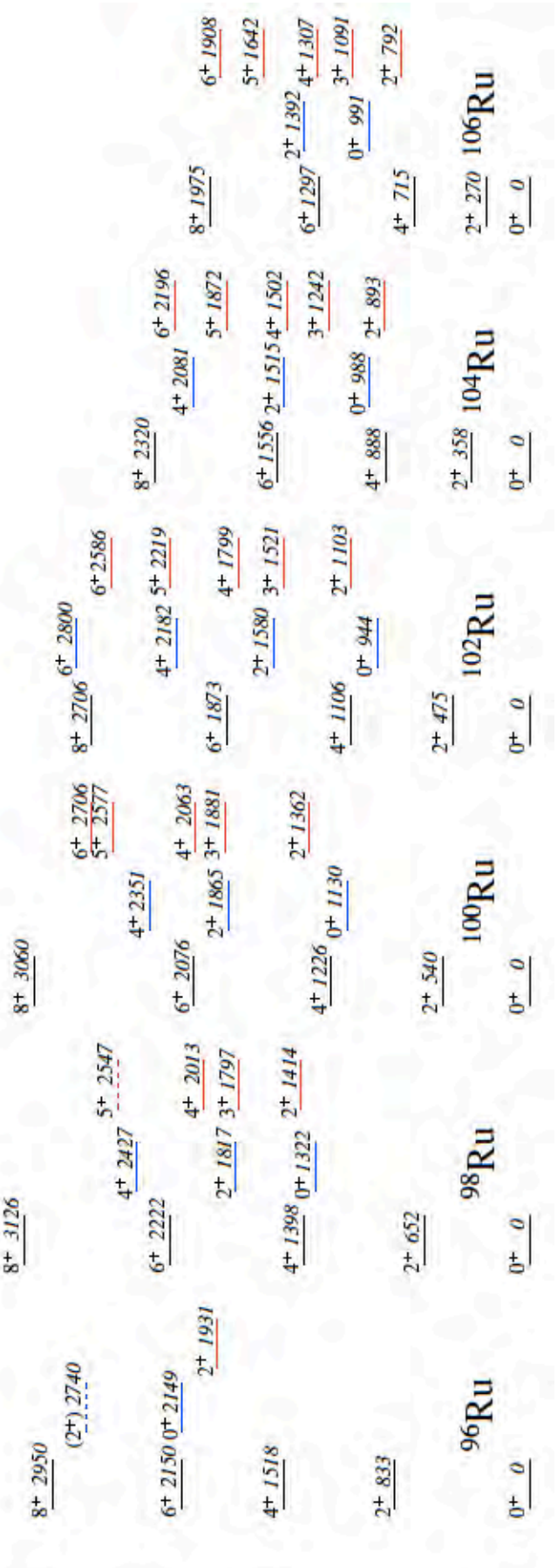

Figure 8.1. Partial level schemes of the even Ru isotopes from A = 96 to A = 106 displaying the ground-state bands, 0_2^+ bands, and bands observed experimentally, extracted from reference [13] and the results of the present work. The levels are labeled with their energies in keV.

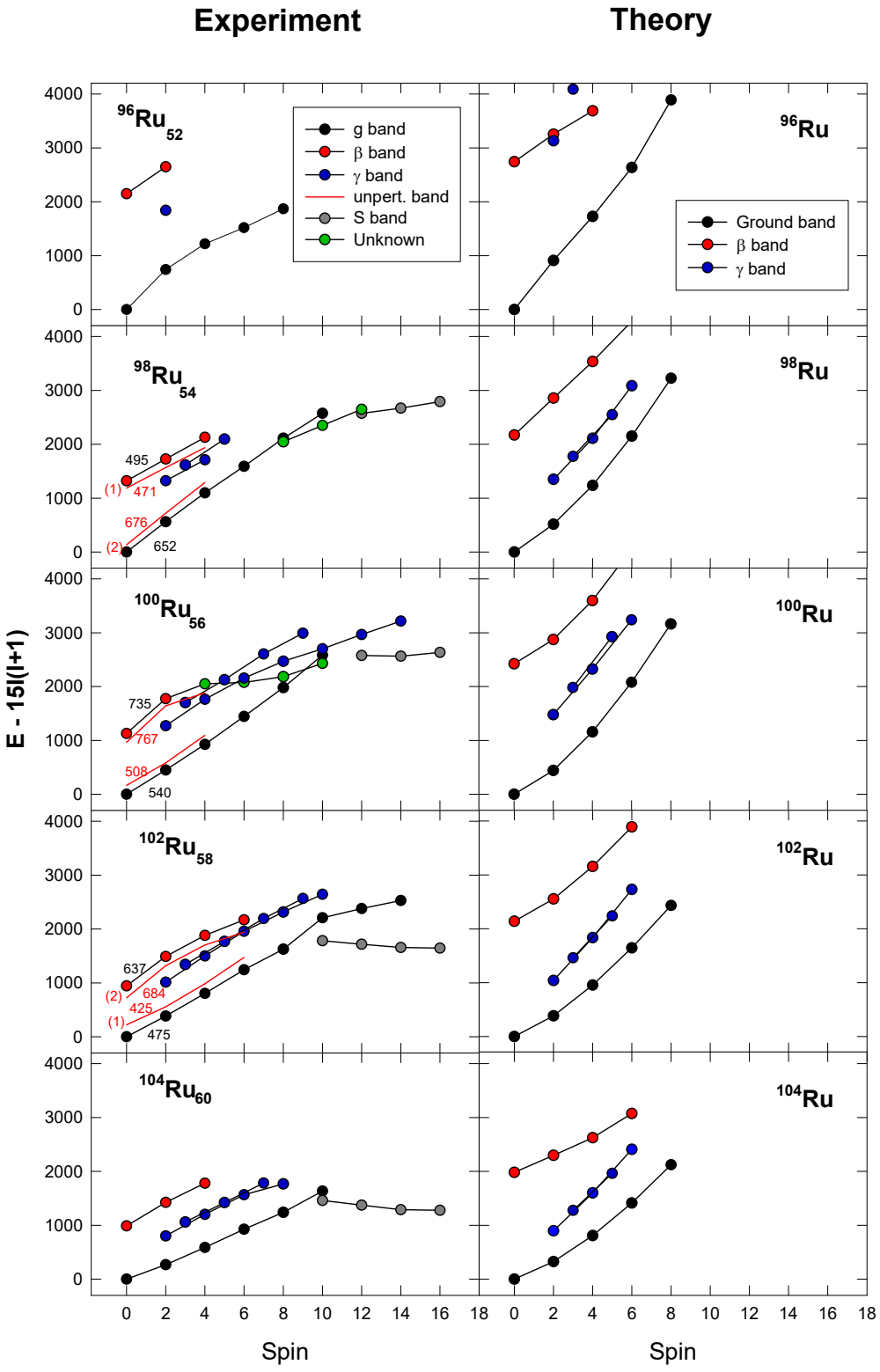

Figure 8.2. Excitation energies minus a rigid-rotor reference for the band in $^{96-104}$Ru. The black, red, blue, red-line, gray and green correspond to the ground-, β-, γ-, unperturbed-, S and unassigned band, respectively. Also shown are the estimated unperturbed energies of the 0_1^+ and 0_2^+ bands assuming two state mixing with a constant 400 keV interaction (red-line) [127, 128].

In these plots, high spin data, [67, 129] has been included to see the effect of mixing, if any from bands at higher spins. The existence of ground, "quasi-β"- and γ-bands is obvious on the plots. Furthermore, in some instances mixing with higher lying bands is important, particularly in the case of ^{100}Ru, where the quasi-β band is seen to be perturbed significantly by a crossing with a band already at spin 4.

The plots also suggest a test of the shape-coexistence hypothesis of Urban *et al.* [54], in which a spherical configuration and a vibrational configuration, that evolves with increasing deformation with neutron number, cross between ^{100}Ru and ^{102}Ru, and interact with a constant interaction, $V = 400$ keV. In this case, the experimental levels of the ground and quasi-β band represent the mixed bands resulting from the mixing of the two configurations through V. Then it is possible to solve for the unperturbed levels E_{unp}, using a two level mixing formalism:

$$E^{\pm}_{unp} = \frac{1}{2}\left\{E_{pu} + E_{pl} \pm \sqrt{(E_{pu} - E_{pl})^2 - 4V^2}\right\}$$

where E_{pu}, and E_{pl} are the levels of upper and lower energy of the two interacting bands (ground and quasi-β). The results are shown as red lines in figure 8.2. Also shown in red are the $2 \rightarrow 0$ energies of the unperturbed bands. The use of these energies as a proxy for the moment-of-inertia, and hence deformation, indicates that the quasi-β band remains less deformed than the ground band in the region of the proposed crossing. There is not an interchange of spherical and deformed configurations as hypothesized by Urban *et al* [54]. On the other hand, an interchange of implied deformation is seen between ^{98}Ru and ^{100}Ru, where the $2 \rightarrow 0$ energies indicate a lower deformation of the quasi-β band compared to the ground band in ^{98}Ru, and vice-versa in ^{100}Ru. To understand this behaviour, and go beyond the phenomenology of band-mixing analyses, a more sophisticated model is required. This is pursued in the next section.

8.2 Theoretical framework

Theoretical calculation in the GCM framework were carried out by Tomaz Rodriguez. The present results are discussed in terms of intrinsic shapes calculated within the Symmetry Conserving Configuration Mixing framework (SCCM) using the Gogny D1S as the underlying nuclear interaction described in reference [26]. This is a fully microscopic method based on an extension of the mean-field approximation that includes particle number and angular momentum projections of Hartree-Fock-Bogoliubov (HFB) states defined along the intrinsic quadrupole degrees of freedom, (β_2, γ).

In this theoretical model, the final nuclear wave functions are obtained as linear combinations

of these symmetry-restored states whose coefficients are found within the generator coordinate method. In the present implementation, the HFB states are produced with the particle-number variation after projection method (PN-VAP) that ensures a better description of pairing correlations than the plain HFB method. In addition, parity and time-reversal symmetries are preserved by the HFB states, and only "quasiparticle vacua" are included in the definition of the SCCM wave functions. Hence, neither negative parity states are described nor an optimal variational exploration of the excited states is performed.

Potential energy surfaces calculated using the SCCM, shown in figure 8.3, predict a gradually increasing deformation with neutron number, along with a tendency to be γ-soft.

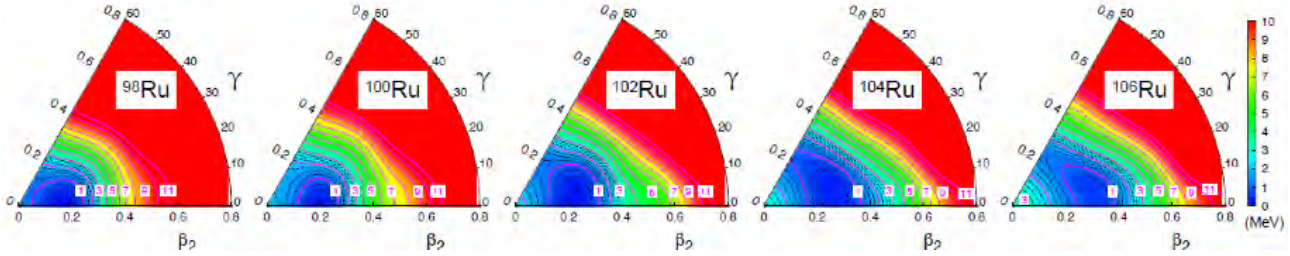

Figure 8.3. Potential energy surfaces calculated using the SCCM for $^{98-106}$Ru [127, 128].

The lowest excited SCCM levels for the $^{96-106}$Ru isotopes group together into three bands, namely, a ground state band and an excited band built on a 0_2^+ state with $\Delta I = 2$, and a $\Delta I = 1$ band based on a 2^+ band-head, corresponding to the "γ-bands. These bands are plotted in the right hand column of figure 8.2, where they are compared with the experimental bands. It is clear that the moments-of-inertia of the SCCM bands are smaller than their experimental counterparts. This is due to the lack of an optimal variational exploration for the excited states. It is, however, valid to compare the results to the low-lying levels such as the bandheads.

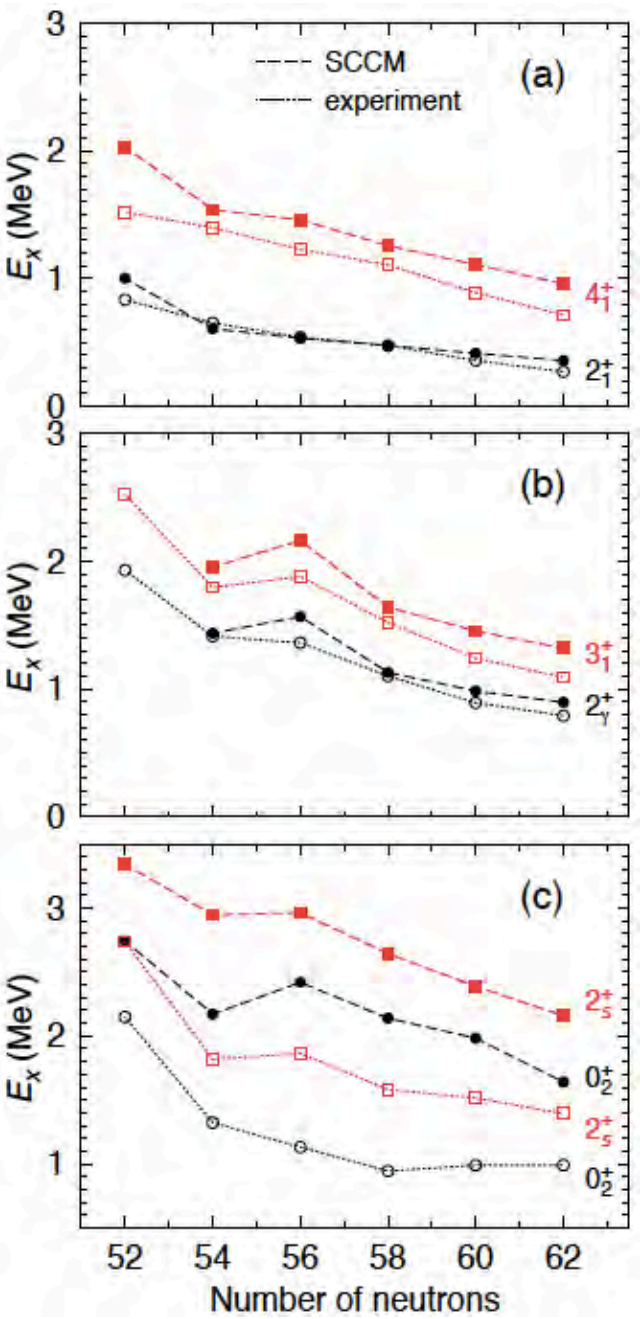

Figure 8.4. Comparison of the experimentally observed energies and the result of the SCCM calculations for (a) the ground-state band, (b) the γ-band and (c) the 0_2^+ band [127].

In Figure 8.4 the experimental and theoretical excitation energies of the bandheads and the first members of those bands along the isotopic chain are compared. For the ground-state and γ-bands, the agreement is very good considering the limitations of the present SCCM implementation. As expected from the potential energy surfaces shown in figure 8.5, the 2_1^+ and 4_1^+ energies decrease with increasing neutron number as the Fermi level departs from the $N = 50$ shell closure, indicating an increase in deformation, and, consequently, a more rotational behaviour. In addition, the 2_γ^+ and 3_1^+ energies also decrease (with the exception for ^{100}Ru, which slightly increases) suggesting that these isotopes become triaxialy deformed.

Also displayed in Figure 8.4(c), is the evolution of energies of the 0_2^+ states and their corresponding 2_s^+ band members. It is clearly seen that the agreement is worse than in the two previous bands although the trend of the 2_s^+ is reproduced well. To understand the results in more detail, the SCCM wavefunctions are plotted in figure 8.5.

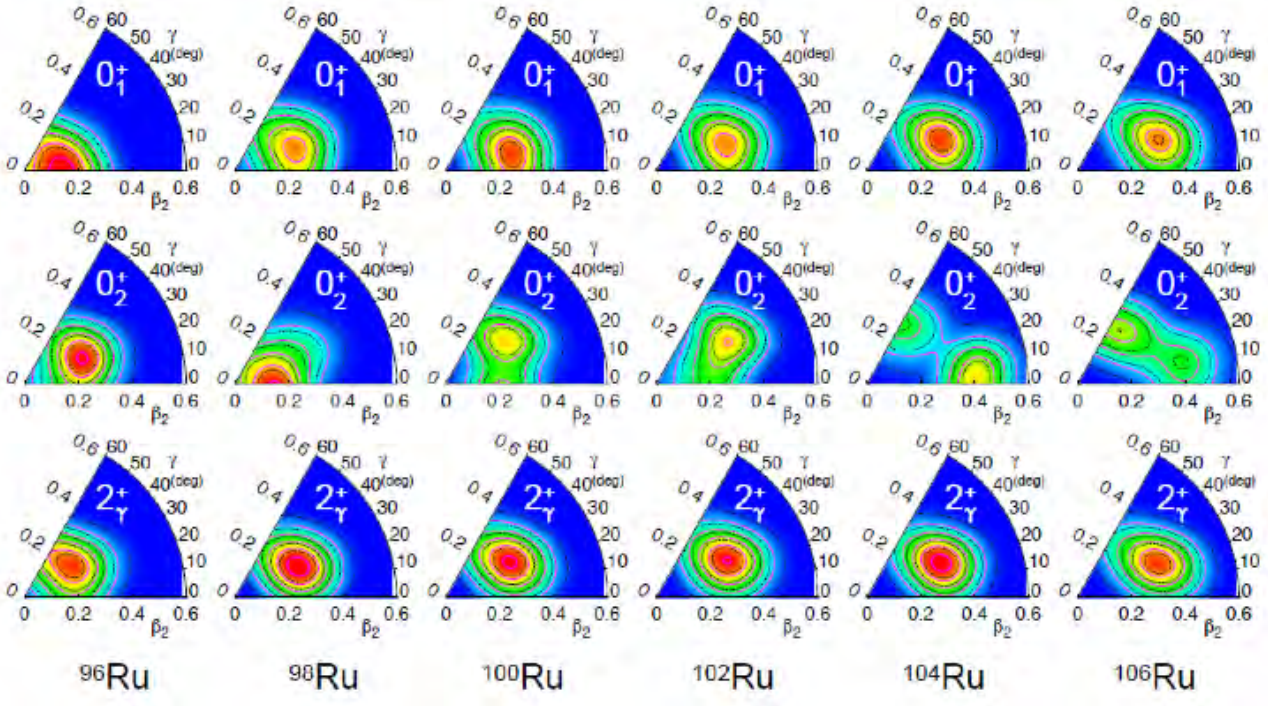

Figure 8.5. Wave function distributions in the (β,γ) plane for the 0_1^+ (top), the 0_2^+ (middle), and 2_γ^+ (bottom) states resulting from the SCCM calculations [127].

An interesting observation is that the wavefunctions generally do not show a good overlap with the minimum in the potential energy surface. In general, triaxial distributions of the wavefunctions are predicted. The 2_γ^+ states correspond to a triaxial deformation - perhaps not surprisingly, since they are the heads of the "γ-band". Surprisingly, given the PES's, the 0_1^+ and 0_2^+ levels are also often triaxial, sometimes giving rise to a "shape coexistence" (e.g. at ^{96,98}Ru) where none existed in the PES.

The (β_2, γ) deformation of the ground state wave functions changes from (0.15, 0°) for ^{96}Ru to (0.3, 20°) for ^{106}Ru. The wave function distributions for the 2_2^+ state have $(\beta_2, \gamma) = (0.2, 35°)$ for ^{96}Ru, and evolve smoothly to larger deformation and smaller values of γ reaching $(0.3, 20°)$ for ^{106}Ru. The wavefunctions of the 0_2^+ levels do not show a vibrational character - that would necessitate the presence of a clear node in the wavefunctions. Rather, in the case of ^{96,98}Ru, they imply shape coexisting levels in these nuclei.

Unfortunately, as inferred from the level spacing, the newly-established 0_2^+ band in ^{98}Ru, has a deformation greater than that of the ground state band. This larger deformation, is not

reflected in the SCCM calculations, where the 0_2^+ wave function distribution has a maximum near $(\beta_2, \gamma) = (0.15, 0°)$, and that for the 0_1^+ state has $(\beta_2, \gamma) = (0.22, 25°)$. The SCCM calculations reflect a crossing occurring between $N = 52$ ^{96}Ru and $N = 54$ ^{98}Ru, but then the 0_2^+ state takes on a completely different character in ^{100}Ru, with $(\beta_2, \gamma) = (0.25, \gamma = 45°)$.

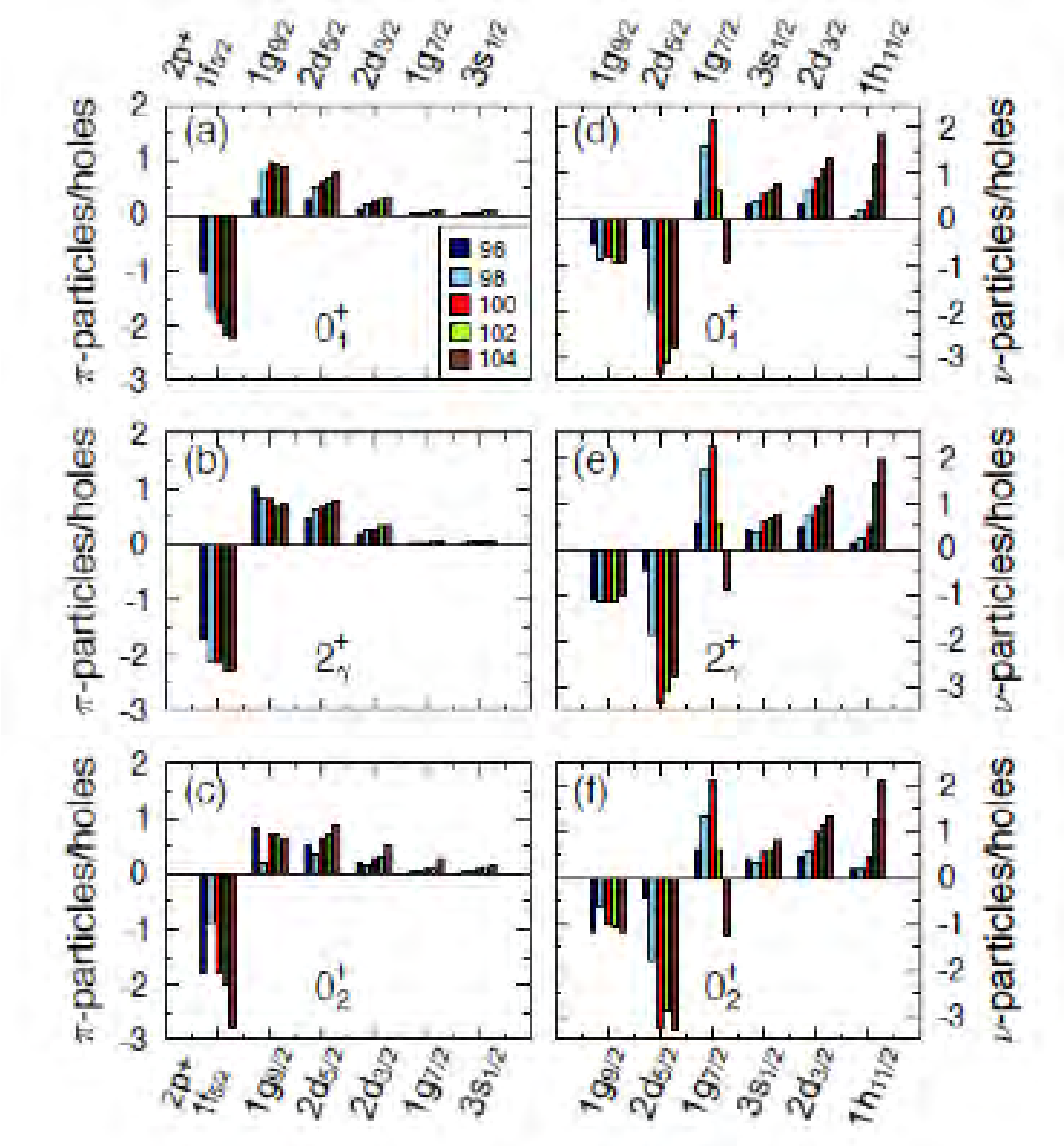

Figure 8.6. Calculated occupancies of the orbitals near the Fermi surfaces in ^{96}Ru–^{104}Ru isotopes for the $^+_1$ 2_γ^+ and 0_2^+ states for protons (panels a) - c)) and neutrons (panels d) - f)), respectively. The height of the bars represent the excess of particles with respect to expected occupancies based on a spherical HF calculation, e.g. four protons in the $g_{9/2}$ orbital for the ground states [127].

Shown in figure 8.6 are the differences between the number of particles expected with a normal filling of the Hartree-Fock (HF) spherical orbitals, and the number of particles computed with the SCCM wave functions [26]. For the protons, four particles are expected in the HF $g_{9/2}$ orbital, and thus systematically for the 0_1^+ state a greater occupancy is calculated (between four and five). Progressively, increasing in neutron number from $N = 52$ ^{96}Ru to $N = 60$ ^{104}Ru, we

observe that the number of holes in the p f orbitals increases monotonically for the ground state, and the number of particles in the $g_{9/2}$ and $d_{5/2}$ orbitals increases substantially. As can be seen from the wave function distributions for the 0_1^+ and 0_2^+ states in figure 8.7, there appears to be an interchange of these states between ^{96}Ru and ^{98}Ru; this is also reflected in the proton occupancies where the distribution for the 0_2^+ state in ^{96}Ru is very similar to that of the 0_1^+ state in ^{98}Ru, and vice versa. Experimentally, the interchange appears to be slightly delayed compared to this prediction, judging by $2^+ \rightarrow 0^+$ energies, occurring between ^{98}Ru and ^{100}Ru. For the neutron occupancy, the situation also changes isotope-by-isotope, especially for $d_{5/2}$ and $g_{7/2}$ orbitals. For example, the $g_{7/2}$ orbital should have, in the spherical HF configuration, zero particles for $^{96-100}$Ru, two particles in ^{102}Ru and four particles in ^{104}Ru. The $g_{7/2}$ occupancy is already substantial for ^{98,100}Ru, essentially in line with expectations for ^{102}Ru, and slightly less than expected for ^{104}Ru.

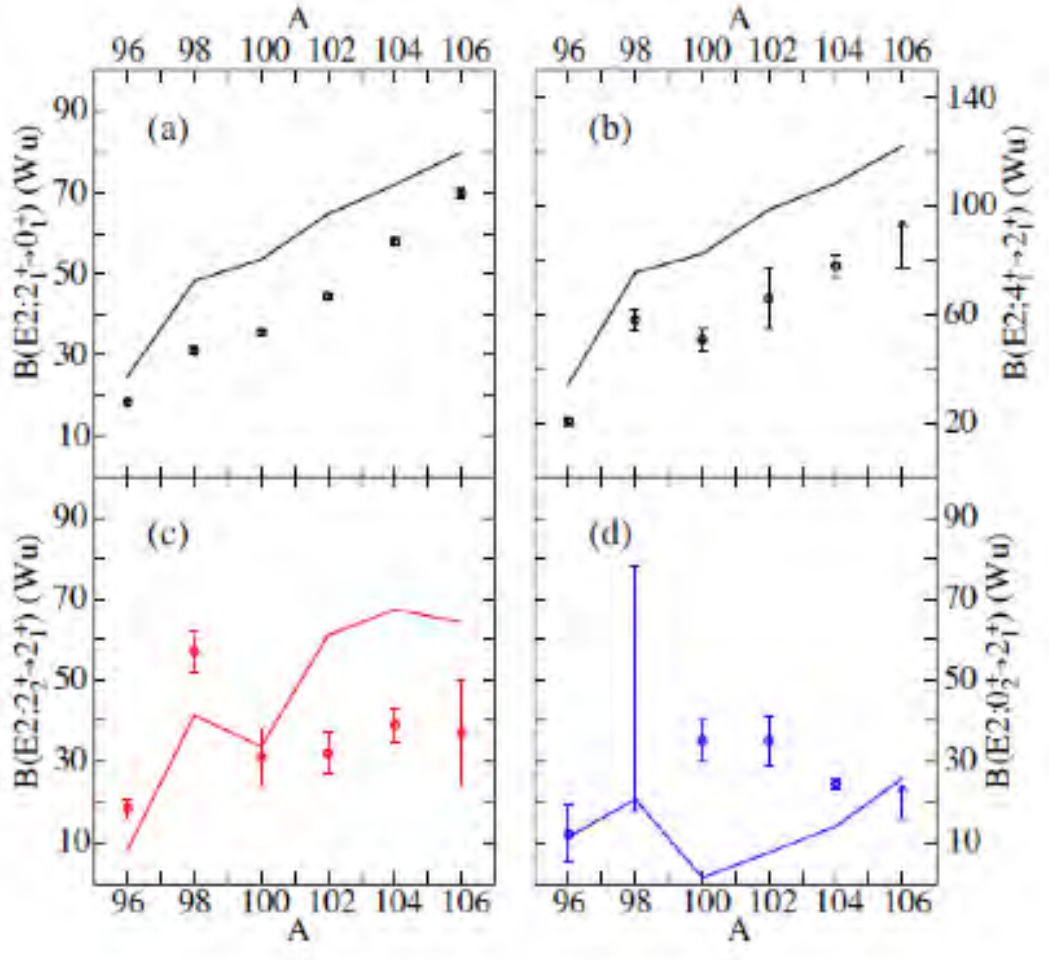

Figure 8.7. B(E2) values, in W.u., for the $2_1^+ \rightarrow 0_1^+$ (panel a), the $4_1^+ \rightarrow 2_1^+$ (panel b), the $2_1^+ \rightarrow 2_1^+$ (panel c) and the $0_2^+ \rightarrow 2_1^+$ (panel d) transitions. The data are taken from [13] except for ^{104}Ru, from [53], and ^{106}Ru from reference [130]. The B(E2; $0_2^+ \rightarrow 2_1^+$) value for ^{98}Ru has a wide range due to uncertainties in signs of matrix elements used in the analysis of the Coulomb excitation data [61]. Lower limits, due to upper limits on life times [130], are given for the B(E2; $2_1^+ \rightarrow 2_1^+$) and B(E2; $0_2^+ \rightarrow 2_1^+$) values for 106Ru. The curves are the results of the SCCM calculations [127, 128].

In figure 8.7, the calculated B(E2) values for selected transitions from the first four excited states are shown. The transition strengths in the yrast band are over-predicted, perhaps reflecting that the deformation is predicted to be too large. The B(E2) values for the decay of the 2_2^+ level, the band head, are underpredicted for ^{96,98}Ru, and over-predicted for $A > 100$, and that for decay of the 0_2^+ state are generally underpredicted, except for ^{96}Ru, and possibly ^{106}Ru for which only a lower limit is known. Of interest in the trend, in both the calculations and the data, is the local peaking observed in the B(E2) values that occurs at $A = 98$, and the dip at $A = 100$. At $N = 56$, in the spherical basis the $d_{5/2}$ shell would be filled, and there is also a sizable gap open between the 3/2[422] and 3/2 [411] or 5/2[413] Nilsson orbitals (see, e.g., figure 9 in reference [131]). Such gaps in the single-particle energies are associated with a drop in the collectivity, and may be responsible for the features in the B(E2) values observed for ^{100}Ru.

Chapter 9

Conclusion

The work presented in this document had two distinctive goals. The first goal: technical tasks. To develop and build the tape station for β-decay studies at iThemba LABS. The second goal: Physics task. To use this newly developed and advanced experimental tool to perform nuclear structure studies in ^{98,100}Ru isotopes by using the β-decay technique. The achievement of these goals has been summarized separately below.

9.1 Technical goal

A β-decay station has been developed, utilizing the tape station to probe the atomic nucleus. This β-decay station presents new opportunities and techniques that were not available at iThemba LABS before. This facility will also be used in the planned radioactive-ion beam project in the near distance future for transporting short-lived nuclei and reading beam current in a certain location along the beam line.

The tape station is versatile system that can be used to study short-lived and long lived nuclei. The performance of the system has been demonstrated and improved especially for short-lived species, with an accuracy of $\pm$ 1 mm. For long-lived species, the system has been proven as a magnificent tool for observing weak branches in long-lived nuclei.

9.2 Physics goal

The newly developed β-decay station was successfully used to perform a β-decay measurement on ^{98,100}Ru. This work presents the first results from this new facility. All the experiments performed with this facility produced good results. In the test experiment, on ^{162}Yb, section 6.7.1, the data collected over the short period of time confirmed the findings of the previous measurement performed by McCutchan [121], while for ^{100}Ru the data confirmed the γ-rays

observed in the previous measurement, while in ^{98}Ru new γ-rays were observed.

The result of the SCCM calculations for the low-lying state properties are in reasonable agreement with the experimental data. The calculations indicate that for low neutrons the ground state of Ru isotopes are near prolate shape, but as the number of neutrons increases the shape smoothly moves into triaxiality. These results are consistent with the findings of H. Abusara *et al* [57] but Abusara suggested that there is no shape coexisting structure in Ru isotopes.

The present observations do not support the existence of multi-phonon vibrational excitations but imply the existence of bands at low excitation energies. The newly assigned γ and 0_2^+ bands in ^{98}Ru fit well in the systematics of these excitations assigned in the heavier Ru isotopes.

We can conclude that the real situation in the Ru isotopes is more complicated than Urban's [54, 132] simplistic model. Beyond-mean-field calculations employing the self-consistent configuration mixing method suggest that the Ru isotopes are triaxiality deformed and that shape coexistence occurs around ^{98}Ru.

9.3 Effect of the tool developed towards iThemba LABS growth

The impact of this new facility opens doors for new research opportunities at iThemba LABS. Previously, iThemba LABS relied on a stable beam to probe the atomic nucleus (nuclear structure studies) and only perform experiments where they can only study properties of a stable nucleus. This facility presents iThemba LABS users with new opportunities to study short-lived nuclides even though RIBs facility is not yet operational. This facility also allows the techniques to perform β-decay measurements to be advancing before the RIBs facility.

Bibliography

[1] Lucky Makhathini. Development of a laser ionization test-bench for radioactive ion beams. Master's thesis, University of Zululand, 2013.

[2] *A Radioactive-ion Beam Facility at iThemba LABS: Scientific And Technical, 2013.*

[3] J.L. Conradie, L.S. Anthony *et al.* A Radioactive Ion Beam And Isotope Production Facility For iThemba LABS. In *Proceedings of RuPAC2016, St. Petersburg, Russia*, 2016.

[4] J. Kern, P.E. Garrett, J. Jolie, H. Lehmann. Search for nuclei exhibiting the U(5) dynamical symmetry. *Nuclear Physics A*, 593:21–47, 1995.

[5] P.E. Garrett, J.L. Wood and S.W. Yates. Critical insights into nuclear collectivity from complementary nuclear spectroscopicmethods. *Physica Scripta*, 93:063001(34), 2018.

[6] P.E. Garrett, K.L. Green and J.L. Wood. Breakdown of vibrational motion in the isotopes $^{110-116}$Cd. *Physcal Review C*, 78:044307, 2008.

[7] K.S. Krane. *Introduction to nuclear physics.* John Wiley and Sons,Ltd, 1987.

[8] Oleg V. Ivanov. *Decay of ^{66}Fe studied with a new β-γ-Detection set-up at LISOL.* PhD thesis, Instituut voor Kern-en Stralingsfysica, 2007.

[9] Juha Sorri. *Electron spectroscopy with the SAGE spectrometer.* PhD thesis, University of Jyvaskyla, 2016.

[10] D.J. Sand. *Nuclear physics: Principle and application.* John Wiley and Sons,Ltd, 2001.

[11] Aage Bohr and Ben R. Mottelson. *Nuclear structure Volume II: Nuclear Deformations.* World Scientific Publishing Co. Pte. Ltd., 1998.

[12] Glen F. Knoll. *Radiation Detection and Measurement.* John Wiley and Sons, Inc, 1989.

[13] *Data extracted from the National Nuclear Data Center, www.nndc.bnl.gov.*

[14] William F. Hornyak. *Nuclear structure.* Academic press, 1975.

[15] W. Greiner and J. A. Maruhn. *Nuclear Models.* Springer, 1996.

[16] Ernest C. Pollard and William L. Davidson. *Applied Nulcear Physics*. J. Wiley and Sons, 1951.

[17] W. David Kulp III. Requim for low-energy beta vibrations. Gordon research conference on Nuclear Chemistry.

[18] P.E. Garrett. Characterization of the β vibration and 0_2^+ states indeformed nuclei. *Journal Of Physics G: Nuclear And Particle Physics*, 27:R1–R22, 2001.

[19] S. G. NIlsson and I. Ragnarsson. *Shapes and Shells in Nuclear Structure*. Cambrige University Press, 1995.

[20] K. Langanke, J. A. Maruhn and S. E. Koonin. *Computational Nuclear Physics 1: Nuclear Structure*. Springer, Berlin, Heidelber, 1991.

[21] P. Bonche *at al.* Self-Consistent study of Triaxial deformation: Application to the isotopes of Kr, Sr, Zr and Mo. *Nuclear Physics A*, 443:39–63, 1985.

[22] M. Dutra *et al.* Skyrme interaction and nuclear matter constraints. *Physics Review C*, 85:035201, 2012.

[23] Siyabonga Ntokozo Thandoluhle Majola. *Exploring the spectroscopy of vibrational levels in the 160 mass region*. PhD thesis, University of Cape Town, 2015.

[24] L. M. Robledo and G. F. Bertsch. Application of the gradient method to hartree-fock-bogoliubov theory. *Physical Review C*, 84:014312, 2011.

[25] Bryan Geddes Wild. *The Hartree-Fock-Bogoliubov Theory of Bose-Einstein Condensates*. PhD thesis, Univesity of Otago, 2011.

[26] Tomas R. Rodrguez and J. Luis Egido. Triaxial angular momentum projection and configuration mixing calculations with the gogny force. *Physical Review C*, 81:064323, 2010.

[27] H. Morinanga. Interpretation of some of the excited states of 4n self-conjugate nuclei. *Physical Review*, 101:254, 1956.

[28] K. Heyde. A focus on shape coexistence in nuclei. *Journal of Physics G: Nuclear and Particle Physics*, 43:020402(4pp), 2016.

[29] K. Heyde and R. A. Meyer. Comment on "Monopole strength and shape coexistence in the A = 100 mass region". *Physical review C*, 42:791–793, 1990.

[30] Wolfgang Norbert Erik Schwerdtfeger. *First Identification of the 0_2^+ State in ^{30}Mg via its E0 Transition*. PhD thesis, Ludwig-Maximilian University of Munich, 2008.

[31] J.L. Wood. Shape coexistence in atomic nuclei. Lecture presentated at UWC, 2017.

[32] P. Federman and S. Pittel . Quenching of the 2p-2p proton spin-orbit splitting in teh sr-zr region. *Physical review C*, 69B(4):385–388, 1984.

[33] R.A. Bark. PhD thesis, Australian National University, 1990.

[34] E.F. Zganjar. Conversion electron spectroscopy and its role in identifying shape coexisting structures in nuclei via E0 transitions. *Journal of Physics G: Nuclear and Particle Physics*, 43:25, 2016.

[35] K. Heyde and John L. Wood. Shape coexistence in atomic nuclei. *Review of modern physics*, 83:1467–1521, 2011.

[36] Marie-Martine BE, Nelcy Coursol, Bernard Duchemin, Frederick Lagoutine and Jean Legrand. *Table of radionuclides*. Commissariat a 1'Energie Atomique, 1999.

[37] Aage Bohr and Ben R. Mottelson. Collective and individual-particle aspects of nuclear structure. *Det Kongekige Danske Videnskabernses Selskab matematisk-fysiske meddeleser*, 1953.

[38] A. Bohr and B. R. Mottelson. *Collective Nuclear Motion and the Unified model*.

[39] H.J. Jensen. *Spectroscopy on rotation Band builts on the $\pi h_{9/2}[541\ 1/2^-]$ configuration, a Challenge for the Cranked Shell Model*. PhD thesis, The Niels Bohr Institute for Astronomy, Physics and Geophysics, University of Copenhagen, DK-2100, Copenhagen, Denmark, 1995.

[40] A. Bohr and B.R. Mottelson. *Nuclear structure*. World Scientific Publishing Co. pte.Ltd, 1998.

[41] A.V. Aldushchenkov and N. A. Voinova. E0 transition in a atomic nuclei. *Nuclear Data table 11*, pages 299–325, 1972.

[42] T. Kibedi and R.H. Spear. Electric monopole transitions between 0^+ statesf or nuclei throughout the periodic table. *Atomic Data and Nuclear Data Tables*, 89:77–100, 2005.

[43] E.L. Church and J. Weneser. Effect of the finite nuclear size on internal conversion. *Physical review*, 104(5):1382–1886, 1956.

[44] J.L. Wood, E.F. Zganjar, C. De Coster, K. Heyde. Electric monopole transitions from the low energy exciatations in nuclei. *Nucl. Phys. A*, 1999.

[45] J.L. Wood, K. Heyde, W. Nazarewicz, M. Huyse and P. van Duppen. Coexistance on even-mass nuclei. *Review Section of Physics Letters*, 215(3 and 4):101–201, 1992.

[46] J.O. Rasmussen. Theory of E0 transition of spheroidal nuclei. *Nuclear Physics*, 19:85–93, 1960.

[47] K. Helariutta, J.F.C. Cocks *et al.* Gamma-ray spectroscopy of $^{192-195}$Po. *The European Physical Journal A*, 6:289–302, 1999.

[48] H. Ejiri and M.J. A. de Voigt. *Gamma-ray and Electron spectroscopy.* Clarendon Press, 1989.

[49] R.F. Casten and D.D. Warner. The interacting boson approximation. *Review of Modern Phsyscis*, 60(2):389–468, 1988.

[50] R.F. Casten. *Nuclear Structure From A Simple Perspective.* Oxford University Press, Inc, 1990.

[51] P.E. Garrett and J.L. Wood. On the robustness of surface vibrational modes: cases studies in the cd region. *Journal of Physics G: Nuclear and Particle Physics*, 37:069701(2pp), 2010.

[52] B. Jigmeddorj, P.E. Garrett. Conversion electron study of ^{110}Cd: Evidence of new E0 transition branches. PAC proposal.

[53] J. Srebrny a, T. Czosnyka, Ch. Droste, S.G. Rohozinski *et al.* Experimental and theoretical investigations of quadrupole collective degrees of freedom in ^{104}Ru. *Nuclear Physics A*, 766:25–51, 2006.

[54] W. Urban, M. Jentschel, R. F. Casten, J. Jolie *et al.* 0_2^+ band in ^{102}Ru and the evolution of nuclear deformation in Ru isotopes. *Physical review C*, 87:031304(R), 2013.

[55] P. Van Isacker J. Stachel and K. heyde. Interpretation of the A=100 transition region in thr framework of the interacting boson model. *Physical review C*, 25(1):650–656, 1982.

[56] K. Nomura, R. Rodrguez-Guzmand L.M. Robledo. Structural evolution in a≈100 nuclei within the mapped interacting boson model based on the gogny energy density functional. *Physical Review C*, 94:044314, 2016.

[57] H. Abusara, Shakeb Ahmad, and S. Othman. Triaxiality softness and shape coexistence in Mo and Ru isotopes. *Physics Review C*, 95:054302, 2017.

[58] Z. Shi and Z.P. Li. Microscopic description of triaxiality in ru isotopes with covariant energy densityfunctional theory. *Physical Review C*, 97:034329, 2018.

[59] J. Xiang *at al.* Covariant description of shape evolution and shapecoexistence in neutron-rich nuclei at N ≈60. *Nuclear Physics A*, 873:1–16, 2012.

[60] D. Radeck, V. Werner, G. Ilie, N. Cooper, V. Anagnostatou *et al.* Simultaneous deorientation and lifetime measurement in ^{98}Ru using the recoil distance Doppler shift method in inverse Coulomb excitation. *Physical Review C*, 85:014302, 2012.

[61] E. Williams, C. Plettner, E. A. McCutchan, H. Levine, N. V. Zamfir el al. Revisiting anomalous B(E2; $4_1^+ \rightarrow 2_1^+$)/B(E2; $2_1^+ \rightarrow 0_1^+$) values in ^{98}Ru and ^{180}Pt. *Physical Review C*, 74:024302, 2006.

[62] R. B. Cakirli, R. F. Casten *at al.*. Breakdown of vibrational structure in ^{98}Ru. *Physical review C*, 70:044312, 2004.

[63] A. Giannatiempo, A. Nannini, A Perego, and P. Sona. Erratum: Spectroscopy of 98Ru [Phys. Rev. C 94, 054327 (2016)]. *Physical Review C*, 95:039904, 2017.

[64] Andrea Perego Adriana Nannini and Pietro Sona. Spectroscopy of ^{98}ru. *European Physical Journal Web of Conferences*, 66:02071, 2014.

[65] A. Giannatiempo. Structure of ^{98}Ru in the IBA-2 interacting boson model. *Physical Review C*, 96:044326, 2017.

[66] A. Giannatiempo, A. Nannini, A. Perego, and P. Sona. Spectroscopy of ^{98}Ru. *Physical review C*, 94:054327, 2016.

[67] Balraj Singh. Nuclear data sheets for A=100. *Nuclear data sheets 109*, 2008.

[68] L. Genilloud, H.G. Borner, F. Corminboeuf, *et al.* Erratum to "Study of the vibrational nucleus ^{100}Ru by the ^{98}Mo(α, 2nγ) and ^{99}Ru(n, γ) reactions". *Nuclear Physics A*, 669: 407–449, 2000.

[69] H.G. Borner, R.F. Casten, M. Jentschel, P. Mutti, W. Urban, and N.V. Zamfir. ^{102}Ru: A pivotial nuceus in the A$\sim$100 region. *Phsysical review C*, 84:044326, 2011.

[70] Masahiro koike, Kazuo Hisatake, Naoki Ono and Kaoru Takahashi. Levels in ^{100}Ru excited in the decay of ^{100}Rh. *Nuclear Physics 54*, 54:129–147, 1964.

[71] G. Berzins, M.E. Bunker and J.W. Starner. Energy level of ^{100}Ru. *Physcial Review C*, 187:1619–1632, 1969.

[72] M.J. Taylor, G. Gurdal, G. Kumbartzki, N. Benczer-Koller. Low-energy structure of the even-A $^{96-104}$Ru isotopes via g-factor measurements. *Physical Review C*, 83:044315, 2011.

[73] L. Genilloud *et al.* Characterization of the "three-phonon" region of ^{100}Ru. *Nuclear Physics A*, 683:287–301, 2001.

[74] Garabed Kenchian. *Espectroscopia gama De ^{100}Rh.* PhD thesis, Universidade De Sao Paule Instituto De Fisica, 1995.

[75] T. Konstantinopoulos *el al.*. Lifetime measurement in ^{100}Ru. *Physical Review C*, 95: 014309, 2017.

[76] F. Iachello. Dynamic symmeries at the critical point. *Physical Review Letters*, 85(17): 3580–3583, 2000.

[77] A. Frank, C. E. Alonso and J. M. Arias. Search for E(5) symmetry in nuclei: The Ru Isotopes. *Physical Reviwe C*, 65:014301, 2001.

[78] *https://en.wikipedia.org/wiki/Magic_number_(physics)#/media/File:Table_isotopes_en.svg.*

[79] *https://tlabs.ac.za/subatomic-physics/afrodite/.*

[80] Linda Mdletshe. *The Study of Low lying Positive Parity Bands in ^{162}Yb.* PhD thesis, University of Zululand, 2017.

[81] Nontobeko Angel Khumalo. Study Of Two Phonon Octupole Vibrations in ^{146}Gd. Master's thesis, University of Zululand, 2013.

[82] S.S. Ntshanganse. *Development of a recoil detector and the study of exotic asymmetric shapes in nuclei.* PhD thesis, University of Cape Town, 2011.

[83] Tshepo Samuel Dinoko. *Search for Low Spin CollectiveStructures in ^{158}Er and ^{159}Er.* PhD thesis, University of the Western Cape, 2013.

[84] TIm Giles. The new fast tape station at isolde. In *ISOLDE workshop*. 2010.

[85] J.C. Thomas and B. Blank. The desir facility at spiral2. Technical report, Grand Accélérateur National dIons Lourds, CEA/DSM - CNRS/IN2P3, 2010.

[86] J.C. Thomas. Technical proposal for the spiral2 instrumentation. Technical report, SPIRAL II, GANIL France, 2008.

[87] A.J. Mitchell, P.F. Bertone, B. DiGiovine *et al.* The X-Array and SATURN: A new decay-spectroscopy station for CARIBU. *Nuclear Instruments and Methods in Physics Research A*, 763:232–239, 2014.

[88] P.E. Garrett, A.J. Radich, J.M. Allmond, C. Andreoiu *et al.* Far From 'Easy' Spectroscopy with the 8 and GRIFFIN Spectrometers at TRIUMF-ISAC. *Journal of physics: Conference Series 639*, page 012006, 2015.

[89] *http://wikipedia/8track.*

[90] *https://8trackheaven.com/the-8-track-story/frank-schmidt/.*

[91] R.L. Mlekodaj, E.F. Zganjar and J.D. Cole. A new concept for a compact tape transport system. *Nuclear instruments and Methods*, 186:239–241, 1981.

[92] W.W. Bowman, T.T Sugihara and R.D. Macfarlane. Precision gamma-ray spectroscopy od short-lived nuclides by the helium-jet recoil-transport method. *Nuclear Instruments and Methods*, 103:61–67, 1972.

[93] V. Matouek, M.Sedlák, M.Venhart. TATRA: a versatile high-vacuum tape transportation system for decay studies at radioactive-ion beam facilities. *Nuclear Instruments and Methods in Physics Research A*, 812:118–121, 2016.

[94] *http://www.8trackheaven.com/archive/frankschmidt3.html.*

[95] *https://www.delta-line.com/86s125-3508a-000-P603.htm.*

[96] *https://www.vesconite.com/vesconite/.*

[97] *http://www.goodfellow.com.*

[98] William Duckitt. *A Digital Low-Level Radio FrequencyControl System for the Particle Accelerators at iThemba LABS.* PhD thesis, University of Stellenbosch, 2018.

[99] *http://beckhoff.com/ek1100/.*

[100] *http://beckhoff.com/el1002/*, .

[101] *https://download.beckhoff.com/download/document/io/ethercat-terminals/EL20xx_EL2124en.pdf.*

[102] *http://beckhoff.com/el2002/*, .

[103] *http://beckhoff.com/el7041/.*

[104] *http://controlsystemstudio.org.*

[105] *https://epics.anl.gov.*

[106] Joele Paulus Mira. *The role played by quasi-elastic and inelasticbreak-up of the* ^{12}C *and* ^{16}O *projectiles in theproduction of Intermediate Mass Fragments at 14-35 MeV/u.* PhD thesis, University of Stellenbosch, 2013.

[107] T.D. Bucher, S.P. Noncolela, T.R.S. Dinoko, J.L. Easton, N. Erasmus, J.J. Lawrie, S.H. Mthembu, W.X. Mtshali, O. Shirinda and J.N. Core . Proportional crosstalk correction for the segmented clover at iThemba LABS. *Physica Scripta*, 92:114004, 2017.

[108] Helmuth Spieler. *Semiconductor Detector system, Physics Devision, Lawrence Berkeley National Laboratory.* Clarendon Press, Oxford, 2005.

[109] *https://www.mirion.com/products/silicon-lithium-sili-detectors-for-charged-particles.*

[110] Canberra. Eslb and eslb-x si(li) detectors for x-ray or beta spectroscopy. Technical report, Canberra, 2013.

[111] *https://www.crystals.saint-gobain.com/sites/imdf.crystals.com/files/documents/bc400-404-408-412-416-data-sheet.pdf*.

[112] M.L. Cortes, R. Hoischen , K. Eisenhauer, J. Gerl and N. Pietralla. Bc404 scintillators as gamma locators studied via geant4 simulations. *Journal of intrumentation:*, 2014.

[113] *https://www.hamamatsu.com/us/en/product/type/H6533/index.html*.

[114] *https://www.xia.com/dgf_pixie-16.html*, .

[115] *Pixie-16 User Manual*, .

[116] *https://daq.tlabs.ac.za/facilities/ddas-1/setup-guide*.

[117] John Cresswell and Janet Sampson. Mtsort langauge-edoc033. Technical report, 07 August 2015.

[118] *https://daq.tlabs.ac.za/facilities/ddas-1/expert-guide*.

[119] *https://radware.phy.ornl.gov*.

[120] *https://radware.phy.ornl.gov/esclev/esclev.html*.

[121] E.A. McCutchan, N.V. Zamfir, M.A. Caprio, R.F. Casten, H. Amro, C.W. Beausang, D.S. Brenner, A.A. Hecht, C. Hutter, S.D. Langdown, D.A. Meyer, P.H. Regan, J.J. Ressler, and A.D. Yamamoto. Low spin states in ^{162}Yb and the X(5) critical point symmetry. *Physical review C*, 69:024308, 2004.

[122] Masahiro Koike, Hirokane Kawakami *at al.* Electric monopole transitions between 0^+ states in ^{100}Ru. *Physical Review C*, 10(5):1996–2001, 1974.

[123] A. Giannatiempo, A. Nannini *et al.* Spin-parity assignments and evidence for mixed-symmetry states in ^{100}Ru. *Physical Review C*, 53(6):2770–2775, 1996.

[124] *http://bricc.anu.edu.au*.

[125] T. Kibedi, T.W. Burrows, M.B. Trzhaskovskay, P.M. Davidson, C.W. Nestor Jr. Evaluation of theoretical conversion coefficients using bricc. *Nuclear Instruments and Methods in Physics Research A*, 589:202–229, 2008.

[126] T. Kibédi, T.W. Burrows, M.B. Trzhaskovskaya, C.W. Nestor, Jr. and P.M. Davidson. Internal conversion coefficients how good are they now? 2006.

[127] P.E. Garrett, L. Makhathini, R.A. Bark, T.R. Rodriguez, S. Valbuena *et al.* Observation of the 0_2^+ and bands in ^{98}Ru, and shape coexistence in the Ru isotopes. *Physics Letter B*, 809:135762, 2020.

[128] P. E. Garrett, L. Makhathini *et al.* Shape Coexistence in the Ru Isotopes; Multi-specoscopy study of ^{98}Ru and Beyond-mean-Field Calculation. *Acta Physica Polonica B*, 51:799, 2020.

[129] J. Timar, J. Gizon *et al.* Terminating bands in ^{98,99,100}Ru nuclei: New information on the neutron $2d_{5/2}$ and $1g_{7/2}$ energy spacing. *Physics Review C*, 62:044317, 2000.

[130] M. Sanchez-Vega, H. Mach, R.B.E. Taylor. Studies of quadrupole collectivity in the γ-soft ^{106}Ru. *The European Physical Journal A*, 2008.

[131] R. A. Meyer. Deformation in odd-mass nuclef near A 100: one- and three-quasiparticle nilsson states in $^{99}_{39}Yb_{60}$. *Nuclear Physics A*, 439:510–534, 1985.

[132] W. Urban, T. Rzaca-Urban, J. Wisniewski, I. Ahmad, A. G. Smith, and G. S. Simpson. Structure of 0^+ excitations in the mass A =100 region: 0_2^+ bands in ^{98}Sr and ^{100}Zr. *Physucal review C*, 99:064325, 2019.

[133] *http://lise.nscl.msu.edu/pace4.html.*

[134] E. Browne and J.K. Tuli. Nuclear data sheets for a=99. *Nuclear Data Sheets*, 2017.

[135] D. Abriola and A.A. Sonzogni. Nuclear data sheets for a = 96. *Nuclear Data Sheets*, 2008.

[136] Jean Blachot. Nuclear data sheets for a = 101. *Nuclear Data Sheets*, 1998.

[137] N. Nica. Nuclear data sheets for a = 97. *Nuclear Data Sheets*, 2010.

Appendix A

Other nuclei populated in the experiment

The following section presents spectra and level schemes observed when sorting the ^{100}Ru experimental data. The reaction not only populated the nucleus of interest, but also populated other reaction channels. Figure A.1 shows the results of a PACE4 [133] calculation for the ^{89}Y(^{14}N, p2n)^{100}Rh reaction. The most populated and visible contaminants in these measurement are presented below. The sensitivity of this facility is demonstrated by observing low γ-ray branches in the low probability reaction channels. The strongest contaminants in this experimental data is presented below.

Z	N	A		events	percent	x-section(mb)
46	55	101	Pd	279	2.79%	8.15
45	56	101	Rh	166	1.66%	4.85
44	57	101	Ru	13	0.13%	0.38
46	54	100	Pd	6009	60.1%	175
45	55	100	Rh	2060	20.6%	60.2
44	56	100	Ru	64	0.64%	1.87
46	53	99	Pd	5	0.05%	0.146
45	54	99	Rh	14	0.14%	0.409
44	55	99	Ru	1	0.01%	0.0292
44	54	98	Ru	206	2.06%	6.02
43	55	98	Tc	16	0.16%	0.467
44	53	97	Ru	1068	10.7%	31.2
43	54	97	Tc	47	0.47%	1.37
42	53	95	Mo	15	0.15%	0.438
42	52	94	Mo	37	0.37%	1.08
TOTAL				10000	100%	292

Figure A.1. PACE4 calculating for reaction ^{89}Y(^{14}N, p2n).

Table A.1 shows dominant contaminants observed in this measurement and their decay mode.

It was not possible to avoid these contaminants because their half-lives are similar to the nucleus under investigation. Even the transport system was not able to suppress these nucleus.

Table A.1. Strongly populated contaminants in this measurement, h = hours, d = days, y = years. * channel of interest.

Parent nucleus	Decay mode	Daughter
^{99}Pd (21.4m)	β^+	^{99}Rh (stable)
^{101}Rh (3.3y)	β^+	^{101}Ru (stable)
* ^{100}Rh (20.8h)	β^+	^{100}Ru (stable)
^{97}Tc (4.21^{6}y)	β^+	^{97}Mo (stable)
^{97}Ru (2.83d)	β^+	^{97}Tc (stable)

Level scheme and spectrum of these contaminants are presented in the following section:

^{99}Rh Spectrum and Level scheme

This nucleus was produced in one of the reaction channel as shown in figure A.1. The γ-rays from this nucleus could not be avoided. The ^{99}Rh was produced from the β-decay of ^{99}Pd with a half-life of 21 minutes. In figure A.2, a gate was set on $2^+ \rightarrow 0^+$ transition (136 keV) the coincidence γ-ray were observed.

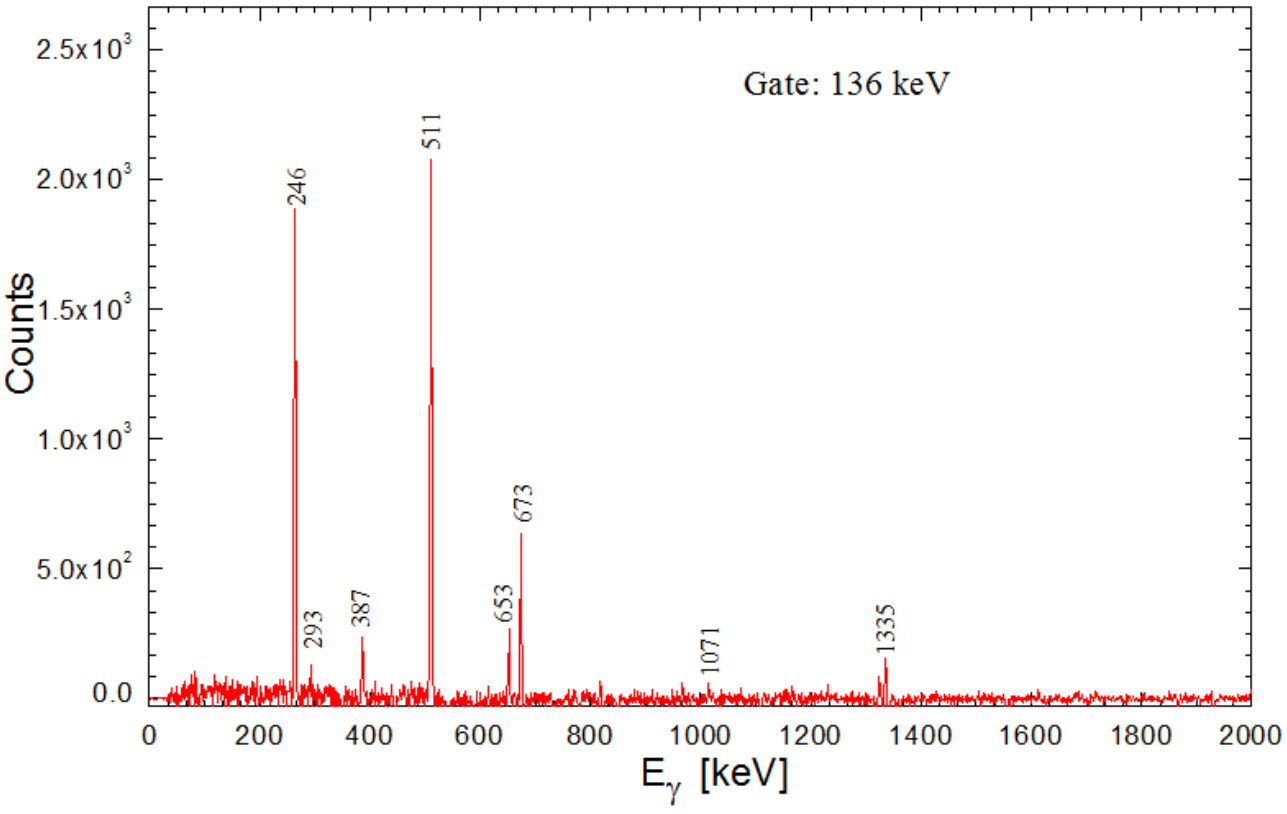

Figure A.2. Spectrum of ^{99}Rh γ-ray obtained when gating on the 2^+ to 0^+ transition.

Level scheme for ^{99}Rh it is presented in figure A.3. The spin and parity were taken from reference [134].

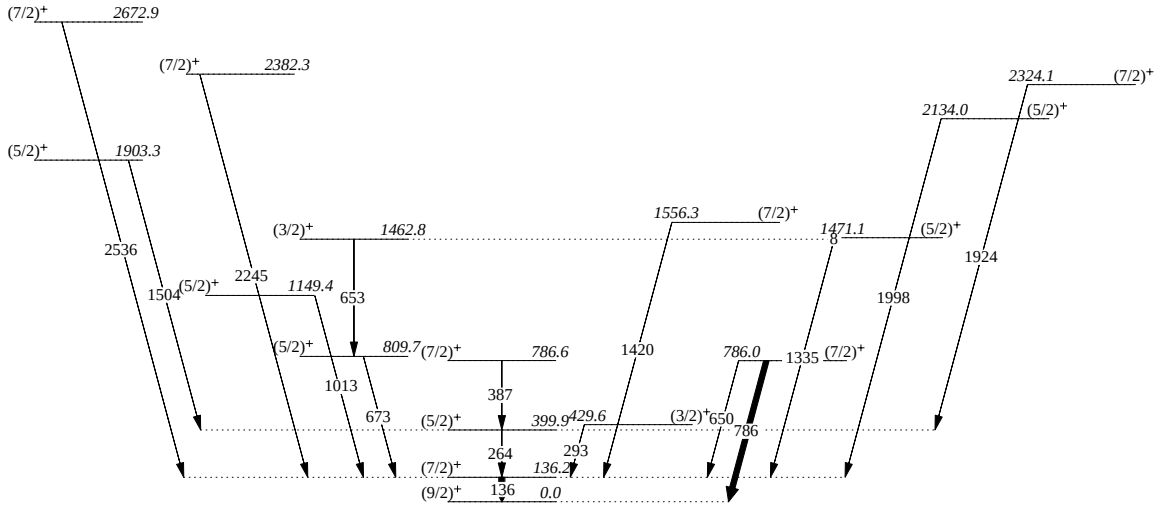

Figure A.3. Partial level scheme of ^{99}Rh observed in this measurement. Spin and parities are taken from [134].

^{96}Mo spectrum and Level scheme

Another strongly populated nucleus in this measurement was ^{96}Mo, from the β-decay of ^{96}Tc. A gate set on the strong $2^+ \rightarrow 0^+$ transition (778.2 keV) is shown in figure A.4.

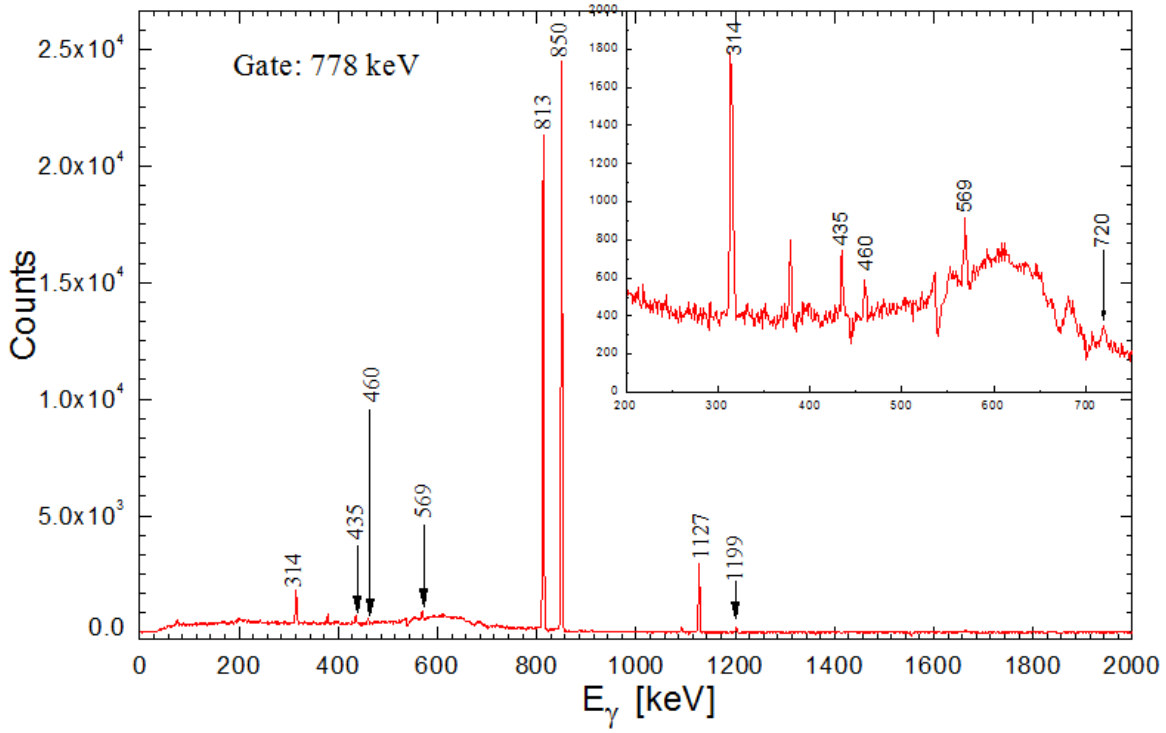

Figure A.4. A typical spectrum of ^{96}Mo obtained when gating on the $2^+ \rightarrow 0^+$ transition.

Figure A.5 shows the level scheme of ^{96}Mo observed in the ^{100}Ru experiment. The spins and parity assignment were taken from [135].

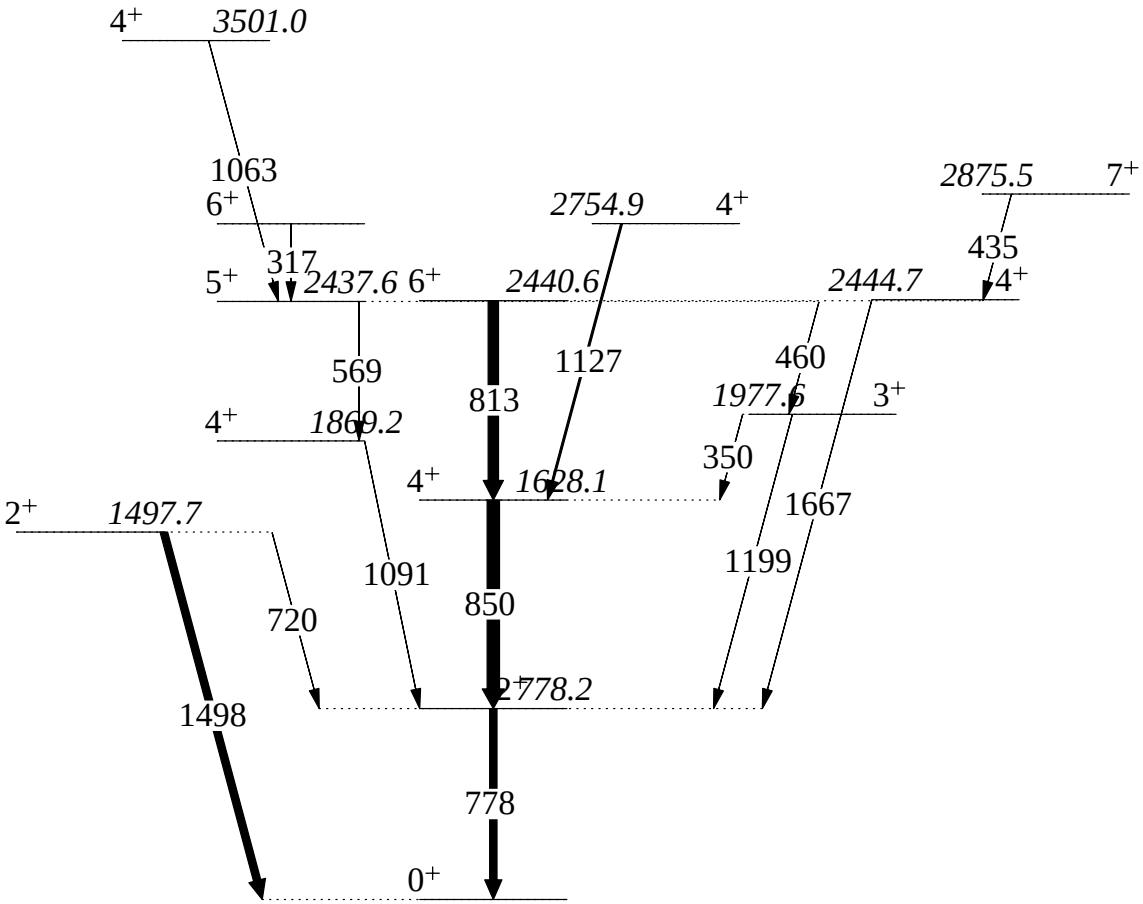

Figure A.5. Partial level scheme of ^{96}Mo observed in this measurement.

^{101}Ru Level scheme

Another strongly populated nucleus was ^{101}Ru. Figure A.6 shows the level scheme of ^{101}Ru observed from the β-decay of ^{101}Rh. Only the level scheme is presented for this nucleus because the coincidence relationship was clearly observed during the construction of the ^{100}Ru level scheme. The spin and parity assignment were taken from this reference [136].

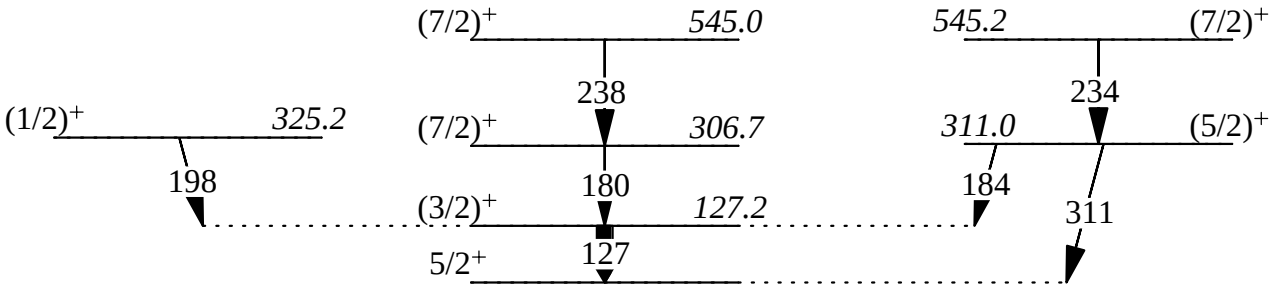

Figure A.6. Partial level scheme of ^{101}Rh observed in this measurement. The spin and parity assignment were taken from [136].

^{97}Tc Level scheme

Another populated nucleus was ^{97}Tu. Figure A.7 show the level scheme of ^{97}Tc from the β-decay of ^{97}Ru. The spin and parity was taken from this reference [137].

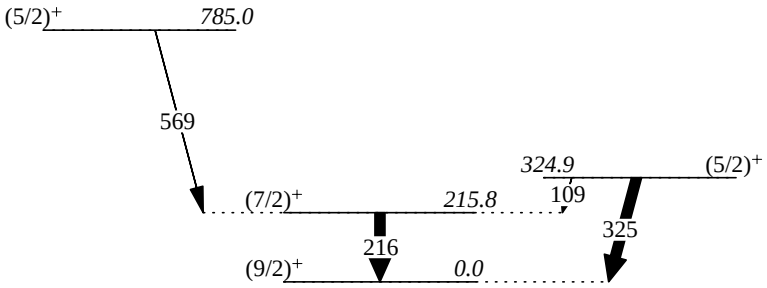

Figure A.7. Partial level scheme of ^{97}Tc observed in this measurement. The spin and parity was taken from [137].

Appendix B

Obtained γ-ray transitions

Gamma-rays obtained from the singles of all the clover detector used during the ^{100}Ru measurement. No spin and parity assignment were deduced for ^{100}Ru. Spins and parities was taken from [67, 68].

The terms used in table B.1, B.2 and B.3 are explained as follows:

♢ E_i represents excitation energy of the initial level of the γ-ray.

♢ E_γ represents the energy of the γ-ray.

♢ I_γ represents the intensity of the γ-ray.

♢ $M\lambda$ represents the multipolarity of the γ-ray.

♢ I_i^π represents the spin and parity of initial level.

♢ I_f^π represents the spin and parity of final level.

Table B.1. Observed γ-ray transition in this measurement.

E_i	E_γ	I_γ	$M\lambda$	I_i^π	I_f^π
3463.8	139.75	25961(169)		$(1,2^+)$	$(1,2^+)$
	175.05	34860(365)		5^-	4^+
2461.4	228.57	29232(376)	E1		
	233.34	5905(237)		2^+	2^+
	238.58	39232(317)			
	241.49	8050(260)		4^-	4^+
	263.63	22646(414)		3^+	4^+
	269.85	29707(312)			
2516.8	276.94	13624(288)		1^-	2^+
	295.05	108597(305)		3^+	2^+
2166.8	302.42	163489(471)	M2+E1	3^-	2^+
	305.87	922662(1565)		3^-	3^-
	314.50	8701(2542)			
	323.49	346096(650)			
	339.81	473145(851)			
2915.5	345.39	0.181(21)	M1+E2	2^+	4^+
2516.8	351.67	219285(497)		1^-	3^-
2915.5	370.30	110709(296)	E1	2^-	2^+
2915.5	378.78	24886(2140)	E1	2^-	3^- ?
	387.88	19741(2514)		1^1	4^+
2915.5	398.86	34833(2391)	M1	2^-	1^-
2569.8	403.01	41075(248)	M1+E1	4^+	3^-
3072.3	409.18	9315(321)	E2	$(1,2)^-$	$(1,2^+)$
	416.95	3554(272)			
	427.11	4177(267)			
	434.78	8340(261)			
	444,14	35.9(11)	E2	4^+	2^+
2915.5	446.16	2318665(2670)	M1+E2	2^-	2^-
	452.83	40558(7192)			
	460.37	18691(3419)			
2516.8	464.43	35826(2600)	E1,E2	1^-	0^+
	479.78	16890(648)			
3069.9	499.99	37619(627)	M2,E2	$(1,2^-)$	3^-
	500.20	32295(406)	M1,E2	2^+	2^+
	510.89	1327061(2204)	E1	2^+	2^+
	511.91	453974(2585)		2^-	4^+
1881.1	518.89	164272(342)	M1,E2	3^+	2^+
	528.66	112293(320)			
539.55	539.55	16001200(17986)	E2	2^+	0^+
3069.9	552.70	21940(364)	M1,E2	4^+	2^+
	563.38	8903(358)			
	566.91	36546(1433)			
	569.40	60168 (607)			
	583.12	204813(473)			
2469.4	588.37	957391(1529)	E1(+M2)	2^-	3^+

E_i	E_γ	I_γ	$M\lambda$	I_i^π	I_f^π
1130.3	590.61	251627(3305)	E2	0^+	2^+
	596.11	24646 (379)			
3069.9	600.18	52590(454)	M1,E2	4^+	2^-
2469.4	604.26	60543(313)	E1	2^-	2^+
	609.32	283423(787)	E0	0^+	0^+
	617.91	94907(416)			
2512.3	631.13	8656(288)	M1+E2	4^+	3^+
1865.2	639.02	9128(319)	E2	2^+4	4^+
	644.98	5977(305)			
	648.43	5286(354)			
2516.8	651.77	98993(505)	E1	1^-	2^+
1881.1	654.59	112854(613)	M1,E2	3^+	4^+
	665.49	5610(240)		3^+	3^+
	673.60	14172(325)		3^+	2^+
2543.7	678.53	4870(302)		2^+	2^+
1226.5	688.98	153509(539)	E2	4^+	2^+
	719.77	18608(273)			
	727.28	65776(365)			
1865.2	734.8	53711(518)	E2	2^+	0^+
2099.1	737.01	25606(491)	M1,E2	2^+	2^+
2915.5	748.72	181489(622)	M1,E2	2^-	3^-
	766.12	137537(848)			
	768.76	44160(606)			
2516.8	778.53	1058376(6367)			3^+
	786.18	32485(431)			
	795.28	43944(376)			
3324.7	811.70	993896(2186)	M1		
2915.5	816.47	56386(318)	E1	2^-	2^+
1362.2	822.64	4591783(10620)	E2+M2	2^+	2^+
	834.27	54115(310)			
	849.09	1227497(2986)	E2		
	859.75	47136(323)			
	868,32	47136(247)			
2099.1	873.23	0.040(10)	E2	2^+	4^+
	895.16	6395(302)			
	898.32	105797(371)		$2^+, 3^+$	2^+
3069.9	903.76	16982(264)	E1	4^+	3^-
	904.40	16662(828)	E1	2^+	3^-
	908.78	31721(487)			
	911.50	307628(677)			
	934.81	224990(507)			
	937.84	18800(329)			
	951.72	10431(310)		$(2^+, 4^+)$	2^+
3069.9	964.99	78215(290)	E2	4^+	2^+

Table B.2. Observed γ-ray transition in this measurement, cont.

E_i	E_γ	I_γ	$M\lambda$	I_i^π	I_f^π
2099.1	969.29	206057(432)	E2	2^+	0^+
	973.19	5400(253)		2^+	2^+
	985.71	13199(250)			
	992.87	523(273)		2^+	2^-
	1001.14	15920(264)			
	1014.56	13901(243)		2^+	4^+
2915.5	1034.84	309703(474)	E1	2^-	3^+
	1040.33	18772(352)	E2	4^+	2^+
2404.7	1043.12	24613(354)			
	1052.04	8106(304)		4^+	2^+
	1063.81	35394(258)			
	1078.81	2571(246)		$(2^+,4^+)$	4^+
	1086.65	5685(320)			
	1092.02	9633(391)			
2469.4	1107.61	2703263(3115)	E1(+M2)	2^-	2^+
	1112.15	37330(316)			
	1115.96	24928(304)			
	1120.64	221284(429)			
	1127.27	178454(401)			
2516.8	1155.27	67912(289)		1^-	2^+
	1173.58	1680391(1987)		3^+	2^+
2542.7	1181.97	7799(431)	M1+E2	2^+	2^+
3069.9	1191.47	7828 (388)		$(1,2)^-$	3^+
1741.0	1202.31	28958(241)	E2	0^+	2^+
3069.9	1204.26	12293(556)	E1	$(1,2)^-$	2^+
2569.8	1207.71	21848(236)	E2	4^+	2^+
	1218.70	2990(266)			
	1238.58	97856(283)			
	1247.13	4402(291)			
3324.7	1255.25	3692(421)		$1,2^+$	2^+
	1261.90	69536(762)			
	1274.53	24383(552)		$1,2^+$	0^+
	1280.98	18110(457)			
	1289.36	8065(388)			
	1294.02	9424(372)			
1865.2	1325.99	88226(336)	M1,E2	2^+	2^+
	1332.89	1906923(2263)			
1881.1	1342.03	1051055(1312)	M1+E2	3^+	2^+
1893.6	1354.55	102077(373)	E2	4^+	2^+
1362.1	1362.66	3145640(3651)	E2	2^+	0^+
	1378.20	67773(255)			
1925.9	1386.87	88557(275)	E1	2^+	0^+
	1401.41	23154(245)			
	1408.01	69396(254)			
1958.4	1419.41	51483(235)	M1	2^+	2^+
	1461.35	2393223(2790)		4^-	0^+
2536.1	1496.62	19709(321)	M1	3^+	4^+
	1502.15	11770(315)			
	1509.55	51484(445)			
2051.6	1512.95	31442(348)	E2	0^+	2^+
2915.5	1554.02	4095122(4670)	E1	2^-	2^+
2099.1	1559.52	197206(351)	M1	2^+	2^+
	1581.34	11699(401)		$(1^+,2)$	3^+
3463.8	1583.99	14032(400)		$(1,2^+)$	3^+
	1588.70	66279(228)		$2^+,3^+,4^+$	2^+
	1593.23	33007(203)			
	1596.62	4891(315)			
	1600.13	8310(278)			
	1609.04	4600(216)			
	1621.35	32321(454)			
2166.8	1627.24	320931(597)	E1	3^-	2^+
	1630.51	36237(458)			
	1638.74	11104(262)			
	1662.18	27624(246)			
	1666.55	4371(225)			
	1684.88	5201(296)		5^-	4^+
2240.5	1701.84	54897(218)	M1+E2	2^+	2^+
2246.4	1707.92	35103(762)	M1	2^+	2^+
3069.9	1710.53	34303(708)		2^+	2^+
	1730.28	58719(228)			
	1765.11	343776(500)			
	1779.45	23227(185)			
	1836.87	110793(260)		0^+	2^+
2387.2	1847.31	47961(205)		0^+	2^+
2404.7	1864.92	215810(2842)		4^+	2^+
	1866.55	235873(2841)	E2	2^+	0^+
2469.4	1929.84	2310260(2688)	E1	2^-	2^+
2516.8	1977.98	53099(217)	E1	1^-	2^+
2536.1	1997.63	12163(188)	E2	2^+	2^+
	2019.87	30279(206)	E2	4^+	2^+
3324.7	2092.00	19771(649)	E2	4^+	2^+
	2103.39	96365(287)			
	2119.71	35509(532)	M1	2^+	2^+
2667.0	2126.70	3092(312)	M1	2^+	2^+
2166.8	2167.82	18955(281)	E3	3^-	0^+
3323.7	2193.16	4822(388)	E2	(2^+)	0^+
2745.6	2203.06	128290(729)	M1	(2^+)	2^+
	2223.31	13590(702)		$(1,2^+)$	2^+
	2274.21	4255(620)			
	2293.70	8840(768)			
	2298.12	2780(536)	M1+E2	$1^+,2^+$	2^+
2915.5	2375.18	621873(6430)			
2915.5	2376.34	6430220(7303)	E1	2^-	2^+
	2448.54	43464(156)			
	2470.12	59058(173)	M2	2^-	0^+
	2518.21	4849(134)	E1	1^-	0^+
3060.3	2522.16	3808(135)	M1	2^-	2^+
	2526.69	32666(439)		4^+	2^+

Table B.3. Observed γ-ray transition in this measurement.

E_i	E_γ	I_γ	$M\lambda$	I_i^π	I_f^π
	2527.93	18028(638)		$(1,2)^-$	2^+
3069.9	2531.22	483421(705)	E2	4^+	2^+
	2534.91	4939(324)			
	2615.73	1096083(1618)	E2	2^+	0^+
	2619.38	7306(432)			
2661.4	2661.44	1576(73)		$1,2^+$	0^+
	2695.26	1258(64)			
	2722.21	282(79)			
	2735.35	1332(67)			
	2742.51	781(90)			
	2753.77	18976(97)			
	2783.21	2206(466)	M1	2^+	2^+
3324.7	2785.59	43841(142)	M1	2^+	2^+
	2793.50	381(122)			
	2801.33	468(101)			
	2813.43	494(79)			
	2822.63	351(71)			
	2864.74	661(72)			
3419.2	2880.00	928(89)		2^+	2^+
	2916.60	69157(173)		2^-	0^+
	2934.98	1827(62)		$(1,2^+)$	0^+
	2959.21	676(57)			
	3028.55	1324(136)			
	3034.92	1421(103)			
	3059.90	15442(93)		$(1,2^-)$	0^+
3069.9	3070.90	5424(623)	M2	$(1,2^-$	0^+
	3073.14	4636(623)		2^+	0^+
	3198.79	1386(94)			
	3202.84	669(92)			
3325.1	3325.09	2330(64)		2^+	0^+
	3418.62	1864(63)		2^+	0^+
	3436.39	523(55)			
	3464.68	1630(61)		$(1^+,2)$	0^+
	3540.77	5071(87)			
	3593.62	472(59)			
	3611.01	384(53)			
	3710.28	585(59)			
	3738.90	677(58)			

Appendix C

Code used to drive the tape station

```
from org.csstudio.opibuilder.scriptUtil import PVUtil
from org.csstudio.opibuilder.scriptUtil import ConsoleUtil
from org.csstudio.opibuilder.scriptUtil import ColorFontUtil
from org.csstudio.opibuilder.scriptUtil import GUIUtil
from java.lang import Thread
from java.lang import Runnable
from time import sleep
from time import time
class MyTask(Runnable):


def run(self):
PVUtil.writePV(("RFM_COUNT:snlState", 0)
sleep(1)
PVUtil.writePV("RFM_COUNT:snlState", 1)
sleep(1)
setpoint = 0
stepSize = PVUtil.getDouble(display.getWidget("distance").getPV())
ConsoleUtil.writeInfo(str(stepSize))
stepSize1 = PVUtil.getDouble(display.getWidget("distance_1").getPV())
ConsoleUtil.writeInfo(str(stepSize1))
sleepImplant = PVUtil.getDouble(display.getWidget("sleepImplantation").getPV())
ConsoleUtil.writeInfo(str(sleepImplant))
#sleeptransport = PVUtil.getDouble(display.getWidget("sleeptransport").getPV())
#ConsoleUtil.writeInfo(str(sleeptransport))


number = PVUtil.getDouble(display.getWidget("number of movement").getPV())
```

```
ConsoleUtil.writeInfo(str(number))
movement = PVUtil.getDouble(display.getWidget("Signal").getPV()) #LED light
security = PVUtil.getDouble(display.getWidget("Signal1").getPV()) #LED light
ConsoleUtil.writeInfo(str(movement))
move = 1


start_process = time()
start_implant = time() #time information
#Disable DRIVE
#PVUtil.writePV("RFM_COUNT:driveEnable", 0)
ConsoleUtil.writeInfo("starting the for loop")


for i in range (0, int(number)):
PVUtil.writePV("RFM_COUNT:driveEnable", 0)
ConsoleUtil.writeInfo("inside the for loop")
start = PVUtil.getDouble(display.getWidget("startB").getPV())
#sleep(sleepImplant) #implantation
while (setpoint < (stepSize)):
ConsoleUtil.writeInfo("inside the while loop")
sleep(sleepImplant) #implantation time e.g. 14sec
#PVUtil.writePV("RFMC:3:CHANNEL1:OUTPUT", 1) #deflecting the beam
#PVUtil.writePV("RF_PSEL_Logic:Beam_Chopper_Control", 0) #deflecting the beam
end_implant = time()
ConsoleUtil.writeInfo("Transporting")
elapsed_time_implant = round(end_implant - start_implant,2)
PVUtil.writePV("loc://elapsed_time_implant", elapsed_time_implant) #implatation time
setpoint = setpoint + stepSize #transportation, beam is deflected or no beam on the target
PVUtil.writePV("RFM_COUNT:CL_setpoint_dist", setpoint) #read increment of the set-
point


#Enable DRIVE
safety = PVUtil.getDouble(display.getWidget("Signal1").getPV())
if safety!=1:
PVUtil.writePV("RFM_COUNT:driveEnable", 1)
start_move = time()
actual = PVUtil.getDouble(display.getWidget("Actual").getPV())
while actual- setpoint < 0:
```

```
ConsoleUtil.writeInfo("Transporting")
actual = PVUtil.getDouble(display.getWidget("Actual").getPV())


#Disable DRIVE
PVUtil.writePV("RFM_COUNT:driveEnable", 0)
end_move = time()
elapsed_time_move = round(end_move - start_move,2)
PVUtil.writePV("loc://elapsed_time_move", elapsed_time_move) #transport time
PVUtil.writePV("loc://move", move)
move = move + 1 #counting the number of movements
ConsoleUtil.writeInfo("Implantation and Counting")
#PVUtil.writePV("RFMC:3:CHANNEL1:OUTPUT", 0) #beam back on the target
#PVUtil.writePV("RF_PSEL_Logic:Beam_Choppe_Control", 1)
#PVUtil.writePV("RF_PSEL_Logic:Beam_Chopper_Control", 0)
#ConsoleUtil.writeInfo(setpoint)
ConsoleUtil.writeInfo("about to enter last loop")
#ConsoleUtil.writeInfo(setpoint)


while setpoint > 0:
sleep(sleepImplant)
#ConsoleUtil.writeInfo("moving back the target")
#PVUtil.writePV("loc://elapsed_time_implant", elapsed_time_implant)
#implatation time
setpoint = setpoint - stepSize1 #transportation, beam is deflected or no beam on target
PVUtil.writePV("RFM_COUNT:CL_setpoint_dist", setpoint) #read increment of the set-
point


#Enable DRIVE
safety = PVUtil.getDouble(display.getWidget("Signal1").getPV())
if safety!=1:
PVUtil.writePV("RFM_COUNT:driveEnable", 1)
start_move_neg = time()
actual = PVUtil.getDouble(display.getWidget("Actual").getPV())
while actual - setpoint > 0:
ConsoleUtil.writeInfo("Transporting")
actual = PVUtil.getDouble(display.getWidget("Actual").getPV())
```

```
#Disable DRIVE
PVUtil.writePV("RFM_COUNT:driveEnable", 0)
end_move_neg = time()
elapsed_time_move_neg = round(end_move_neg - start_move_neg,2)
PVUtil.writePV("loc://elapsed_time_move_neg", elapsed_time_move_neg) #transport time
#ConsoleUtil.writeInfo("Implantation and Counting, moving back")
#if setpoint < -1:
#setpoint == actual


if start == 1:
PVUtil.writePV("RFM_COUNT:snlState", 0)
sleep(1)
PVUtil.writePV("RFM_COUNT:snlState", 1)
sleep(1)
end_process = time()
elapsed_time_process =round(end_process - start_process,2)
PVUtil.writePV("loc://elapsed_time_process", elapsed_time_process)
thread =Thread(MyTask());
thread.start()
```